THERMODYNAMIC MODELING OF METAL IMMOBILIZATION BY BIOCHAR

by

Md Samrat Alam

A thesis submitted in partial fulfillment of the requirements for the degree of

Doctor of Philosophy

Department of Earth and Atmospheric Sciences
University of Alberta

ABSTRACT

Biochar is a cost-effective sorbent owing to its low production cost and its ability to efficiently remove metals and organics from water. Developing mechanistic and predictive geochemical models of metals immobilization by biochar that are predictive across wide ranges of environmental conditions is important to understand its behavior toward metals in nature and to enhance its use for remedial application. Such models, requires detailed information about biochar surface chemistry and reactivity. The studies in this thesis provide critical insights into metal-biochar surface reactions at molecular-scale by answering questions including: (1) Can the adsorption of divalent cations and radionuclides at the biochar surface be predicted by the surface complexation modeling (SCM) approach across a wide range of water chemistry conditions? (2) Can the SCM approach predict metal adsorption in multi-sorbent systems involving biochar? (3) To what extent can biochar, whether by itself or as part of a composite material, reduce redox-sensitive metals such as Cr(VI)?

Following thorough characterization of biochar, I employ two thermodynamic approaches, (i) surface complexation modeling (SCM) and (ii) isothermal titration calorimetry (ITC), supported by synchrotron based X-ray absorption spectroscopy (XAS), to develop predictive and mechanistic models of the binding of divalent metals (Ni(II) and Zn(II)) and a radionuclide (U(VI)) to biochar. The results show that Ni (II), Zn(II) and U(VI) adsorbed through proton-active -COOH and -OH functional groups on the biochar surface, as confirmed by FT-IR studies coupled with EXAFS. The SCM approach is able to accurately predict the adsorption of Ni(II), Zn(II) and U(VI) across a wide range of water chemistries and at varying adsorbent to adsorbate concentrations. The thermodynamic driving forces of protonation adsorption reactions on the biochar surface suggest that the biochar surface contains anionic

oxygen ligands, and Ni(II), Zn(II) and U(VI)-biochar surface adsorption reactions have slightly exothermic to slightly endothermic enthalpies. Ni(II), Zn(II) and U(VI) form both inner- and outer-surface complexes with the biochar surface. The combined SCM-ITC approaches, supported by EXAFS, enhance our understanding of the molecular scale mechanisms of divalent cations and radionuclides adsorption to the surface of biochar. I also test a non-electrostatic SCM approach to predict the adsorption of Cd and/or Se in mixtures of biochar to two agricultural soils. The results show that the metal adsorption to biochar amended soils is successfully predicted by SCM the approach. However, it may be necessary to invoke ternary complexes to accurately predict metal removal from solution if organic ligands are present in solution. Generally, this approach could be useful to develop predictive models of metal distribution in biochar containing multi-sorbent systems. Moreover, I test the redox properties of biochar to reduce chromate from solution, and the efficiency of biochar as a composite material combined with magnetite nanoparticles to enhance Cr(VI) removal from aqueous solution. The results show that both adsorption and reduction of Cr(VI) is enhanced by magnetite nanoparticle – biochar composites compared to biochar and magnetite nanoparticles alone, suggesting a synergetic interaction between magnetite nanoparticle and biochar. Cr(VI) immobilization by magnetite nanoparticle – biochar composites occurs through adsorption and intraparticle diffusion followed by reduction. Synchrotron-based XAS shows that all of the Cr(VI) is reduced to Cr(III) and that the Cr(III)-bearing precipitates $Cr(OH)_3$ and chromite (Cr_2FeO_4) are formed. This result has important implications for the use of magnetite nanoparticle – biochar composites as a low-cost and efficient material for treating chromate-containing solutions.

PREFACE

This thesis is an original work by Md. Samrat Alam. The main body of this thesis is consisting of four chapters, described as following:

Chapter 2 of this thesis has been published as Alam, M.S., Gorman-Lewis, D., Chen, N., Flynn, S.L., Ok, Y.S., Konhauser, K.O., Alessi, D.S. (2018b) "Thermodynamic analysis of nickel (II) and zinc (II) adsorption to biochar." *In press, Environmental Science & Technology.* Md. Samrat Alam designed and conducted the experiments, analyzed the experimental results, and wrote and revised the manuscript under the supervision of Drs. Daniel S. Alessi and Kurt Konhauser. Dr. Drew Gorman-Lewis assisted in running ITC experiments and in modeling ITC data. Dr. Ning Cheng helped with modeling and interpreting XAS data. Dr. Shannon Flynn helped with analyzing samples using ICP-MS and in interpreting wet chemical data. Dr. Yong Sik Ok provided SSBC biochar, and helped interpreting biochar characterization.

Chapter 3 of this thesis has been submitted to a *peer-reviewed journal* as Alam, M.S., Gorman-Lewis, D., Chen, N., Safari, S., Baek, K., Konhauser, K.O., Alessi, D.S. "Mechanisms of the removal of U(VI) from aqueous solution using biochar: A combined spectroscopic and modeling approach". Md. Samrat Alam designed and conducted the experiments, analyzed the experimental results, and wrote and revised the manuscript under the supervision of Drs. Daniel S. Alessi and Kurt Konhauser. Dr. Drew Gorman-Lewis guided the ITC experiments and conducted the modeling of ITC data. Dr. Ning Cheng assisted XAS analyses and with modeling of XAS data. Dr. Salman Safari conducted zeta potential measurements and aided with interpreting data, and Dr. Kitae Baek helped with analyzing experimental results.

Chapter 4 of this thesis has been published as Alam, M.S., Swaren, L., von Gunten, K., Cossio, M., Bishop, B., Robbins, L. J., Hou, D., Flynn, S. L., Ok, Y. S., Konhauser, K. O.,

Alessi, D. S. (2018a) “Application of surface complexation modeling to trace metals uptake by biochar-amended agricultural soils.” *Applied Geochemistry* 88: 103-112. Md. Samrat Alam designed and conducted the experiments, analyzed the experimental results, and wrote and revised the manuscript under the supervision of Drs. Daniel S. Alessi and Kurt Konhauser. Logan Swaren helped with running batch adsorption experiments. Konstantin von Gunten assisted with sequential extraction and interpreting data. Manuel Cossio collected soil samples. Brendan Bishop helped with potentiometric titration. Leslie Robbins and Dr. Deyi Hou helped with analyzing experimental results. Dr. Shannon Flynn helped with analyzing samples using ICP-MS and in interpreting wet chemical data. Dr. Yong Sik Ok provided WPC biochar, and helped with interpreting biochar characterization.

Chapter 5 of this thesis will be submitted to a *peer-reviewed journal* as Alam, M.S., Bishop, B., Chen, N., Safari, S., Warter, V., Byrne, J., Warchola, T., Kappler, A., Konhauser, K.O., Alessi, D.S. Magnetite nanoparticle – biochar composites for efficient removal of chromate from water”. Md. Samrat Alam designed and conducted the experiments, analyzed the experimental results, and wrote and revised the manuscript under the supervision of Drs. Daniel S. Alessi and Kurt Konhauser. Brendan Bishop helped with running batch adsorption and reduction experiments. Dr. Ning Cheng helped with modeling and interpreting XAS data. Dr. Salman Safari conducted zeta potential measurements and interpreting data. Viola Water and James Bryne helped with running Mössbauer measurements and interpreting data. Tyler Warchola helped with running ferrozine and interpreting data. Dr. Andreas Kappler helped with analyzing experimental results.

ACKNOWLEDGEMENTS

I would like to express my sincere gratitude to my supervisors, Drs. Daniel S. Alessi and Kurt Konhauser, for their mentoring, guidance and support. It has been an extraordinary experience working with them. They provided me with unwavering encouragement in various ways during my doctoral studies. I would also like to thank my committee member, Dr. Tariq Siddique, for providing me advice and assistance.

I would like to thank the Natural Sciences and Engineering Research Council of Canada for providing funding to support our research work. I would also like to thank Canadian Light Sources for providing me travel award for my research work.

I would like to thank the members of our research group for their assistance. Special thanks to Nathan Gerein in the Scanning Electron Microscopy Lab and Diane Caird in the XRD Diffraction Laboratory, Department of Earth and Atmospheric Sciences, for their help with SEM and XRD analysis. I would like to thank Arlene Oatway in the Microscopy Unit, Biological Sciences, for her help with TEM imagining, and Anqiang He in the nanoFAB Fabrication and Characterization Centre for his assistance with HRTEM-SAED and XPS measurement.

Finally, I am grateful to my parents, my wife and friends and family members for their support and encouragement during my studies. I dedicate my thesis to them.

TABLE OF CONTENTS

LIST OF TABLES

LIST OF FIGURES

CHAPTER 1

INTRODUCTION

1.1 Overview and Research Questions

The fate, mobility and bioavailability of heavy metals in the natural environment are largely governed by their speciation (Tack and Verloo, 1995; Van Leeuwen et al., 2005; Reeder et al., 2006). A range of processes, including adsorption of aqueous ions and complexes onto environmental surfaces (i.e., bacterial, organic and mineral surfaces), precipitation, dissolution of minerals and oxidation-reduction reactions, control the fate, mobility, distribution and bioavailability of heavy metals (Sparks, 2005). Developing a predictive geochemical model of the mobility of heavy metals in the environment and the removal of heavy metal cations and radionuclides from solution by sorbents depends on accurate quantification of the surface functional groups (sites), their protonation constants, and the reactivity towards specific metals (Koretsky, 2000; Borrok et al., 2005; Alessi and Fein, 2010).

Biochar, a carbon-rich solid, can be produced through reductive thermal processing and/or pyrolysis of biomass derived from a variety of feedstocks (Cao et al., 2009; Cao et al., 2010; Dong et al., 2011; Ahmad et al., 2014; Alam et al., 2016). It is also a major byproduct of forest fires globally, and has profound influences on nutrient cycling, such as soil nitrogen (N) dynamics, in the underlying soils and sediments (DeLuca et al., 2005; Thomas and Gale, 2015). Biochar contains a range of surface functional groups which are activated by thermal alteration of the parent organic materials (Ahmad et al., 2014). Time, heat, pressure and physical characteristics of biomass are important parameters to consider during the commercial production of biochar. In particular, pyrolysis temperature plays important role in the density and

nature of functional groups on the resulting biochar (Uchimiya et al., 2012; Ahmad et al., 2014; Vithanage et al., 2015). Variability of biochar quality can be minimized if the parameters are well constrained within the production plant (Woolf et al., 2010; Ahmad et al., 2014).

Biochar has recently been received worldwide attention as a sorbent to remediate contaminated soils and waters (Cao et al., 2009; Cao et al., 2010; Mohan et al., 2011; Choppala et al., 2012; Alam et al., 2016; Thompson et al., 2016), to improve soil fertility by increased retention of nutrients (Uchimiya et al., 2012; Laird and Rogovska, 2015; Lehmann et al., 2015) and to play an important role as a sink for atmospheric carbon dioxide (CO_2) (Woolf et al., 2010). Biochar is cost-effective compared to many sorbents, including activated carbon (AC), graphene oxides, wheat straw, activated sludge, bagasse fly ash, blast furnace waste and coals that have been used to remove metals from aqueous media, and it has also been shown to have among the highest sorption capacity for contaminant removal from aqueous solution (Chen and Lin, 2001, Mohan and Pittman, 2006; Mohan et al., 2011; Choppala et al., 2012; Teixidó et al., 2013; Hadjittofi and Pashalidis, 2015; Thompson et al., 2016).

Determining biochar surface chemistry and reactivity is not only important for engineered remediation solutions, but also for understanding its behavior toward metals in nature. An understanding of specific metal-biochar adsorption reactions is needed in order to develop mechanistic and predictive geochemical models of metals adsorption to biochar. Two metal adsorption modeling approaches are common: empirical models and surface complexation models (SCM) (Bethke and Brady, 2000; Koretsky, 2000). Empirical models, which do not often consider the formation of discrete surface complexes, may not be reliable because they are not able to account for changes to factors such as pH, ionic strength, and sorbent-to-sorbate ratio in dynamic environmental systems (Bethke and Brady, 2000; Koretsky, 2000). On the other hand,

surface complexation modeling (SCM) is a quantitative approach, and is premised on considering the full aqueous speciation of the metal(s) of interest, and is grounded on balanced chemical reactions. Therefore, it can account for changes in water chemistries including pH and adsorbent:adsorbate ratios (Beveridge and Murray, 1980; Manceau and Charlet, 1994; Bethke and Brady, 2000; Koretsky, 2000; Borrok et al., 2005; Alessi and Fein, 2010). Indeed, almost all recent studies of metal uptake by biochar have relied on empirical models, without understanding the underlying metal adsorption reactions at the biochar surface (Mohan and Pittman, 2006; Cao et al., 2009; Cao et al., 2010; Mohan et al., 2011; Chen et al., 2012; Choppala et al., 2012; Zhang et al., 2013; Hadjittofi and Pashalidis, 2015; Zhou et al., 2017). To address this gap, my dissertation research focuses on developing a molecular-level understanding of heavy metal adsorption and reduction by biochar, in order to develop predictive and mechanistic models of metal binding to its surface. This thesis focuses on several key questions within this overall aim that relate to the immobilization of metals or radionuclides by biochar, including:

1. Can the SCM approach, grounded in thermodynamic theory, predict the distribution of divalent cations (Ni (II) and Zn (II)) and a radionuclide (UO_2^{2+}) at the surface of the biochar across changes in pH, water chemistries and metal-to-sorbent ratios? What are the optimum geochemical conditions needed to achieve maximum co-sorption of Ni (II) and Zn (II), and UO_2^{2+} adsorption on the surface of the biochar? How is metal uptake impacted by the pyrolysis temperature of biochar? Testing such research questions is important, as few studies have applied a SCM approach to biochar. Examples include Zhang and Luo (2014), who used the SCM approach to model copper (Cu) adsorption to biochar, and Vithanage et al. (2015) who used SCM to model antimony (Sb) adsorption; however, these authors did not directly measure the surface coordination of adsorbed ions at the biochar surface, and thus the coordinations they

invoke are speculative. In Chapter 2 and 3, I employ synchrotron-based extended X-ray absorption fine structure (EXAFS) spectroscopic analyses to better understand the surface coordination of metals onto the surface of the biochar. In Chapters 2 and 3, I report on studies that employed two thermodynamic approaches, (i) surface complexation modeling (SCM) and (ii) isothermal titration calorimetry (ITC), which were supported EXAFS, to develop predictive and mechanistic models of metal binding to biochar.

2. Can the SCM approach be used to predict the uptake of trace metals by biochar-amended agricultural soils? Understanding the effects of biochar amendment on the distribution of trace metals in soil is critical to its use in agricultural applications. Therefore, developing a flexible approach that can predict the impacts of biochar amendment on metal mobility in complex geologic media such as agricultural soils is needed. While the application of SCM to soils is well-studied, the application of surface complexation theory to biochar is now just emerging, as noted above. To my knowledge, a multi-sorbent SCM approach that includes biochar has not yet been developed. In this study (Chapter 4), I investigate the impact of biochar amendment on the adsorption of Cd(II) and Se(VI), a model cation and anion, respectively, to two agricultural soils. Following, I use a non-electrostatic SCM to predict the distribution of Cd and/or Se in soil-biochar mixtures.

3. Can biochar reduce redox-sensitive metals such as Cr(VI)? What are the kinetics of adsorption and electron transfer (reduction) of Cr(VI) at the surface of the biochar, and what are the products of Cr(VI) reduction by biochar? Can biochar be used as a component of a composite material, such as with magnetite nanoparticles, to enhance Cr(VI) immobilization? What are the products of Cr(VI) reduction by magnetite nanoparticle-biochar composites? How does solution chemistry influence the extent and kinetics of Cr(VI) adsorption and reduction? Biochar can

donate, accept and transfer electrons either biotic or abiotic pathways in their surrounding environments (Keiluweit et al., 2010; Kappler et al., 2014; Yu et al., 2015). While the adsorption capacity of biochar has been well studied, biochar-mediated reduction processes are not well understood. To enhance the use of biochar as a technology to treat redox-sensitive metals, it is important to understand the kinetics of redox reactions involving biochar across a range of solution pH. To answer these questions (Chapter 5), I synthesized magnetite nanoparticle – biochar composites, and tested the kinetics of Cr(VI) immobilization by the composite material and its component parts at acidic to neutral pH. Finally, the chemistry of the resulting Cr(III) products of were determined using spectroscopic methods.

1.2 Thermodynamic Modeling of Divalent Cation and Radionuclide Adsorption on Biochar

To accurately predict the fate and transport of heavy metals by biochar, it is critical to know the identity and density of surface functional groups (sites) at its surface, and their reactivity to protons (i.e., to changes in pH) and metals (Koretsky, 2000; Borrok et al., 2005; Alessi and Fein, 2010). It is well-established that bacteria, clay, hydrous ferric oxides (HFO) and silica can adsorb metals to their functional groups (Beveridge and Murray, 1980; Manceau and Charlet, 1994; Manning and Goldberg, 1997; Uchimiya et al., 2012), and that they play important roles in the distribution and mobility of metals in many geologic systems (Karthikeyan and Elliott, 1999; Marmier et al., 1999; Borrok et al., 2005; Alessi and Fein, 2010; Tan et al., 2011). Metal adsorption data are modelled using two general categories of models: empirical models and surface complexation models (SCM). Studies using empirical formulas to model adsorption data may not be able to make reliable predictions, because they do not consider factors including metal competition for attachment to surface functional groups and surface heterogeneity of sorbents in dynamic environmental systems (Bethke and Brady, 2000;

Koretsky, 2000). For example, the distribution coefficient (K_d) is a type of empirical model that defines the partitioning of a metal between aqueous solution and the bulk geologic solids as a simple linear ratio. Though K_d models are an easy way to model heavy metal distribution, molecular-scale information on binding mechanisms is not considered. Furthermore, the K_d model assumes an unlimited number of available surface sites for metal sorption, which, for example, ignores the metal saturation of the sorbent surface (Bethke and Brady, 2000; Koretsky, 2000). The Freundlich and Langmuir adsorption modeling approaches (K_F, K_L) expand on the K_d approach by allowing for decreasing metal adsorption capacity with increasing saturation of the solids with metal; however metal speciation in solution or on the solid sorbent is not considered. The K_L approach also does not consider a sorbent's surface heterogeneity and competition of metals for sorption at the biochar surface sites (Bethke and Brady, 2000; Koretsky, 2000; Borrok et al., 2005). Generally the constants calculated using empirical models are not valid across changes in metal concentration, pH, competing ions, and temperature (Bethke and Brady, 2000; Koretsky, 2000; Borrok et al., 2005). If these factors change, new experiments must be conducted in the laboratory to calculate a new empirical constant (K_d K_F, or K_L) that is valid for the new system conditions (Bethke and Brady, 2000; Koretsky, 2000; Borrok et al., 2005). Therefore, the application of empirical partitioning constants can be problematic to dynamic environmental systems.

On the other hand, the SCM approach can predict the acid/base and ion/metal binding behaviors onto a variety of environmental surfaces (Fein et al., 1997; Karthikeyan and Elliott, 1999; Marmier et al., 1999; Bethke and Brady, 2000; Koretsky, 2000; Borrok et al., 2005; Fein et al., 2005, Alessi and Fein, 2010; Tan et al., 2011). Thus, using the SCM approach, the overall distribution of metals in a system can be predicted from stability constants of sorbent-metal

surface complexes (Fein et al., 1997; Bethke and Brady, 2000; Borrok et al., 2005). The SCM approach can also account for heterogeneity of the sorbents, electrostatic effects due to change in the surface charge of the sorbent, changes in pH, ionic strength, and metal speciation, and competition of the metal of interest with other metals in solution for adsorption onto the solid surfaces (Bethke and Brady, 2000; Koretsky, 2000; Borrok et al., 2005). In the most general sense, protonation/deprotonation and metal-binding reactions of the functional groups present on the biochar surface can be described as (Borrok et al., 2005):

$$R - A(H)^0 \leftrightarrow H^+ + R - A^- \quad (1)$$

$$R - A(H)^0 + M^{++} \leftrightarrow R - A(M)^+ + H^+ \quad (2)$$

where, R represent the biochar macromolecule to which the functional group type A is attached, and M^{++} represents metals that biochar can sorb.

The acidity constant, K_a, for reaction (1) can be calculated as:

$$K_a = \frac{[R-A^-]a_{H^+}}{[R-AH^0]} \quad (3)$$

where, a_{H^+} represents the activity of protons in the bulk solution and, [R-A^-] and [R-AH^0] represent the concentration of deprotonated and protonated sites at equilibrium, respectively.

The metal binding equilibrium constant for metal M^{++}, $K_{M,}$ for reaction (2) can be written as:

$$K_{M^{++}} = \frac{[R-AM^+]a_{H^+}}{[R-AH^0]a_{M^{++}}} \quad (4)$$

where, [R-AM^+] represents the concentration of biochar functional group A that is complexed with M^{++}, and $a_{M^{++}}$ is the activity of M^{++} in solution after equilibrium is attained.

While SCM can model the adsorption of metal ions onto sorbents across variable chemical condition, the SCM approach does not provide any direct evidence about the surface

coordination of adsorbed ions. Synchrotron-based EXAFS studies are a powerful tool that can provide insights into metal-surface complexes formed, at an atomic level, and this information is key for developing rigorous predictive models by the SCM approach (Scheidegger et al., 1997; Elzinga and Reeder, 2002; Tan et al., 2011; Betts et al., 2013). However, they do not provide information to determine the thermodynamic driving forces that may involve processes such as bond formation, dehydration, enthalpy and entropy of the metal-surface reaction(s) (Gorman-Lewis et al., 2006 Gorman-Lewis, 2014; Du et al., 2016). Isothermal titration calorimetry (ITC) provides direct measurements of the enthalpy of reactions (ΔH) (Gorman-Lewis et al., 2006; Gorman-Lewis, 2014). Formation constants calculated from surface complexation modeling can be used to calculate Gibbs energy (ΔG_r), where R is the gas constant and T is the absolute temperature, according to equation (5). The entropy of reaction (ΔS_r) can then be calculated using equation (6). Combining calorimetric data and surface complexation modeling yields necessary data to determine the driving forces for reactions (Gorman-Lewis et al., 2006; Gorman-Lewis, 2014).

$$\Delta G = 2.3026 \times R \times T \times \log K \quad (5)$$

$$\Delta G = \Delta H - T\Delta S \quad (6)$$

In our study, we use a combination SCM, XAS and ITC for the first time to understand the molecular scale mechanisms of Ni(II), Zn(II) and U(VI) adsorption onto various types of biochar. In Chapters 2 and 3, after thorough characterization of the biochar, I conduct potentiometric titrations to measure the proton (H^+) reactivity of each biochar, and then I develop protonation models. Following, metal adsorption experiments were conducted, and the adsorption data used to model metal-biochar binding constants. Information on molecular scale metal-biochar surface reactions was obtained thorough EXAFS modeling, and the surface

reactions further used to inform the SCM. Finally, the SCM results were combined with ITC data to determine the thermodynamic driving forces of metal adsorption. Overall, these combined approaches provide a better understanding of molecular scale mechanisms of divalent cation and radionuclide adsorption onto the surface of biochar.

1.3 Surface Complexation Modeling of Trace Metal Adsorption by Biochar-Amended Agricultural Soils

Long-term risks to ecosystems and humans could be caused by high concentrations of potentially toxic metals in soils, which are often persistent and difficult to remove once they accumulate in soils (Gray et al., 2006; Querol et al., 2006; Liu et al., 2009; Jiang et al., 2012). Inorganic minerals and organic materials including zeolite, lime and red-mud and chicken manure have been proposed and studied as soil amendments to immobilize these metals in soils. However, their uses have been costly and have not produced sufficiently positive results (Gray et al., 2006; Querol et al., 2006; Liu et al., 2009). In contrast, recent studies have showed that biochar is highly effective to increase soil fertility and immobilize trace metals because of its microporous structure, charged functional groups and cation exchange capacity (CEC) (Chean and Lin, 2001; Uchimiya et al., 2012; Rees et al., 2014; Laird and Rogovska, 2015; Lehmann et al., 2015). In order to understand how biochar amendment will influence soil chemistry, it is critical to determine the underlying reactions that occur between metals and biochar in complex, multi-component systems. This knowledge forms the basis for developing a flexible model that can predict the metal mobility in biochar amended agricultural soils. Multi-sorbent systems including soils and microbes have been well studied (Dzombak and Morel, 1990; Fein et al., 1997; Cox et al., 1999; Fein, 2006; Komárek et al., 2015; Flynn et al., 2017). There are two methods, based in SCM theory, to model metal distribution in multi-component systems or complex assemblages of sorbents: the component additivity (CA) approach and the general

composite (GC) approach (Davis et al., 1998). The CA approach can predict the adsorption of metals onto multi-component sorbents by invoking the proton- and metal-surface complex stability constants for each individual sorbent in the mixture (Davis et al., 1998; Fowle and Fein, 1999; Pagnanelli et al., 2006). In contrast, the GC approach investigates the reactivity of a multi-component sorbent by assigning generalized sites to the mixture, rather than groups specific to individual sorbents (Davis et al., 1998; Fowle and Fein, 1999; Pagnanelli et al., 2006). Such an approach does not identify specific metal-surface functional group pairs, but allows for metal adsorption data to be considered within the flexible and predictive framework of SCM theory. Previous studies showed that the non-electrostatic modeling (NEM) approach, when combined with the CA approach, can successfully predict metal adsorption to mixtures of pure minerals and bacteria, respectively (Davis et al., 1998; Fowle and Fein, 1999; Pagnanelli et al., 2006; Alessi and Fein, 2010). To date, no studies involving multi-component sorbents that include biochar have employed a surface complexation model.

To test if the SCM approach can be applied to complex, multi-sorbent systems involving biochar, I tested whether the CA approach is successful in predicting metal adsorption to biochar amended agricultural soils collected from Alberta, Canada. To conduct the experiments, I use Cd(II) and Se(VI) as a model cation and anion, metals that could be present in soils as contaminants of concern. I employ a non-electrostatic SCM approach to model Cd(II) and Se(VI) adsorption to soils and biochar individually, and by using the resulting binding constants, I further develop predictions of Cd(II) and Se(VI) adsorption in mixed systems containing both soil and biochar. Broadly, this approach is useful in developing predictive models of multi-component systems that contain biochar as a sorbent, that are capable of accounting for changes in factors such as pH, ionic strength and metal-to-sorbent ratios.

1.4 Enhanced Chromate Removal by Magnetite Nanoparticles – Biochar Composites

The presence of hexavalent chromium [Cr(VI)] in aquatic systems and drinking water sources as a result of human activities and natural processes poses a serious risk to the environment and human health (Palmer and Wittbrodt, 1991; Costa and Klein, 2006; Zhitkovich, 2011). Cr(VI) is highly mobile in the environment, and is shown to be toxic and carcinogenic (Katz and Salem, 1993; Shevchenko et al., 2008). Following adsorption, the reductive immobilization of Cr(VI) to Cr(III) presents a potential remediation strategy in reducing risk to the environment and human health posed by chromium contamination, because the reduced valence state of Cr is insoluble and stable (Fendorf et al., 2000; Han et al., 2007; Owlad et al., 2009).

Besides its high sorption capacity for metals, biochar has significant redox capacity and can function as a reducing agent (Joseph et al., 2010; Kappler et al., 2014), although the reduction of redox-sensitive metals by biochar is not well studied. To date, only Cossio (2017) and Rajapaksha et al. (2018) showed preliminary direct spectroscopic evidence of Cr(VI) reduction to Cr(III) by biochar using synchrotron based X-ray absorption spectroscopy (XAS). Further study was needed to better constrain the kinetics of redox reactions involving biochar across a range of solution pH, and to determine the chemistry of the products of Cr(VI) reduction.

Fe^{II}-bearing minerals and Fe^{II} adsorbed to clay minerals provide a pool of reduction capacity whereby redox-sensitive contaminant metals can be reduced and immobilized via abiotic reduction (Eary and Rai., 1988; Patterson et al., 1997; Fredrickson et al., 2000). Magnetite (Fe_3O_4) nanoparticles are shown to be effective in removing Cr(VI) from aqueous solution because they are inexpensive, easily separable and possess high surface area (He et al.,

2005; Jung et al., 2007). However, magnetite start to aggregates at neutral pH, resulting in dramatically lower adsorption and reduction capacity of redox-sensitive metals (Peterson et al., 1997). Magnetite - biochar composites could have tremendous potential to remove Cr(VI) from aqueous solution at a range of pH because the biochar component can enhance the dispersity of MNPs and avoid agglomeration and passivation of magnetite under near-neutral and basic pH. Biochar has been used as a substrate to support zero valent iron (ZVI) and magnetite to enhance the sorption of Cr(VI). However, the underlying Cr(VI) reduction processes were not well studied (Su et al., 2016; Mandal et al., 2017).

In this study (Chapter 5), I test the kinetics of Cr(VI) reduction biochar, and determine the product of Cr(VI) reduction to Cr(III). In addition, I synthesize composites of magnetite nanoparticles and biochar in order to efficiently remove Cr(VI) from aqueous solution at acidic to neutral pH. Following, I use high resolution electron microscopy and X-ray absorption spectroscopy (XAS) analyses to develop an understanding of the molecular-scale reaction mechanisms of Cr(VI) onto the surface of the biochar and composites, and to determine the products of Cr(VI) reduction. The results from this study show that magnetite nanoparticle – biochar composites exhibit a strong synergetic effect that enhances both adsorption and reduction of aqueous Cr(VI) species as compared to each component sorbent alone. This study also provides a mechanistic understanding of adsorption and reduction of Cr(VI) on the surfaces of biochar and magnetite nanoparticle – biochar composites.

1.5 Organization of the Thesis

As noted above, the main objectives of this thesis are to gain a mechanistic understanding of the mechanisms of trace metals and radionuclide immobilization by biochar and magnetite nanoparticle – biochar composites, to develop predictive models of biochar-induced metal

removal from aqueous solution. This is a paper-based thesis, and the main body of this thesis consists of four manuscripts. Chapter two constitutes the manuscript entitled "Thermodynamic Analysis of Nickel (II) and Zinc (II) Adsorption to Biochar", which has been published in *Environmental Science & Technology* (Alam et al., 2018b). Chapter three constitutes the manuscript entitled "Mechanisms of the Removal of U(VI) from Aqueous Solution using Biochar: A Combined Spectroscopic and Modeling Approach", and a version of this manuscript is under review in a *peer-reviewed journal*. Chapter four constitutes the manuscript entitled "Application of Surface Complexation Modeling to Trace Metals Uptake by Biochar-Amended Agricultural Soils", which has been published in *Applied Geochemistry* (Alam et al., 2018a). Chapter five constitutes the manuscript entitled "Magnetite Nanoparticle – Biochar Composites for Efficient Removal of Chromate from Water", which is planned to be submitted to *a peer-reviewed journal*.

CHAPTER 2

THERMODYNAMIC ANALYSIS OF NICKEL (II) AND ZINC (II) ADSORPTION TO BIOCHAR

ABSTRACT

While numerous studies have investigated metal uptake from solution by biochar, few of these have developed a mechanistic understanding of the adsorption reactions that occur at the biochar surface. In this study, we explore a combined modeling and spectroscopic approach for the first time to describe the molecular level adsorption of Ni(II) and Zn(II) to five types of biochar. Following thorough characterization, potentiometric titrations were carried out to measure the proton (H^+) reactivity of each biochar, and the data was used to develop protonation models. Surface complexation modeling (SCM) supported by synchrotron-based extended X-ray absorption fine structure (EXAFS) was then used to gain insights into the molecular scale metal-biochar surface reactions. The SCM approach was combined with isothermal titration calorimetry (ITC) data to determine the thermodynamic driving forces of metal adsorption. Our results show that the reactivity of biochar towards Ni(II) and Zn(II) directly relates to the site densities of biochar. EXAFS along with FT-IR analyses, suggest that Ni(II) and Zn(II) adsorption occurred primarily through proton-active carboxyl (–COOH) and hydroxyl (–OH) functional groups on the biochar surface. SCM-ITC analyses revealed that the enthalpies of protonation are exothermic and Ni(II) and Zn(II) complexes with biochar surface are slightly exothermic to slightly endothermic. The results obtained from these combined approaches contribute to the better understanding of molecular scale metal adsorption onto the biochar

surface, and will facilitate the further development of thermodynamics-based, predictive approaches to biochar removal of metals from contaminated water.

2.1 INTRODUCTION

Biochar is a carbon-rich solid produced through the carbonization and/or pyrolysis of biomass derived from a variety of feedstocks, including straw, wood, and organic industrial wastes (Cao et al., 2009; Cao et al., 2010; Ahmad et al., 2014). It has proven effective in the removal of organic and metal contaminants from water (Mohan et al., 2006; Mohan et al., 2011; Choppala, et al., 2012; Alam et al., 2016), is considered a prospective alternative to activated carbon (AC) for water treatment and soil amendment purposes due to its lower production cost, and it is also thought to act as a global "carbon-sink" (Wolf et al., 2010; Thompson et al., 2016; Yang et al., 2016). The efficiency of contaminant removal from water by biochar depends on several factors, including contaminant concentration and the distribution and types of surface functional groups, the latter of which can vary widely depending on the pyrolysis temperature and types of feedstock used during production (Ahmad et al., 2012; Chen et al., 2012; Zhou et al., 2017). Relatively modest concentrations of Ni and Zn in water (> 10 µg/L for Ni and > 5 mg/L for Zn) are shown to have toxic effects on human health. Geogenic and anthropogenic inputs, especially from tanneries, smelters, or sewage sludge application, can increase Ni and Zn concentrations in the environment (Scheidegger et al., 1996; He at al., 2005). Therefore, understanding the mechanisms by which environmentally relevant divalent metals such as Ni and Zn are removed from aqueous solution by biochar is critical to assessing its use as an adsorbent.

Key to developing rigorous geochemical models that can accurately predict the removal of metal cations from solution by biochar is the identification and quantification of surface functional groups (sites), their protonation constants, and the reactivity towards specific metals

(Beveridge and Murray, 1980; Manning et al., 1997; Marmier et al., 1999; Bethke and Brady, 2000; Koretsky, 2000; Borrok et al., 2005; Lalonde et., 2007a, Alessi and Fein, 2010; Dong et al., 2013, Flynn et al., 2014; Liu et al., 2015; Hu et al., 2017). Metal adsorption data can be modeled using two general categories of models: (i) empirical models such as isotherms such as Freundlich and Langmuir, and (ii) thermodynamic approaches such as surface complexation modeling (SCM). Empirical models normally cannot account for changes in metal concentration, pH, ionic strength, temperature and complexation or for the effect of competing ions for sorbent sites. For this reason, the application of empirical partitioning constants to predict metal distribution in dynamic environmental systems can be problematic (Beveridge and Murray, 1980; Manning et al., 1997). In contrast, the SCM approach has been proven to be an effective method to predict the acid/base and ion/metal binding behaviors of a variety of environmental surfaces, and in systems approaching the complexity of those found in nature (Beveridge and Murray, 1980; Manning et al., 1997; Marmier et al., 1999; Bethke and Brady, 2000; Koretsky, 2000; Borrok et al., 2005; Lalonde et., 2007a, Alessi and Fein, 2010; Dong et al., 2013; Flynn et al., 2014; Liu et al., 2015). The primary advantage of using a SCM approach over empirical approaches is that the distribution of metals in a system can be predicted using the stability constants determined experimentally for individual sorbent-metal surface complexes, because the surface complexation theory is grounded in balanced chemical reactions, and ultimately, in chemical thermodynamics (Beveridge and Murray, 1980; Manning et al., 1997).

Recent studies which have modeled metal sorption by biochar have primarily relied on empirical metal adsorption models (Mohan et al., 2006; Cao et al., 2009; Cao et al., 2010; Mohan et al., 2011; Choppala, et al., 2012; Dong et al., 2013; Zhou et al., 2017). To our knowledge, few studies have applied a SCM approach to biochar: Zhang and Luo (2014) modeled copper (Cu)

adsorption to biochar; Vithanage et al. (2015) modeled antimony (Sb) adsorption to biochar; and Alam et al. (2018a) modeled the adsorption of selenium (Se) and cadmium (Cd) to biochar-amended agricultural soils. While these studies proposed SCMs that successfully describe the adsorption of metal ions onto sorbents across variable chemical conditions, they do not provide direct measurements of the surface coordination of adsorbed ions.

Here we apply two thermodynamic approaches, (i) surface complexation modeling (SCM) and (ii) isothermal titration calorimetry (ITC), supported by synchrotron-based X-ray absorption spectroscopy (XAS) to develop a predictive and mechanistic model of metal binding to biochar. Synchrotron-based extended X-ray absorption fine structure (EXAFS) studies are a powerful tool to identify the atomic metal-surface coordination environment (Scheidegger et al., 1997; Elzinga and Reeder, 2002; Tan et al., 2011; Betts et al., 2013). ITC measurements were further conducted to determine the thermodynamic driving force (e.g., bond formation, dehydration, enthalpy and entropy) of the metal-surface reaction(s). Understanding the thermodynamic driving forces of adsorption provides critical insights into the reasons why spontaneous adsorption reactions occur, as well as the temperature dependence of these reactions (Gorman-Lewis et al., 2006; Gorman-Lewis, 2011; Chen et al., 2012; Harrold and Gorman-Lewis, 2013; Gorman-Lewis, 2014). In this study, we aim to: (1) determine whether the surface complexation modeling approach can accurately predict Ni(II) and Zn(II) adsorption (as model divalent cations) to five types of biochar, (2) explore the metal-biochar surface reactions at molecular level, and (3) determine the thermodynamic driving forces of metal-biochar surface reactions. Using a varied set of biochar allowed us to investigate the potential effects of production scale, differing sources of biomass, and pyrolysis temperature on the metal adsorption behavior. Our study is the first to develop a predictive model of metal adsorption to biochar

underpinned by a mechanistic understanding of the adsorption processes at the surface of biochar. As such, our work opens the door to future studies that use the SCM approach as a flexible, predictive method to determine the removal of metals from water by biochar in variable water chemistries.

2.2 MATERIALS AND METHODS

2.2.1 Biochar Preparation

Biochar produced from wheat straw (WS) and wood pin chips (WPC) were obtained from the Alberta Biochar Initiative (ABI; Vegreville, Alberta, Canada). The raw feedstocks of WS and WPC were placed in a prototype 1.0, batch carbonizer (Alberta Innovates Technology Futures, AITF), and in an auger retort carbonizer (ABRI- Tech, 1 Tonne Retort system; ABI, Vegreville, Alberta), respectively, and pyrolized under limited oxygen conditions. The residence time in both cases was 30 min at 500°C to 550°C. The biochar yield was 30 to 33% on the basis of dry mass. Sewage sludge biochar (SSBC) was produced at the Korea Biochar Research Center, Kangwon National University, at a lab scale as described in Ahmad et al. (2012). The raw feedstocks were ground to <1 mm, and then dried at 60°C for 3 days. A muffle furnace (MF 21GS, Jeio Tech, Seoul, Korea) was used to pyrolyze the feedstock as follows: temperature was increased at a rate of 7°C/min under limited oxygen conditions, and the feedstocks were held for 3 hours at 300°C, 500°C and 700°C, respectively, followed by cooling to room temperature inside the furnace (Ahmad et al., 2012). These biochar are hereafter referred to as SSBC 300°C, SSBC 500°C, and SSBC 700°C.

2.2.2 Biochar Characterization

The proximate analyses, X-ray powder diffraction (XRD), elemental analysis, Brunauer-Emmett-Teller (BET) surface area analysis, Barret-Joyner-Halender (BJH) pore volume and pore

size distribution, surface morphological characterizations using Scanning Electron Microscopy (SEM) coupled with Energy Dispersive Spectroscopy (EDS) and Fourier transform infrared spectroscopy (FT-IR) analyses of WS, WPC, SSBC 300°C, SSBC 500°C, and SSBC 700°C were carried out as described in Alam et al. (2016, 2018a). A detailed explanation of the biochar characterization methods is given in Appendix A.

2.2.3 Potentiometric Titrations

Potentiometric titrations were conducted to determine the concentrations and protonation constants (K_a) values of proton-active surface functional groups. For each titration, approximately 0.2 g of dry biochar was suspended in 50 mL of 0.01 M $NaNO_3$ electrolyte solution. The sample containers were then sealed with Parafilm and purged with N_2 gas for 30 min prior to each titration and throughout the titration process to maintain a CO_2-free solution. For the forward titrations (pH 3-11) a solution of 0.1 M NaOH was used, and for the reverse titrations (pH 11-3) a 0.1 M HCl solution was used. Detailed titration methods and corresponding data modeling methods are reported in Appendix A.

2.2.4 Ni and Zn Adsorption Experiments

Batch adsorption experiments were carried out using aqueous solutions of Ni(II) and Zn(II). A 8.5 mM stock solution of Ni was prepared from $Ni(NO_3)_2.6H_2O$, and a 1.7 mM of Zn stock solution from $ZnCl_2$. In polypropylene test tubes, 10 g/l of biochar was suspended in 0.01M $NaNO_3$ electrolyte solution and a volume of Ni and Zn stock solution was added to achieve the target initial metal concentrations of 170 µM and 17 µM, for both Ni and Zn. The final volume of each experiment was approximately 10 mL. The pH of metal adsorption experiments ranged from approximately 2.0 to 6.5, and was achieved by adding small volumes of concentrated NaOH or HCl. This pH range was selected to avoid the precipitation of Ni and/or

Zn-hydroxides and/or carbonates, which were observed in control experiments above pH 6.5 and were predicted in aqueous Ni and Zn speciation diagrams generated for our experimental conditions (Figure A.S2.1).

Following pH adjustment, test tubes were then placed on a rotary shaker for 36 h to allow the pH to stabilize and for the adsorption of Ni and/or Zn to biochar surface functional groups to achieve equilibrium. Kinetics experiments were carried out to ensure that equilibrium had been achieved in 36 h (Figure A.S2.2). The tubes were then centrifuged at 5000 g for 10 min and the resulting supernatant was filtered through 0.45 μm nylon membranes (Millex HP). The filtered supernatants were then diluted 1:1 with 4 N HNO_3 before Ni and Zn were analyzed using inductively coupled plasma - mass spectroscopy (ICP-MS/MS; Agilent 8800). Control experiments showed that there was no adsorption of Ni(II) and Zn(II) onto the tubes used for the metal adsorption experiments. Aqueous Ni and Zn standards for ICP-MS/MS calibration were prepared from SPEX CertiPrep Ni and Zn ICP-MS standards and diluted with 0.01M $NaNO_3$ to match the experimental matrix. The difference between the initial Ni or Zn concentration in each experiment and the measured remaining Ni or Zn concentration in solution after equilibration was considered to be the amount adsorbed. To test competitive sorption of Ni and Zn to the biochar surface, Ni and Zn were mixed to a total initial concentration of 170 μM (85 μM Ni + 85 μM Zn) and 17 μM (8.5 μM + 8.5 μM Zn). The stock solution, pH adjustment, centrifugation, filtration, and acidification sampling procedures were the same as those described above for the individual-metal experimental systems. The experimental details of the kinetics experiments and details of the SCM approach used to model metal adsorption data are provided in Appendix A.

2.2.5 XAS Data Collection and Analysis

X-ray absorption spectroscopy (XAS) was used to study the coordination environments of Ni(II) and Zn(II) adsorbed to WS biochar, in experiments conducted at pH 6.5 at initial metal concentrations of 17 μM for single-metal systems, and at 170 μM for both single-metal and Zn+Ni systems. EXAFS analyses of Ni- and Zn-sorbed biochar were carried out at the Ni and Zn K-edges (8333 eV and 9659 eV, respectively) at the Canadian Light Source (CLS) 06ID-1 Hard X-ray Micro-Analysis (HXMA) beamline. A Si (220) double crystal monochromator was calibrated to the pre-edge feature of Ni and Zn at 8333 eV and 9659 eV, respectively, and detuned 40% the monochromator second crystal to reject higher harmonic intensities. Spectra for $Ni(OH)_2$, $Zn(OH)_2$, and Ni acetate were recorded in transmission mode. Spectra for the Zn acetate reference material and Ni- and Zn-sorbed biochar samples were recorded in fluorescence mode using a 32-element Ge solid state detector.

IFEFFIT and the graphical interface ATHENA were used for background subtraction and X-ray absorption near edge structure (XANES) linear combination fitting (Ravel and Newville, 2005). EXAFS data fitting R space curve fitting was carried out using WinXAS (version 2.3) (Ressler, 1997). The phase shift and backscattering amplitude function were generated theoretically with the FEFF 7 code (Ressler, 1997) from the crystal structure data of the crystal structure of Ni(II) (aq), NiO, β-$Ni(OH)_2$, ZnO, $Zn(OH)_2$. The R-space between 0.8 and 4.2 Å was considered for the fits of Fourier transform (FT) k^3-weighted EXAFS data to FEFF models, and a k space data range used for the Fourier Transform is of 3 – 10 $Å^{-1}$. The amplitude reduction factor (S_0^2) was set to 1 for all fits. The shift in the threshold energy (E_0) was allowed to vary for R space fitting (Ankudinov and Rehr, 2000; Rihs et al., 2014).

2.2.6 Isothermal Titration Calorimetry (ITC)

The ITC experiments were carried out as described in Harrold and Gorman-Lewis (2013) and Gorman-Lewis et al. (2006). Briefly, a TAM III nanocalorimeter was used to measure the heat flux between a reference and reaction vessel as a function of time. Electrical heating, a procedure verified by the heat of protonation of trishydroxymethylaminomethane (TRIS/THAM) at 25°C, was used to calibrate the heat flow response by the calorimeter (Grenthe et al., 1970; Turkarslan et al., 2017). Initially, both cells were filled with 10 g/L biochar suspensions in 0.01M NaCl and placed in the calorimeter bath. Biochar suspensions for proton adsorption measurements were purged with N_2 for 30 min prior to loading the suspensions into the reaction vessels, which were purged with N_2 and sealed. The reaction vessels were lowered into the calorimeter in 3 steps, pausing with each step to allow the calorimeter to equilibrate. After achieving thermal equilibration and a stable heat flow with the reaction cell stirred at 80 rpm, individual titrant doses were delivered into the reaction cell via cannula by a computer controlled syringe. The experimental details and modeling procedure for the ITC data are provided in Appendix A.

2.3 RESULTS AND DISCUSSION

2.3.1 Characteristics of Biochar

The WS and WPC yield from the parent biomasses was approximately 30% (Table A.S2.1). The SSBC yield decreased from 70.1% to 50.3% as the temperature of pyrolysis increased from 300°C to 700°C, with the variation in yield in WS, WPC and SSBC due to differences in types of feedstock and production conditions. According to Keiluweit et al. (2010) and Chen et al. (2015) the decomposition of lignin, cellulose, H_2O, CO_2, CO, CH_4 and H_2 from feedstock increases with increasing pyrolysis temperature, indicating mostly the loss of oxygen

containing functional groups and contributing to the lower yield. The XRD patterns (Figure A.S2.3) of WS and WPC show that quartz and calcite are the major detectable mineral phases. In SSBC, other minerals including albite, muscovite, kaolinite, microcline and pyrite are also detected as minor phases. WS and WPC are mainly composed of C, 70 wt% and 85 wt%, respectively, indicating higher carbonization (Table A.S2.2). However, SSBC has lower %C as compared to WS and WPC, and %C decreases with increasing pyrolysis temperature. The molar ratios of elements in each biochar were calculated to estimate their aromaticity (H/C) and polarity (O/C) (Wolf et al., 2010; Alam et al., 2016). Both WS and WPC have relatively lower H/C and O/C molar ratios compared to the SSBC, except H/C at SSBC 700°C (Table A.S2.2); the difference was attributed to the different feedstocks. The molar H/C and O/C ratios in WS and WPC are likewise influenced by the relatively higher C content in their feedstocks as compared to SSBC. Higher pyrolysis temperatures generally lead to the removal of polar functional groups (Spokas, 2010; Liu et al., 2011; Chen et al., 2015). The surface area of WPC was markedly higher (224 m^2/g) than that of WS and SSBC (Table A.S2.2). In SSBC, a strong correlation between higher pyrolysis temperatures and higher surface area in the resulting biochar was observed (Table A.S2.2).

WS and WPC particles exhibit a flaky and rough surface (Figure A.S2.4A and A.S2.4B) (Alam et al., 2016), with a size range of 100 to 1000 μm, while SSBC particles (Figure A.S2.4C to A.S2.4E) are mostly angular and semi-spherical, and range in diameter between approximately 100 to 200 μm. There is no visible effect of pyrolysis temperature on the particle morphologies. Semi-quantitative elemental compositions estimated from EDS (Figure A.S2.5 and Table A.S2.3A and A.S2.3E) show that WS, WPC and SSBC are mainly composed of C and O, followed by Si, Al, Fe, P, K, Ca, Mg and S. The silica nodules observed in WS and WPC

likely contain silanol functional groups (>Si-OH) which would be proton-active and could complex metals (Alam et al., 2016).

2.3.2 Potentiometric Titrations

All biochar types studied showed significant buffering capacity from pH 4 to 10 (Figure A.S2.6). Minimal variance was observed between forward and reverse titrations, suggesting reversibility of the protonation and deprotonation reactions on the biochar surface during the timescale of the experiments. Potentiometric titration data were modeled using a non-electrostatic, discrete site surface complexation model to determine the proton binding constants and site concentrations for the reactive surface sites for each biochar (Table 2.1). We defined three discrete site functional groups from lowest to highest pK_a (-log K_a) values for all five types of biochar. The three-site models were calculated using a least-squares optimization routine, as implemented in FITEQL 4.0 (Herbelin and Westall., 1996). In all cases the variance, or V(Y), values were in the range of $0.1 < V(Y) < 20$ (Table 2.1), which indicates a good fit to the titration data (Herbelin and Westall., 1996). Modeling with three sites yielded a better fit than did modeling with one, two, or four sites.

The surface acidity of biochar is normally attributed to carboxyl groups (pK_a = 1.7−4.7), lactones or lactols (pKa = 6.37−10.25), and phenolic hydroxyl groups (pK_a = 9.5−13) (Chen et al., 2008; Cao et al., 2009; Cao et al., 2010; Spokas, 2010; Chia et al., 2012; Li et al., 2014; Zhang et al., 2014; Chen et al., 2015). According to Achadu et al. (2014) the hydrolysis of silicon dioxide during ashing produces silanol surface group (–SiOH) with a weak acidity (pK_a = 6-8). The modeling results show that the pK_a values for site 1 (pK_a 4.24 to 4.70) are similar for all five biochar types, and fall in the pK_a range for carboxyl groups. The proton-active site concentrations are highest for site 1 for all five biochar types, except SSBC at 700°C. pK_a values

for site 2 and/or site 3 are variable across biochar types; however, they do correspond well to the pK_a values of lactones, phenolic hydroxyl and weak acidic silanol groups. With increasing temperature, the pK_a value of site 3 also increases, which is consistent with previous studies by Ahmad et al. (2012) and Chen et al. (2015) that suggested a total acidity decrease with increasing pyrolysis temperature.

Due to the structural diversity of biochar, pK_a values vary widely, and it is, therefore, difficult to designate unequivocal chemical identities to each site based on pK_a values alone (Li et al., 2014). Therefore, employing FT-IR is crucial to identify the surface chemistry of biochar. In this regard, the C=O and C=C infrared stretching vibrations at 1700 and 1600 cm^{-1} intensify, indicating the presence of carboxyl C, and potentially the formation of lactones and esters (Figure A.S2.7A) (Pastorova et al., 1994; Guo and Bustin, 1998; Chen et al., 2008; Spokas, 2010; Chia et al., 2012; Achadu et al., 2014; Li et al., 2014; Chen et al., 2015; Xiao and Chen, 2017). The prominent peaks at 1440 cm^{-1} and 1375 cm^{-1}, representing C=O stretching of ketones and O-H bending of phenols, respectively, are present in all five biochar types. The band at approximately 900 cm^{-1} could be attributed to Si-OH groups, due to the presence of Si nodules in biochar that identified by SEM-EDS and XRD analyses (Shahata, 2016). As the pyrolysis temperature increased for SSBC, the -OH stretching (3200-3600 cm^{-1}) attributed to water molecules loses intensity due to diminished hydration. Aliphatic and aromatic C-H stretching from 2850 to 3050 cm^{-1} also decreases as the pyrolysis temperature increases, which is supported by the proximate analyses. Both FT-IR analyses (Figure A.S2.7) and the pK_a values calculated from modeling potentiometric titration data (Table 2.1) suggest that -OH groups belong to both organic phenols and inorganic silanol groups.

2.3.3 Ni and Zn Adsorption onto Biochar

The adsorption of Ni and Zn increases with increasing pH from 2 to 6.5 for both 17 μM and 170 μM Ni and Zn concentrations for all five biochar types (Figure 2.1). Removal of both metals from aqueous solution is greatly influenced by biochar surface chemistry and surface area (Cao et al., 2009; Cao et al., 2010). The Ni adsorption capacity of WPC is much higher than that of WS, an expected result as WPC has both higher surface area and site concentrations (Figure 2.1). SSBC 500°C showed the highest Ni adsorption amongst the three SSBC biochars, despite SSBC 700°C having a higher surface area than SSBC 500°C. However, SSBC 500°C has a higher site concentration than either SSBC 300°C and SSBC 700°C, suggesting that Ni adsorption to SSBC is controlled by total site concentration. WPC (production temperature ~500°C) and SSBC 500°C have higher Ni adsorption capacities, even though SSBC 300°C and SSBC 700°C have higher site concentrations than WPC. In contrast, WPC has higher surface area compared to SSBC 300°C and SSBC 700°C, suggesting both physical and chemical adsorption played important roles in Ni adsorption.

Studies have shown the effectiveness of biochar and soil organic matter at removing Zn from aqueous solution than Ni, which is consistent with our adsorption experimental results (Figure 2.1) (Yasuda et al., 1960; Ma et al., 1994; Xia et al., 1997a). Leaching studies (Table A.S2.4) showed that WPC and SSBC 300°C leached a maximum of 3 μM and 2 μM Zn, respectively, which is 10 to 20% of the 17 μM of Zn used in the lower concentration adsorption experiments. However, Zn leaching from WS, SSBC 500°C and SSBC 700 was negligible (a few ppb). Because of the potential interference of Zn leaching on the observed removal of Zn from solution, we did not use WPC and SSBC 300°C for 17 μM Zn adsorption experiments. Zn leaching from WPC and SSBC at 300°C in 170 μM experiments only accounted for 1 to 2% of

the total initial Zn concentration, and therefore, 170 μM was used for Zn adsorption experiments to these biochar types and subsequent surface complexation modeling. In the 17 μM experiments, SSBC 500°C and SSBC 700°C showed a higher adsorption capacity than WS. The higher site concentrations of SSBC 500°C and SSBC 700°C than for WS likely correspond to the higher degree of Zn adsorption. WPC also showed highest Zn adsorption capacity of all five biochar types, as was observed for Ni adsorption.

The adsorption capacity was further normalized by the surface area of the five biochar samples. This normalization procedure helped us to understand and compare the performances of each biochar in removing Ni and Zn from solution, independent of the structure (i.e., the surface area and porosity of biochar). The results showed that SSBC 300°C has the highest metal adsorption densities while WPC has the lowest, for both Ni and Zn (Figure A.S2.8). The difference in metal adsorption densities of SSBC 300°C and WPC is consistent with the fact that SSBC 300°C and WPC also have the highest and lowest proton-active site densities, respectively (Table 2.1). Metal adsorption densities and reactive site densities decreased with increasing pyrolysis temperature for SSBC (Ahmad et al., 2012). The molar H/C and O/C ratios also decreased with increasing pyrolysis temperature for SSBC (Table A.S2.2), and WS has higher reactive site densities and molar H/C and O/C ratios than does WPC (Table 2.1 and Table A.S2.2). Overall, the results suggest that the biochar properties are highly influenced by pyrolysis temperature, and the adsorption densities are directly dependent on the proton-active site densities and molar O/C ratios.

2.3.4 Ni(II) and Zn(II) Coordination at the Surface of Biochar

Ni EXAFS analyses revealed that the Ni-O shell had a radial distance of 1.97 Å to 2.10 Å, with a coordination number of 6, indicating that Ni is in an octahedral environment (Figure

2.2; for a summary of fitting parameters see Tables A.S2.5 and A.S2.6). In contrast, the Zn-O distance of 1.97 Å indicates tetrahedral coordination. The first shell metal-oxygen distance could result from either hydration of the metal cations or the acidic functional groups of –OH and –COOH that adsorbed Ni and Zn at the biochar surfaces (Dong et al., 2013; Zhang et al., 2014). The parameters of the Ni-O and Zn-O first shell are similar to those of the aqueous Ni(II) and Zn(II) cations, suggesting that the primary hydration shell remains intact after sorption, and form outer-sphere complexes. The second Ni-O shell is best represented with 3.5 to 4 oxygen atoms ranging from 2.65 to 2.71 Å. There is no evidence of Ni-Ni and Zn-Zn in the second shell, excluding the possibilities of surface precipitation and polymerization. The assignment of the Ni-C shell at approximately 3.3 Å and Zn-C at 2.08 Å to 2.16 Å indicates that Ni and Zn form organo-metallic complexes with the surface of the biochar. This leads to the formation of inner-sphere surface complexes, and is consistent with acidic ligands (i.e., -COOH and -OH) coordinating with Ni and Zn (Elzinga et al., 2002; Tan et al., 2011). The Ni-Si and Zn-Si distances at 3 to 3.3 Å indicate that Ni and Zn form inner-sphere complexes, and show that Ni and Zn may also bind to Si-OH groups.

To further investigate Ni and Zn coordination to the biochar surface, FT-IR spectra of biochar before and after Ni(II) and Zn(II) sorption were subsequently compared (Figure S2.7). After Ni(II) and Zn(II) sorption, there is a decrease in the infrared band at approximately 1700 cm^{-1} and 3200 cm^{-1}, which correspond to the C=O stretching mode of the free carboxyl group and –OH groups (Figure S2.7B) (Chen et al., 2008). These changes further support the coordination of carboxyl ions and phenolic hydroxyl groups with Ni(II) and Zn(II). Taken together, it can be concluded that the Ni(II) and Zn(II) are adsorbed to biochar primarily through coordination with both carboxyl and hydroxyl ligands at the surface of the biochar.

2.3.5 Surface Complexation Modeling

A non-electrostatic surface complexation modeling (NEM) approach was used to model the adsorption behavior of Ni and Zn onto each biochar, an approach previously confirmed to be effective in low ionic strength solutions (e.g., 0.01M $NaNO_3$) (Fein et al., 1997; Fowle and Fein, 1999; Fein et al., 2005). It was assumed that proton, Ni and Zn adsorption were due to proton and metal cation interactions with discrete negatively charged organic acid functional groups on the biochar, similar to that demonstrated for various sorbents including, bacteria, clay, ferric hydroxides, and silica (Beveridge and Murray, 1980; Manning et al., 1997; Bethke and Brady, 2000; Koretsky, 2000; Borrok et al., 2005; Alessi and Fein, 2010; Flynn et al., 2014). The NEM approach considers the protonation or deprotonation of each type of surface functional group and the equilibrium equation to quantify the metal adsorption reactions according to the following stoichiometries:

$$\mathrm{R-A(H)^0 \leftrightarrow H^+ + R-A^-} \quad (1)$$

$$\mathrm{R-A^- + M^{++} \leftrightarrow R-A(M)^+} \quad (2)$$

where, R is the bulk biochar, and A represents the proton active functional groups to which a divalent metal M^{++} (that is, Ni^{++} or Zn^{++} in this study) can adsorb. We calculated the stability constants for Ni(II) and Zn(II) adsorption to biochar using the stoichiometry shown in reaction (2). The model also considered Ni(II) and Zn(II) aqueous hydrolysis reactions presented in Table A.S2.7. The model that invokes Ni and Zn adsorption to first two sites of the 3-site protonation model showed the best fit to the experimental data (Figure 2.1). A 3-site adsorption model that uses three pK_a values and corresponding site concentrations from the protonation model was unable to fit the experimental data, and a 1-site adsorption model poorly fit the experimental data

(Figure A.S2.9 and Table A.S2.8). In 2-site adsorption models, the first two pK_a values and corresponding site concentrations from the 3-site protonation model were used.

In the 2-site adsorption models, the Zn adsorption stability constant ($K_{1,Zn}$) is marginally higher than that of Ni ($K_{1,Ni}$) in the 17 μM experiments for all types of biochar; however, WS, WPC and SSBC 300°C showed slightly lower K_1 values for Zn binding than for Ni in 170 μM experiments (Table 2.2). Numerous studies report that the stability of Zn complexed with carboxylic acids is higher than for -COO-Ni^+ complexes (Yasuda et al., 1960; Ma et al., 1994; Xia et al., 1997a). The presence of -OH functional groups in the biochar could play a role in the higher K_2 values for Ni-ligand complexes than for analogous Zn-ligand complexes (Yasuda et al., 1960; Ma et al., 1994; Xia et al., 1997a). It is expected that carboxylic and hydroxyl groups (–OH groups belong both to organic phenols, and to inorganic silanol groups) would be the predominant binding sites of WS, WPC, SSBC 300°C, SSBC 500°C and SSBC 700°C since FTIR, EXAFS and Ni and Zn speciation diagram (Figure A.S2.10) revealed that Ni and Zn coordinate at these biochar surface sites.

Using the binding constant (K) values for individual metals (Ni and Zn) determined in biochar-metal adsorption experiments, and the pK_a values and site concentrations determined from potentiometric titrations, we predicted the adsorption of Ni(II) and Zn(II) to WS when both metals were present in solution (competitive adsorption). This exercise tests the robustness of the SCM approach in predicting metal adsorption to biochar in more complex or environmentally-relevant systems. After making the predictions, we performed the corresponding two-metal adsorption experiments to determine the accuracy of the model predictions (Figure 2.3A and 2.3B; A.S2.11). In the 17 μM (8.5 μM Ni + 8.5 μM Ni) system, the model slightly over predicts Ni(II) adsorption from pH 4 to 5.5 and under predicts at pH 6.5. Zn(II) adsorption is under

predicted across the entire pH range. The two-site model to predict metal adsorption in 170 μM (85 μM Ni + 85 μM Ni) experiments yielded better results. Overall, the predictive models reasonably reproduced experimental results. The observed adsorption of Ni(II) and Zn(II) are quite similar to the 17 μM mixture predictions, but Zn(II) adsorption is higher than is Ni(II) at the 170 μM mixture concentration, showing similar trends as those observed in the single metal experiments (Figure 2.1).

2.3.6 Titration Calorimetry Data Analysis

XAS and surface complexation modeling provide information on the coordination environment and the means to quantify surface reactivity, while calorimetric measurements can also provide coordination information and determine the thermodynamic driving force behind the observed reactions. The corrected heats of protonation of the 3-site protonation model are exothermic for both WS and WPC, with WS being slightly more exothermic (Figure 2.4A and 2.4B). The site-specific enthalpies of protonation show that as pH decreases, corrected heats become less exothermic which is a result of a combination of less sites available to protonate and the low pK_a sites being less exothermic (Table 2.3) (Gorman-Lewis et al., 2006). The enthalpies of protonation are mildly exothermic to mildly endothermic. Site 1 on both WS and WPC have entropies of protonation of about 80 J/mol K, which are indicative of anionic oxygen ligands that participate in hydrogen bonding with other nearby functional groups. These results indicate the potential for bidentate coordination on the surface, which is consistent with the XAS results. Entropies of protonation > 80 J/mol K like those for sites 2 and 3 for both WS and WPC, are consistent with anionic oxygen ligands that behave more independently without direct interactions with other surface functional groups. The combination of enthalpies, entropies, and log K values are consistent with protonation of monofunctional carboxylic acids, some of which

may be close enough together to behave more like multifunctional carboxylic acids. Typical heat flow curves of acid titration and Zn(II) and Ni(II) adsorption titration are presented in SI (Figure A.S2.12 and A.S2.15).

Corrected heats of Ni and Zn adsorption onto WS and WPC are shown in Figure 2.4. The stability constants produced from 170 μM Ni and Zn adsorption experiments and the 2-site Ni and Zn adsorption models fit the calorimetric data best for both WS and WPC (Figure 2.4C to 2.4F). The enthalpies are mildly endothermic for the L_1Ni^+ complex (<4 kJ/mol) and exothermic for the L_2Ni^+ complex (Table A.S2.9). Calorimetric results of Zn adsorption onto both WS and WPC produced mildly exothermic (< -1 kJ/mol) to endothermic enthalpies on surface sites (Figure 2.4E and 2.4F and Table A.S2.10). Entropies of complexation can provide information on coordination environments based on the disruption or stability of the hydration spheres of ligands and ions (Choppin, 1997; Jensen et al., 2000). Negative entropies of the L_2Ni^+ complex suggests an outer sphere complexation with minimal disruption of hydration spheres and possible complex stabilization through hydrogen bonding. The positive entropies of the L_1Ni^+ complex are consistent with inner sphere complexation, which dehydrates the ligand and metal ion. Positive entropies of Zn complexation indicate dehydration as binding occurs and inner sphere complexation.

Site specific ITC results are dependent on the surface complexation models to derive the enthalpies and entropies of complexation; therefore, consistencies and differences between the ITC and XAS results also have implications for the surface complexation models. Both ITC and XAS indicated the presence of inner sphere surface complexes with anionic oxygen ligands. ITC, which is more sensitive than the XAS measurements, also indicated the presence of some outer sphere complexation. Surface site 2 of WS and WPC produced outer sphere complexes for

Ni according to entropies of complexation. The stability constants for these site 2 complexes were also lower than for the site 1 complexes. These two lines of evidence indicate a lower affinity for metal adsorption onto site 2 for WS and WPC. This would result in lower portions of Ni at these sites, which increases the difficulty of detecting these outer sphere complexes with spectroscopic techniques.

Using the thermodynamic parameters derived in this work with the Van't Hoff equation allows us to make predictions about the temperature dependence of proton, Ni, and Zn adsorption onto WS and WPC. These predictions assume that the relative heat capacities of the products and of the reactants (ΔC_P) are zero for the reaction. The magnitudes of the enthalpies of protonation are not large enough to impart much temperature dependence on the protonation of the biochar surface. The maximum change in the log K value for protonation of the biochar surface from 25°C is approximately 0.2 over the temperature range of 5 to 75°C. The temperature dependence of metal adsorption is predicted to be more substantial given that the enthalpies of Ni and Zn adsorption onto site 2 are approximately an order of magnitude more endothermic or exothermic than protonation enthalpies. For example, the change in log K for Ni adsorption onto WPC site 2 is predicted to increase by approximately 2 at 75°C. The log K for Zn adsorption onto WS site 2 is predicted increase by approximately 2.5 at 75°C. These predictions illustrate the utility of calorimetric investigations and the potential temperature dependence of Ni and Zn adsorption onto the biochar investigated.

2.4 ENVIRONMENTAL IMPLICATIONS

Biochar is a promising material for the adsorptive removal of metals and organics from water. This is the first study combining spectroscopic data (EXAFS and FTI-R) with thermodynamic data (SCM and ITC) to explore molecular scale metal adsorption at biochar

surface functional groups. The study demonstrates that feedstock type and pyrolysis temperature during biochar production profoundly influence biochar characteristics, including chemical properties, structure, and metal binding mechanisms. Higher reactive site densities/functional group concentrations for metal removal are obtained from biochar produced at lower pyrolysis temperature (~300°C), and Ni(II) and Zn(II) adsorption densities are directly related to the reactive site densities and molar O/C ratios of biochar. Thus, to improve the performance of metal removal and soil amendment, biochar selection should be made on a case-by-case based on the biochar physical and chemical properties.

EXAFS characterization combined with FT-IR analysis further suggest that Ni(II) and Zn(II) adsorption to biochar primarily occurred through the coordination of carboxyl anions (-COOH) and hydroxyl (-OH) with Ni(II) and Zn(II). The SCM approach applied in this study accurately predicts the metal adsorption behavior to the surface of the biochar for single (Ni or Zn) and multi-metal (Ni + Zn) systems. By using a combined SCM-ITC approach, the thermodynamic parameters of the metal-biochar surface complexation reactions were determined. Enthalpies of Ni- and Zn-ligand reactions were consistent with the presence of anionic oxygen ligand corresponding to –COOH and –OH functional groups. The development of predictive SCMs is a key step towards optimized design and operation of biochar-based water treatment systems, which have promise to replace more costly technologies such as activated carbon. These combined approaches will help to identify the reaction pathways of metals with biochar, and provide new tools to remove metals from water using biochar in variable water chemistries.

Table 2.1. Parameters obtained from 3-site best-fit protonation models, of titration data of WS, WPC, SSBC 300°C, SSBC 500°C and SSBC 700°C.

Biochar	Total Sites	pKa_1	pKa_2	pKa_3	Site 1 concentration (mol/g)	Site 2 concentration (mol/g)	Site 3 concentration (mol/g)	Total reactive site (mol/g)	Surface area Reactive sites densities (mol/m^2)	V(Y)
WS	3	4.24	5.82	7.87	7.5E-04	1.2E-04	1.0E-04	9.7E-04	3.7E-05	5.71
WPC	3	4.23	6.18	7.94	9.8E-04	1.1E-04	1.4E-04	1.2E-03	5.4E-06	11.43
SSBC 300°C	3	4.50	7.00	8.42	1.1E-03	3.3E-04	4.1E-04	1.8E-03	4.0E-04	1.55
SSBC 500°C	3	4.54	7.21	8.55	2.7E-03	2.9E-04	1.0E-03	4.0E-03	1.5E-04	2.44
SSBC 700°C	3	4.70	7.76	9.30	8.0E-04	5.7E-04	6.8E-04	2.0E-03	3.6E-05	1.33

Table 2.2. Stability constants obtained from 2-site best-fit adsorption models of Ni and Zn adsorption to WS, WPC, SSBC 300°C, SSBC 500°C and SSBC 700°C.

Biochar	Ni 17 µM		V(Y)	Ni 170 µM		V(Y)	Zn 17 µM		V(Y)	Zn 170 µM		V(Y)
	log K_1^*	log $K_2^\dagger$		log K_1^*	log $K_2^\dagger$		log K_1^*	log $K_2^\dagger$		log K_1^*	log $K_2^\dagger$	
WS	2.74	0.40	3.7	2.24	2.22	14	2.17	2.42	0.2	2.44	2.82	5
WPC	2.83	4.68	0.4	2.53	1.88	23	NA	NA	NA	2.83	2.38	20
SSBC 300°C	2.50	3.5	0.2	1.90	2.90	12	NA	NA	NA	2.45	3.0	9
SSBC 500°C	2.74	4.61	0.5	2.24	2.61	20	1.34	5.21	2	1.84	4.61	36
SSBC 700°C	2.70	3.76	1	2.20	2.76	13	2.50	5.16	0.9	2.20	4.76	24

NA = Not available

$^*R\text{-}A_1^- + M^{++} \leftrightarrow R\text{-}A_1(M)^+$

$^\dagger R\text{-}A_2^- + M^{++} \leftrightarrow R\text{-}A_2(M)^+$

Table 2.3. Site-specific thermodynamic parameters for the reaction of H+ derived from calorimetric titrations, and 3-site models from potentiometric titration data.

Protonated Sites	logK	Gibbs free energy, $\Delta G_r°$ (KJ/mol)	Enthalpy, $\Delta H_r°$ (KJ/mol)	$-T\Delta S_r°$ (KJ/mol)	Entropy, $\Delta S_r°$ (J/molK)
			WS		
HL1	4.24(0.05)	-24.20(0.29)	-0.18(0.02)	-24.02(0.29)	80 (1)
HL2	5.82(0.17)	-33.22(0.97)	-3.88(0.20)	-29.34(0.99)	98 (3)
HL3	7.87(0.09)	-44.92(0.51)	-2.93(0.15)	-41.99(0.53)	141 (2)
			WPC		
HL1	4.23(0.02)	-24.15(0.11)	-0.09(0.01)	-24.06(0.11)	81(1)
HL2	6.18(0.15)	-35.28(0.86)	-2.97(0.10)	-32.31(0.86)	108 (3)
HL3	7.94(0.07)	-45.32(0.40)	1.54(0.12)	-46.86(0.42)	157 (1)

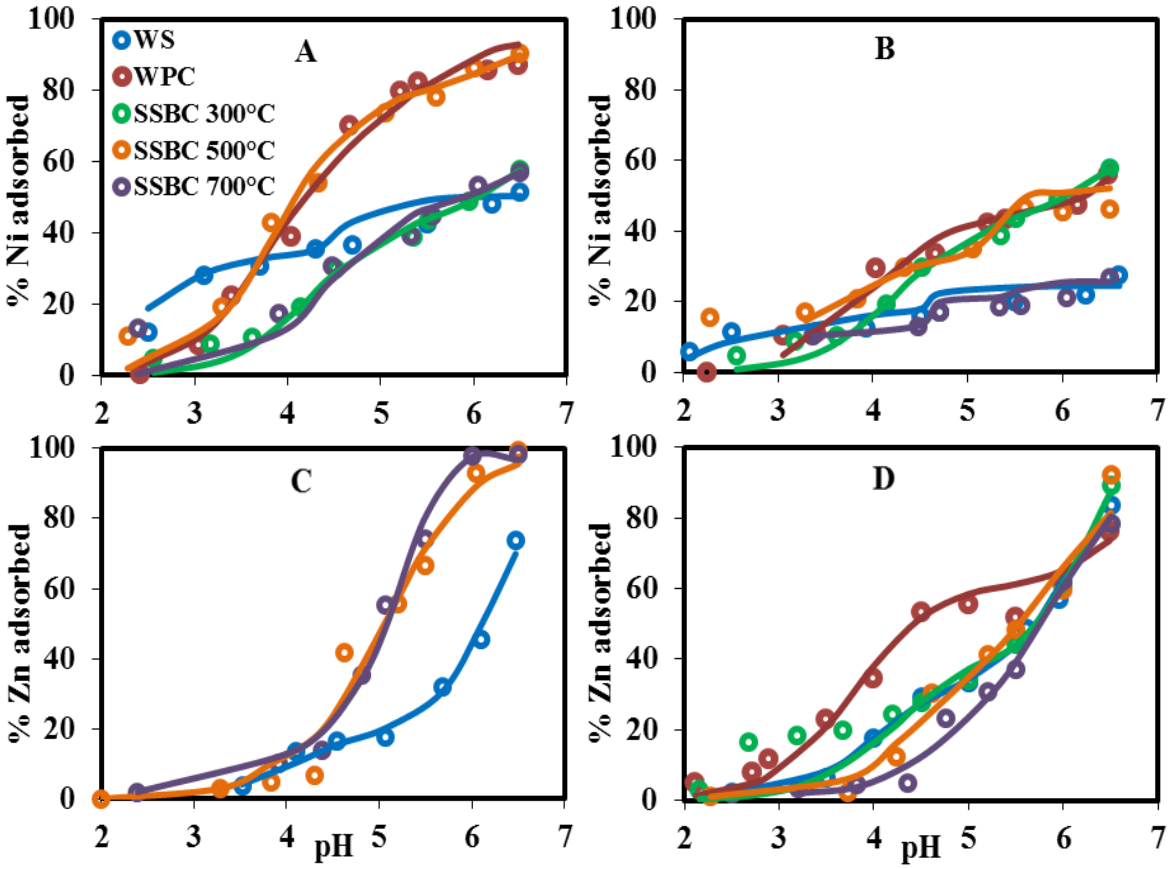

Figure 2.1. Adsorption of Ni and Zn onto WS, WPC, SSBC 300°C, SSBC 500°C and SSBC 700°C, showing the 2-site best-fit adsorption models: A. 17 µM Ni; B. 170 µM Ni; C. 17 µM Zn; D. 170 µM Zn. The open symbols represent experimental data and solid lines represent best-fit models.

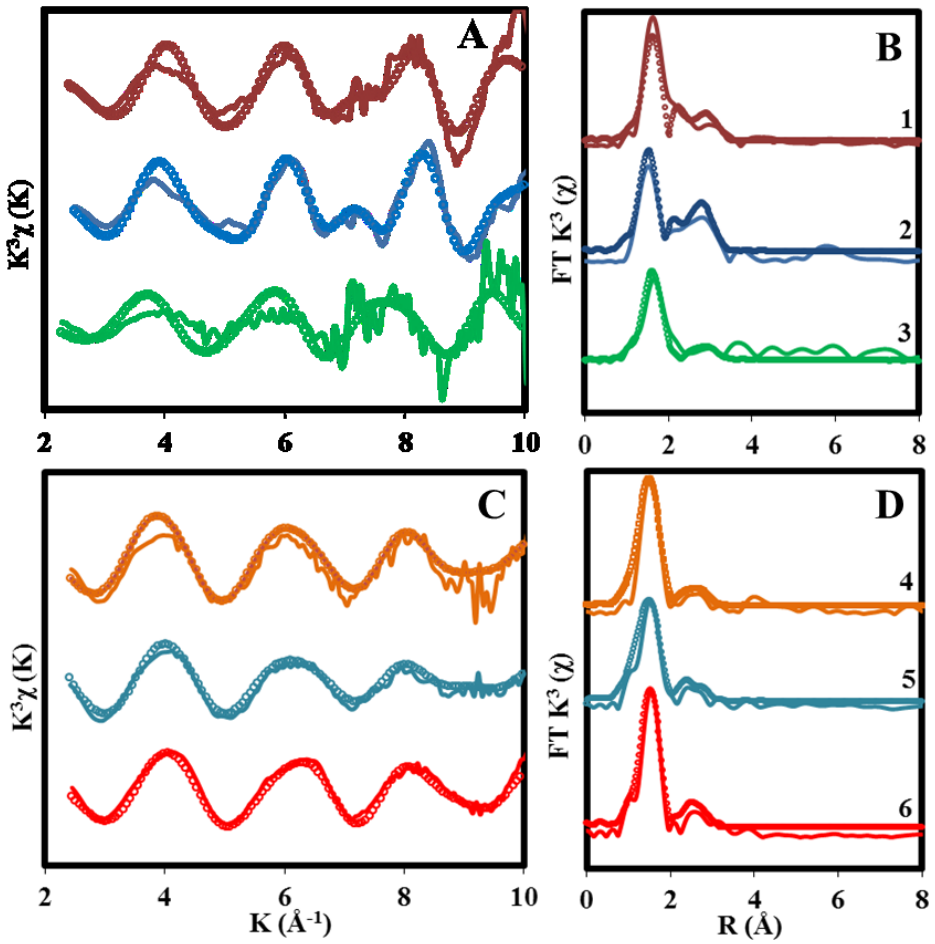

Figure 2.2. EXAFS signals weighted by k^3 spectra and R space curve fitting results for Ni and Zn adsorbed to WS. A. k^3 spectra of Ni; B. R space of Ni; C. k^3 spectra of Zn; D. R space of Zn; (1) 170 µM Ni; (2) 85 µM Ni; (3) 17 µM Ni; (4) 170 µM Zn; (5) 85 µM Ni and (6) 17 µM Zn.

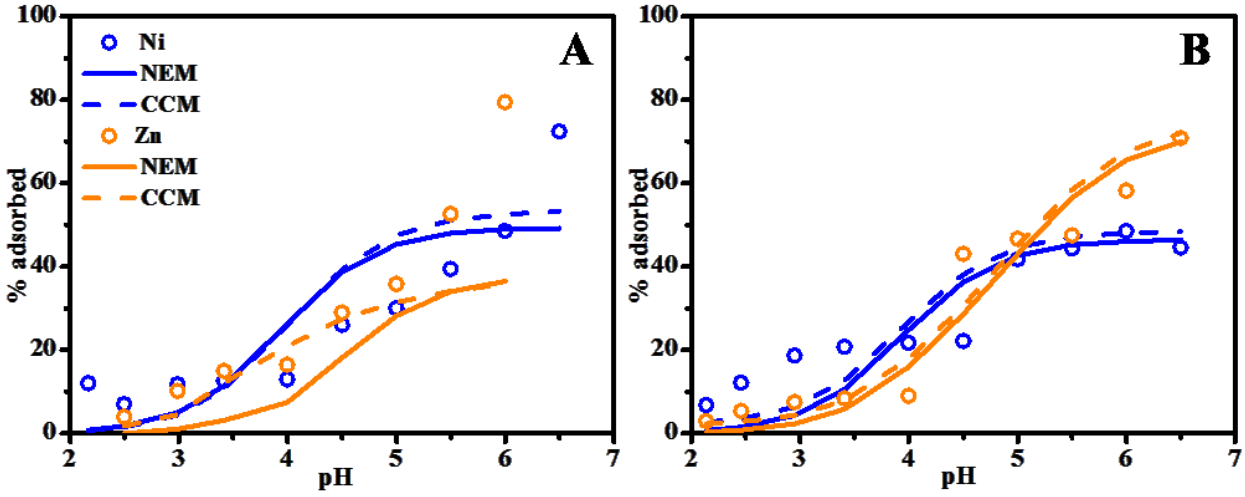

Figure 2.3. Competitive adsorption of Ni and Zn (A and B) onto WS A. 8.5 µM Ni + 8.5 µM Zn with the 2-site predictive adsorption model; B. 85 µM Ni + 85 µM Zn with 2-site predictive adsorption model. The open symbols represent experimental data, and solid lines and dashed lines represent predictive models.

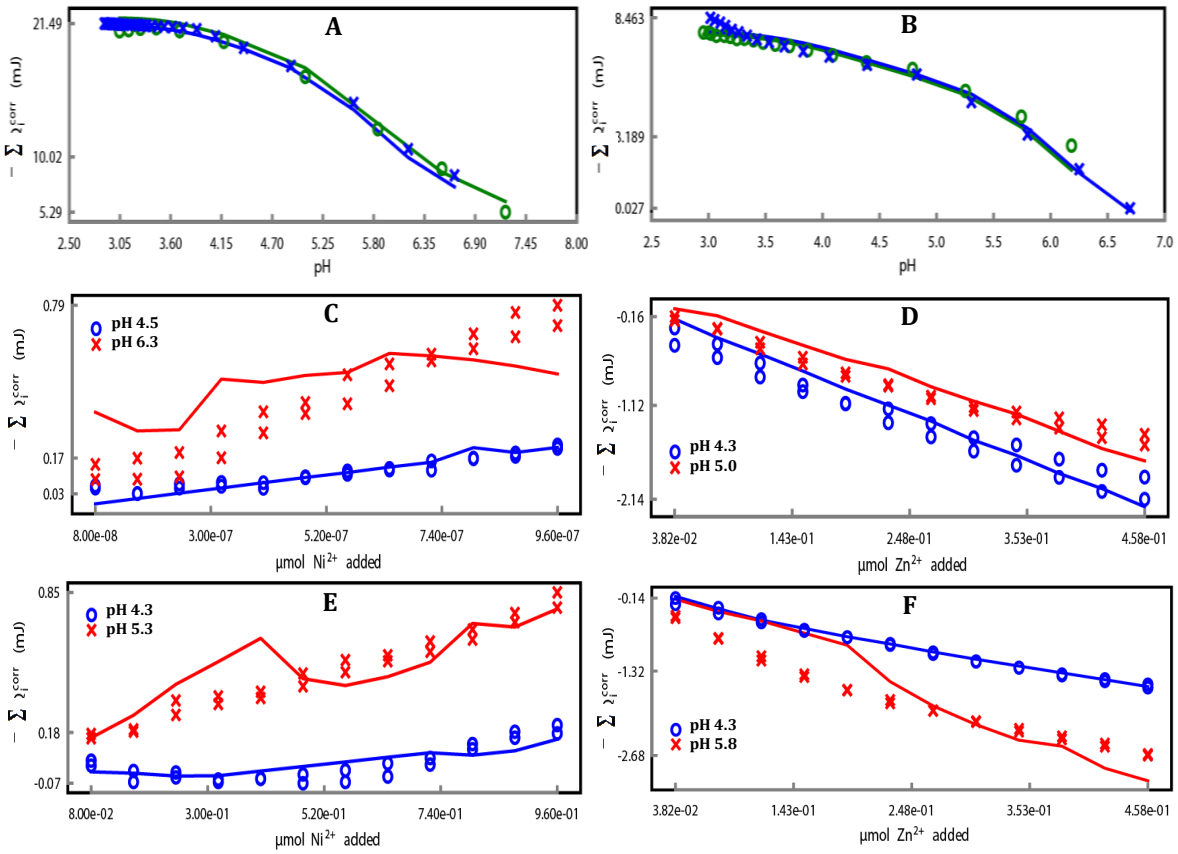

Figure 2.4. Corrected heat generated from proton, and Ni and Zn adsorption titrations of WS and WPC. A. Proton adsorption on WS; B. Proton adsorption on WPC; C. Ni adsorption on WS; D. Zn adsorption on WS; E. Ni adsorption on WPC; F. Zn adsorption on WPC. The open symbols and solid lines represent the experimental data and the fit, respectively. The open symbols and solid lines in blue and green colors in proton adsorption model (A,B) represents replicates. The Ni and Zn adsorption titration experimental data (open symbol) also have replicates.

CHAPTER 3

MECHANISMS OF THE REMOVAL OF U(VI) FROM AQUEOUS SOLUTION USING BIOCHAR: A COMBINED SPECTROSCOPIC AND MODELING APPROACH

ABSTRACT

Biochar, the product of the pyrolysis of numerous types of biomass, has been touted as a promising sorbent for the removal of inorganic contaminants, such as uranium (U), from water. However, the molecular-scale mechanisms of aqueous U(VI) species uptake remain poorly-understood. In this study, two approaches, grounded in equilibrium thermodynamics, were employed to investigate the U(VI) adsorption mechanisms: (1) batch U(VI) adsorption experiments coupled to surface complexation modeling (SCM) and (2) isothermal titration calorimetry (ITC), supported by synchrotron-based X-ray absorption spectroscopy (XAS) analyses. The biochar tested have considerable proton buffering capacity and most strongly adsorb U(VI) between approximately pH 4 to 6. Fourier transform infrared spectroscopy (FT-IR) and X-ray photoelectron spectroscopy (XPS) studies, along with XAS analyses, shows that U(VI) adsorption occurs primarily at proton-active carboxyl (-COOH) and phenolic hydroxyl (-OH) functional groups on the biochar surface. The SCM approach is able to predict U(VI) adsorption behavior across a wide range of pH, in the presence of dissolved Ca^{2+}, and at varying initial U(VI) and biochar concentrations, and based on our experimental results, we demonstrate that U adsorption is strongly influenced by aqueous U(VI) speciation. Supporting ITC measurements indicate that the calculated enthalpies of protonation reactions of wheat straw biochar (WS) and wood pin chip biochar (WPC), as well as the adsorption of U(VI), are

consistent with anionic oxygen ligands, and are indicative of both inner- and outer-sphere complexation. Our results provide new insights into the modes of U(VI) uptake by biochar, and more generally improve our understanding of its potential to remove radionuclides from contaminated waters.

3.1 INTRODUCTION

Uranium (U) contamination in soil and groundwater systems from abandoned mine tailings and former nuclear weapons facilities is a major concern due to its potentially toxic and carcinogenic effects on human health and aquatic life (Catalano et al., 2006; Stubbs et al., 2006; Mkandawire, 2013; Alam and Cheng, 2014; Pan et al., 2016). The chemical composition of the aqueous environment affects the speciation of U(VI), the oxidized form of U, which, in turn, can greatly influence its fate and mobility (Langmuir, 1978; Waite et al., 1994; Welch and Lico, 1998; Alessi et al., 2014). The removal of U(VI) by adsorbents, including clay and metal oxyhydroxides is a widespread approach for its remediation in contaminated systems (Sylwester et al., 2000; Dickinson and Scott, 2010; Ren et al., 2010), however, most natural adsorbents have relatively low adsorption capacities (Zeng et al., 2009 and Sun et al., 2014). Hence, developing an efficient material with a high adsorption capacity to treat U(VI) has been the focus of recent research studies. For example, porous carbon materials (e.g., activated carbon and graphene oxides nanosheets) (Mellah et al., 2006; Duster et al., 2017) have shown a high efficiency to remove metals from aqueous solution, but the cost of these materials has limited their widespread application in remediation. Biochar, a porous and carbon-rich material produced from biomass and biological waste via thermal decomposition, has attracted attention due to its low production cost compared to other sorbents, and has proven efficient in metals and organic contaminants removal from water (Cao, et al., 2009; Teixidó et al., 2013; Alam et al., 2016;

Thompson et al., 2016; Alam et al., 2018a). In the case of metals adsorption, biochar is very efficient because of its abundance of charged surface functional groups (Cao, et al., 2009; Teixidó et al., 2013; Alam et al., 2016; Thompson et al., 2016; Alam et al., 2018a).

Recent studies have reported that biochar exhibits a strong affinity to adsorb U(VI) (Kumar et al., 2011; Zhang et al., 2013; Hadjittofi and Pashalidis, 2015; Alam et al., 2018a). However, these studies only present bulk U(VI) metal adsorption data, which do not provide molecular-scale insights into the coordination of aqueous uranyl species adsorbed to the biochar surface (Kumar et al., 2011; Zhang et al., 2013; Hadjittofi and Pashalidis, 2015; Ashry et al., 2016) and, therefore, they cannot be used to calculate intrinsic stability constants of U(VI)-biochar surface complexes (Bethke and Brady, 2000; Koretsky, 2000; Borrok et al., 2005). Since U(VI) has a complex aqueous speciation, especially in the presence of the common calcium (Ca^{2+}), carbonate (CO_3^{2-}) and hydroxyl (OH^-) ions in natural waters, it is critical to consider changes in aqueous speciation when performing adsorption modeling (Zheng et al., 2003; Dong et al., 2005; Fox et al., 2006).

Surface complexation modeling (SCM) is a robust and quantitative approach to modeling metal adsorption behavior, because it considers the full aqueous speciation of the metal(s) in question, is based on balanced chemical reactions, and can account for changes in pH and adsorbent:adsorbate ratios (Beveridge and Murray, 1980; Bethke and Brady, 2000; Koretsky, 2000; Borrok et al., 2005; Alessi et al., 2010; Alam et al., 2018b). The SCM approach can be informed with direct analyses of the surface coordination of adsorbed ions using approaches such as synchrotron-based extended X-ray absorption fine structure (EXAFS) studies (Sherman et al., 2008; Sun et al., 2016). Although SCM complemented with XAS is key to understanding the metal-surface coordination following adsorption, it does not provide information about the

thermodynamic driving force (e.g., bond formation, dehydration, enthalpy and entropy) of these reaction(s). In this regard, isothermal titration calorimetry (ITC) measurements can provide insights into the thermodynamic driving forces of adsorption reactions (Gorman-Lewis, 2011; Harrold and Gorman-Lewis, 2013).

In this study, we use a unique combination SCM, XAS and ITC to understand the molecular scale mechanisms of U(VI) adsorption onto the surfaces of two types of biochar. The objectives of this study are to: (i) identify the U(VI) adsorption behavior by biochar over a wide range of pH conditions and water chemistries, (ii) develop a reaction-based framework through which predictions of U(VI) adsorption onto biochar can be made across varying solution chemistry, and (iii) determine the thermodynamic driving forces of U(VI) reactions at the biochar surface. By integrating these approaches, we are able to develop, for the first time, a predictive model of U(VI) adsorption onto biochar across a wide range of water chemistries. Ultimately, our models can be used to optimize pilot-scale experiments that could enable commercial exploitation of biochar in the remediation of U(VI)-contaminated waters.

3.2. MATERIALS AND METHODS

3.2.1 Biochar Preparation and Characterization

Wheat straw biochar (WS) and wood pin chip biochar (WPC) were obtained from the Alberta Biochar Initiative (ABI; Vegreville, Alberta, Canada). A prototype 1.0 batch carbonizer (Alberta Innovates Technology Futures, AITF), and an auger retort carbonizer (ABRI- Tech, 1 Tonne Retort system; ABI, Vegreville, Alberta), respectively, were used to pyrolyze wheat straw and wood pine chip feedstocks under limited oxygen conditions, with a residence time of 30 min at 500°C to 550°C (Alam et al., 2018b).

The elemental analysis, Brunauer-Emmett-Teller (BET) surface area analysis, X-ray powder diffraction (XRD), surface morphological characterizations and Fourier transform infrared (FT-IR) spectroscopy analyses of WS and WPC were carried out as described in Alam et al. (Alam et al., 2016 and 2018a). To determine the concentrations of acidic functional groups on each biochar, the modified Boehm titration method (Fidel et al., 2013) was used, as described in Alam et al. (2016). Zeta potential measurements, X-ray photoelectron spectroscopy (XPS) and Boehm titrations were also conducted, and a detailed description of these methods is given in Appendix B.

3.2.2 Potentiometric Titrations

Potentiometric titrations were carried out to determine the protonation constants (K_a) and corresponding site concentrations of proton-active surface functional groups of WS and WPC as describe in Alam et al. (2018a). Briefly, for each titration, 4 g L^{-1} biochar was suspended in 50 mL 0.01 M $NaNO_3$ electrolyte solution. To maintain a CO_2-free solution, prior to each titration the resulting suspension was purged with N_2 gas for 30 min and throughout. To test the reversibility, forward titrations (pH 3-11) using 0.1 M NaOH and reverse titrations (pH 11-3) using 0.1 M HCl were conducted (Alam et al., 2018a and 2018b)

3.2.3 U(VI) Adsorption Experiments

Batch U(VI) adsorption experiments were conducted using aqueous uranyl nitrate $UO_2(NO_3)_2$ solutions. Experiments were carried out in 15 mL polypropylene test tubes over three sorbent concentrations (0.2 g/L, 0.5 g/L and 1 g/L) and three U concentrations (5 µM, 10 µM and 20 µM) for both WS and WPC. The final volume of each experiment was approximately 10 mL, and experiments were carried out from pH 2.0 to 10, achieved by adding small volumes of concentrated NaOH or HCl. To avoid potential precipitation at near-neutral pH, experiments

were conducted at low U concentrations. A speciation diagram generated at experimental conditions shows that U(VI) may precipitate at near neutral pH levels (Figure B.S3.1); however, control experiments conducted under identical conditions, but in the absence of biochar, did not exhibit any loss of aqueous U(VI) after 24 h. Since equilibrium U(VI) adsorption had been achieved in 4 h, as observed in kinetics experiments (SI text in Appendix B and Figure B.S3.2), it is clear that equilibrium U(VI) adsorption was achieved prior to the formation of measureable uranyl precipitates.

The test tubes were placed on a rotary shaker for 24 h to ensure that a stable pH and an equilibrium adsorption of U(VI) onto biochar had been achieved. After 24 h, the test tubes were centrifuged at 5000 g for 10 min and the resulting supernatant filtered through 0.20 μm nylon membranes (Millex HP). The filtered supernatants were analyzed using ICP-MS/MS (Agilent 8800) to measure the concentration of U remaining in each solution. The difference between the initial U concentration used in the experiments and the remaining U concentration left in solution after equilibrium was considered to be the amount adsorbed. All experiments were conducted in duplicate.

Dissolved Ca^{2+} and CO_3^{2-} species can form ternary aqueous complexes with U(VI) that influence its adsorption to environmental surfaces (Dong et al., 2005; Fox et al., 2006). Thus, we conducted a set of U(IV) adsorption experiments for each biochar in the presence of Ca^{2+}. To do so, 10 mM $CaCl_2.6H_2O$ was added to a solution containing 20 μM U(VI) and 1g L^{-1} biochar. The experimental procedures and samples analysis was carried out as described for the U(VI) adsorption experiments.

3.2.4 Surface Complexation Modeling

The stability constants of U(VI)-biochar complexes were determined using a least-squares optimization routine, as implemented in FITEQL 4.0 (Herbelin and Westall, 1996). U(VI)-ligand stability constants for individual U(VI) species were calculated using the following generalized equation:

$$K_{U(VI)} = \frac{[R-L_i(U(VI))]a_{H^+}}{[R-L_i^-]a_{U(VI)}} \quad (1)$$

where, *R* is the biochar particle to which the surface functional group L_i is attached, *a* represents the activity of subscribed species (FITEQL uses the Davies equation calculate the activity coefficients), and [] represents the molal concentrations of the biochar surface species. To solve for the binding constant ($K_{U(VI)}$) values for each U(VI)-biochar surface complex, the acidity constants and corresponding sites concentrations modelled from potentiometric titration data for each biochar were used. Our models also considered reactions that led to the formation of aqueous U(VI) complexes (see Table B.S3.1). We used a non-electrostatic surface complexation modeling (NEM) approach to model the adsorption behavior of U(VI) onto WS and WPC, a widely-accepted approach for low ionic strength solutions (Fein et al., 1997; Fein et al., 2005). The calculated site concentrations and acidity constants of WS and WPC from the titration models (Table B.S3.2), along the with the measurement of the total adsorbed U as a function of pH, enabled us to solve for the stability constants for U-biochar surface complexes for each condition studied.

3.2.5 X-ray Adsorption Spectroscopy Data Collection and Analysis

Synchrotron-based X-ray absorption spectroscopy (XAS) was used to investigate the oxidation states and coordination environments of U adsorbed to WS biochar. The XAS data were collected at U L_{III}-edge (17.16 keV) at the 06ID-1 Hard X-ray Micro-Analysis (HXMA)

beamline of the Canadian Light Source (CLS) in Saskatoon, Canada. Analyses were performed on U(VI) adsorption experiments conducted at pH 5, 8 and 10, and then in the presence of U(VI) and Ca at pH 7. All experiments had a starting U(VI) concentration of 20 μM. A Si (220) double crystal monochromator was used during the experiment. To reject higher harmonic components of the incident X-ray beam, the second crystal of the monochromator was detuned by 60%. Reference spectra for uranyl nitrate and chemically precipitated UO_2 were recorded in transmission mode, and also in fluorescence mode using a 32-element Ge solid state detector, respectively.

The graphical interface ATHENA from DEMETER was used for processing raw data, background subtraction and X-ray absorption near edge structure (XANES) linear combination fitting (Ressler, 1997; Ravel and Newville, 2005). WinXAS (version 2.3) was use to model k-space and Fourier transformed (FT) spectra. FEFF 7 was used to generate phase shifts and backscattering amplitude functions theoretically based on the crystallography data of the crystal structure of the U(VI) mineral schoepite, $(UO_2)_8O_2(OH)_{12}.12H_2O$ (Rihs et al., 2014), and for UO_2^{2+}, using the Hanning window function. During fitting with FEFF models, Fourier transform (FT) k^3-weighted EXAFS data were modeled between R-space values of 1.1 and 2.4 Å, and between a k-range of 3-12 $Å^{-1}$. The amplitude reduction factor (S_0^2) for all fits was set to 0.99 (Ankudinov and Rehr, 2000; Ravel and Newville, 2005).

3.2.6 X-ray Fluorescence (XRF) Mapping

Synchrotron X-ray fluorescence (XRF) mapping was carried out on thin sections of U-sorbed biochar at the Very Sensitive Elemental and Structural Probe Employing Radiation (VESPERS 07B2-1) beamline at CLS. The distribution of the U(VI) in the thin sections was measured using single-element dispersive silicon drift XRF detector (Hitachi Vortex-90EX). The

fluorescence data was collected using the "Pink Beam" mode, during which the sample is continuously exposed to X-ray energy between 2-30 keV during mapping. A Kirkpatrick-Baez (KB) mirror system was used to focus the beam down to 5 μM, and mapping was carried out using a 3 μm step size resolution, dwelling one second at each analysis point.

3.2.7 Isothermal Titration Calorimetry (ITC)

ITC experiments were conducted using a nanocalorimeter (TAM III) to measure the heat flux as a function of time between a reference and reaction vessel. The response of the calorimeter to the heat flow was calibrated by electrical heating (Grenthe et al., 1970; Turkarslan et al., 2017). Initially, both reaction and reference cells were filled with 2.5 ml of a 10 g L^{-1} biochar suspensions in 0.01 M NaCl and placed in the calorimeter bath. After thermal equilibration with regards to heat flow in the cells, a cannula from a computer-controlled 250 μL syringe was used to deliver a predetermined number of individual titrant doses of 0.1 mM $UO_2(NO_3)_2$, adjusted to the same pH as the biochar suspension, into the reaction cell while the heat flow was monitored. The modeling procedure of the ITC data was carried our as described in Alam et al. (2018b) and details can be found in Appendix A.

3.3. RESULTS AND DISCUSSION

3.3.1 Characterization of Biochar

SEM imaging indicated that WS and WPC particles display a flaky and rough surface (Figure 3.1A and 3.1B), with dimensions ranging from approximately 100 to 1000 μM. XRD patterns (Figure B.S3.3) from analysis of WS and WPC show that quartz and calcite are the major detectable mineral phases (Alam et al., 2018a and 2018b). The presence of oxygen-containing functional groups of WS and WPC are demonstrated by both FT-IR and XPS analyses (Figures 3.1C and B.S3.4). The infrared vibrational bands at 3425 cm^{-1} and 1710 cm^{-1}

correspond to -OH and –C=O groups, respectively (Keiliweit et al., 2010; Chen et al., 2015; Sun et al., 2016). Bands at 2929, 1662 and 1425 cm^{-1} were assigned to stretching vibrations of C-H, C=C and C-OH bonds, respectively (Keiliweit et al., 2010; Chen et al., 2015; Sun et al., 2016). According to the zeta potential measurements (Figure 3.1D), both WS and WPC have isoelectric points near pH 2, after which their surfaces are negatively charged, consistent with the deprotonation of their functional groups at higher pH.

Elemental analyses show that WS and WPC are composed of 70% and 85% C, respectively (Table B.S3.3). WPC has relatively lower H/C and O/C molar ratios compared to the WS (Table B.S3.3), a difference attributable to the different feedstocks and the initial C content. The surface area of WPC is markedly higher (224 m^2/g) than that of WS (26.6 m^2/g), which can be attributed to the differing compositions of the feedstock biomasses (Table B.S3.3).

3.3.2 Surface Chemistry

To determine the proton binding constants and corresponding site concentrations for reactive surface sites of WS and WPC, potentiometric titration and Boehm titration were used. Potentiometric titration data were modeled using a non-electrostatic, discrete site surface complexation model, using the software FITEQL 4.0 (Herbelin and Westall, 1996). A model that considered three proton-active functional groups (i.e., 3-site protonation model) yielded a better fit than did modeling with different sites; the variance, V(Y), values were in the range of $0.1<V(Y)<20$ (Herbelin and Westall, 1996) that indicates a good fit to the titration data (Alam et al., 2018 and 2018b). pK_a values in WS and WPC, calculated from titration modeling, is within the range of carboxyl groups and phenolic hydroxyl groups (Table B.S3.2 and Figure B.S3.5) (Chen et al., 2008; Keiliweit et al., 2010; Chia et al., 2012; Li et al., 2014; Chen et al., 2015; Alam et al., 2018a and 2018b). Boehm titrations were also used to estimate the total reactive

sites per gram of biochar for three cumulative pK_a ranges (i.e., pKa 5 to 6.4; pKa 6.4 to 10.3 and pKa 10.3 to 13) (Goertzen et al., 2010; Fidel et al., 2013). WPC has higher number of reactive sites (4.72 mmol/g) as compared to WS (1.5 mmol/g) (Table B.S3.4). According to Fidel et al. (2013) and Goertzen et al. (2015) $NaHCO_3$ accepts protons from functional groups with $pK_a <$ 6.4 (carboxylic acids; silanol group); Na_2CO_3 accepts protons from functional groups with $pK_a <$ 10.3 (carboxylic acid) and NaOH accepts proton from functional groups with $pK_a >$ 10.3 including phenols and carboxylic acids. The total reactive sites calculated from Boehm titrations for WS and WPC are higher than concentrations determined by potentiometric titration, 1.0 mmol/g and 1.23 mmol/g, for WS and WPC, respectively. This result is consistent with the fact that the Boehm titration tests a wider pH range (down to pH <2 and pH ~13) as compared to that of the potentiometric titrations, which start from approximately pH 3. Therefore, the difference in pK_a ranges covered by ligands corresponding to surface functional groups by both the titrations likely caused the observed differences in total densities of reactive sites. The functional groups calculated from titration model correlate well with FT-IR and XPS analyses, as carboxyl and phenolic hydroxyl groups appear to be the main functional groups in these analyses.

3.3.3 Binding of U(VI) Species to Biochar

Maximum U(VI) adsorption occurs between pH 5 to pH 6 (Figure 3.2), then decreases at higher pH (pH > 6), consistent with previous studies (Rihs et al., 2014; Sun et al., 2016; Duster et al., 2017). The adsorption edges for WS and WPC show similar features at all three U loadings and sorbent ratios (Zheng et al., 2003; Chen et al., 2015; Duster et al., 2017). The maximum U(VI) loadings observed at our experimental conditions (0.2 g L^{-1} biochar) are 25 mg/g and 35 mg/g for WS and WPC, respectively. WPC has a higher U(VI) adsorption capacity than WS,

attributed to its higher surface area and more reactive sites as compared to WS (Table B.S3.2 and B.S3.4).

WS and WPC have negatively charged surfaces at pH >2 to 3 (Figure 3.1D), and positively charged U(VI) species (e.g., UO_2^{2+}, UO_2OH^+ and $(UO_2)_2(OH)_2^{2+}$) dominate the aqueous speciation at pH < 6 (Figure B.S3.1) (Chia et al., 2012; Rihs et al., 2014; Sun et al., 2016; Duster et al., 2017). Therefore, the strong electrostatic attraction between negatively charged biochar and positively charged U(VI) species causes the increasing trend of U(VI) adsorption from pH 2 to pH 6. The observed decrease of U(VI) adsorption on WS and WPC at pH > 6 was due to the electrostatic repulsion between negatively charged U(VI) species (e.g., $(UO_2)_3(OH)_7^-$ and $UO_2(OH)_3^-$ and $(UO_2)_3(CO_3)_6^{6-}$) that are dominant at pH > 6, and negatively charged WS and WPC surface sites. The occurrence of dissolved inorganic carbon and formation of carbonato-uranyl complexes (e.g., $UO_2(CO_3)_2^{2-}$ and $(UO_2)_3(CO_3)_3^{4-}$) also dramatically decrease the adsorption U(VI) at pH > 6.5 (Sun et al., 2015; Pan et al., 2017).

Natural systems are considerably more complex as they contain a larger variety of inorganic and organic competing ions (Ren et al., 2010; Alam et al., 2014). As Ca^{2+} is one of the key components of ternary complexes with U(VI), Ca^{2+} was used to investigate how the presence of a divalent cation could affect the U(VI) adsorption capacity of WS and WPC. For both biochar samples, U(VI) adsorption was lower in the presence of Ca^{2+} (Figure 3.3), presumably because the presence Ca^{2+} causes the formation of dominant uranyl-calcium-carbonato ternary complexes above pH 7 (e.g., $Ca_2UO_2(CO_3)_3^0$ and $CaUO_2(CO_3)_3^{2-}$) (Dong et al., 2005; Fox et al., 2006). The adsorption of U(VI) was reduced dramatically above pH 7 since $Ca_2UO_2(CO_3)_3^0$ (aq) species become prominent at that pH value (Dong et al., 2005; Fox et al., 2006). It is also evident that dissolved Ca^{2+} also influences U(VI) adsorption at pH <7, i.e., Ca^{2+} reduced U(VI)

adsorption at by approximately 20%. Slightly acidic waters are typical of freshwater systems, including many U contaminated aquifers (Zheng et al., 2003; Dong et al., 2005), and thus it is important to account the effects of divalent cations, especially Ca^{2+}, on U(VI) aqueous speciation in order to predict more accurately the sorption behavior of U(VI) onto biochar.

3.3.4 U(VI) Adsorption Analysis

XANES of WS loaded with U(VI) indicate no reduction of adsorbed U(VI) species by WS (Figure 3.4), although it is possible that reduced U(IV) species were rapidly reoxidized in the presence of oxygen during the analysis at CLS. The k^3 U L_{III}-EXAFS spectra show a low signal-to-noise ratio at $k > 7Å^{-1}$ for most samples. This may be attributed to the relatively low U(VI) concentration used in our experiments (Sun et al., 2015; Sun et al., 2016). The bond distance (R+ΔR) in Fourier-transform (FT) peaks revealed the existence of U-Oax and U-Oeq shells. The shell at distances between ~1.3 and ~1.8 Å in the FT data can be satisfactorily fitted by two axial oxygen atoms (Oax-U-Oax) (Table 3.1), which is consistent with previous studies (Arai et al., 2006; Sun et al., 2015; Sun et al., 2016). The FT feature at a distance ~1.9 Å, corresponding to equatorial U-Oeq shells, can be fitted by U-Oeq at ~2.4 Å, revealing the possibility of an O=U=O transdioxo structure. The splitting of the U-Oeq shell itself can be attributed to the presence of inner-sphere surface complexes. The similarities of EXAFS spectrum of WS at pH 5 and 8 to UO_2^{2+} indicate the formation of outer-sphere surface complexes at pH 5 and 8. The FT feature at approximately 3.0 Å in the samples can be fitted with a U-C shell, indicative of inner-sphere surface complexation (Sun et al., 2015; Sun et al., 2016). Finally, the FT shell found in samples prepared at pH 8 and 10 were fitted with a U-U shell at a distance of 3.4 to 3.7 Å (Table 3.1). The fitted U-U shell is comparable to the parameters of the first U-U shell (i.e., R = 3.80 Å and CN = ~0.5) of schoepite ($(UO_2)_8O_2(OH)_{12}.12H_2O$),

suggesting that this U(VI) mineral, or a similar mineral phase, may form at pH 7 or above (Sun et al., 2015), and beside inner and outer sphere complexes, and there was limited surface precipitation of U(VI) at high pH (Bargar et al., 1999).

The adsorption mechanisms of U(VI) to WS and WPC were also investigated by XPS analysis (Figure 3.5). The relative intensity of the O 1s spectra for U(VI) sorbed onto WS and WPC decreased and the binding energy shifted to higher energy compared to WS and WPC. This indicates that a variety of oxygenated functional groups, including –OH, -O-, and –COOH, were responsible for U(VI) adsorption (Alam et al., 2018b). FT-IR analyses (Figure B.S3.6) shows that the intensity of band at 1710 cm^{-1}, assigned to the -C=O stretching vibration of the -COOH group, decreases significantly after U(VI) binding (Fein et al., 1997; Ankudinov and Rehr, 2000; Keiluweit et al., 2010). The reduction in the intensity of the band is likely due to the interaction of uranyl species with this functional group (Alessi et al., 2014). XRF mapping of U(VI)-laden biochar shows that the distribution of U(VI) on the biochar grains is highly heterogeneous (Figure 3.6), presumably related to varying local concentrations of available U(VI) biding sites.

The zeta potentials of U(VI)-sorbed biochar samples are more negative than bare biochar particles at $3 < pH < 10$. This observation is somewhat counterintuitive as one would expect sorption of U(VI) cations to render the biochar surface more positively charged (Figure B.S3.7). We speculate that the behavior observed arises from cation bridging by UO_2^{2+} and aggregation of UO_2^{2+} coupled biochar particles and their subsequent separation from the suspension during centrifugation, leaving only highly negatively charged biochar particles in the supernatant. At the same time, bare biochar particles would remain polydispersed, yielding a lower zeta potential.

3.3.5 Surface Complexation Modeling

A non-electrostatic surface complexation model was developed using U(VI) adsorption data for both biochar samples in order to predict U(VI) adsorption across a wide range of pH, water composition, sorbent ratios and U(VI) loading. The adsorption data was modeled using EXAFS structural investigation which showed that U(VI) was adsorbed on WS mostly through -COOH and -OH functional groups by forming inner- and outer-sphere complex. EXAFS also show direct evidence of U(VI) surface precipitation at pH >8, possibly as schoepite.

UO_2^{2+} dominates the aqueous U(VI) speciation at pH < 5, and it is expected that UO_2^{2+} adsorption at low pH would be primarily due to the availability of deprotonated Site 1 which corresponds to carboxyl groups in both WS and WPC. Consequently, at Site 1 correspond to –COOH and pH < 5, the following adsorption reaction and corresponding mass action expression are used to describe the binding of the uranyl cation to biochar as monodentate complex and the resulting stability constant, respectively:

$$\text{R-L}_1^- + UO_2^{2+} \leftrightarrow \text{R-L}_1(UO_2^+) \quad (2)$$

$$K_{UO_2^{2+}} = \frac{[\text{R}-\text{L}_1UO_2^+]a_{H^+}}{[\text{R}-\text{L}_1^-]a_{UO_2^{2+}}} \quad (3)$$

where, L_1 is the discrete surface functional group attached to biochar particle R, *a* represents the activity of subscribed species (FITEQL uses the Davies equation calculate the activity coefficients), and [] represents the molal concentrations of the biochar surface species.

Invoking only the first site in the biochar 3-site protonation model for U(VI) adsorption results in a model that fits U(VI) adsorption data well up to pH 4, but does not adequately describe U(VI) adsorption between pH 4 and 8 (Figure B.S3.8). Consequently, we infer that additional U(VI)-bearing surface complexes are present at higher pH, and they can sorb in site 2 and/or site 3 in 3-proton active sites. Aqueous uranyl hydroxide and uranyl carbonate species

become dominant between pH 5 to 8 (Sun et al., 2016; Duster et al., 2017). For this reason, we tested the adsorption of uranyl hydroxide and uranyl carbonate aqueous species in site 2, and found that allowing for the adsorption of $UO_2CO_3^0$ provides the best fit to the experimental data (Figure 3.2), as follows:

$$\text{R-L}_2^- + UO_2CO_3^0 \leftrightarrow \text{R-L}_2UO_2CO_3^- \quad (4)$$

$$K_{UO_2CO_3^0} = \frac{[\text{R}-\text{L}_2UO_2CO_3^-]a_{H^+}}{[\text{R}-\text{L}_2^-]a_{UO_2CO_3^0}} \quad (5)$$

This 2-site adsorption model, invoking U(VI) adsorption to the first two sites (i.e., UO_2^{2+} to site 1 and $UO_2CO_3^0$ to site 2) using the first two pK_a values and corresponding site concentrations from the 3-site protonation model, provided the best fit to the experimental data. The contribution of the first and second sites to the total modeled U(VI) adsorption is presented in Figure B.S3.9. The stability constants calculated from this model (Table 3.2), based on reactions 4 and 6, provide the best fit to the experimental data up to pH 8. However, the model underestimates the observed U(VI) adsorption at pH > 8. Duster et al. (2017) noted that the adsorption of one uranyl tricarbonate species (e.g., $(UO_2)(CO_3)_3^{4-}$) could contribute to the better fit at higher pH (Duster et al., 2017). Therefore, we attempted to invoke an additional reaction to allow for the adsorption of such a uranyl tricarbonate species, but this did not result in an improved fit. The misfit at pH >8 is probably due to the precipitation of a U(VI) phase as discussed above and evidenced by the EXAFS results. We additionally tested bidentate (Eqn. 6) and tridentate surface complexes (Eqn. 7), according to the reactions:

$$\text{R-2L}_1^- + 2UO_2^{2+} \leftrightarrow \text{R-2L}_1(UO_2^+) \quad (6)$$

$$\text{R-3L}_1^- + 3UO_2^{2+} \leftrightarrow \text{R-3L}_1(UO_2^+) \quad (7)$$

Invoking bidendate surface complexes to fit the experimental data provided the same goodness of fit as for the monodentate models (Figure B.S3.10), and models that used tridentate surface complexes did not converge. Because EXAFS modeling was consistent with formation of monodentate bonding, we used that coordination for surface complexation modeling.

The binding constant (K) values for uranyl sorption to site 1 are consistent across varying U(VI) loadings and sorbent concentrations for both WS and WPC, except at lower sorbent concentrations (0.2 g L^{-1}) (Table 3.2). The K values for site 2 vary with the U(VI) and sorbent concentrations, which may be attributed to the sorption of additional U(VI) species to site 2, due to the complex speciation of uranyl at circumneutral pH. Overall, the 3-site protonation model that invokes U(VI) adsorption to the first two sites provides an excellent fit to the observed U(VI) data at all three sorbent concentrations and U(VI) loadings tested in this study.

The effects of Ca^{2+} on U(VI) adsorption were also been modeled using both reaction 1 and 3, and the aqueous U(VI) complexation reactions (Table B.S3.1). In the presence of Ca^{2+}, the model fits the experimental data well except at pH >7, similar to what was observed in the models of U adsorption in the absence of Ca^{2+} (Figure 3.3).

3.3.6 Titration Calorimetry Data Analysis

The bulk corrected heats values for WS and WPC showed different trends in heat produced as U was complexed. These corrected heats are modelled independently and illustrate bulk trends in U adsorption onto the biochar. Overall heats of U complexation onto WS were exothermic, while WPC produced endothermic heats (Figure 3.7 and B.S3.11). Despite these different overall heats for WS and WPC, one similar trend in both systems is that heats become more endothermic as pH increases. The pH for the ITC experiments were chosen between 5 to 6 as the U(VI) adsorption was highest at these pHs for the experimental conditions tested (Figure 3.2). As pH

increased from 5.1 to 5.9 for WS, heats of U complexation became about 70% more endothermic (though still exothermic overall). As pH increased from 5.2 to 5.8 for WPC, heats of U complexation became about 60% more endothermic. This trend may be related to changes in U speciation as pH increases. From pH 5.1 to 5.2, U speciation is dominated by the UO_2^{2+} under the calorimetric conditions, while at pH 5.9 the U speciation is started dominating by hydroxyl and carbonate complexation. As U speciation changes, the hydration sphere of the U also changes. The endothermic trend as pH increases may be, in part, be related to the breaking the hydration bonds (an endothermic process) of aqueous uranyl complexes that are adsorbing onto the biochar surface. There are multiple reactions that contribute to the bulk corrected heats (e.g., redistribution of protons on the surface, aqueous U complexation, etc.). To deconvolve these reactions and determine the U-surface complex contribution to the measured heats, a surface complexation model must be applied to the data to speciate the system. Consequently, site-specific enthalpies of complexation are dependent on the surface complexation model.

Site specific enthalpies of U adsorption onto WS were strongly exothermic. U complexation onto L_1 produced exothermic enthalpies of approximately -100 to -120 kJ/mol, while complexation onto L_2 produced smaller exothermic enthalpies around -50 kJ/mol (Table 3.3 and B.S3.5). Comparing enthalpies with $-T\Delta S$ values shows the thermodynamic driving force of U complexation onto WS is enthalpically driven by U-biochar bond. Entropies of U adsorption are substantially negative for the L_1 site and moderately negative for the L_2 site. Typically, small entropies of complexation are interpreted as outer sphere complexation with the hydration shells remaining in place imparting more order within the solution (Ahrland et al., 1958; Pearson, 1968a and 1968b; Beck and Nagypal, 1990; Martell and Hancock, 1996). However, the EXAFS results indicate the formation of both inner sphere and outer sphere

surface complexes. While entropies of complexation are highly dependent on hydration they are also dependent on statistical and physical effects (King, 1965; Nancollas, 1966). These influences can include the formation of H-bonds that would cause enthalpies of complexation to become more exothermic while entropies become smaller. Nash et al. (1995) observed these effects for Eu^{III} complexation with 1-hydroxyethylidene-1,1-diphosphonic acid, which was confirmed to be an inner sphere complex by fluorescence spectroscopy. The WS biochar surface may be conducive to forming an extensive H-bonding network to equatorial hydrating water molecules of the uranyl ion bound to L_1; hence, the very small entropy yet the possibility of inner sphere formation. The larger entropy of the L_2 surface complex may suggest the partial or complete lack of H-bond stabilization, and retention of hydration sphere typical of outer sphere complexes.

Site specific enthalpies of U complexation on to WPC were mildly exothermic (approximately -10 kJ/mol) for L_1 and endothermic (approximately 50 to 100 kJ/mol) for L_2 (Table 3.3 and B.S3.5). Comparing these enthalpies with $-T\Delta S$ values shows the thermodynamic driving force of U complexation onto WPC is entropically driven by dehydration reactions. Entropies of complexation are large and positive, consistent with increased disorder in the system because of the liberation of water molecules through dehydration, which is indicative of inner sphere complex formation. These results are also consistent with uranyl complexation by anionic oxygen ligands, which produce mildly exothermic to endothermic enthalpies and large positive entropies of complexation (Jiang et al., 2002; Rao et al., 2002; Rao et al., 2004; Pettit and Powell, 2005). These results contrast with the characterization of U complexation onto WS, which suggests that U adsorption by WS and WPC is driven by different thermodynamic mechanisms. Characterization of WS and WPC does indicate some differences in terms of

surface area, N and S content, and protonation enthalpy (Table B.S3.3 and B.S3.6). How these different biochar properties impact mechanisms of U adsorption are not borne out by less sensitive methods of in investigation like surface complexation modeling alone. Nonetheless, surface complexation modeling coupled with calorimetric characterization highlights mechanistic differences that may be imparted by properties of the biochars.

3.4 ENVIRONMENTAL IMPLICATIONS

In this study, we combined thermodynamic modeling with spectroscopic evidence to better understand how aqueous U(VI) species adsorb to the surface of biochar, and obtained site specific thermodynamic parameters for U(VI) adsorption on biochar. Such molecular-level studies coupled to SCM are important for determining correct surface coordination of metals and in calculating accurate intrinsic stability constants of the corresponding metal adsorption reactions. In this study, the resulting model allows for improved predictions of U(VI) adsorption by the sorbent, biochar.

The flexible surface complexation modeling approach applied in our study successfully simulated the adsorption behavior of U(VI) on biochar across a wide range of water chemistry. EXAFS, FT-IR and XPS suggest that U(VI) is coordinated to the surface of the biochar primarily through –COOH and –OH functional groups. EXAFS analyses also indicated that U(VI) adsorption on biochar occurred via the formation of both inner- and outer-sphere complexes, and surface precipitation of a schoepite-like phase was observed at pH >7. ITC revealed that proton adsorption reactions are exothermic to mildly endothermic and U(VI) adsorption reactions are generally exothermic with –COOH and endothermic with -OH. However, the enthalpic behavior of the reactions is site-specific and depends on protonation states for the functional groups. This findings are important for understanding the how U(VI) complexes with carbonaceous materials

such biochar, and lead to better predictive models of U(VI) adsorption to enhance the use of biochar as a tool to efficiently to treat U(VI) contaminated water.

Table 3. 1. EXAFS fit results for U(VI) adsorbed onto wheat straw biochar (WS*).*

Samples	Paths	CN	R(Å)	σ^2(Å^2)
UO_2^{2+}	U-O_{ax}	2.0[a]	1.86	0.0028
pH 5	U-O_{eq}	6.0[a]	2.45	0.0100 [a]
	U-O_{ax}	2.0	1.77	0.0028
	U-O_{eq}	6.0	2.36	0.0100[a]
	U-C	3.1	2.95	0.005
pH 8	U-O_{ax}	2.0[a]	1.79	0.0050
	U-O_{eq}	6.0[a]	2.40	0.0100[a]
	U-C	2.9	2.95	0.0050
	U-U	1.6	3.40	0.0090
pH 10	U-O_{ax}	3.1	1.80	0.0040
	U-O_{eq}	2.2	2.40	0.0100[a]
	U-C	2.4	3.01	0.0050
	U-U	0.5	3.44	0.0090
U-Ca	U-O_{ax}	4.0	1.80	0.0050
	U-O_{eq}	4.0	2.4	0.0030
	U-Ca	1.6	3.04	0.0050
	U-C	4.7	3.13	0.0050
	U-U	1.0	3.72	0.0010 [a]

[a]High limit for parameter floating

Table 3. 2. Stability constants obtained from U(VI) adsorption onto the first two sites of the 3-site protonation models of WS and WPC.

Biochar concentration	U(VI) concentration	WS			WPC		
		$logK_1$	$logK_2$	V(Y)	$logK_1$	$logK_2$	V(Y)
1 gL^{-1}	10 µM U	4.30	6.13	1.30	4.95	6.42	1.4
	20 µM U	4.31	6.40	7.0	4.80	7.0	10.0
0.5 gL^{-1}	5 µM U	4.62	7.16	0.36	4.83	4.32	0.3
	10 µM U	4.64	6.28	2.5	4.60	6.48	3.7
	20 µM U	4.45	6.75	5.0	4.30	7.76	3.0
0.2 gL^{-1}	5 µM U	5.25	6.66	0.83	5.42	6.85	0.6
	10 µM U	4.81	6.86	1.20	4.08	9.52	3.7
	20 µM U	3.16	8.44	7.82	3.75	9.50	7.8

Table 3. 3. Site-specific thermodynamic parameters for U(VI) adsorption onto WS and WPC, derived from calorimetric titrations and U(VI) adsorption onto the first two sites of the 3-site protonation model.

U(VI) concentration	Species	logK	Gibbs free energy, $\Delta G_r°$ (KJ/mol)	Enthalpy, $\Delta H_r°$ (KJ/mol)	$-T\Delta S_r°$ (KJ/mol)	Entropy, $\Delta S_r°$ (J/molK)	χ^2
				WS (1 gL^{-1})			
10 µM U	$L_1UO_2^+$	4.30(0.13)	-24.54(0.74)	-107.82(0.67)	83.27(1.00)	-279(3)	8.525e-8
	$L_2UO_2CO_3^-$	6.13(0.13)	-34.99(0.74)	-50.85(0.71)	15.86(1.03)	-53(3)	
20 µM U	$L_1UO_2^+$	4.31(0.07)	24.60(0.40)	-110.29(0.70)	85.69(0.81)	-287(3)	8.384e-8
	$L_2UO_2CO_3^-$	6.40(0.08)	-36.53(0.46)	-53.25(0.66)	16.99(0.81)	-57(3)	
				WPC (1 gL^{-1})			
10 µM U	$L_1UO_2^+$	4.95(0.15)	-28.25(0.86)	-7.51(0.87)	-20.75(0.87)	70(4)	1.498e-7
	$L_2UO_2CO_3^-$	6.42(0.13)	-36.65(0.74)	87.00(2.19)	-123.64(2.32)	415(8)	
20 µM U	$L_1UO_2^+$	4.80(0.07)	-27.40(0.46)	-11.89(0.96)	-15.51(1.06)	52(4)	1.496e-7
	$L_2UO_2CO_3^-$	6.99(0.08)	-39.90(0.46)	44.58(1.07)	-84.48(1.16)	283(4)	

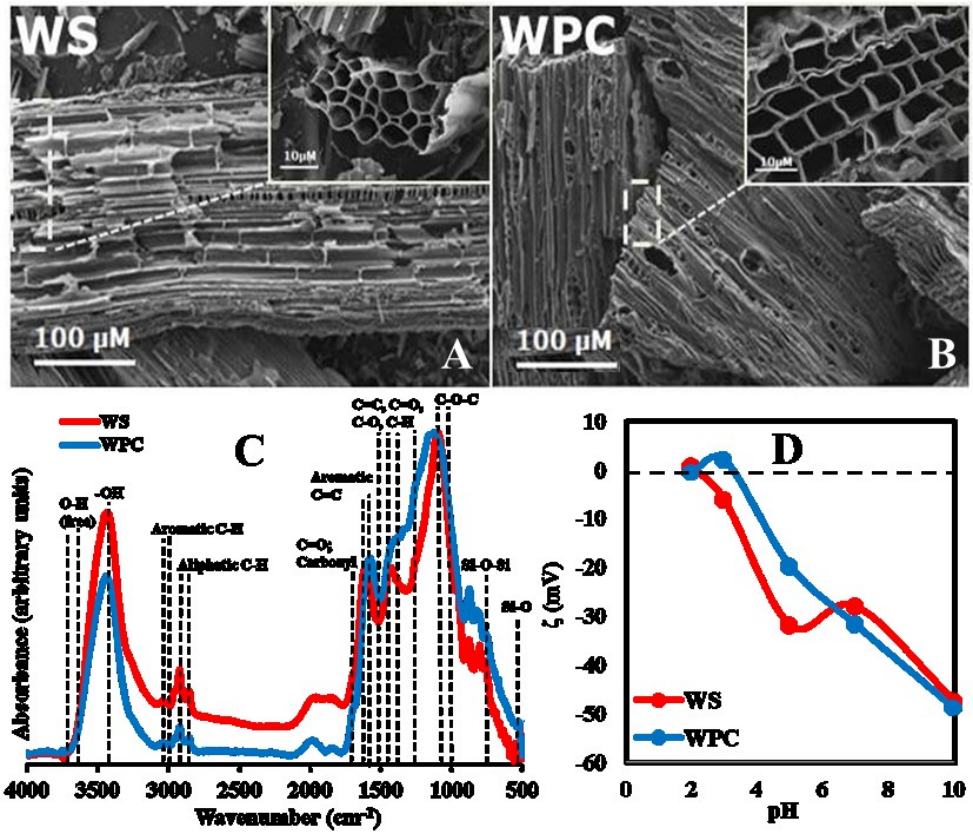

Figure 3.1. Characterization of WS and WPC. (A) and (B) SEM images; (C) FT-IR; and (D) Zeta-potential.

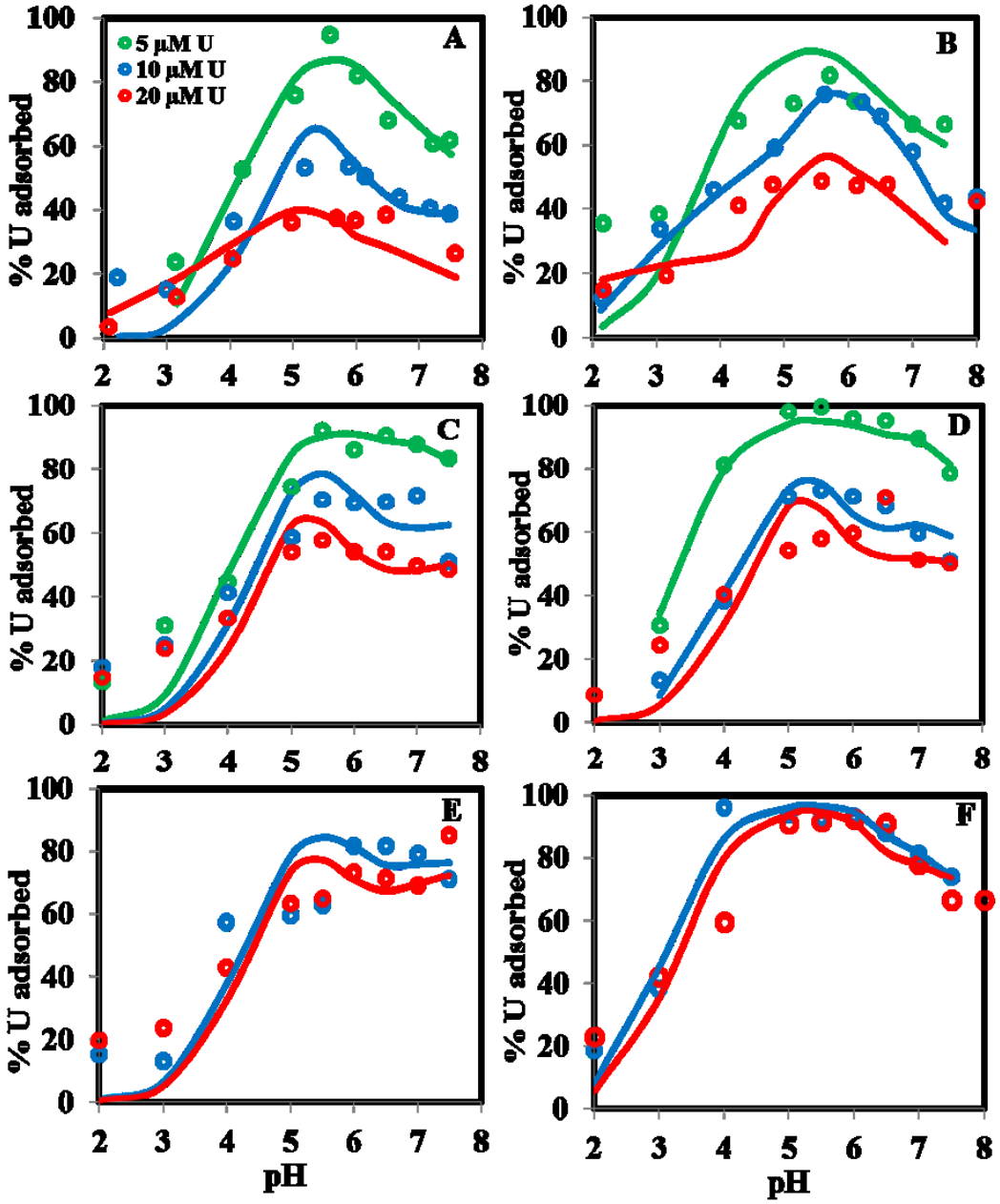

Figure 3.2. Adsorption of U(VI) onto WS and WPC, and models of U(VI) adsorption onto the first two sites of the 3-site protonation model: (A) 0.2 g/L WS; (B) 0.2 g/L WPC; (C) 0.5 g/L WS; (D) 0.5 g/L WPC; (E) 1 g/L WS; and (F) 1 g/L WPC. Open symbols and solid lines Open symbols and solid lines represent experimental data and models, respectively.

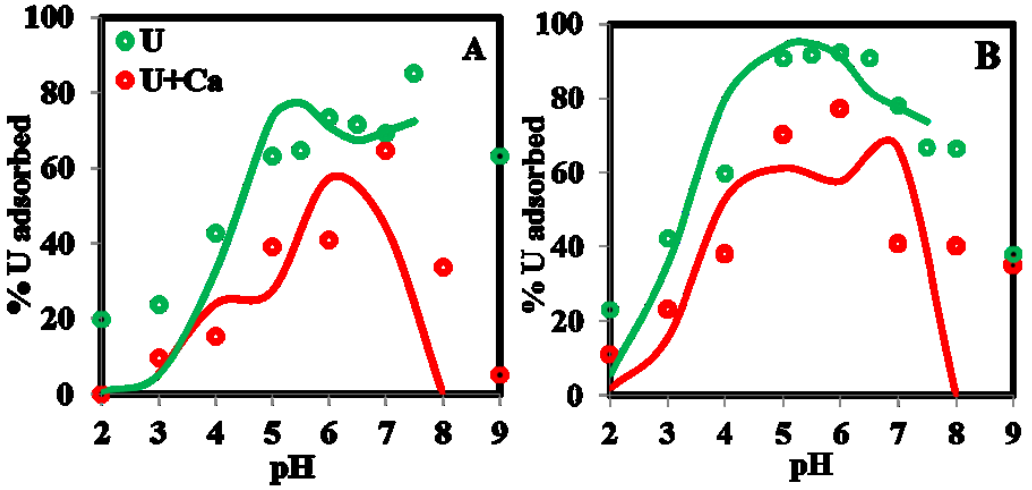

Figure 3.3. Effect of 10 mM Ca^{+2} on the adsorption of U(VI) onto WS (A) and WPC (B) at 20 µM U(VI) and 1g/L biochar concentrations. Open symbols and solid lines represent experimental data and models, respectively.

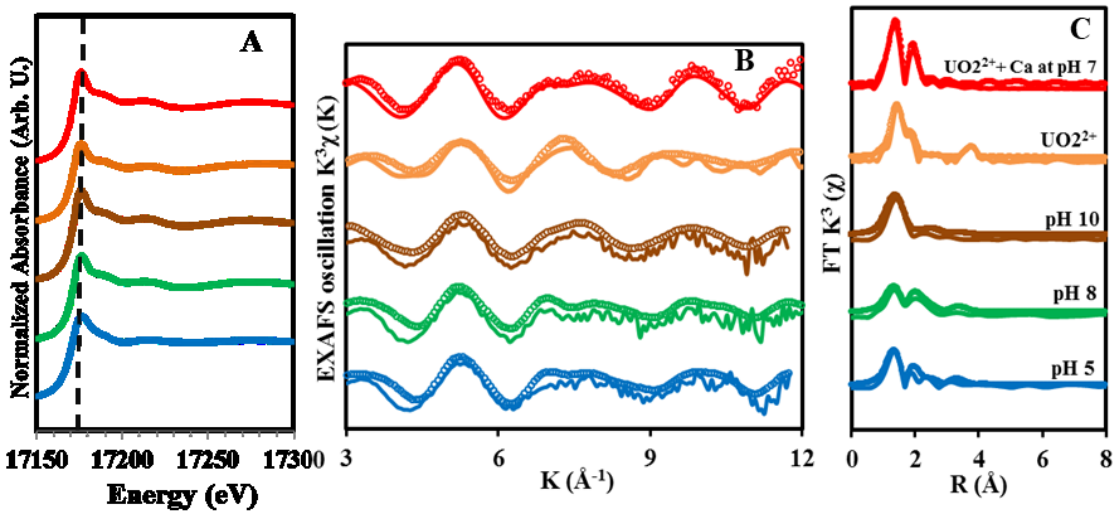

Figure 3.4. XANES and EXAFS spectra of U(VI) adsorbed onto WS.(A) XANES spectra of U(VI) adsorbed samples and uranyl reference. (B) EXAFS signals weighted by k^3 spectra. (C) R space curve fitting results. Solid lines are experimental data and dotted lines are fitted data.

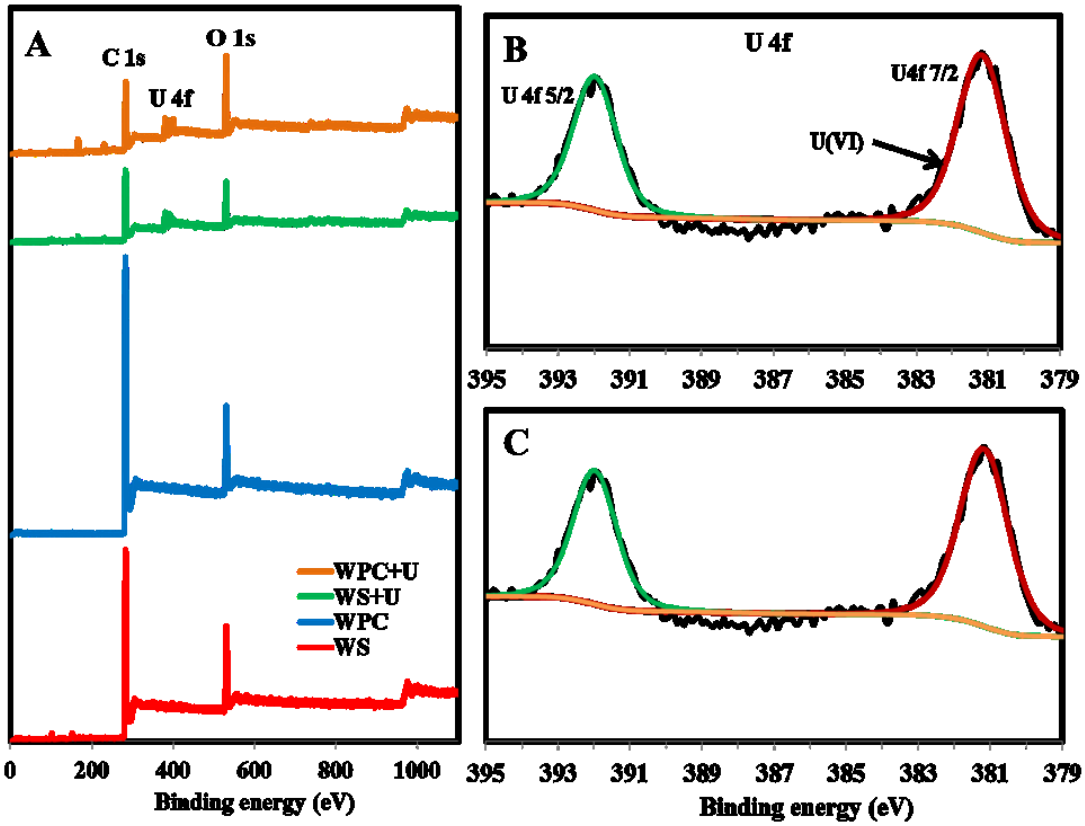

Figure 3.5. XPS analysis of the WS and WPC. (A) survey scans of WS, WPC and U(VI) adsorbed to WS. (B-C) high resolution U 4f of U(VI) adsorbed WS and WPC, respectively.

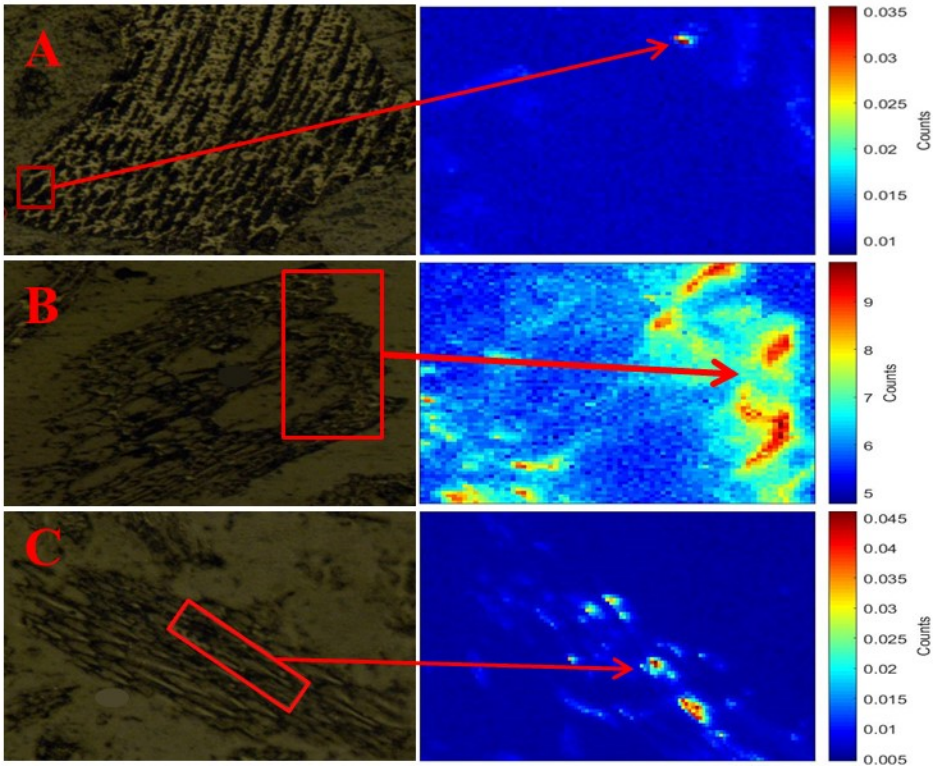

Figure 3.6. Synchrotron-XRF map of U(VI) distribution onto WS at pH (A) 5, (B) 7; and (C) 10.

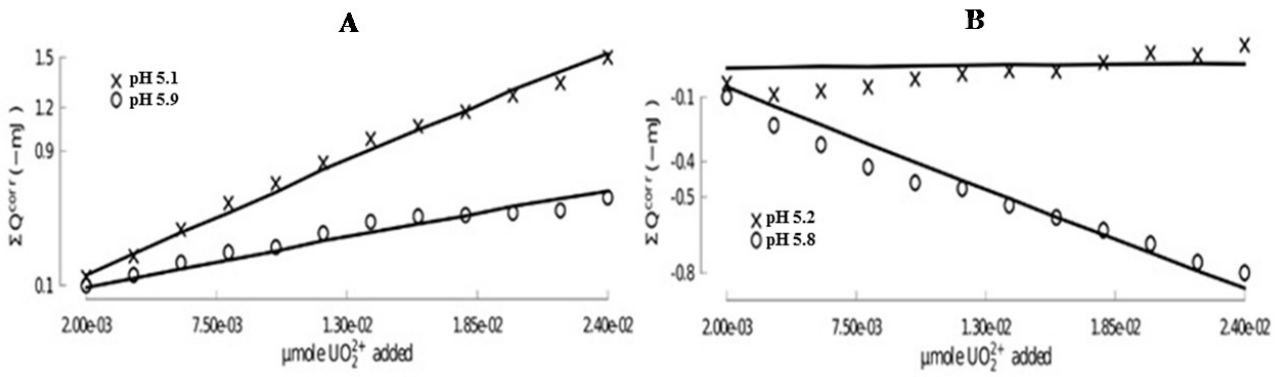

Figure 3.7. Corrected heat generated from 10 µM U(VI) adsorption titrations with (A) WS and (B) WPC at 1 g L-1 concentration. The scattered curve and solid line represent the experimental data and fit, respectively.

CHAPTER 4

APPLICATION OF SURFACE COMPLEXATION MODELING TO TRACE METALS UPTAKE BY BIOCHAR-AMENDED AGRICULTURAL SOILS

ABSTRACT

Biochar has emerged as an amendment to release nutrients into agricultural soil to increase crop productivity and as a sorbent to remediate metals and organics contamination. Since soils have heterogeneous physical properties across a given crop field or over a growing season, it is imperative to select the most appropriate biochar for the intended purpose and in defining the amendment level. In this study, we investigate the adsorption of Cd(II) and Se(VI) to two agricultural soils amended with a wood pin chip biochar (WPC). The proton reactivity of each sorbent was determined by potentiometric titration, and single-metal, single-sorbent experiments were conducted as a function of pH. The resulting data were modeled using a non-electrostatic surface complexation modeling (SCM) approach to determine the proton and metal binding constants and surface functional group concentrations of each soil and WPC. The SCM approach is a considerable advance over empirical modeling approaches because SCM models can account for changes in pH, ionic strength, temperature, and metal-to-sorbent ratio that may happen over the course of a growing season. The constants derived from the single-metal, single-sorbent experiments were then used to predict the extent of metal adsorption in more complex mixtures of Cd, Se, soil and WPC. Overall the SCM approach was successful in predicting metal distribution in multi-component mixtures. In cases where the predictions were not as good, we

identify reasons and discuss future experiments needed to further the application of SCM to sorbent mixtures containing biochar.

4.1 INTRODUCTION

Biochar is an increasingly popular soil amendment used to enhance or modify natural microbial activity (Anders et al., 2013; Masillo et al., 2013; Kappler et al., 2014; Zhang et al., 2014), to release nutrients critical for crop growth (Uchimiya et al., 2010; Laird and Rogovska, 2015; Lehmann et al., 2015), and as a remediation technique to immobilize contaminants in soil and water (Rees et al., 2014; Ahmad et al., 2014; Alam et al., 2016). In part because biochar has promise in contributing to global carbon sequestration (Woolf et al., 2010), research on its properties and uses has expanded dramatically in the past decade (Verheijen et al., 2014). Understanding how biochar amendment impacts the distribution of trace metals, and ultimately their transport in soils, is critical to its ongoing use in agricultural applications. Römkens et al. (2002) and Bonten et al. (2008), using agricultural soils in the Netherlands as an example, point out that metal leaching is an underappreciated and understudied contributor to the metals loads of surface waters. Furthermore, soil and water geochemistry in crop fields are not static; considerable temporal and spatial variations in pH, and nutrient and metals phytoavailability occur (Andersson and Bingefors, 1985; Cambardella et al., 1994; López-Granados et al., 2002; Zhao et al., 2011). In this context, a flexible approach to predicting the impacts of biochar amendment on metal mobility in agricultural soils is required.

Most of the current literature on metals adsorption to biochar-amended soil, and indeed on biochar and soils separately, employs empirical adsorption models such as the linear distribution coefficient (K_D) and various adsorption isotherms (e.g., Freundlich, Temkin, Langmuir) to fit data from adsorption experiments. While useful at the conditions under which

the experiments are conducted, predictions of metal distribution from these models are often not valid if parameters such as pH, solution ionic strength, sorbate-to-sorbent ratios, and temperature change in the system of interest (Bethke and Brady, 2000; Koretsky, 2000). In addition, the models do not consider the aqueous speciation of metals or the underlying mechanisms of metal adsorption. By contrast, surface complexation models (SCMs) offer an alternative, and more mechanistic approach. SCMs use a system of equations approach to consider the chemical speciation of solutes, the type and concentration of discrete reactive surface sites on sorbents in the system, and the formation of surface complexes with defined stoichiometries. For equations in the system, which represent individual chemical reactions, a mass action constant (K) is defined which describes conditions at which the reactants and products are at equilibrium, because K satisfies conditions for which the Gibbs free energy of reaction ($\Delta_r G$) is nil (Garrels and Christ, 1965; Anderson, 2005). These systems of equations can then be solved to predict the equilibrium distribution of sorbates of interest in the system over a wide range of pH, ionic strength, and sorbate-to-sorbent ratios, and can also consider the competition of multiple sorbates for binding to discrete sites on the sorbent surfaces.

As SCMs consider numerous molecular-scale reactions, they are inherently more complex and data-intensive than empirical adsorption modeling approaches. As Goldberg (1992) notes, SCMs of soil-metal interactions often use only a few types of surface sites, while in reality soils are always far more complex and contain numerous types of sites. In fact, describing the protonation and metal adsorption behavior of individual soil components themselves, such as bacteria (Fein et al., 1997; Cox et al., 1999; Fein, 2006), metal oxides (Davis et al., 1978; Dzombak and Morel, 1990; Lalonde et al., 2007a; Komárek et al., 2015), carbonates (Lalonde et al., 2007b, Flynn et al., 2017) organic matter (Smith and Kramer, 1999), and clays (Schroth and

Sposito, 1997; Kraepiel et al., 1999), typically requires invoking more than one binding site. Because of this complexity, Davis et al. (1998) proposed two methods to model metal distribution in complex assemblages of sorbents using the SCM approach: the component additivity (CA) approach and the general composite (GC) approach. The CA approach is premised on first developing protonation and metal adsorption models for each major sorbent in the complex assemblage, which yields binding site densities, pK_a values, and mass action constants for metal binding for each sorbent. Predictions about the equilibrium metal distribution in admixtures of the sorbents can then be made by invoking combinations of the models developed for each sorbent, at the ratios in which those sorbents are present in the admixture being considered. There are some limitations to the CA approach. For example, it is well known that organic ligands can both complex metals in solution and lead to the formation of ternary metal-ligand-surface complexes on sorbents (Davis, 1984). In an application of the CA approach, Alessi and Fein (2010) successfully described Cd(II) adsorption to admixtures of kaolinite, planktonic *Bacillus subtilis* cells, and hydrous ferric oxide. However, when a model organic ligand, acetate (CH_3COOH), was added to the system, it was necessary to invoke the adsorption of $Cd(CH_3COO)^+$ to sorbent surface sites to explain the observed Cd(II) adsorption behavior. Additionally, blockage of reactive sites may occur when sorbents aggregate in mixtures; for example, this was noted by Zachara et al. (1992) who reported that Fe oxides may block fixed-charge sites on kaolinite, thereby inhibiting Cd(II) adsorption. Kulczycki et al. (2005) observed similar impacts of site blockage when modeling the adsorption of Pb(II) and Cd(II) to admixtures of ferrihydrite and bacteria. Thus, the formation of ternary complexes and sorbent site blockage are two potential limitations that should be considered when applying the CA approach.

The general composite (GC) approach uses a single protonation model to describe complex, multi-component sorbents. In the case of a soil, generic functional groups - derived from the modeling of potentiometric titration data - are assigned to describe the protonation behavior of the whole soil. Assigning these generic sites allows for the flexibility and predictive ability inherent in the SCM approach, but without specific knowledge of the identity of those surface sites. Davis et al. (1998) used the GC approach to overcome difficulties in modeling Zn(II) adsorption to complex mineral assemblages.

While the application of SCMs to soils and their components is well-studied, research that applies surface complexation theory to model metal adsorption to biochar is now just emerging. Zhang and Luo (2014) successfully modeled Cu(II) adsorption to a biochar produced from anaerobic digester sludge, and Vithanage et al. (2015) developed a two-site electrostatic SCM to describe the adsorption of antimony (Sb) to a soybean-stover biochar. Despite this recent progress, to the knowledge of the authors, no multi-sorbent surface complexation model that includes biochar has been developed. In this paper, we investigated the impact of biochar amendment on Cd(II) and Se(VI) adsorption to two agricultural soils collected from a canola (*Brassica rapa*) and an alfalfa (*Medicago sativa*) field in Alberta, Canada. While Cd and Se are contaminants of concern in agricultural soils and to human health (Holmgren et al., 1993; Tan et al., 2002; Grant and Sheppard, 2008; Banuelos et al., 2013), these metals are used in this study primarily as a model cation and anion, respectively, in order to test the SCM approach on biochar-soil mixtures. A non-electrostatic SCM was developed for Cd and Se adsorption to the biochar and each of the two whole soils. Using these models, the CA approach is then used to predict the distribution of Cd and/or Se in mixtures of one of the soils and the biochar. Where the CA approach does not predict Se or Cd adsorption well, we discuss reasons for those disparities,

and more broadly identify ongoing challenges in applying the SCM approach to sorbent mixtures that contain biochar.

4.2 MATERIALS AND METHODS

4.2.1. Soil and Biochar Collection and Preparation

Two agricultural soils were collected in September 2016 approximately 60 km NNW of Edmonton, Alberta, Canada from a canola field (54° 5' 26" N 113° 52' 29" W) and an alfalfa field (54° 2' 45" N 113° 59' 60" W), hereafter referred to as CFS and AFS, respectively. The CFS was a solonetzic to solonetz soil, moderately well drained, with a 15-25 cm thick A horizon and a 15-25 cm thick B horizon; the AFS was a luvisolic soil, well drained, with a 15-30 cm thick A horizon and a 10-20 cm thick B horizon (Kjeargsgaard, 1972). To collect soil samples representative of each field, sampling locations were selected to be away from the entrances/exits and close to the center of the fields. The topsoil was removed with a shovel to a depth of five to eight centimeters below the surface with another shovel that was cleaned before sampling. Sampling went as deep as 20 cm below surface (12 to 15 cm below the bottom of the topsoil) and approximately 5 kg of soil was obtained from both the canola and alfalfa fields. Plastic bags containing the soils were sealed and transported to the University of Alberta. Once samples are dried, sieves were used to separate soil fractions by size. The soil fraction smaller than 1 mm was used for potentiometric titrations and metal adsorption experiments.

A wood pin chip biochar (WPC) from the Alberta Biochar Initiative (ABI) was produced by the pyrolysis of wood pin chip feedstock in a batch carbonizer under oxygen-limited conditions. Temperature in the pyrolysis unit was raised from 20°C to 500°C over a period of 60 min, and then held between 500°C and 550°C for 30 min. The resulting WPC was sieved to 2 mm prior to use in titration and metal adsorption experiments. The pH of each material was

determined by suspending 0.5 g of solids in 50 ml of water, and placing the mixture on a rotary shaker for 24 h prior to measuring pH (Novak et al., 2009).

4.2.2. Materials Characterization

4.2.2.1. Elemental Composition

Total metal composition of soil and biochar samples was determined by digestion with hydrofluoric acid (HF). Prior to the described digestion, the biochar was ashed at 500 °C during 8 hours to digest the material (von Gunten et al., 2017). For this purpose, 0.1 g of the dried soil sample were pretreated with 5 mL 70% nitric acid (HNO_3, ACS grade, Fisher Scientific) and 5 mL 30% hydrogen peroxide (H_2O_2, ACS grade, Fisher Scientific) and left to react for 1 h. The samples were then heated on a hot plate at 130°C for 3 h. 5 mL HF (47-51%, ACS grade, Fisher Scientific) were added to each vessel and evaporated at 130°C. 3 mL 37% hydrochloric acid (HCl, ACS grade, Fisher Scientific) and 1 mL HNO_3 were added to dissolve the remaining residue. The solution was heated to near dryness at 130°C, and finally diluted to 50 mL with 2% HNO_3 and 0.5% HCl. Aqua regia extractable metals were determined for the soil samples to account for possible Se losses through evaporation. This was done by adding 6 mL HCl (37%) and 2 mL HNO_3 (70%) to 0.1 g of dried soil material. The solution was heated to near dryness at 130°C on a hot plate, and finally diluted to 50 mL with 2% HNO_3 and 0.5% HCl. The reference material STSD-3 (CANMET Mining and Mineral Sciences Laboratories) was digested in parallel to verify elemental recovery. Metals and metalloids were analyzed using inductively coupled plasma mass spectrometry (ICP-MS/MS; Agilent 8800) operated with two mass separating quadrupoles and using a reaction cell with collision gases according the manufacturer's instruction. Sample analyses were conducted in triplicate, and Indium (500 ppb) was used for internal calibration. The contents of C, H, O, and N in the soils and biochar were measured by

combustion at 1000°C using an elemental analyzer (Carlo Erba EA1108). Dry combusted total organic carbon (TOC) and water extracted dissolved organic carbon (DOC) of AFS, CFS and WPC were determined using a TOC analyzer (Shimadzu TOC-V/TN).

4.2.2.2. Sequential Extractions for Metals

The two soils were characterized by sequential extraction according to a modified method by Tessier et al. (1979) and Li et al. (1995) to determine the elemental composition and distribution of elements in various sediment fractions. Extractions were performed on untreated, fresh samples and samples to which metals were sorbed. A more detailed account of the sequential extraction method is provided in Appendix C.

4.2.2.3. Powder X-ray Diffraction, Clay Content, Pedogenic Oxides and Cation Exchange Capacity (CEC)

Powder X-ray diffraction (XRD) was conducted on each of the soils and WPC to identify major crystalline phases in the materials. Prior to analysis, the materials were ground to a fine powder using a mortar and pestle, and analyzed using an X-ray diffractometer (Rikagu Ultima IV) with a cobalt source, between a 2θ ranges of 5° to 90°. Resulting diffraction patterns were fit using the JADE 9.5 analysis package (KS Analytical Systems).

The clay fraction in the soils, defined as less than 2 μm, was determined using particle size analyses (PSA) using the hydrometer method, and laser PSA using the Fraunhofer optical model. Major and minor oxides were calculated based on the total digestion data. Loss of ignition (LOI) was calculated from the elemental analysis data (see Table 4.1). Cation exchange capacity (CEC) of AFS, CFS and WPC was determined as described in Robertson et al. (1999).

4.2.2.4 Scanning Electron Microscopy

Materials were imaged using a scanning electron microscope (SEM; Zeiss EVO LS15) equipped with an energy dispersive X-ray spectroscopy (EDS) system (Bruker Quantax 200) for semi-quantitative measurement of elemental composition. Prior to analysis, samples were carbon coated using an evaporative carbon coater (Leica EM SCD005). Secondary electron images were captured using an Everhart-Thornley detector, and backscatter electrons were collected with a Si-diode detector.

4.2.3. Titration and Metal Adsorption Experiments

4.2.3.1. Potentiometric Titrations

Potentiometric titrations of each soil sample and biochar were conducted to determine their proton buffering capacities. To prepare for a titration, the pH electrode (Metrohm 905 Titrando) was calibrated using a set of three pH buffers, and then placed in a covered sample cup containing a magnetic stir bar, dispensers for acid (0.1 M HCl) and base (0.1 M NaOH) titrants, and 50 ml of electrolyte solution (0.01 M $NaNO_3$) containing 0.2 g of soil or biochar. The solution was bubbled for 30 min prior to the start of a titration, and continuously for the duration of the titration with N_2 gas, to prevent the introduction of atmospheric CO_2(g) into the solution. Titrations were conducted by initially adding acid to bring the solution to pH 3, then a forward (base) titration to pH 10, and finally a reverse titration to pH 3. Forward and reverse titrations were preformed to monitor for irreversible alterations to the soils and biochar which could result in hysteresis. All titrations were performed in dynamic addition mode whereby the titrator adds a variable volume acid or base (0.5 µl to 0.15 ml) depending on the buffering capacity observed during the previous addition. New additions were only made after the pH electrode achieved a stability 0.2 mV s^{-1}. A blank titration of just the background electrolyte solution (0.01 M $NaNO_3$)

was performed to quantify its proton buffering capacity, which was subtracted from the titrations of each of the materials.

Non-electrostatic surface complexation models were developed for AFS, CFS, and WPC. To solve for proton binding constants (pK_a) and site concentrations for each material, we fit the potentiometric titration data for each material using the least-squares optimization software FITEQL 4.0 (Herbelin and Westall, 1999). In the models, the deprotonation of a discrete number of surface functional groups is represented by the equilibrium reaction:

$$> R - A_i - H^0 \;\leftrightarrow\; > R - A_i^- + H^+ \qquad (1)$$

where $>R$ represents the soil or biochar particle to which proton-active surface functional group A_i is attached. The associated mass action equation for reaction (1) is defined as:

$$K_a = \frac{[>R-A_i^-]\, a_{H^+}}{[>R-A_i-H^0]} \qquad (2)$$

where K_a is the protonation constant, a_{H^+} represents the activity of protons in solution, and terms in brackets represent the molal concentrations of protonated and deprotonated surface functional groups.

To fit the titration data for each material, between one to four ($i = 1 - 4$) discrete sites were tested. FITEQL solves simultaneously for the functional group concentration and pK_a for each site. Best fit was determined by: (a) whether model convergence was achieved, and (b) the value of the variance parameter, V(Y), calculated in FITEQL; values of $1 \leq V(Y) \leq 20$ are generally considered to be good fits (Westall, 1982).

4.2.3.2. Metal Adsorption Experiments

Batch metal adsorption experiments were conducted with Se(VI) and Cd(II). To initiate an experiment, the soils were suspended to a concentration of 10 g l^{-1} or the biochar to 1 g l^{-1} in a solution containing either 0.1 mM Cd(II) as $Cd(NO_3)_2$, or 0.1 mM Se(VI) as Na_2SeO_4. While being agitated with a stir bar, 10 ml aliquots of a suspension were transferred to a set of twelve 15 ml polypropylene test tubes. Individual test tubes in the set were adjusted with small volumes of concentrated acid or base to cover a pH range between approximately 2 and 8. Higher pH was avoided to prevent Cd(II) precipitation as solid carbonate or hydroxide species (Liu et al., 2015) (Figure C.S4.1). Tubes were sealed and placed on an end-over-end rotator. As needed, the pH of tubes was adjusted with acid or base to maintain the target pH. The experiments were allowed to equilibrate for 12 h after the final pH adjustment, after which they were centrifuged at 10,000 g for 10 min (Sorvall Lynx 4000). The resulting supernatants were filtered through 0.45 µm nylon membranes, acidified with 5 µl of 10 M HNO_3, and stored in the dark at 4°C until analysis. Concentrations of Cd and Se were measured using an ICP-MS/MS (Agilent 8800) with an in-line internal standard addition system. Cd was analyzed using no-gas mode (i.e., no additional gas was introduced to the reaction chamber). Se was analyzed in two different modes: in no-gas mode, and by introducing 10% O_2 gas into the reaction chamber to apply a mass shift of 16. The resulting pH adsorption edge data were used to calculate the binding constants of Cd(II) and Se(VI) to each soil and the biochar.

Multi-sorbent and multi-metal experiments were conducted according to the protocol outlined above. In multi-sorbent experiments, 10 g l^{-1} of a soil was mixed with 1 g l^{-1} biochar, and either 0.1 mM Cd(II) or 0.1 M Se(VI). Multi-metal experiments included 10 g l^{-1} of a soil or 1 g l^{-1} of biochar, added to a mixture of 0.1 mM Cd(II) and 0.1 mM Se(VI). Finally, dual-metal /

dual-sorbent experiments were conducted by combining 10 g l^{-1} soil, 1 g l^{-1} biochar, 0.1 mM Cd(II), and 0.1 mM Se(VI). An additional set of experiments containing 5 g l^{-1} soil, 5 g l^{-1} biochar, and 0.1 mM each of Cd(II) and Se(VI) were conducted to further test the predictive capability of the SCM CA approach. For all data sets, binding constants calculated from the single-metal, single-sorbent systems, described above, were used to predict the extent of metal adsorption in the multi-component systems.

Using the protonation models developed for each sorbent (Section 2.3.1), metal binding constants were calculated. Cd(II) adsorption to the sorbent surface functional groups defined in the protonation models is described by:

$$> \mathrm{R-A_i^-} + \mathrm{Cd^{2+}} \;\leftrightarrow\; > \mathrm{R-A_i-Cd^+} \tag{3}$$

and the corresponding Cd binding constant, $K_{i\text{-}Cd}$, is defined by:

$$\mathrm{K_{i-Cd}} = \frac{[\mathrm{R-A_i-Cd^+}]}{[\mathrm{R-A_i^-}]\,\mathrm{a_{Cd^{2+}}}} \tag{4}$$

where $a_{Cd^{2+}}$represents the activity of the Cd^{2+} species in aqueous solution, and $[R - A_i - Cd^+]$ is the molal concentration of the Cd-surface complex formed at functional group A_i of a sorbent.

Selenate adsorption is best described by invoking two types of surface complexes, following reactions described in Goldberg (2014) as follows:

$$> \mathrm{R-O-H^0} + \mathrm{HSeO_4^-} + \mathrm{H^+} \;\leftrightarrow\; > \mathrm{R-HSeO_4^0} + \mathrm{H_2O} \tag{5}$$

$$> \mathrm{R-O-H^0} + \mathrm{HSeO_4^-} \;\leftrightarrow\; > \mathrm{R-SeO_4^-} + \mathrm{H_2O} \tag{6}$$

With Se(VI) surface complexation mass action constants defined for reactions (5) and (6) as:

$$K_{1-Se} = \frac{[>R-HSeO_4^0]}{[>R-O-H^0]\, a_{HSeO_4^-}\, a_{H^+}} \quad (7)$$

$$K_{2-Se} = \frac{[>R-O-SeO_4^-]}{[>R-O-H^0]\, a_{HSeO_4^-}} \quad (8)$$

respectively. The models then invoke outer-sphere complexation of Se at site 1 of the sorbents (equations 5, 7), and inner-sphere Se complexation at site 2 (equations 6, 8). The major Cd(II), Se(VI) and carbonate aqueous species were considered in the models (Table C.S4.1).

4.3. RESULTS AND DISCUSSION

4.3.1. Soil and Biochar Physical Properties

The complete results of HF digestion for AFS, CFS and WPC are listed in Table C.S4.2, and presented for selected major elements in Figure 4.1. The average elemental recovery for the standard STSD-3 for the HF digestion and the sequential extraction (sum) were 99% and 81%, respectively, suggesting some elemental losses through the extraction procedure. The soil metal compositions of AFS and CFS are qualitatively similar. The major mineral phases found in both soils include quartz, albite, and phyllosilicates such as kaolinite, muscovite, and clinochlore (Figure C.S4.2). The pedogenic oxides calculation also supports the interpretation of a dominant quartz fraction in the two soils (Table C.S4.3). Silicate-rich soils are further characterized by the high concentrations of Si measured during SEM-EDS analyses (Figures C.S4.3, C.S4.4). Only the Mn concentration was notably different, with AFS containing approximately 33% more than CFS. WPC biochar contained relatively lower concentrations of Mg, Al, Ca, and Fe than the soils. Quartz was the only mineral phase identified by XRD (Figure C.S4.2). In all cases the digestion of soils with aqua-regia released less metals than the digestion with HF (Figure 4.1); no Se or Cd was measured in the soils or biochar (Tables C.S4.1, C.S4.3, C.S4.4). Despite the

similarities in metals and mineral content, AFS contains considerably more C, H, N, and O, and a higher soil pH, than CFS (Table 4.1).

Sequential extraction results for unaltered AFS, CFS, and WPC samples are shown in Figure 4.1. In the soils, phosphorus was mainly found in the residual fraction (74% to 80% of the total) suggesting the presence of highly insoluble phosphate-bearing solids. In the soils, S was dominant in the organic matter fraction (62% to 71%), indicating the presence of sulfide phases, while in WPC, S was found in the exchangeable and residual fractions (39% and 33% of the sum, respectively). The total digestion of biochar suggests an even larger residual fraction with up to 84% S. Calcium was primarily found in the exchangeable fractions of the soils (67% to 71% of the sum) and in the carbonate fraction of WPC (39% of the sum). Most of the Ca in all materials was not released by aqua regia extraction, indicating that more resilient Ca-containing phases are present. Potassium and Fe were bound mostly to the residual fraction of soils, dominantly in silicate minerals. The contribution of the (amorphous) Fe/Mn-oxide fraction for Fe was very small in the soils (18%), but greater in WPC (41%). This was in stark contrast to Mn, with a Fe/Mn-oxide fraction of 63% to 73% of the total value in the soils, and 17% in WPC. These results imply the presence of amorphous Mn phases in soils and Fe phases in biochar. Trace metals, such as Ni, Zn, and Pb, were dominant in the residual fractions of the untreated samples (Figure C.S4.5). On average only 11% of those metals were bound to Fe/Mn-oxides, while approximately 9% are found in the organic matter fraction.

Sequential extractions were repeated after Cd(II) and Se(VI) were sorbed to the soils and WPC. After the sorption experiments, Cd was dominantly found in the exchangeable fractions of soils and biochar (Figure 4.2). At pH 3, no other fraction contributed substantially to Cd sorption. At pH 7, more Cd was adsorbed, and the exchangeable fractions contained on average

81% of all Cd. In all 3 samples, only a minor fraction of Cd uptake was associated with the carbonate and the amorphous Fe/Mn extraction fractions. Thus, Cd is likely bound to the samples by cation exchange and adsorption to amorphous Mn oxides and clay minerals (soils) and Fe oxides (biochar).

Selenium was mostly found in the organic matter/sulfide fraction of the soils at both pH levels tested (Figure 4.2). On average, 58% of Se in soils was in this fraction, in contrast to the biochar at pH 7, where approximately 6% of Se was found in the organic matter/sulfide fraction and 86% was in the exchangeable fraction. We can conclude that the uptake of Se is dominated by organic particles and sulfides in the soils under acidic and neutral pH conditions. At neutral pH conditions WPC contributes considerably to Se uptake, but it is only weakly bound to the material matrix. The cation exchange capacity (CEC) of WPC is high as compared to the soils (Table C.S4.5). The NH_4-N extraction method revealed that Ca exchange is highest in both the soils and the biochar, followed by Mg in the soils and by K in WPC. The exchange of Fe, Mn and Al is negligible in both soils and the biochar.

4.3.2. Protonation Models of the Sorbents

For all three materials, a two-site model provided the best fit for the potentiometric titration data (Table 4.2; Figure C.S4.6). The pK_a values for AFS and CFS are similar (2.3 and 6.5 for AFS; 2.4 and 7.0 for CFS), which is consistent with their similar mineralogy and composition. The pK_a values for WPC, 4.3 and 7.5, are considerably different than those of the soils.

4.3.3. Single Metal Adsorption Experiments

Single metal adsorption experiments to each sorbent showed the expected increase in Cd(II) adsorption with increasing pH, and decreasing Se(VI) adsorption with increasing pH

(Figure 4.3). AFS adsorbs both Cd and Se somewhat stronger than CFS, perhaps due to a somewhat higher organic content (Table 4.1) and higher concentration of proton-active functional groups (Table 4.2). Generally, the Cd and Se metal binding constants to the two surface functional groups used to describe the soils are similar, while binding constants for WPC differ from the two soils (Table 4.3). By invoking Cd adsorption to the two binding sites determined in the protonation models, we fit the Cd experimental adsorption data for all three sorbents (Figure 4.3a; Figure C.S4.7). However, we were unable to explain Se adsorption to AFS or CFS by invoking any combination of inner- and/or outer-sphere Se complexation to the two binding sites. Operationally, this was due to the nearly linear decline in Se(VI) adsorption between pH 2 and 8, an unusual pH edge shape that suggests that another Se(VI) reaction should be considered. The presence of dissolved organic carbon (DOC) may explain the observed discrepancy, either by its forming complexes with Se(VI) that keep it in dissolved form, or by promoting the formation of Se(VI)-DOC-surface ternary complexes. For example, Bolan et al. (2003) observed that DOC derived from soils formed soluble complexes with Cu, and Beesley et al. (2015) note that they observed the co-mobilization of DOC and metals in soils amended with biochar. To test whether DOC in solution contributed significant proton-active functional groups to the solutions in soil metal adsorption experiments, we allowed AFS and CFS to equilibrate with the solution for 24 h, and then conducted potentiometric titrations of the supernatants after filtration through 0.45 μm nylon membranes. The DOC titration data were fit with a 1-site non-electrostatic SCM, using the methods described in Section 3.2. DOC in solution contributed considerable buffering capacity, comparable to the soils themselves, and the low pK_a values calculated (Table 4.3) are consistent with those of soil DOC, which are known to be low (Nambu and Yonebayashi, 1999). These DOC protonation models were used to solve for the formation of

an inner-sphere Se-DOC complex, according to Equation 6 above.Invoking a solution Se-DOC complex resulted in acceptable Se fits to AFS and CFS adsorption data (Figure 4.3b; Figure C.S4.8).

4.3.4. Multi-component Adsorption Experiments and Model Predictions

To test the non-electrostatic SCMs developed in Sections 3.2 and 3.3, sorbents and sorbates were mixed in various combinations. The pK_a values, site concentrations, and metal binding constants calculated from the single-metal, single-sorbent experiments were used to predict the extent of metal removal from solution in the more complex systems. Figure 4.4 illustrates the adsorption of Cd(II) (panel A) and Se(VI) (panel B) to mixtures containing one of the soils and WPC, thus simulating a biochar-amended agricultural soil. The addition of 1 g l^{-1} WPC to 10 g l^{-1} of soil did not greatly increase the extent of metal removal from solution as compared to the soils-only experiments (Figure 4.3). In all four cases tested, model predictions were a close match to the experimental data (Figure 4.4). Similarly, model predictions were excellent for systems containing one sorbent and two metals (0.1 mM Cd(II) and 0.1 mM Se(VI); Figure 4.5), and the adsorption behavior of each metal was again similar to that of the single-metal, single-sorbent experiments (Figure 4.3). This indicates that Cd and Se were not competing measurably for binding onto surface functional groups of AFS, CFS, or WPC.

Two-sorbent, two-metal experiments were conducted at two sorbent ratios to fully test the predictive capability of the SCM. At 10 g l^{-1} soil and 1 g l^{-1} WPC, the extent of Cd and Se adsorption was predicted with reasonable accuracy from pH 2 to 8 (Figure 4.6). Further experiments were conducted at sorbent concentrations of 5 g l^{-1} soil and 5 g l^{-1} biochar. Clearly an agricultural soil will not be amended with 50% (w/w) biochar, and so this was an experimental exercise to further test the SCM CA approach under more extreme conditions. The

model yielded acceptable predictions of Cd(II) adsorption, but poor predictions of Se(VI) removal from solution (Figure 4.7). There are several potential explanations. Firstly, only modest Se(VI) removal is observed in the data modeled to calculate Se(VI) binding constants to WPC (Figure 4.3b). This may result in a high inherent error in that fit, manifested as higher V(Y) values for models that calculated WPC metal-sorbent binding constants (Table 4.3). Secondly, WPC may contribute carbon nanoparticles to solution, which are known to exist in woody biochar (Yan et al., 2014; Naghdi et al., 2017). Such nanoparticles may sorb Se (or Cd), pass through the 0.45 μm nylon membranes used to filter experimental supernatants, and then be mistakenly quantified as free metal in solution during ICP-MS/MS analysis. On a per-gram basis, WPC has a high capacity to sorb both Cd and Se (Figure 4.2). Thirdly, it may be that components of the soils (e.g., clay, DOC) do interact substantially with the surface of WPC, and these artifacts only become measurable in the 5 g l^{-1} soil, 5 g l^{-1} WPC experiments. Finally, cation-induced anion adsorption might influence the degree of Se adsorption and thus the match of the adsorption experiment results with those of the predictive models (Bolan et al., 1999). As noted earlier (Zachara et al., 1992; Alessi and Fein, 2010), interactions between sorbents and complexation of metals by solution ligands are two considerable limitations of the CA approach. However, it would be rare for soil to be amended with >10% (w/w) biochar (Novak et al., 2009; Van Zwieten et al., 2010; Igalavithana et al., 2017), and the predictions of our models in mixtures containing 10% or less biochar (w/w) match well to the experimental data.

4.4. CONCLUSIONS

The application of SCMs to predict metals distribution in biochar-amended soil systems has clear benefits because these models have the capability to account for the impacts of changes in pH, ionic strength, sorbent-to-sorbate ratio, and even temperature. The non-electrostatic

surface complexation approach used here, the first ever SCM application to biochar-soil mixtures, was generally successful in predicting the equilibrium distribution of Cd and Se in mixtures containing those metals, biochar, and agricultural soil. However, several challenges remain. Above we note the presence of Se-DOC aqueous complexes, or Se and/or Cd bound to biochar-derived carbon nanoparticles, as potential explanations for the poor model predictions of experiments containing high concentrations of biochar. If the latter is true, nanoparticles could act as an additional vector of metals mobility in agricultural soils amended with biochar. Spectroscopic and microscopic investigations are needed to confirm the association of Cd and Se with nanoparticles and/or DOC in solution. Finally, to advance the application of surface complexation theory to soil-biochar systems, SCM studies on different types of biochar (e.g., pyrolysis temperature, feedstock) and biochar-soil mixtures are needed. The results of such studies can be combined with a robust extant literature of SCMs of soils and soil components, which can then be used to develop predictive models of numerous multi-component systems containing biochar as a sorbent.

Table 4. 1. Physical properties of alfalfa field soil (AFS), canola field soil (CFS), and wood pin chip biochar (WPC).

Properties	**Sample**		
	AFS	CFS	WPC
pH	5.30	5.00	9.70
%C	2.90	2.05	84.60
%H	0.70	0.50	2.10
%O	4.90	3.36	9.40
%N	0.25	0.20	0.20
Molar H/C	2.80	3.00	0.30
Molar O/C	1.25	1.22	0.08
TOC (w/w%)	2.90	2.26	82.11
DOC (mg/L)	14.04	23.84	105.90
Clay fraction (<2.0μM) in volume (%)	19.16	18.37	NA
Clay fraction (<3.806M) in volume (%)	28.79	27.72	NA

NA = not available

Table 4. 2. Best-fit pKa and site concentrations for each sorbent, and the supernatants leached from AFS and CFS soils at pH 7, following equilibration.

Materials	Sites	pKa_1	pKa_2	Site 1 concentration (mol/g)	Site 2 concentration (mol/g)	V(Y)
WPC	2	4.3	7.5	1.03E-03	1.93E-04	13
AFS	2	2.3	6.5	8.58E-04	3.01E-04	15
CFS	2	2.4	7.0	8.43E-04	2.41E-04	23
AFS DOC	1	2.7		1.32E-03		10
CFS DOC	1	1.5		1.26E-04		1

Table 4. 3. Best-fit metal binding constants (K) for Cd(II) and Se(VI) adsorption to AFS, CFS, and WPC.

Samples	Sites	log K_{Cd1}	log K_{Cd2}	V(Y)	log K_{Se1}	log K_{Se2}	log K_{DOCSe}	V(Y)
AFS	2	0.31	-0.90	6	-0.60	7.40	9.70	17
CFS	2	0.16	-1.38	6	-0.50	7.40	5.40	6
WPC	2	-2.34	-3.62	26	-1.85	7.92		37

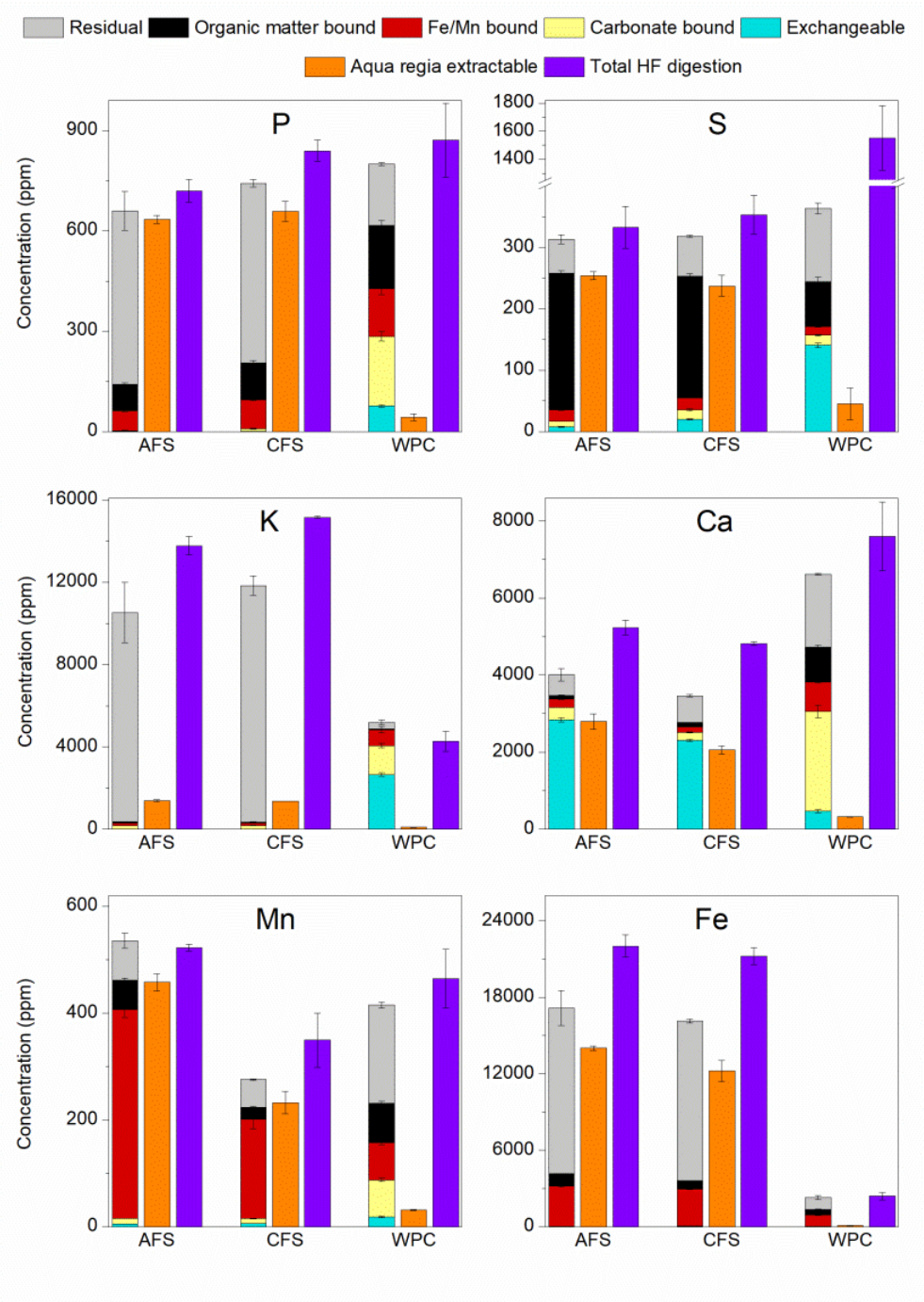

Figure 4.1. Sequential extraction results for the soils AFS and CFS and the biochar WPC.The values are shown together with aqua regia extractable metals and HF digestion results. The symbol "*" indicates values below the calibration range. Error bars represent standard deviation (n=3) at a 95% confidence interval.

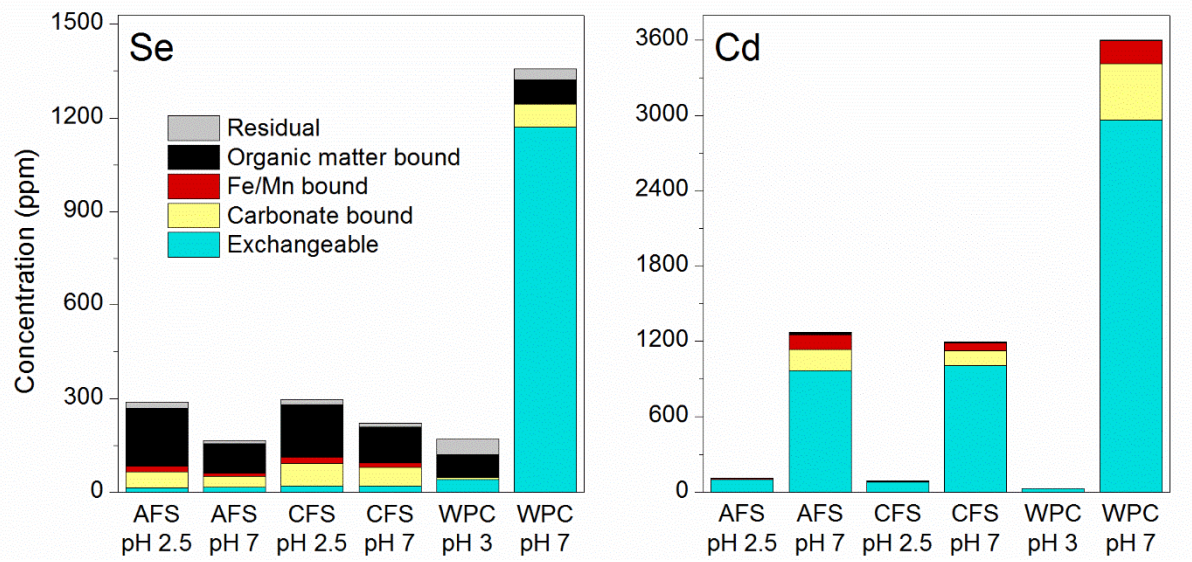

Figure 4.2. Sequential extraction results from soils and biochar to which Se and Cd had been pre-sorbed at pH 2.5 and pH 7 (soils) and pH 3 and pH 7 (biochar).

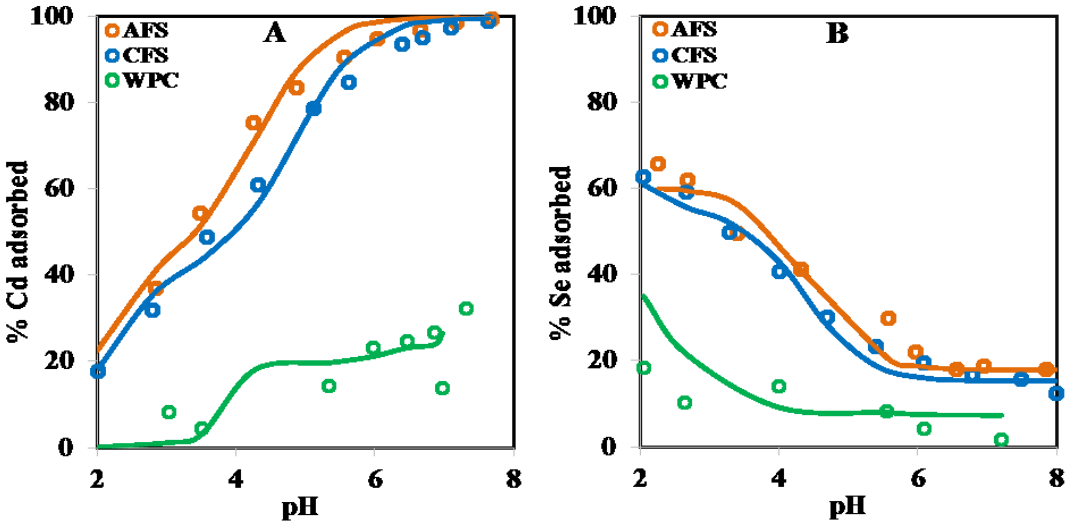

Figure 4.3. Adsorption of (A) 100 µM Cd and (B) 100 µM Se, to AFS (10 gl^{-1}), CFS (10 g l^{-1}), and WPC (1 gl^{-1}). Open symbols represent experimental data and solid lines represent best-fit surface complexation modeling fits.

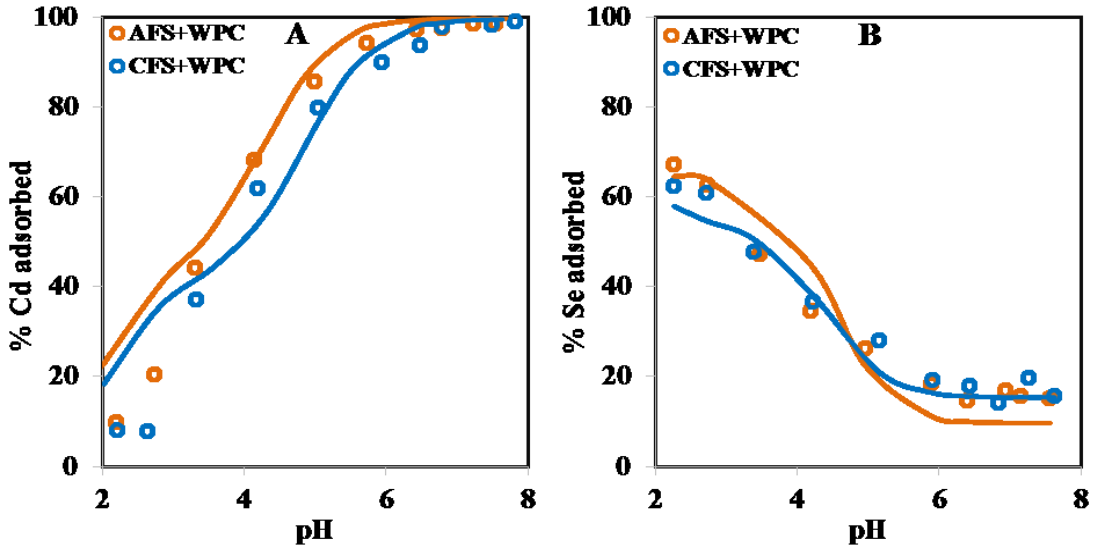

Figure 4.4. Adsorption of (A) 100 µM Cd and (B) 100 µM Se, to mixtures of AFS (10 gl^{-1}) and WPC (1 gl^{-1}), and CFS (10 gl^{-1}) and WPC (1 gl^{-1}). Open symbols represent experimental data and solid lines represent model predictions of adsorption.

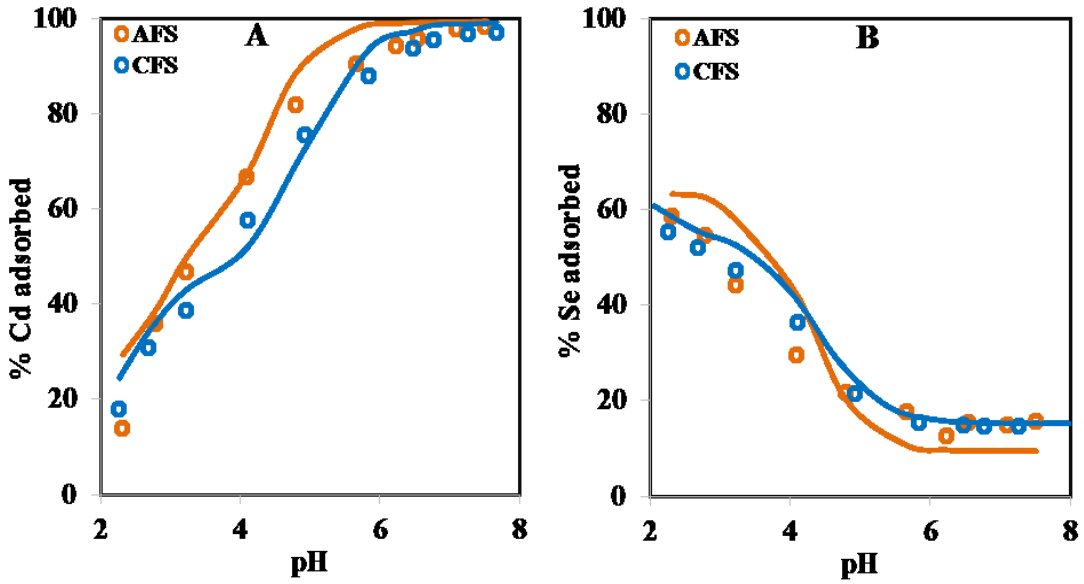

Figure 4.5. Adsorption of a solution containing both 100 µM Cd and 100 µM Se to AFS (10 gl^{-1}) or CFS (10 gl^{-1}). Panel (A) shows Cd data, and (B) shows Se data. Open symbols represent experimental data and solid lines represent model predictions of adsorption.

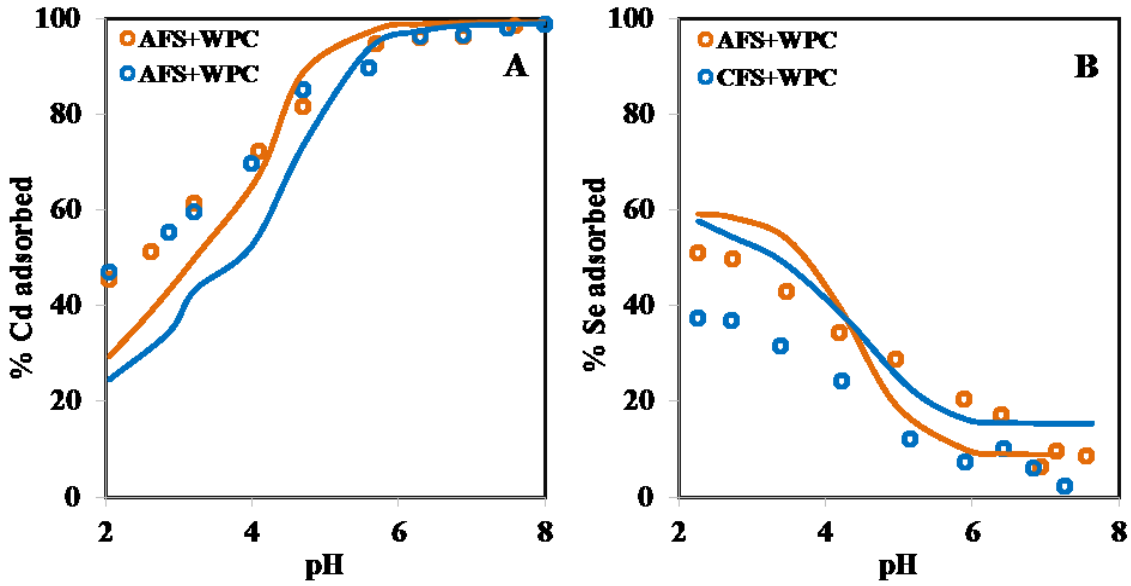

Figure 4.6. Adsorption of a solution containing both 100 µM Cd and 100 µM Se adsorption to mixtures of either AFS (10 gl^{-1}) and WPC (1 gl^{-1}), or CFS (10 gl^{-1}) and WPC (1 gl^{-1}). Panel (A) shows Cd data, and (B) shows Se data. Open symbols represent experimental data and solid lines represent model predictions of adsorption.

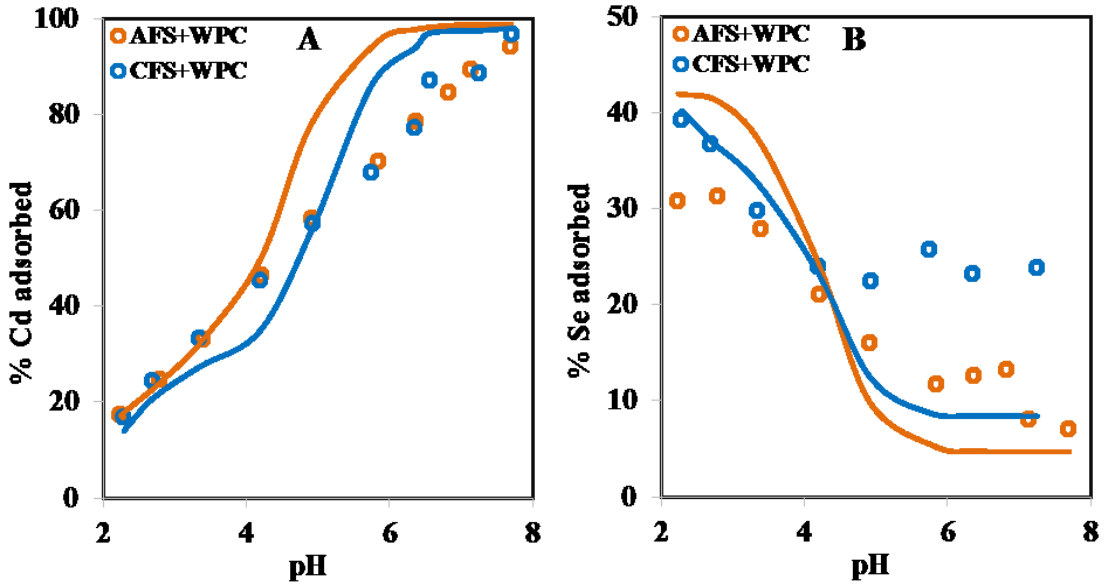

Figure 4.7. Adsorption of a solution containing both 100 µM Cd and 100 µM Se adsorption to mixtures of either AFS (5 g l^{-1}) and WPC (5 gl^{-1}), or CFS (5 gl^{-1}) and WPC (5 gl^{-1}). Panel (A) shows Cd data, and (B) shows Se data. Open symbols represent experimental data and solid lines represent model predictions of adsorption.

CHAPTER 5

MAGNETITE NANOPARTICLE – BIOCHAR COMPOSITES FOR EFFICIENT REMOVAL OF CHROMATE FROM WATER

ABSTRACT

Biochar (BC) and magnetite nanoparticles (MNP) have both received considerable recent attention in part due to their potential use in water treatment. While both are effective at the removal of Cr(VI) – the soluble and oxidized form of chromium - from acidic aqueous solutions, the efficiency of its removal by these materials decreases greatly at neutral pH. At present, it is not known whether composites of MNPs and BC can increase the efficiency of chromate, CrO_4^{2-}, removal at the acidic to neutral pH values characteristic of most natural aqueous environments. Accordingly, in this study, magnetite (Fe_3O_4) nanoparticles and biochar produced from ground willow were synthesized to form composites (MNP-BC) to test their capacity to remove CrO_4^{2-} from fresh water. Batch studies show that MNP-BC enhanced both adsorption and reduction of CrO_4^{2-} from aqueous solution at acidic to neutral pH compared to MNP and BC alone, suggesting a strong synergetic effect of hybridizing Fe_3O_4 with BC. The Cr(VI) removal processes occurred through both adsorption and intraparticle diffusion. Synchrotron-based X-ray absorption spectroscopy (XAS) analysis shows that Cr(VI) was subsequently reduced to Cr(III) at the surface of MNP-BC. Extended X-ray absorption fine structure (EXAFS) fitting results confirm that the Cr(III) precipitates consist of both $Cr(OH)_3$ and chromite (Cr_2FeO_4) nanoparticles on the MNP-BC surface. Our results demonstrate that MNP-BC have great potential as a remediation strategy for the treatment of chromate-containing solutions across a wide range of pH values.

5.1 INTRODUCTION

Iron (II)-bearing minerals have received considerable attention as a remediation option for chromium-contaminated water (Eary and Rai, 1988; Fendorf et al., 2000). In particular, Fe(II) is an effective reductant of Cr(VI), either in the form of bichromate ($HCrO_4^-$ at acidic pH) or chromate (CrO_4^{2-} at alkaline pH) (Patterson, 1997). Among Fe(II)-containing materials, magnetite (Fe_3O_4) nanoparticles (MNP) are attractive for remediation applications because they are inexpensive to produce, recyclable, easily separable from admixtures, and possess high surface area (He and Traina, 2005; Jung et al., 2007). The Fe(II) in magnetite can reduce Cr(VI) to Cr(III), producing Cr(III) precipitates such as $Cr(OH)_3$ and $Fe_xCr_{1-x}(OH)_3$ in aqueous solutions (Rai et al., 1987; Saas and Rai, 1987). However, the reaction kinetics of Cr(VI) and Fe(II) in MNPs is strongly dependent on solution pH. Magnetite alone is not effective under near-neutral and basic conditions, and the Fe(II) in magnetite is highly susceptible to auto-oxidation, leading to the formation of Fe(III) materials (He et al., 2004; Chowdhury and Yanful, 2010). Under neutral to basic pH conditions, MNPs aggregate, resulting in a dramatic diminishment of their metal adsorption and/or reduction capacity (Patterson et al., 1997; He et al., 2004; Chowdhury and Yanful, 2010). For instance, Peterson el at. (1997) showed that the reduction reaction of Cr(VI) at the surface of MNPs was passivated at pH 7 due to the aforementioned aggregation, demonstrating that MNPs have little capacity to reduce Cr(VI) at neutral pH.

Carbon-based materials have also received considerable attention in the field of water purification because of their high surface area, electrical conductivity and chemical stability (Georgakilas et al., 2015; Yao et al., 2015). Biochar (BC), a 3D porous carbonaceous material, can be produced by the pyrolysis of carbon-rich biomass such as crop residue, manure and solid waste, under limited oxygen conditions (Cao et al., 2009 and Chen et al., 2012). Biochar has

been shown effective at removing metals and organics from aqueous solution due to its pore-rich structure, oxygen-containing functional groups and elevated cation exchange capacity (Cao et al., 2009 and Chen et al., 2012). It is also cost-effective compared to activated carbon and graphene oxides (Thompson et al., 2016). While the adsorption capacity of BC for metals has been well studied (Cao et al., 2009 and Chen et al., 2012; Alam et al., 2016; Alam et al., 2018a). BC-mediated redox processes are far less studied. A few studies show that BC can donate, accept and transfer electrons via either biotic or abiotic pathways (Keiluweit et al., 2014; Kappler et al., 2014; Yu et al., 2015). For example, Kappler et al. (2014) and Yu et al. (2016) showed that BC enhanced the microbial reduction ferrihydrite ($Fe(OH)_3$) and hematite (Fe_2O_3) by functioning as an electron shuttle. More recently, Rajapaksha et al. (2018) and Cossio (2017) showed direct evidence of Cr(VI) reduction to Cr(III) by BC using synchrotron-based X-ray absorption spectroscopy (XAS). Cossio (2017) further showed that Cr(VI) reduction by BC depends on solution pH, and that it was essentially unable to reduce Cr(VI) once solution pH > 4. A deeper understanding of the kinetics of redox reactions involving BC at a range of pH values is still needed to enhance its application to treating redox-sensitive metals.

Organic-inorganic composites and hybrid materials for reductive immobilization of Cr(VI) are less well-investigated, as it is difficult to achieve synchronous reduction and adsorption efficiency (Deshpande et al., 2005; Cheng et al., 2010; Zaitseva et al., 2013; Beller et al., 2014). Jiang et al. (2014) and Wang et al. (2015) successfully used humic acid-coated magnetite and Fe_3O_4 at core-shell of m-phenylenediamine to efficiently remove Cr(VI) from solution. While effective, the application of these methods could be challenging due to their complicated and costly nature. A few studies have demonstrated that BC can be used as a substrate to support zero valent iron magnetite for enhanced removal of metals from solution,

including Cr(VI) (Su et al., 2016; Mandal et al., 2017; Hu et al., 2018). These studies focused primarily on adsorption processes, while the mechanisms underlying Cr(VI) reduction and the kinetics of the redox reactions were not well characterized (Su et al., 2016; Mandal et al., 2017; Hu et al., 2018). The doping of MNPs onto BC is promising because the latter is a considerably less expensive substrate than other carbonaceous materials, such as activated carbon or graphene. MNPs have excellent magnetic properties, stability, wide availability, and are not toxic to aquatic life. Coupling MNPs with BC will increase the effective surface area of the MNPs by preventing their agglomeration and concomitant passivation of reactivity that is shown to occur at near-neutral and basic pH levels (Jiang et al., 2014; Wang et al., 2015).

Here we prepared, for the first time, composites of MNPs and BC to enhance the reduction and adsorption of Cr(VI) across a wide range of water chemistries. The objectives of the study were to: (1) gain a mechanistic understanding of the interaction (adsorption and reduction) of Cr(VI) onto the surfaces of MNP-BC composites; (2) determine the effects of pH and oxidants on Cr(VI) removal and the kinetics of Cr(VI) adsorption and reduction; and (3) characterize the products of Cr(VI) reduction that form on the composite surface. Results from high resolution electron microscopy and X-ray absorption spectroscopy (XAS) analyses allowed us to develop an understanding of the molecular scale reaction mechanisms of Cr(VI) onto the surface of the composites. The resulting composite is highly efficient, and may be a cost-effective sorbent for the reductive immobilization of chromate from aqueous solution.

5.2. MATERIALS AND METHODS

5.2.1 Materials

Ferric chloride hexahydrate ($FeCl_3.6H_2O$), ferrous chloride tetrahydrate ($FeCl_2.4H_2O$), ammonium hydroxide (NH_4OH), sodium hydroxide (NaOH), hydrochloric acid (HCl), sodium

chlorite ($NaClO_2$), sodium nitrate ($NaNO_3$), potassium dichromate ($K_2Cr_2O_7$), potassium permanganate ($KMnO_4$), 1,5-Diphenylcarbohydrazide (DPC) were all of ACS grade or higher, and purchased from Fisher Scientific, Canada. To prepare stock solutions and for all experiments, 18.2 MΩ water was used. Ground willow biochar (BC) was used for all experiments. It was obtained from the Alberta Biochar Initiative (ABI; Vegreville, Alberta, Canada).

5.2.2 Preparation of Fe_3O_4 nanoparticles (MNPs) and Fe_3O_4-biochar composites (MNP-BC)

The MNPs and MNP-BC composites were prepared according to Liu et al. (2008) and Yuan et al. (2009). Briefly, 2 g $FeCl_3 \cdot 6H_2O$ and 1 g $FeCl_2 \cdot 4H_2O$ were dissolved in 200 mL water that had been bubbled with N_2 gas for 30 min. While continuing to bubble with N_2, the solution was vigorously stirred for 5 min at 60°C. A solution of 1.5 M NH_4OH was added dropwise into solution until the pH value of the mixture reached 8.0 and a black precipitate formed. The mixture was then aged for 30 min at 60°C. Following, the solid precipitate was washed four times with water and then dried at 40°C in vacuum oven. To prepare MNP-BC, BC was added to the ferric/ferrous chloride solution described above, at several MNP to BC ratios. The subsequent preparation steps were identical to those conducted for the synthesis of MNPs.

5.2.3 Characterization of Adsorbents

The BC, MNPs and MNP-BC were characterized by X-ray powder diffraction (XRD, Rikagu Ultima IV), high resolution transmission electron microscopy equipped with selected area diffraction (HRTEM-SAED, JEM-ARM200cF S/TEM), scanning electron microscopy (SEM, Zeiss EVO® MA 15). Fourier transform infrared spectroscopy (FTIR, Thermo Nicolet 8700) was employed to analyze the molecular structure. The particle size distributions and zeta potential of BC, MNPs and MNP-BC were measured using dynamic light scattering (DLS)

analysis (ZetaSizer Nano, Malvern Instruments, UK). X-ray photoelectron spectroscopy (XPS) measurements were carried out using a Kratos Axis 165 instrument to determine the functional groups and Cr and Fe speciation. To ascertain the ratios of Fe(II) and Fe(II) in MNPs, the ferrozine method (Viollier et al., 2000) was used. The detailed procedure these methods are given in Appendix B, except for the HRTEM-SAED methods, which are provided in Appendix D. Potentiometric titrations were carried out to determine the protonation constants (K_a) and corresponding site concentrations of proton-active surface functional groups, as described in Alam et al. (2018a). To determine the sheet resistance of BC, it was mixed with a polyethylene oxide (PO) polymer. The sheet resistance of the BC and PO composites at different weight ratios (20mg:200mg; 100mg:100mg; 200mg:20mg) was measured using a linear four point probe with 1 mm spacing (Lucas Pro-4 4000, USA) and a Keithley 2601A source meter at room temperature. Dry combusted and water extracted total organic carbon (TOC) of BC were determined using a TOC analyzer (Shimadzu TOC-V/TN).

5.2.4 Cr(VI) Adsorption and Reduction Experiments

Batch adsorption and reduction kinetics experiments were conducted at various initial Cr(VI) concentrations (85µM, 170µM and 350µM) and sorbent concentrations (1 g L^{-1} BC, 10 mM Fe, 4 mM Fe, 0.5 g L^{-1} BC + 10 mM Fe, 1 g L^{-1} BC + 4 mM Fe, and 1 g L^{-1} BC + 2 mM Fe) at pH 2, 3, 5 and 7. Initially, a 10 g L^{-1} MNPs and MNP-BC stock slurry was prepared. The reported Fe and BC+Fe iron concentrations reported were calculated and from dilutions of the stock MNPs and MNP-BC slurry, respectively. To initiate an experiment, the sorbent was introduced into a 100 mL serum bottle and mixed with ultrapure water. Then the mixture was adjusted to the desired pH by adding small aliquots of 1 M NaOH or 12 M HCl. The serum bottles were then sealed with rubber stoppers and metal caps, and the contents bubbled with N_2

for 1 h to remove O_2 and CO_2 from the head space and the solution. Aliquots from the 3.5 mM Cr(VI) stock solution, prepared from $K_2Cr_2O_7$, were injected to the serum bottle using sterile syringe to achieve the desired Cr(VI) concentration. The serum bottles were then placed on a shaker (New Brunswick Scientific Excella E5 Plataform shaker) at 200 rpm. In order to capture the initial adsorption and reduction kinetics, frequent sampling was carried out for the first 24 h: at 0, 5 min, 15 min, 0.5 h, 1 h, 2 h, 4 h, 8 h, 12 h and 24 h, followed by daily sampling for 10 days thereafter. Experiments were conducted in duplicate, and aliquots were taken from the serum bottles for both Cr(VI) reduction and adsorption analyses. To sample for Cr(VI) reduction, 500 μL of the slurry in the serum bottle was removed, mixed with 500 μL 1 M NaOH (1:1 volume ratio) in order to desorb Cr(VI) from the surface of the solids (method 7196A from the United States Environmental Protection Agency (EPA, 1992)). This method has been shown to be desorb Cr(VI) while leaving reduced Cr(III) species attached to the solid surface method (Cossio, 2017; 7196A from the United States Environmental Protection Agency (EPA, 1992)). Adsorption samples were collected from serum bottles in an identical manner, but were not mixed with NaOH. Both reduction and adsorption aliquots were filtered through 0.2 μm nylon membranes. The concentrations of Cr(VI) in the resulting filtrates were measured using the 1,5-Diphenylcarbohydrazide (DPC) spectrophotometric method on a Thermo Scientific Evolution 60S UV-vis Spectrophotometer (λ_{max} = 540 nm). Total aqueous Cr was measured using by Inductively Coupled Plasma - Mass Spectroscopy (ICP-MS; Agilent 8800). The concentration of Cr(III) in solution and potentially precipitated as solid was calculated by the subtraction of Cr(VI) from total Cr.

To test the effects of oxidants on the kinetics of Cr(VI) reduction by MNP-BC, 1 mg L^{-1} potassium permanganate ($KMnO_4$), sodium chlorite ($NaClO_2$) and sodium hypochlorite

(NaClO), respectively, were injected into 100 mL serum bottles containing 10 mM Fe + 0.5 g L^{-1} BC, and spiked with 350 μM Cr(VI). The effect of dissolved oxygen (DO) was tested by purging 10 mM Fe + 0.5 g L^{-1} BC containing 350 μM Cr(VI), for two hours with a 23.5% O_2 + 76.5% N_2 gas mixture. All experiments were conducted at pH 7, and the experimental procedures and samples analyses were carried out as described above for Cr(VI) reduction experiments.

5.2.5 Adsorption Modeling

The equilibrium adsorption capacity (Q_e, mg/g) for Cr(VI) was calculated using Eq. (1),

$$Q_e = \frac{(C_0 - C) \times V}{\mathrm{m}} \quad (1)$$

where C_0 (mgL^{-1}) and C (mgL^{-1}) are the initial concentration and equilibrium concentration of Cr(VI) in solution after adsorption, respectively. The parameters of m(g) and V(mL) are the mass of adsorbents and the volume of the suspension, respectively.

Reaction kinetics were assessed using pseudo-first order kinetics, pseudo-second order kinetics and intra-particle diffusion models. The pseudo-first order adsorption kinetics was calculated using Eq. (2)

$$Log(Q_e - Q_t) = k_1 t \quad (2)$$

where, k_1 is the rate constant of pseudo-first order model (min^{-1}), t is time (min), Q_e is the adsorption capacity at adsorption equilibrium (mg/g) and Q_t is the adsorption capacity at a specific reaction time, respectively.

The pseudo-second order adsorption kinetics was calculated using Eq. (3)

$$dQ_t/_{dt} = k_p(Q_e - Q_t)^2 \quad (3)$$

where, k_p is the rate constant of pseudo-second order model (g/mg•min)

The intraparticle diffusion rate was calculated using:

$$Q_t = k_{id} t_{1/2} + c \quad (4)$$

where, k_{id} is the intrapartcle diffusion rate constant and c is the intercept (Jiang et al., 2014).

5.2.6 Solid Phase Analyses after Adsorption and Reduction

Synchrotron X-ray absorption spectroscopy (XAS) analyses were carried out at the Hard X-ray Microanalysis beamline (HXMA 06ID-1) of the Canadian Light Source (CLS). Cr-loaded BC, MNPs and MNP-BC were analyzed to evaluate the average oxidation states and coordination environments of Cr on the solid surfaces. Cr K-edge (5989 eV) XAS measurements were conducted using a double Si (111) crystal monochromator detuned to 40% of the maximal intensity to reduce the influence of higher-order harmonics. Data for the reference materials (see below) were collected in the transmission mode, while absorption spectra for samples were collected in fluorescence mode using a 32-element solid state Ge detector. The Cr standards included $K_2Cr_2O_7$, Cr(III)-acetate and $Cr(OH)_3$. Spectra were also collected at the Fe K-edge (7112 eV) for Cr-loaded MNPs and MNP-BC samples, to determine the transformation of MNPs to other oxidized phases of Fe mineral and coordination with Cr. Fe reference materials analyzed include magnetite, ferrihydrite and goethite. X-ray absorption near edge structure (XANES) data was processed using the graphical interface ATHENA from DEMETER. ATHENA was used for processing raw data, background subtraction and linear combination fitting to determine average Cr and Fe valence states (Ressler, 1997; Ravel and Newville, 2005). EXAFS fitting was conducted using WinXAS (version 2.3). The theoretical phase shift and backscattering amplitude function from the crystal structure data of Cr and Fe was calculated using the FEFF 7 code (Ankudinov and Rehr, 2000).

Thin sections of Cr-loaded BC, MNPs and MNP-BC were mapped using Synchrotron-based X-ray fluorescence (XRF) mapping technique at the Very Sensitive Elemental and

Structural Probe Employing Radiation beamline (VESPERS 07B2-1) at CLS. The Cr and Fe distributions in the thin sections were measured using a single-element dispersive silicon drift XRF detector (Hitachi Vortex-90EX), and resulting fluorescence data were collected using the "Pink Beam" mode, with X-ray energy between 2-30keV during mapping. Mapping was carried out using a 3 μm step size resolution, with a dwell time of one second per pixel.

Mössbauer measurements were conducted to characterize the changes in the crystallography of Fe minerals in MNP-BC exposed to variable concentrations of Cr(VI). The detailed method is described in Appendix D. Cr-loaded BC, MNPs and MNP-BC samples were further analyzed by XRD, FTIR and XPS to determine the crystallographic transformation of MNPs and the functional groups that interacted with Cr after the adsorption and reduction processes.

5.3 RESULTS AND DISCUSSION

5.3.1 Characterization of Adsorbents

The elemental analysis of BC showed that it is primarily composed of C (76%) followed by O (10%). The surface area of BC is 319 m^2/g (Table D.S5.2). BC is conductive; the sheet resistance of the BC-PO composite decreased as BC concentration increased (Figure D.S5.1). TEM and HRTEM-SAED images (Figure 5.1) of MNP-BC show highly crystalline magnetite nanoparticles in the composites in all of the various MNP to BC weight ratios. The MNP particles exhibited generally spherical morphology, had a size range between approximately 10 nm to 20 nm, and showed Fe(II)/Fe(III) ratios of approximately 0.3. DLS analysis showed that size ranges of MNPs increased with increasing pH (Figure D.S5.2); this is likely attributed to their agglomeration at higher pH, as shown in previous studies (Rai et al., 1987; Sass and Rai,

1987; He and Traina, 2005). SEM images of MNP-BC composites (Figure D.S5.3) showed MNPs are homogeneously distributed on the surface of BC, preventing their agglomeration.

FT-IR spectra (Figure 5.2A) of MNPs and MNP-BC shows a distinct band at 594 cm^{-1} that can be ascribed to Fe-O groups, consistent with the presence of magnetite (Venkateswarlu et al., 2016). The spectra also showed stretching vibration bands of water molecules (free O-H) of MNPs and MNP-BC at 3210 cm^{-1} and 1410 cm^{-1}, respectively. BC has strong bands at 3425 cm^{-1} and 1590 cm^{-1}, corresponding to –OH and –C=O groups (Keiluweit et al., 2010; Chen et al., 2015), respectively. The same bands are observed in the MNP-BC composite. The vibrational band at 1110 cm^{-1} is assigned to stretching of the C-O-C bond.

XRD analyses confirmed that MNPs and MNP-BC contain Fe_3O_4, and no detectable transformation of the XRD pattern for magnetite was observed 15 days after synthesis and exposure to atmospheric conditions, i.e., exposure to O_2 (Figure D.S5.4). No other phases were detected, indicative of the high purity of the sample. Zeta potential measurements – an indicator of surface charge – versus pH (Figure 5.2B) of MNPs, MNP-BC and BC showed that the isoelectric points – the pH at which the particle carries no net electrical charge - for MNP and MNP-BC are near pH 6 and pH 5, respectively, whereas BC has an isoelectric point near pH 2. This demonstrates that the presence of organic functional groups lowers the isoelectric point.

XPS spectra (Figure 5.2C and 5.2D) of MNPs and MNP-BC showed that the $Fe2p_{3/2}$ peak is centered at 711.1 eV, a result which can be ascribed to the convolution of both Fe(II) and Fe(III) signals from Fe_3O_4 (Cuenca et al., 2016). XPS spectra (Figure 5.2E and 5.2F) also exhibited the presence –C=O groups in both MNP-BC and BC (Alam in review).

The potentiometric titration data were modeled to calculate the proton binding constants and corresponding site concentrations for proton-active sites of BC, MNPs and MNP-BC. A

model that uses three sites for BC and MNP-BC and one amphoteric site for MNPs yielded the best fits to the experimental data for each sorbent, where variance, V(Y), values were in the range of 0.1<V(Y)<20 (Herbalin and Westall, 1996) (Figure D.S5.5). The pK_a values for site 1 in BC and MNP are approximately 2.4 to 3.0, within the range of pK_a values of carboxyl groups (pK_a = 1.7−4.7) (Chen et al., 2008; Chia et al., 2012; Li et al., 2014). The pK_a value for site 1 in MNPs of 5.0 corresponds to Fe-O (pK_a = ~5). The pK_a values calculated for sites 2 and 3 of BC and MNP-BC, ranging between 6.3 to 9.0, correspond to lactones (pK_a = ~6) and phenolic hydroxyl (pK_a = ~9.5) groups (Table D.S5.3) (Chen et al., 2008; Chia et al., 2012; Li et al., 2014; Venkateswarlu et al., 2016). The proton-active functional groups, including –C=O, -OH and Fe-O, that were used in modeling the potentiometric titration data were also detected in both FT-IR and XPS analyses.

5.3.2 Effect of pH on Adsorption and Reduction of Cr(VI)

The pH-dependent adsorption and reduction kinetics of Cr(VI) for BC, MNPs and MNP-BC were studied in the pH range of 2-7, relevant to pH levels ranging from acid mine drainage (AMD) and natural waters associated with rivers and groundwater (Figure 5.3 and 5.4). pH significantly influences the adsorption capacities of sorbents, as both the sorbent net surface charge and the aqueous speciation of Cr(VI) change with pH (Figure D.S5.6) (Wang et al., 2015). At the lowest pH tested (pH 2), complete removal of Cr from solution was achieved for all of sorbents (Figure 5.3A). At pH 3, BC only removed 60% of the total Cr(VI) from solution, which further reduced to 10% at pH 5, and to no measureable removal at pH 7 (Figure 5.3B to 5.3D). However, MNPs and the MNP-BC composites showed higher Cr(VI) removal efficiencies of between 90 to 100% at pH 3. The adsorption capacity of MNP-BC at 4 mM Fe + 1 gL^{-1} BC and 2 mM Fe + 1 gL^{-1} BC was nearly 100% at pH 7, considerably higher than the 60% removal

performance of MNPs at 4 mM Fe (Figure 5.3D). The results clearly indicate that doping with Fe_3O_4 enhances Cr(VI) removal from solution. Zeta potential measurements also show that the isoelectric points of BC, MNP, and MNP-BC were approximately 2.2, 5.8 and 5.5, respectively (Figure 5.2B), and the pH of these isoelectric points increased with Cr-loading, to 7.0, 7.8, and 3.5 for MNPs, MNP-BC and BC, respectively (Figure D.S5.7). Above the pH of the isoelectric point, the surface of the adsorbents becomes negative. Since the most common aqueous species for Cr(VI) are CrO_4^{2-}, $HCrO_4^-$, $Cr_2O_7^{2-}$, (Jiang et al., 2014) electrostatic repulsion between the adsorbent and adsorbate inhibits Cr(VI) adsorption to BC above pH 2 and MNPs above pH 6. However, our results show that the repulsive electrostatic interaction between the MNP-BC and Cr(VI) species does not inhibit the removal of Cr(VI) from solution to MNP-BC even at pH 7, above the isoelectric point at pH 5. The lack of pH effects on Cr(VI) removal by MNP-BC at neutral pH suggests that adsorption is governed by surface complexation rather than electrostatic interactions (Jiang et al., 2014 and Wang et al., 2015). Our results show that MNPs are effective to adsorb Cr(VI) up to pH 5; however, the removal efficiency decreases by pH 7, likely due to aggregation of Fe_3O_4 as shown in DLS measurement (Figure D.S5.2). The results clearly shows that Cr(VI) removal efficiency of MNP-BC, even with a lower BC loading of 1 gL^{-1} BC, much higher at neutral pH compared to MNP and BC, suggesting a positive effect of BC on the reactivity of MPNs in the composite materials.

The Cr(VI) reduction capacity of BC, MNPs and MNP-BC was also tested at pH 2 to 7 (Figure 5.4). BC alone is effective in reducing Cr(VI) to Cr(III) at pH 2 (Figure 5.4A), and after 10 days, 1 g L^{-1} BC was able to completely reduce a solution of 170 μM Cr(VI). At pH 3, only 20% of the total Cr(VI) in solution was reduced by BC in 10 days (Figure 5.4B), and BC did not reduce a measureable concentration of Cr(VI) at pH 5 or 7, even at lower Cr(VI) concentrations

of 85 μM (Figure 5.4C and 5.4D; Figure D.S5.8). The reduction capacity of Cr(VI) to Cr(III) by BC is almost certainly controlled by the adsorption step. At lower pH, where the BC surface is more positively charged, adsorption is more favorable and electron transfer from BC to Cr(VI) can occur, as shown in previous biochar studies (Yuan et al., 2009; Venkateswarlu et al., 2016). The transformation products generated by pyrolysis of lignin and cellulose of the parent biomass are thought be the source of electron-donating moieties in biochar (Yuan et al., 2017). These moieties include phenolic and carboxylic functional groups to which Cr(VI) species can bind, while quinones and polycondensed aromatic structures (graphene sheets) are a source of π-electrons and capable of transporting π-electrons to phenolic and carboxylic functional groups (Kappler et al., 2014; Yu et al., 2015; Yuan et al., 2017). Our results demonstrate that Cr(VI) reduction by BC is influenced by protonation state of the functional groups and Cr(VI) speciation.

The kinetics of the Cr(VI) reduction to Cr(III) by MNP-BC is much higher compared than those of MNPs at all pH values tested (pH 2 to 7) (Figure 5.4). Cr(VI) reduction was measured concurrently with Cr(VI) sorption over time for each pH experiment, and we found the Cr(VI) reduction kinetics closely matched Cr(VI) adsorption kinetics (Figure 5.3 and 5.4). The results suggest that adsorption was the rate limiting step for Cr(VI) reduction to BC, MNPs and MNP-BC. Since BC is conductive and enhance transfers electron, as well as preventing aggregation of MNPs, the cooperation between MNPs and BC leads to the higher efficiency in Cr(VI) reduction by the composite across a range of pH. The strong cooperative behavior of MNP-BC for both adsorption and reductive immobilization could make it a promising material for removal of Cr(VI) from aqueous solution.

5.3.3 Effect of Oxidants on Reduction of Cr(VI)

In natural waters and wastewaters, oxidants can coexist with heavy metals (Schroeder, 1975; Eary and Rai, 1987; Rogers, 2016). Thus, it is essential to evaluate how oxidants could influence the reduction capacity of MNP-BC composites. The effects of dissolved oxygen (O_2) and the most prevalent oxidants in drinking and wastewater systems [e.g., potassium permanganate ($KMnO_4$), sodium chlorite ($NaClO_2$) and sodium hypochlorite (NaClO)] (Rogers, 2016) on the reduction of Cr(VI) by MNP-BC were tested (Figure 5.5). O_2 did not have a measureable influence on the rate or extent of Cr(VI) reduction. However, the presence of $KMnO_4$, $NaClO_2$ and NaClO slowed down the kinetics of reduction. The removal efficiency of Cr(VI) was reduced from approximately 100% to 70% in the presence of $KMnO_4$ and $NaClO_2$, and reduced further to 40% by NaClO over the 10 day course of the experiments. The results clearly show that these oxidants impede Cr(VI) reduction by consuming electrons from MNP-BC. Nonetheless, the composites still removed Cr(VI) from solution, even in the presence of these relatively concentrated oxidants.

5.3.4 Cr(VI) Adsorption and Reduction Kinetics

The kinetics of adsorption and reduction are key factors in designing an adsorptive material for Cr(VI) removal from solution (Jiang et al., 2014; Venkateswarlu et al., 2016). Adsorption proceeded rapidly for the first few hours of each experiment, and then gradually reached equilibrium (Figure 5.3). Both pseudo-first-order and pseudo-second-order models suggested better fits of Cr(VI) adsorption data onto BC ($R^2 \sim 0.9$; Figure 5.6A and D.S5.9A). In contrast, higher correlation coefficients were achieved using a pseudo-second-order model ($R^2 > 0.92$) for Cr(VI) adsorption to MNP-BC than using a pseudo-first order model ($R^2 < 0.6$), indicating that chemical adsorption could be the rate-limiting step in the reduction process for

Cr(VI) by both BC and MNP-BC (Figure 5.6B and D.S5.9B; Table D.S5.4). The adsorption processes is also diffusion or intraparticle-diffusion controlled. Intraparticle diffusion reactions occur as soon as the reactants (i.e., sorbate) enter into solution (Jiang et al., 2014; Wang et al., 2015). BC is mesoporous as observed from the porosity analysis. It is also hydrophobic. The process of wetting of biochar mesopores likely influences the Cr adsorption/reactions process in these mesopores. Therefore, the kinetics data were also analyzed using an intraparticle diffusion model to determine if the adsorption/reactions mechanisms by BC and MPS-BC were controlled by varying diffusion rates. The results indicate that the adsorption of Cr(VI) onto BC and MNP-BC occurs through both surface adsorption and intraparticle diffusion, followed by the redox reaction that reduces Cr(VI) to Cr(III) (Figure 5.6C and 5.6D; Table D.S5).

The kinetics of Cr(VI) reduction by BC, MNPs and MNP-BC were additionally modeled to determine the order and rates of Cr(VI) reduction at varying pH. The reaction kinetics of a pseudo-first-order kinetic model are typically rate proportional to dissolved Cr(VI) concentration ([$Cr(VI)_{soln}$]) (Buerge and Hug, 1997; Alowitz and Scherer, 2002):

$$d[Cr(VI)]/dt = -K_{int}[Cr(VI)_{sol}] \quad (5)$$

where, K_{int} (hr^{-1}) is the intrinsic first-order rate coefficient.

Previous studies determined that Cr(VI) reduction by biosorbents follows a pseudo-first-order model (Hsu et al., 2009; Cossio, 2017). Our results show that a pseudo-first-order fits the experimental data of Cr(VI) reduction by BC at pH 2 fairly well (liner correlation coefficient R^2 = ~0.8), but provides a poor fit to reduction experiments conducted at pH 3 (R^2 = ~0.5) (Figure D.S5.10A and D.S5.10B). Since Cr(VI) reduction by BC was rapid during the first two hours, modeling the kinetics data using two pseudo-first-order kinetics relationships, one for the fast step (<2hrs) and a second for the slow step (>2hrs), provides the best fit to our experimental data

(Figure D.S5.10C and D.S5.10D). The reduction rate constant (K_{int}) decreased with increasing pH and Cr(VI) concentration; a similar observation was also shown in other Cr(VI) reduction studies ((Table D.S5.6). The higher Cr(VI) concentration could add more complexity to the system by changing chromate aqueous speciation and polymerization, thereby influencing the reduction rate (Park et al., 2007).

The reduction experiments by MNP-BC were modeled using second-order kinetics, according to the following rate law (Buerge and Hug, 1997; Alowitz and Scherer, 2002):

$$-\frac{d[Cr(VI)]}{dt} = K_{int}(pH)[Cr(VI)][Fe(II)] \quad (6)$$

The second-order kinetics model provides better fit than does the pseudo-first-order model for MNPs and MNP-BC (Figure D.S5.11). The Fe(II) concentration in the composite material also influenced the rate of Cr(VI) reduction by MNPs loading on MNP-BC. With decreasing Fe(II) concentration in the composite, the reduction rate constant (K_{int}) is decreased (Table D.S5.7). Overall, the kinetics models suggest that Cr(VI) reduction by BC followed 1st order kinetics, and the rate and order of the reduction depended on both pH and Cr concentration. Cr(VI) reduction could also be influenced by BC concentrations at acidic pH levels (e.g., pH 2 and 3). Since BC could not reduce measurable Cr(VI) at pH 5 and 7, it is expected that pH is the dominant factor for Cr(VI) reduction by BC. The 2nd order kinetics model best fits the results for Cr(VI) reduction by MNPs and MNP-BC, as Cr(VI) reduction was controlled by pH and Cr concentration as well as the Fe concentration in the MNPs and in MNP-BC.

5.3.5 Cr(VI) Adsorption and Reduction Mechanisms

To better understand the processes of adsorption and reduction, we studied the local molecular coordination environment of Cr on BC, MNPs and MNP-BC using XPS, FT-IR,

XANES and extended X-ray absorption spectroscopy (EXAFS). The XPS results indicate that after Cr(VI) adsorption, the intensity of the O 1s peak at the binding energy of 530.3 eV increased. This suggests that the Cr(VI) adsorption involved Fe-OH and C-OH functional groups, resulting in changes to the O 1s intensity (Figure D.S5.12). The FT-IR spectra show that the relative intensity of Fe-O peaks in MNPs, Fe-O and –OH peaks in MNP-BC, and C=O and –OH peaks in BC, shifted downward in the Cr-loaded samples (Figure D.S5.13), suggesting that Cr(VI) complexed with these functional groups. Synchrotron based-XRF mapping of Cr(VI)-laden MNP-BC shows the highly heterogeneous distribution of Cr on the composite surface (Figure 5.7 and D.S5.14), while Fe had a varied correlation with Cr over the sample matrix (R^2 = 0.66 to 1.00) suggesting that both Cr sorption and reduction might occur simultaneously for both MNPs and BC (Figure D.S5.15).

The XANES spectra of the Cr-laden samples clearly indicate the reduction of Cr(VI) to Cr(III) (Figure 5.8). The Cr(VI) standard ($K_2Cr_2O_7$) has a distinct and well-characterized pre-edge feature at 5990eV, which is absent in the spectrum of trivalent Cr ($Cr(OH)_3$). The linear combination fitting (LCF) of the XANES spectra show that more than 80% of the Cr(VI) reduced to Cr(III) by BC, MNPs and MNP-BC (Table D.S5.8).

The local coordination environment of Cr associated with BC, MNPs and MNP-BC was analyzed using EXAFS fitting (Figure 5.9). Converted to R space, the first shell at 1.98 to 2.02 Å in the samples are consistent with literature values Cr(III)-O bonds having lengths of 1.98 Å (Table 5.1). The coordination number of Cr(III)-O is 6 in the samples, likely representing an octahedral geometry. Since BC contains a variety of ligands, including carboxylate, quinone and phenolic groups, Cr(III) can complex with any of them (Jiang et al., 2014). The second shell present in all samples is consistent with Cr-Cr bonding at a distance ~3.1Å, and indicates the

presence of amorphous $Cr(OH)_3$ precipitates, formed as a result of Cr(VI) reduction to Cr(III). The Cr 2p at binding energy of 577.20 eV from XPS analysis also supports the presence of a $Cr(OH)_3$ precipitate (Figure D.S5.16) (Chowdhury et al., 2012). The Cr-C shells in BC and MNP-BC are indicative of inner-sphere surface complexation. Cr-Fe pathways in MNPs and MNP-BC suggest that chromite nanoparticles (Cr_2FeO_4) formed on the surface of MNP and MNP-BC. To test this hypothesis, XANES model was carried out. XANES modeling showed that of Cr local structural environment containing Cr_2FeO_4 nanoparticles exists in the sample system (Figure D.S5.17). The size of the Cr_2FeO_4 particle in the sample system is between approximately 0.5 nm to less than 1.0 nanometer in diameter.

5.3.6 Crystal Transformation of Magnetite Nanoparticles

The binding of MNPs on BC was analyzed by FT-IR (Figure D.S5.13). The free stretching C=O band in BC is usually assigned at 1590 cm^{-1}. In the composite upon complexation with MNPs, the intensity of the $C=O_{BC}$ band in MNP-BC is decreased. However, the interaction between BC and MNPs appears not to be affected by Cr(VI) adsorption, as shown by the unchanging C=O band, indicative of strong binding and complexation with magnetite (Jiang et al., 2014; Wang et al., 2015).

To better understand the transformation of magnetite in the composites after Cr(VI) adsorption and reduction, Cr(VI)-loaded MNPs and MNP-BC samples were analyzed with XRD, XPS, Fe K-edge XANES and EXAFS, and Mössbauer spectroscopy. The XRD and XPS spectra indicated no detectable difference between magnetite in the original MNP-BC at higher Fe concentration (10 mM Fe + 1 g L^{-1} BC) and Cr(VI)-loaded MNP-BC implying no transformation from magnetite to maghemite (Figures D.S5.18 and D.S5.19). However, XRD analysis of Cr(VI)-loaded MNP-BC at the lower Fe concentration (2 mM Fe + 1gL^{-1}) showed that

diffraction peak at 2θ = 35.42° and 43.05° which correspond to the (311) and (400) planes, respectively, are not well indexed to face-centered cubic inverse spinal structure of crystalline Fe_3O_4, indicating some transformation in magnetite (D.S5.18C and D.S5.18D).

Fe $2p_{1/2}$ and Fe K-edge XANES of Cr(VI)-loaded MNP-BC (Figure D.S5.19 and D.S5.20) showed some transformation of magnetite in MNP-BC after Cr(VI) reduction to Cr(III). The coordination number, the inter atomic distance calculated from Fe K-edge EXAFS spectra ($k^3 \bullet \chi(k)$) fitting, shows samples exhibited better fit to the magnetite crystallography (Figure D.S5.21 and Table D.S5.9) compared to the oxidized Fe minerals phases suggesting that magnetite did not convert completely to an oxidized Fe(III) mineral. The linear combination fitting (LCF) (Table D.S5.10) of the Fe XANES spectra showed that magnetite had partially transformed to the oxidized phase of Fe minerals (i.e., ferrihydrite and goethite) after complete reduction of 350 μM Cr(VI) to Cr(III) in 4 days, implying that the Cr(VI) reduction to Cr(III) consumed a certain fraction of the Fe(II) (Figure D.S5.20).

Cr-loaded MNP-BC was further analyzed by Mössbauer spectroscopy. The spectra of Cr-loaded MNP-BC (10 mM Fe + 1 g L^{-1}) are dominated by two magnetically ordered hyperfine sextets (HFD Site 1 and HFD Site 3) which constitute approximately 65% of the complete spectral area; they are assigned to the octahedral and tetrahedral lattice sites, respectively (Figure 5.10). The relatively small values for the hyperfine field result from poor crystallinity in combination with non-stoichiometry (i.e., Fe(II)/Fe(III) ratio is not 0.33) and weak magnetic ordering within the lattice of MNP crystals in comparison to more crystalline bulk magnetite. The prominent doublet at lower Fe concentration (2 mM Fe + 1 g L^{-1}) in MNP-BC, located in the middle of both spectra, accounts for about 10% of the spectral area and likely corresponds to a paramagnetic Fe(III) phase, such as lepidocrocite or nano-goethite (Figure D.S5.22).

5.4 ENVIRONMENTAL IMPLICATIONS

Cr(VI) is highly toxic and carcinogenic, and its reductive immobilization to nontoxic Cr(III) via a coupled reduction-sorption process is amongst the best remediation strategies to treat Cr(VI)-contaminated water. Magnetite and biochar can effectively remove Cr(VI) from aqueous solutions at low pH, but their individual efficiencies decrease at neutral pH (Peterson et al., 1997). Here we demonstrate that magnetite nanoparticle-biochar composites provide a robust adsorbent that can transform Cr(VI) to Cr(III). The adsorption-reduction processes suggest that the strong cooperation between MNP and BC underpins the improved adsorption and reduction capacity. Moreover, the kinetics of Cr(VI) adsorption by MNP-BC is rapid, reaching equilibrium within an hour. The chemical process of Cr(VI) removal by MNP-BC occurs through adsorption and intraparticle diffusion, followed by the redox reactions that reduce chromium to its trivalent state. XANES showed the complete reduction Cr(VI) to Cr(III) by MNP-BC, leading to an immobilized Cr(III)-complex including $Cr(OH)_3$ and chromite (Cr_2FeO_4). The MNP-BC composite's ability to both absorb and reduce redox-sensitive metals suggests it as a cost-effective, promising and reliable sorbent in treatment of Cr(VI)-contaminated water.

Table 5. 1. R-space curve fitting results of Cr K-edge EXAFS data of Cr-laden BC, MNPs and MNP-BC.

Samples	Paths	CN	R(Å)	σ^2 (Å^2)
1 g L^{-1} BC at pH 2	Cr-O	6.0	2.04	0.005
	Cr-Cr	3.1	3.10	0.009
	Cr-C	4.0	3.15	0.01
	Cr-C	8.4	2.38	0.009
	Cr-C	3.9	4.13	0.009
	Cr-C	2.0	4.41	0.009
1 g L^{-1} BC at pH 3	Cr-O	6.0	2.02	0.004
	Cr-Cr	4.7	3.04	0.009
	Cr-C	6.5	3.25	0.009
	Cr-C	6.3	3.30	0.009
	Cr-C	9.7	4.00	0.009
	Cr-C	9.9	4.44	0.009
10 mM Fe at pH 5	Cr-O	6.0	1.99	0.002
	Cr-Cr	3.9	3.03	0.005
	Cr-Fe	1.7	3.53	0.005
10 mM Fe at pH 7	Cr-O	6.0	2.02	0.002
	Cr-Cr	2.6	3.01	0.005
	Cr-Fe	2.2	3.62	0.005
10 mM Fe + 0.5 g L^{-1} BC at pH 5	Cr-O	6.0	2.02	0.002
	Cr-Cr	3.7	3.03	0.005
	Cr-C	10.0	3.15	0.005
	Cr-Fe	1.9	3.55	0.006
4 mM Fe + 1 g L^{-1} BC at pH 5	Cr-O	6.0	2.02	0.003
	Cr-Cr	0.4	2.93	0.005
	Cr-C	5.6	3.08	0.005
	Cr-Fe	0.8	3.54	0.006
2 mM Fe + 1 g L^{-1} BC at pH 7	Cr-O	6.0	1.97	0.003
	Cr-Cr	0.9	2.98	0.004
	Cr-C	5.0	3.06	0.005
	Cr-Fe	0.7	3.51	0.006

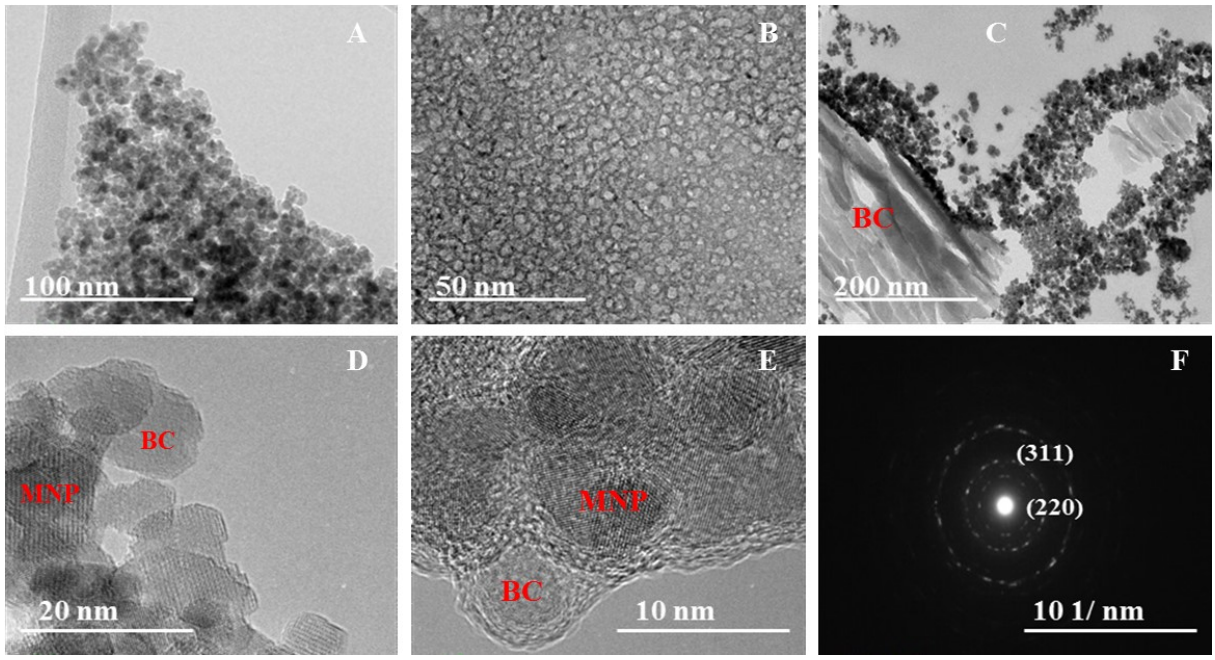

Figure 5.1. HR-TEM images of (A-B) MNPs; (C) MNP-BC (high Fe concentration); (D-E) MNP-BC (low Fe concentration); and (F) SAED pattern of MNP-BC.

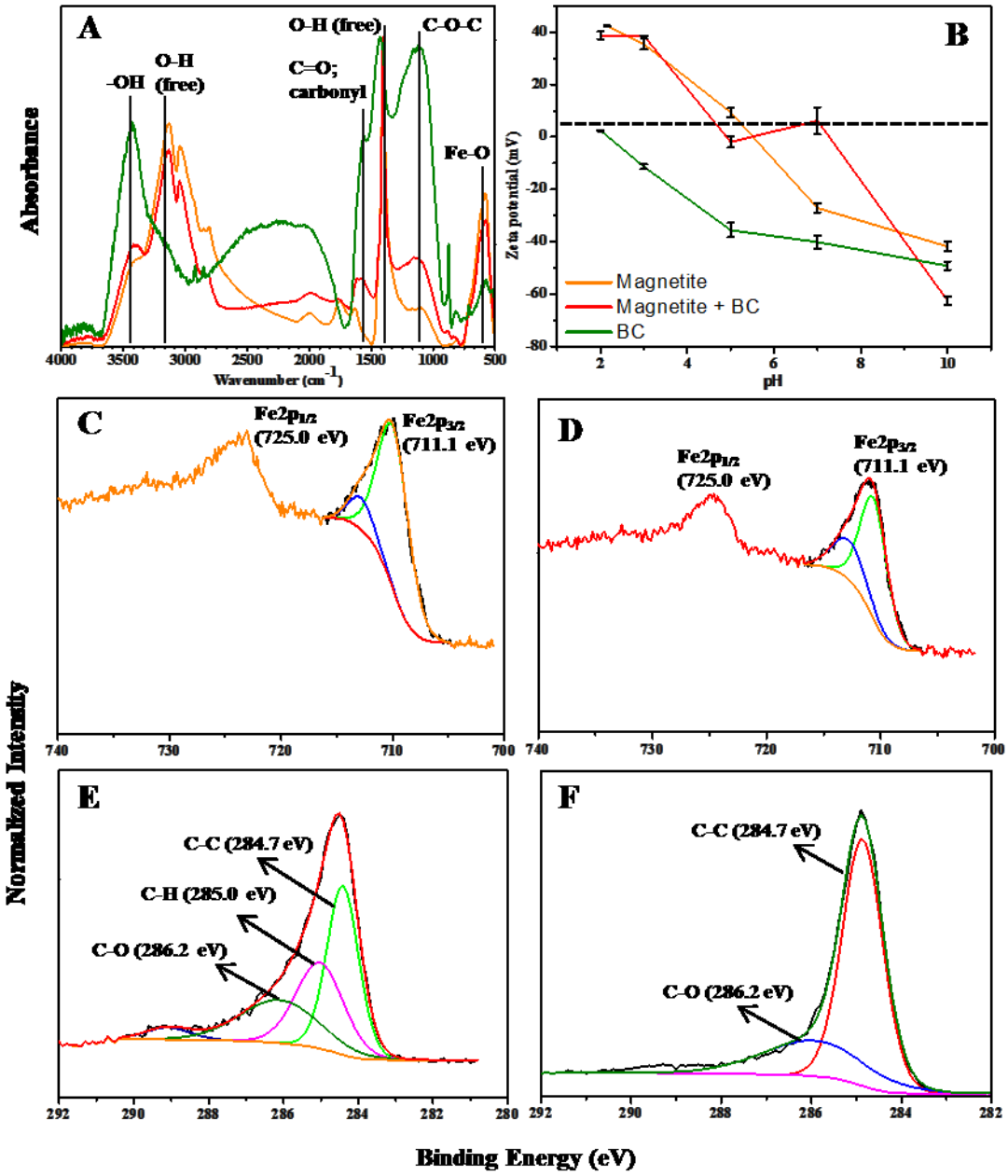

Figure 5.2. FT-IR, zeta potentials and XPS spectra. (A) FT-IR spectra of MNPs, MNP-BC and BC; (B) Zeta potentials of MNPs, MNP-BC and BC; (C) Fe 2p of MNPs; (D) Fe 2p of MNP-BC; (E) C 1s of MNP-BC and (F) C 1s of BC.

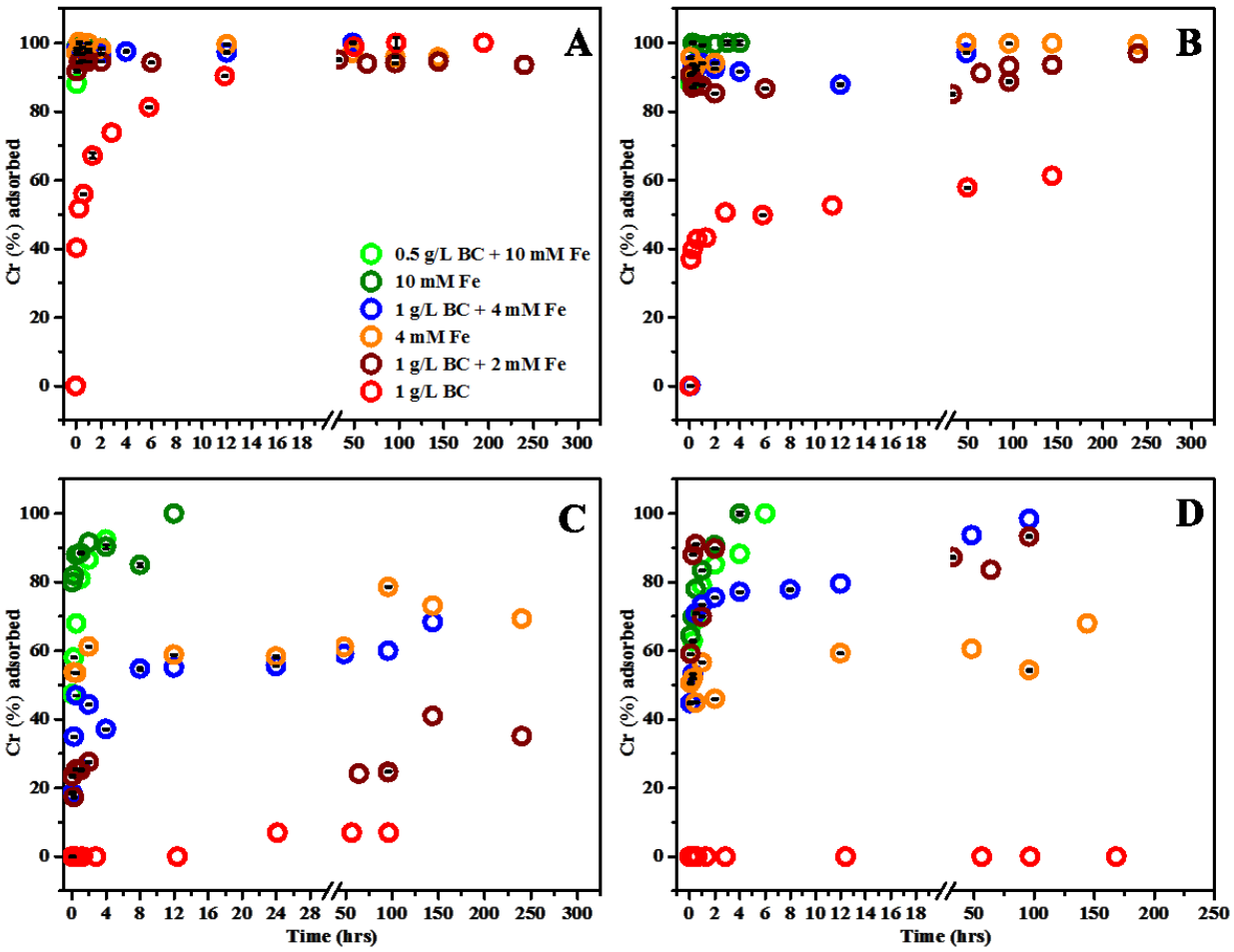

Figure 5.3. Cr(VI) adsorption by MNP-BC; MNPs and BC at different pH conditions. (A) pH 2; (B) pH 3; (C) pH 5 and (D) pH 7.

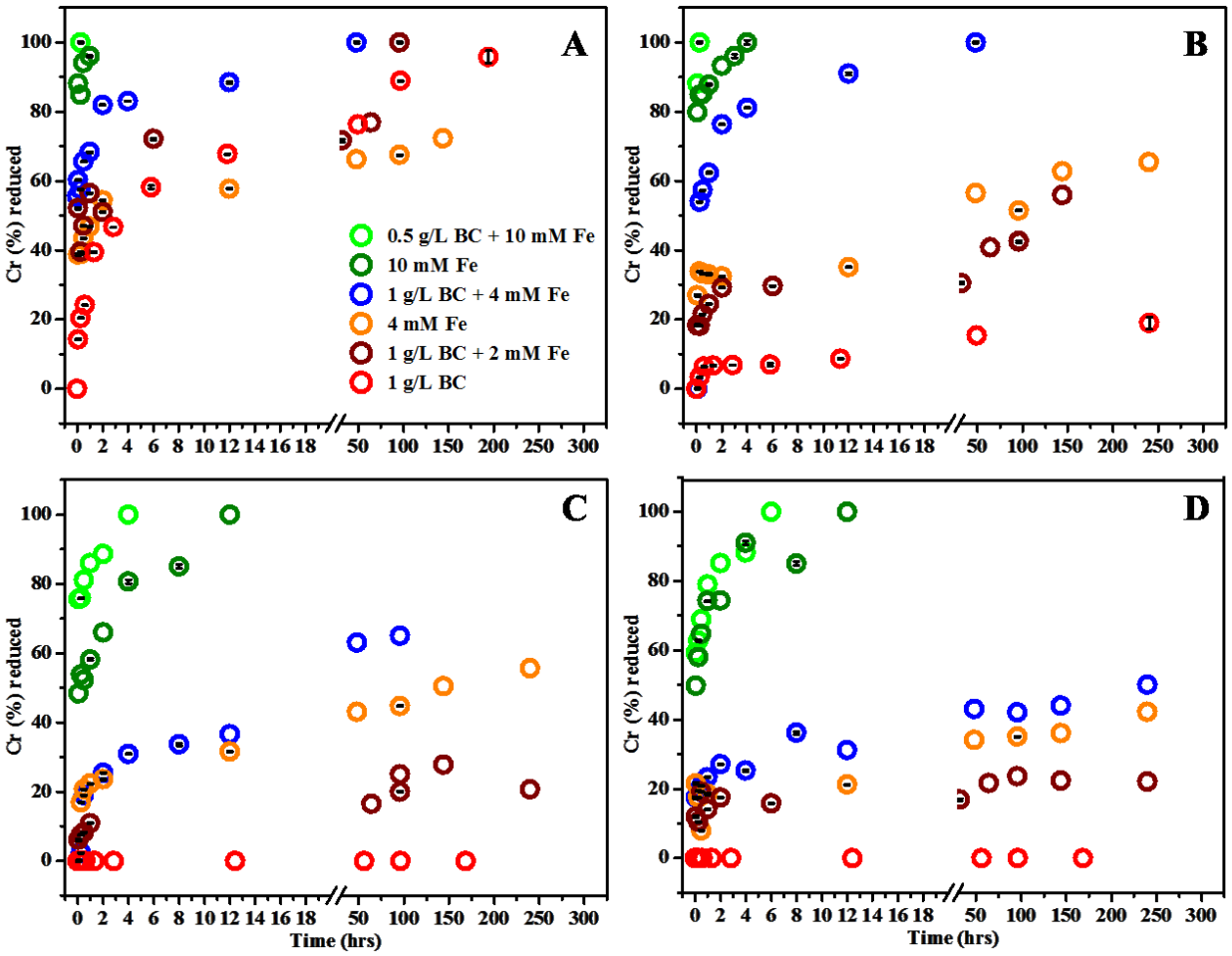

Figure 5.4. Cr(VI) reduction by MNP-BC; MNPs and BC at different pH conditions. (A) pH 2; (B) pH 3; (C) pH and (D) pH 7.

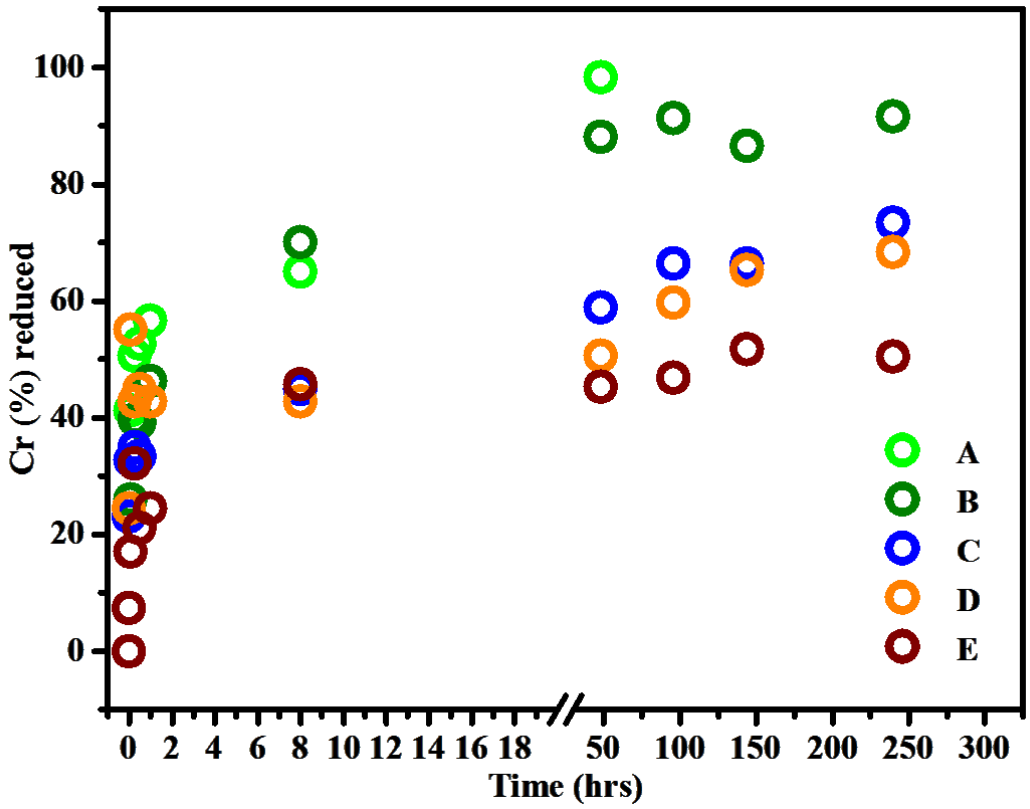

Figure 5.5. Effects of dissolved oxygen (DO) and selected oxidants on Cr(VI) reduction by MNP-BC. (A) 10 mM Fe + 1 gL^{-1} BC (no oxidants); (B) DO; (C) $KMnO_4$; (D) $NaClO_2$ and (E) NaClO.

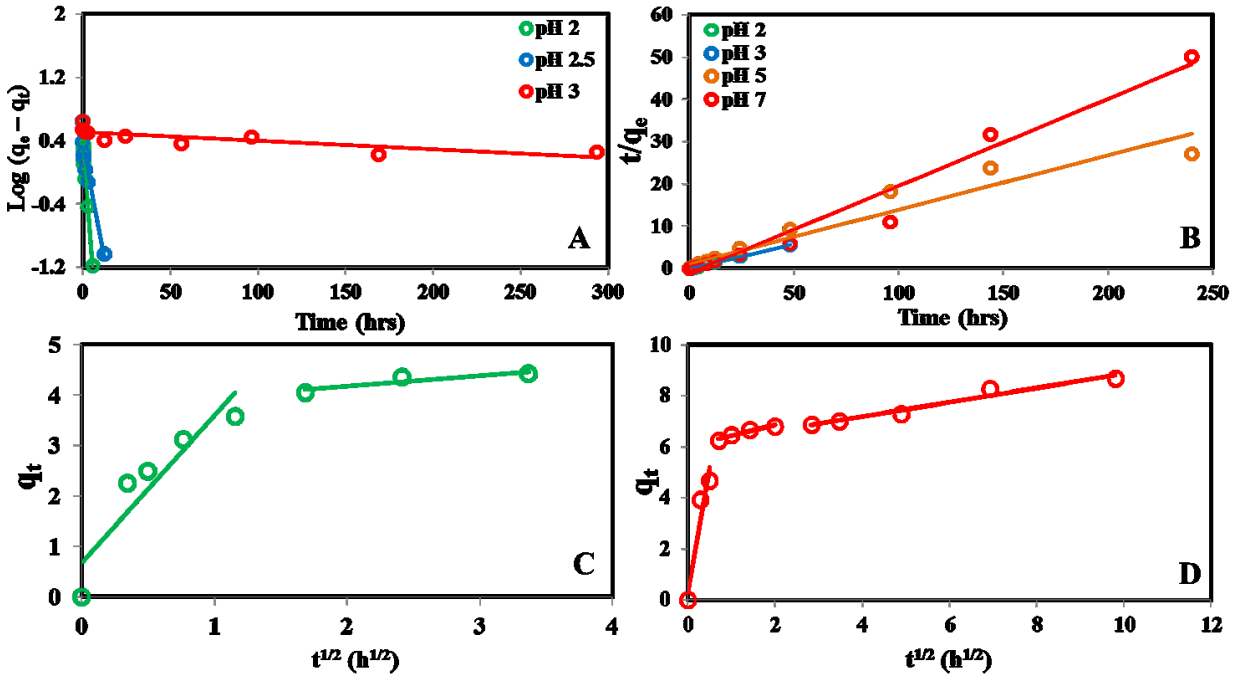

Figure 5.6. Adsorption kinetics and intraparticle-diffusion for Cr(VI) adsorption on BC and MNP-BC. (A) Cr(VI) adsorption on BC fitted with pseudo-first-order; (B) Cr(VI) adsorption on MNP-BC fitted with pseudo-second-order models and (C,D) intraparticle diffusion plot for Cr(VI) adsorption on BC and MNP-BC, respectively.

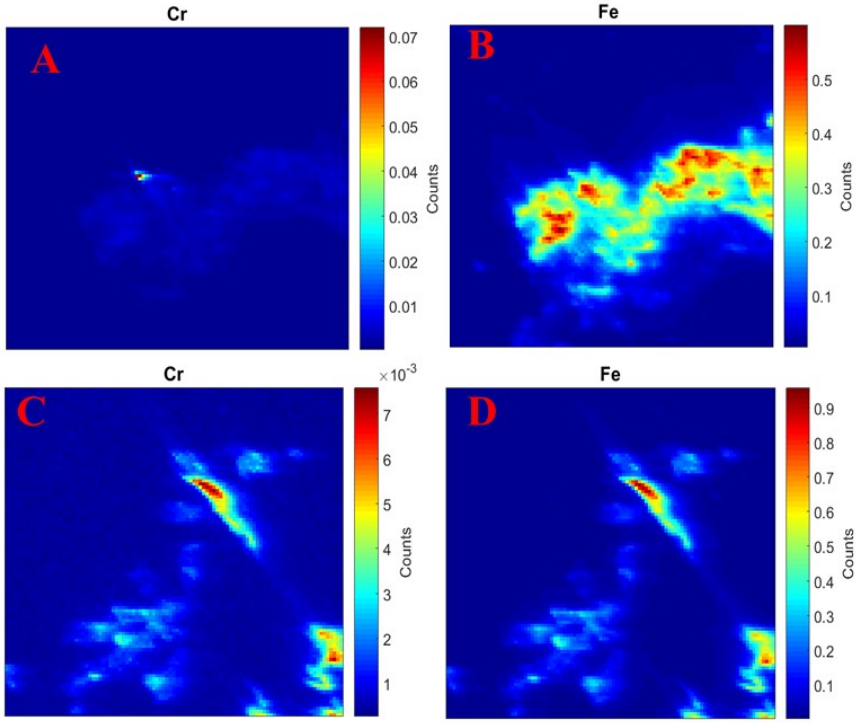

Figure 5.7. XRF map of Cr distribution onto MNP-BC: (A,B) pH 5 and (C,D) pH 7.

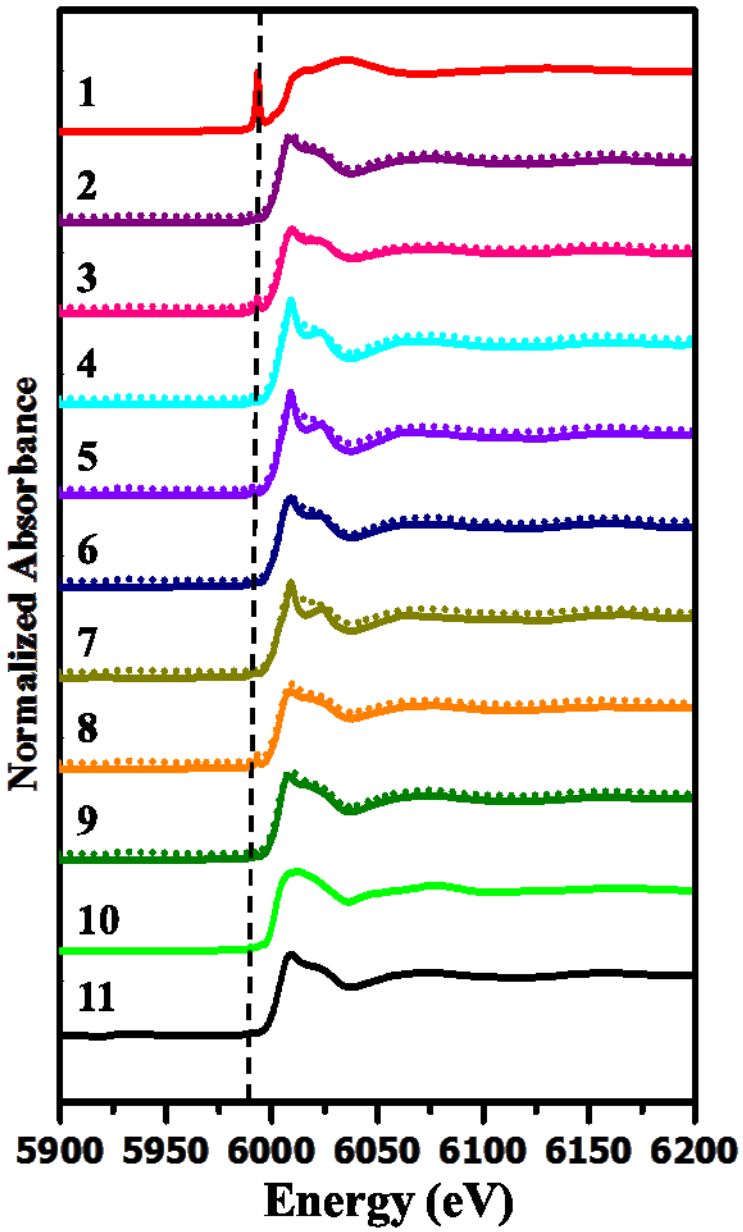

Figure 5.8. Cr K-edge XANES spectra of chromium references and Cr-loaded MNP-BC, MNPs and BC at different pH conditions **(1)** $K_2Cr_2O_7$ standard; **(2)** 2 mM Fe + 1 gL^{-1} BC at pH 7; **(3)** 4 mM Fe + 1 gL^{-1} BC at pH 5; **(4)** 10 mM Fe + 0.5 gL^{-1} BC at pH 5; **(5)** 10 mM MNP + 0.5 gL^{-1} BC at pH 7; **(6)** 10 mM MNP at pH 5; **(7)** 10 mM MNP at pH 7; **(8)** 1 gL^{-1} BC at pH 3; **(9)** 1 gL^{-1} BC at pH 2; **(10)** Cr(III) acetate standard and **(11)** $Cr(OH)_3$ standard. Solid lines represent experimental data and dotted lines represent fit, respectively.

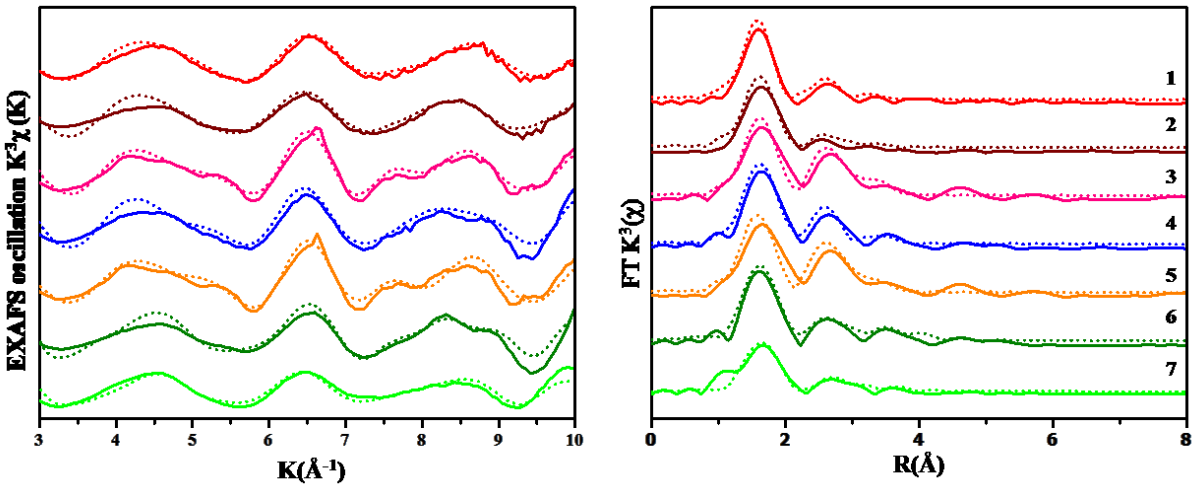

Figure 5.9. Cr K-edge EXAFS signals weighted by (A) k^3 spectra and the (B) radial distribution function of Cr-loaded samples. **(1)** 2 mM Fe + 1 gL^{-1} BC at pH 7; **(2)** 10 mM Fe + 0.5 gL^{-1} BC at pH 5; **(3)** 10 mM MNP + 0.5 gL^{-1} BC at pH 7; **(4)** 10 mM MNP at pH 5; **(5)** 10 mM MNP at pH 7; **(6)** 1 gL^{-1} BC at pH 3 and **(7)** 1 gL^{-1} BC at pH 2. Solid lines represent experimental data and dotted lines represent fit, respectively.

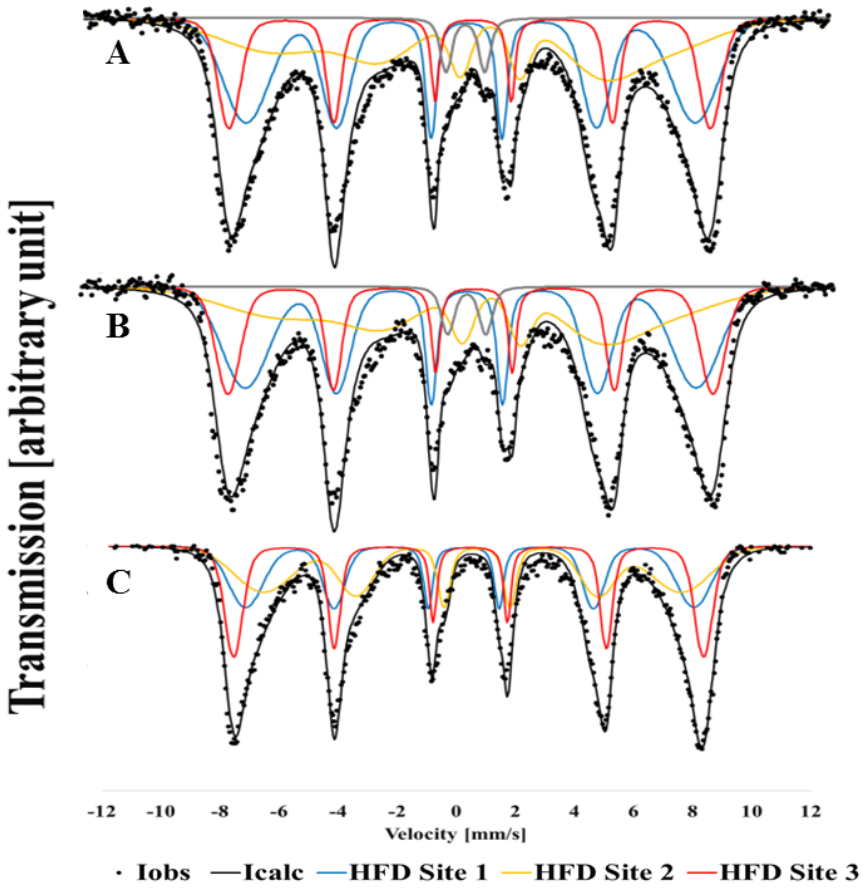

Figure 5.10. Mössbauer spectroscopy of Cr-loaded MNP-BC (10 mM Fe + 1 gL^{-1} BC + 350 µM Cr(VI)) at different reaction time with Cr(VI). (A) t = 0; (B) t = 2 days and (C) t = 4 days.

CHAPTER 6

CONCLUSIONS AND RECOMMENDATIONS FOR FUTURE STUDIES

This thesis provides new insights into molecular-scale reactions that occur between metals and biochar, including the determination of thermodynamic driving forces of Ni(II), Zn(II) and U(VI) adsorption, the application of surface complexation modeling (SCM) to metal adsorption onto mixtures of soil and biochar, and building a mechanistic understanding of the immobilization processes (adsorption and reduction) of Cr(VI) onto biochar – magnetite nanoparticle composites. In Chapter 2, I characterize biochar produced at both the commercial scale (WS and WPC) and lab scale (SSBC) from diverse feedstock materials that include straw, wood and sewage sludges at varying pyrolysis temperatures, and determine their metal removal capacity. The results contribute to a better understanding of how feedstock biomass properties and the pyrolysis temperature during biochar production impact biochar physical and chemical properties and metal removal capacity. I also develop a mechanistic model of Ni(II) and Zn(II) binding to these biochar, which is capable of predicting competitive metal adsorption across wide changes in solution chemistry.

In Chapter 2, I explore molecular scale metal–biochar surface adsorption reactions by thermodynamic analysis with a combined SCM-ITC approach supported by spectroscopic data (EXAFS and FTIR). I also determine the thermodynamic driving forces of Ni(II) and Zn(II) reactions at the biochar surface. The proton-active -COOH and -OH functional groups on the biochar surface adsorb Ni(II) and Zn(II), as confirmed by FT-IR studies coupled with EXAFS. The resulting surface complexation models are able to predict the adsorption behavior of single metals (Ni and Zn separately) and multi-metal (Ni+Zn) systems across a wide range of pH. The

calculated enthalpies of protonation reactions of WS and WPC from the ITC measurements suggest the presence of anionic oxygen ligands on the biochar surface. SCM combined with ITC analyses show that the enthalpies of protonation of biochar are exothermic. Ni(II) and Zn(II) adsorption to biochar surface produced slightly exothermic to slightly endothermic enthalpies depending on the protonation state of biochar surface functional groups to which the metals complex. The combined approach adds considerably to our understanding of the specific mechanisms and coordination of metals adsorbed onto the surface of biochar.

In Chapter 3, I determine the behavior of aqueous uranyl adsorption behavior to biochar. The complex aqueous speciation of U(VI) greatly influences its fate and mobility (Waite et al., 1994); therefore, understanding the molecular coordination of U(VI)-biochar complexes is critical to writing accurate surface reactions. Similar to the Ni(II) and Zn(II) research discussed above, I develop a reaction-based framework to predict U(VI) adsorption onto biochar across varying solution chemistry, and determine the thermodynamic driving forces of U(VI) reactions at the biochar surface. In the case of U(VI), the results show that maximum adsorption occurs between pH 5 to pH 6, and the adsorption is strongly influenced by U(VI) aqueous speciation. By forming uranyl-calcium-carbonato ternary complexes above pH, Ca^{2+} reduce U(VI) adsorption at pH >7. FT-IR and XPS along with EXAFS shows U(VI) adsorption occurring through -COOH and -OH functional groups on the biochar surface, forming both inner- and outer-sphere surface complexes. EXAFS further shows evidence of U(VI) precipitation of the mineral schoepite at pH > 8. The SCM approach is able to predict the U(VI) adsorption behavior across a wide range of pH, adsorbent:adsorbate ratios and in the presence of Ca^{2+}. ITC results show that the overall exothermic heats are produced by U complexation onto WS, while for WPC it produces endothermic heats. However, the heats become more endothermic as the pH

increases (though still exothermic overall for WS), suggesting changes in the hydration sphere of U(VI) as the speciation of U(VI) at the surface changes with increasing pH, and the also changes. Overall, the combined SCM-ITC results show that the U(VI)-surface complexes are indicative of both inner- and outer-sphere complexation. This unique combination of the SCM, XAS and ITC techniques provides novel insights into how U(VI) is bound by biochar functional groups.

In Chapter 4, I determine the effects of biochar amendment on Cd(II) and Se(VI) adsorption (a model cation and anion, respectively) to two agricultural soils. In the process, I rigorously test the component additivity (CA) approach of SCM in a complex soil-biochar mixture. The results of the predictive models show that the metal distribution in multi-component mixtures is successfully predicted by the SCM approach. However, poorer model predictions were observed for the higher biochar to metal ratio. These poor predictions could be due to the presence of Se-DOC aqueous complexes or other complex organic ligands, or Se and/or Cd could be bound to biochar-derived carbon nanoparticles. Using synchrotron EXAFS or FT-IR studies could help to better understand the complex organic ligands that are likely present in multi-component soil-biochar mixtures, and ultimately lead to improved predictive models. The results of this study show that the SCM approach is generally appropriate for these systems, and opens a door to developing predictive models of models of multi-sorbents systems involving biochar as a sorbent.

In Chapter 5, I develop a mechanistic understanding of the adsorption and reduction of Cr(VI) by biochar and a cost-effective and environmental friendly magnetite nanoparticle - biochar composite. In the process, I determine the kinetics of Cr(VI) reduction and used spectroscopic techniques to characterize the products of Cr(VI) reduction that precipitate on the sorbents. The results suggest a strong synergetic cooperation between magnetite nanoparticles

and biochar in the composite material to enhance both adsorption and reduction of Cr(VI) from aqueous solution at acidic to neutral pH ranges, as compared to magnetite nanoparticles and biochar alone. Adsorption and intraparticle diffusion followed by reduction at the composite surface are the primary removal mechanisms of Cr(VI) by biochar and the magnetite nanoparticle – biochar composites, as shown by a second-order dependence in removal kinetics. XAS analysis further showed that nearly all adsorbed Cr(VI) is reduced to Cr(III), and EXAFS fitting results confirm the formation of the Cr(III)-bearing precipitates $Cr(OH)_3$ and chromite (Cr_2FeO_4). Fe K-edge EXAFS, XRD and Mössbauer spectroscopy measurements indicate partial transformation the Fe_3O_4 to maghemite during Cr(VI) reduction. The study provides both a better understanding of the adsorption and reduction processes of Cr(VI) by biochar, and demonstrates that magnetite nanoparticle – biochar composites have great potential for the removal of Cr(VI) from aqueous media.

My dissertation has added considerably to our understanding of molecular-scale mechanisms of biochar reactivity, and metal removal by biochar and mixed systems containing biochar. It has been estimated that approximately 40 million to 250 million tons of charcoal/biochar is generated globally every year from biomass burning, and that approximately 10% of the global riverine flux of DOC is contributed from soluble charcoal (Jaffe et al., 2013). The molecular understanding of biochar surface chemistry and reactivity may provide novel insight into metal sequestration and metal cycling by biochar in the global environment. Furthermore, a better understanding of biochar surface chemistry and reactivity may enhance the predictive capability of metal distribution in multi-sorbent systems that involve biochar, and aid in the use of biochar as a composite material for diverse applications including in permeable reactive barriers, wastewater treatment plants, as a catalyst, for improving soil fertility, and for

greenhouse gas mitigation. In many of these applications, biochar has the potential to replace more costly carbonaceous materials such as activated carbon and graphene oxides.

Recommendations for Future Studies

Since biochar often contains considerable amounts of inorganic components, including alikali metals, clays and minerals, future studies should focus on understanding the effects of these inherent inorganic materials on the biochar reactivity towards various potential sorbates. Future studies should also consider the impacts of complex organic ligands, including fulvic and humic acids, on metal adsorption by biochar, as most natural systems and many engineered systems will contain such organic ligands. Finally, biochar will age and its properties will change over time. Thus, the effects of biochar aging on its surface characteristics and metals adsorption capacity should be tested. While several such studies are extant, to my knowledge none show the molecular-scale changes in surface functionality of biochar. This information would help in developing better predictive models that consider the impacts of changing biochar reactivity.

The relationship between biochar surface properties and its reactivity, as it is produced from various feedstocks and under differing production conditions, is still poorly understood. Future studies can focus on generalizing the relationship between biochar surface properties and its reactivity, irrespective of source materials and production conditions, in order to enhance the efficiency of biochar application in metal immobilization, and will aid in the continued development of rigorous and predictive geochemical models. Furthermore, future studies should investigate how charcoal distribution and ageing worldwide influences global metal cycling and forest regeneration. Using molecular tools to understand the major controls on biochar reactivity could, in turn provide novel insights into the carbon cycle, including CO_2 dynamics, in the environment.

The adjustment of pyrolysis temperature, modification/temperature holding time, and type of feedstocks play important roles in controlling biochar physical and chemical properties, and metal removal capacity (Igalavithana et al., 2017). The production technologies, such as, slow pyrolysis, fast pyrolysis, and gasification of multi-component feedstocks or biomass that contains complex organic and inorganic component mixture should be different than feedstocks or biomass that has single component (i.e., cellulose, hemicelluloses, and lignin) in order to produce biochar with better physical and chemical characteristic including higher surface area, pore volume and reactive site densities. Future studies could employ online or in-situ detection and monitoring technologies such as a Thermogravimetric Analyzer (TGA) coupled with Fourier Transform Infrared Spectrometry (TG-FTIR) and Pyrolysis-gas Chromatography and Mass Spectrometry (Py-GC/MS) analysis to better understand the biochar formation mechanisms. Using these data, the physical and chemical properties of biochar could be optimized (Gao et al., 2013; Liu, et al., 2015).

Biochar surface has been modified and functionalized after post-pyrolysis with different chemicals and by different methods including impregnation and oxidation to enhance biochar physical and chemical properties (Igalavithana et al., 2017). Future studies should also focus on mechanistic understanding of the reactivity of these surface functionalized of biochar towards metals. A better understanding of the surface functionalization of biochar could lead to the production of biochar with improved catalytic activity and manufacture of engineered composite materials, in applications such as enhanced metal removal from solution or through increased electron transfer capacity to participate in contaminant redox reactions.

Biochar can also be used as a substrate to grow microbial biofilm to apply them to wastewater treatment plants to enhance biological aerobic and/or anaerobic treatment of organic

pollutants, micro-pollutants, and trace elements. Future studies can focus on a deeper understanding of the microbes-biochar interactions to enhance biochar use in wastewater treatment plant, an inoculant carrier for many microbial species and enhance soil's microbial activity and population. While several such studies are present, there is no study on molecular level understanding of microbes-biochar interactions. Synchrotron based soft X-ray scanning transmission X-ray microscope (STXM) and microbial molecular studies can help to better understand the microbes-biochar interactions.

BIBLIOGRAPHY

Achadu, O.J., Ayejuyo, O.O., Ako, F.E., Dalla, C.L. and Olaoye, O.O., 2014. Synchronous Adsorption of Cadmium and Lead ions from Aqueous Media by Rice Husk Ash and Sodium Dodecyl Sulfate Combination. Int. J. of Modern Analytical and Separation Sci., 3(1), 20-39.

Ahmad, M., Lee, S.S., Dou, X., Mohan, D., Sung, J.K., Yang, J.E., Ok, Y.S., 2012. Effects of pyrolysis temperature on soybean stover- and peanut shell-derived biochar properties and TCE adsorption in water. Bioresour. Technol. 118, 536-544.

Ahmad, M., Rajapaksha, A.U., Lim, J.E., Zhang, M., Bolan, N., Mohan, D., Vithanage, M., Lee, S.S. and Ok, Y.S., 2014. Biochar as a sorbent for contaminant management in soil and water: a review. Chemosphere, 99: 19-33.

Ahrland, S., Chatt, J., Davies, N.R., 1958. The relative affinities of ligand atoms for acceptor molecules and ions. Q. Rev. Chem. Soc., 2 (3), 265-276.

Alam, M.S., Cheng, T., 2014. Uranium release from sediment to groundwater: Influence of water chemistry and insights into release mechanisms. J. Contam. Hydrol., 164, 72−87.

Alam, M.S., Cossio, M., Robinson, L., Kenney, J.P.L., Wang, X., Konhauser, K.O., MacKenzie, M.D., Ok, Y.S., Alessi, D.S., 2016. Removal of organic acids from water using biochar and petroleum coke. Environ. Technol. Innovat., 6: 141-151.

Alam, M.S., Swaren, L, Gunten, K.V., Cossio, M., Robbins, L.J., Flynn, S.L., Konhauser, K.O, Alessi, D.S., 2018a. Application of surface complexation modeling to trace metals uptake by biochar-amended agricultural soils. App. Geochem., 88:103-112.

Alam, M.S., Lewis, D.G., Chen, N., Konhauser, K.O., Alessi, D.S., 2018b. Thermodynamic analysis of nickel (II) and zinc (II) adsorption to biochar. In press, Environ. Sci. Technol.

Alam, M.S., Lewis, D.G., Chen, N., Safari, S., Baek, K., Konhauser, K.O., Alessi, D.S., Mechanisms of the removal of U(VI) from aqueous solution using biochar: A combined spectroscopic and modeling approach. In review.

Alessi, D.S. and Fein, J.B., 2010. Cadmium adsorption to mixtures of soil components: Testing the component additivity approach. Chem. Geol., 270(1): 186-195.

Alessi, D.S., Lezama-Pacheco, J.S., Stubbs, J.E., Janousch, M., Bargar, J.R., Persson, P., Bernier-Latmani, R., 2014. The product of microbial uranium reduction includes multiple species with U(IV)-phosphate coordination. Geochim. Cosmochim. Acta., 131, 115−127.

Alessi, D S. et al., 2014. Speciation and Reactivity of Uranium Products Formed during in Situ Bioremediation in a Shallow Alluvial Aquifer. Environ. Sci. Technol., 48, 12842−12850.

Alowitz, M.J.; Scherer, M.M., 2002. Kinetics of nitrate, nitrite, and Cr(VI) reduction by iron metal. Environ. Sci. Technol., 36 (3), 299-306.

American Public Health Association, American Water Works Association, & Water Environment Federation., 1991. Standard Methods for the Examination of Water and Wastewater. Standard Methods. 541.

Anders, E., Watzinger, A., Rempt, F., Kitzler, B., Wimmer, B., Zehetner, F., Stahr, K., Zechmeister-Boltenstern, S., Soja, G., 2013. Biochar affects the structure rather than the total biomass of microbial communities in temperate soils. Agric. Food Sci. 22(4): 404-423.

Andersson, A., Bingefors, S., 1985. Trends and annual variations in Cd concentrations in grain of winter wheat. Acta Agric. Scand. 35(4): 339-344.

Anderson, G.M., 2005. Thermodynamics of Natural Systems, 2nd Edition, Cambridge University Press, Cambridge, United Kingdom, 664 pp.

Ankudinov, A., Rehr, J.J., 2000. Theory of solid state contributions to the x-ray elastic scattering amplitude. Phys. Rev. B., 62, 2437-2445.

Arai, Y., McBeath, M., Bargar, J.R., Joye, J., Davis, J.A., 2006. Uranyl adsorption and surface speciation at the imogolite−water interface: Self-consistent spectroscopic and surface complexation models. Geochim. Cosmochim. Acta., 70, 2492−2509.

Ashry, A., Bailey, E.H., Chenery, S.R.N., Young, S. D., 2016. Kinetic study of time-dependent fixation of U-VI on biochar. J. Hazard. Mater., 320, 55–66.

Baes, C.F., Mesmer, R.E., 1976. Hydrolysis of Cations, Wiley Interscience Publication. NewYork, NY.

Banuelos, G., Schulin, R., Bitterli, C., 2013. Fate and movement of selenium from drainage sediments disposed onto soil with and without vegetation. Environ. Pollut. 180: 7-12.

Bargar, J.R., Reitmeyer, R., Davis, J.A., 1999. Spectroscopic confirmation of Uranium(VI)-carbonato adsorption complexes on hematite. Environ. Sci. Technol., 33, 2481−2484.

Beck, M., Nagypal, I. 1990. Chemistry of complex equilibria. Ellis Horwood, Chichester.

Beesley, L., Moreno-Jimenez, E., Fellet, G., Carrijo, L., Sizmur, T., 2015. Biochar and heavy metals. In: Lehmann, J. and Joseph, S. (eds.) Biochar for environmental management: science, technology and implementation. 2nd ed. Earthscan, London, pp. 563-594.

Beller, H.R., Yang, L., Varadharajan, C., Han, R., Lim, H.C., Karaoz, U., Molins, S., Marcus, M. A., Brodie, E.L., Steefel, C.I., 2014. Divergent aquifer biogeochemical systems converge on similar and unexpected Cr (VI) reduction products. Environ. Sci. Technol., 48(18), 10699-10706.

Bethke, C.M. and Brady, P.V., 2000. How the Kd approach undermines ground water cleanup. Ground Water, 38(3): 435-443.

Betts, A.R., Chen, N., Hamilton, J.G., Peak, D., 2013. Rates and mechanisms of Zn^{2+} adsorption on a meat and bonemeal biochar. Environ. Sci. Technol., 47, 14350-14357.

Beveridge, T. and Murray, R., 1980. Sites of metal deposition in the cell wall of Bacillus subtilis. Journal of Bacteriology, 141(2): 876-887.

Bolan, N.S., Naidu, R., Tillman, R.W., Khan, A., Syers, J.K., 1999. Effect of anion sorption on cadmium sorption by soils. Aust. J. Soil Res. 37, 445-460.

Bolan, N.S., Adriano, D.C., Mani, S., Khan, A.R., 2003. Adsorption, complexation and phytoavailability of copper as influenced by organic manure. Environ. Toxicol. Chem. 22, 450-456.

Bonten, L.T.C., Römkens, P.F.A.M., Brus, D.J., 2008. Contribution of heavy metal leaching from agricultural soils to surface water loads. Environ. Forensics., 9: 252-257.

Borrok, D., Turner, B.F. and Fein, J.B., 2005. A universal surface complexation framework for modeling proton binding onto bacterial surfaces in geologic settings. American J. of Science, 305(6-8): 826-853.

Buerge, I. J.; Hug, S. J., 1997. Kinetics and pH dependence of chromium(VI) reduction by iron(II). Environ. Sci. Technol., 31, 1426-1432.

Cambardella, C.A., Moorman, T.B., Parkin, T.B., Karlen, D.L., Novak, J.M., Turco, R.F., Konopka, A.E., 1994. Field-scale variability of soil properties in central Iowa soils. Soil Sci. Soc. Am. J. 58(5): 1501-1511.

Cao, X.D., Ma, L.N., Gao, B., Harris, W., 2009. Dairy-manure derived biochar effectively sorbs lead and atrazine. Environ. Sci. Technol., 43, 3285-3291.

Cao, X., Harris,W., 2010. Properties of dairy-manure-derived biochar pertinent to its potential use in remediation. Bioresour. Technol., 101, 5222-5228.

Catalano, J.G.; McKinley, J.P.; Zachara, J.M.; Heald, S.M.; Smith, S.C.; Brown, G.E., 2006. Changes in uranium speciation through a depth sequence of contaminated Hanford sediments. Environ. Sci. Technol., 40 (8), 2517-2524.

Chen, B., Zhou, D., Zhu, L., 2008. Transitional adsorption and partition of nonpolar and polar aromatic contaminants by biochars of pine needles with different pyrolytic temperatures. Environ. Sci. Technol., 42(14), 5137-5143.

Chen, J.P., Lin, M., 2001. Equilibrium and kinetic of metal ion adsorption onto a commercial H-type granular activated carbon: experimental and modelling studies. Water Res. 35 (10), 2385–2394.

Cheng, Y., Yan, F., Huang, F., Chu, W., Pan, D., Chen, Z., Zheng, J., Yu, M., Lin, Z., Wu, Z., 2010. Bioremediation of Cr(VI) and immobilization as Cr(III) by Ochrobactrum anthropi. Environ. Sci.Technol., 44 (16), 6357-6363.

Chen, Z., Chen, B., Chiou, C.T., 2012. Fast and slow rates of naphthalene sorption to biochars produced at different temperatures. Environ. Sci. Technol., 46, 11104-11111.

Chen, Z., Chen, B., Zhou, D., Chen, W., 2012. Bisolute Sorption and Thermodynamic Behavior of Organic Pollutants to Biomass-derived Biochars at Two Pyrolytic Temperatures. Environ. Sci. Technol., 46, 12476-12483.

Chen, Z., Xiao, X., Chen, B., Zhu, L., 2015. Quantification of chemical states, dissociation constants and contents of oxygen-containing groups on the surface of biochars produced at different temperatures. Environ. Sci. Technol., 49 (1), 309-317.

Chia, C. H., Gong, B., Joseph, S. D., Marjo, C. E., Munroe, P., Rich, A. M., 2012. Imaging of mineral-enriched biochar by FTIR, Raman and SEM−EDX. Vib. Spectrosc., 62, 248-257.

Choppala, G., Bolan, N., Megharaj, M., Chen, Z. and Naidu, R., 2012. The influence of biochar and black carbon on reduction and bioavailability of chromate in soils. J. Environ. Qual, 41(4): 1175-1184.

Choppin, G.R., 1997. Factors in Ln(III) complexation. J. Alloy. Compd., 249 (1–2), 1–8.

Chowdhury, S.R., Yanful, E.K., 2010. Arsenic and chromium removal by mixed magnetite-maghemite nanoparticles and the effect of phosphate on removal. J. Environ. Manage., 91 (11), 2238-2247.

Chowdhury, S.R., Yanful, E.K., Pratt, A.R., 2012. Chemical states in XPS and Raman analysis during removal of Cr(VI) from contaminated water by mixed maghemite-magnetite nanoparticles. J. Hazard. Mater., 235, 246-256.

Costa, M.; Klein, C. B., 2006. Toxicity and carcinogenicity of chromium compounds in humans. Crit. Rev. Toxicol. 36, 155-163.

Cossio, M., 2017. Mechanisms of the reductive immobilization of hexavalent chromium by Wheat Straw biochar. MSc Thesis. University of Alberta.

Cox, J.S., Smith, D.S., Warren, L.A., Ferris, F.G., 1999. Characterizing heterogeneous bacterial surface functional groups using discrete affinity spectra for proton binding. Environ. Sci. Technol. 33: 4514-4521.

Cuenca, J.A., Bugler, K., Taylor, S., Morgan, D., Williams, P., Bauer, J., Porch, A. 2016. Study of the Magnetite to Maghemite Transition Using Microwave Permittivity and Permeability Measurements. J. Phys.: Condens. Matter, 28, 106002.

Davies, C.W., 1938. The extent of dissociation of salts in water. Part VIII. An equation for the mean ionic activity coefficient of an electrolyte in water, and a revision of the dissociation constants of some sulphates. J. Chem. Soc. 1938, (Resumed)(0), 2093-2098.

Davis, J.A., James, R.O., Leckie, J.O., 1978. Surface ionization and complexation at the oxide/water interface, I. Computation of electrical double layer properties in simple electrolytes. J. Colloid Interface Sci. 63(3): 480-499.

Davis, J.A.,1984. Complexation of trace metals by adsorbed natural organic matter. Geochim. Cosmochim. Acta 48(4): 679-691.

Davis, J.A., Kent, D., 1990. Surface complexation modeling in aqueous geochemistry. Rev. Mineral. Geochem. 1990, 23(1), 177-260.

Davis, J.A., Coston, J.A., Kent, D.B., Fuller, C.C., 1998. Application of the surface complexation concept to complex mineral assemblages. Environ. Sci. Technol. 32:2820-2828.

DeLuca, T.H., MacKenzie, M.D., Gundale, M.J., Holben, W.E., 2006. Wildfire-produced charcoal directly influences nitrogen cycling in ponderosa pine forests. Soil Sci. Soc. Am. J. 70, 448–453.

Deshpande, K., Cheung, S., Rao, M. S., Dave, B. C., 2005. Efficient sequestration and reduction of hexavalent chromium with organosilica sol-gels. J. Mater. Chem., 15 (29), 2997-3004.

Dickinson, M., Scott, T. B., 2010. The application of zero-valent iron nanoparticles for the remediation of a uranium-contaminated waste effluent. J. Hazard. Mater., 178 (1−3), 171−179.

Dong, W., Ball, W. P., Liu, C., Wang, Z., Stone, A., Bai, J., Zachara, J. M., 2005. Influence of calcite and dissolved calcium on uranium(VI) sorption to a Hanford subsurface sediment. Environ. Sci.Technol., 39, 7949-7955.

Dong, X., Ma, L.Q. and Li, Y., 2011. Characteristics and mechanisms of hexavalent chromium removal by biochar from sugar beet tailing. J. Hazardous Materials, 190(1): 909-915.

Dong, X., Ma, L.Q., Zhu, Y., Li, Y., Gu, B., 2013. Mechanistic investigation of mercury sorption by Brazilian pepper biochars of different pyrolytic temperatures based on X-ray photoelectron spectroscopy and flow calorimetry. Environ. Sci. Technol., 47, 12156-12164.

Du, H., Chen, W., Cai, P., Rong, X., Dai, K., Peacock, C.L., Huang, Q., 2016. Cd(II) sorption on montmorillonite-humic acid-bacteria composites. Sci. Rep. 6, 19499.

Duster, T.A., Szymanowski, V J.B., Fein, J., 2017. Experimental measurements and surface complexation modeling of U(VI) adsorption onto multilayered graphene oxide: The importance of adsorbate-adsorbent ratios. Environ. Sci. Technol., 51(15), 8510-8518.

Eary, L.E.; Rai, D. 1987. Kinetics of chromium(III) oxidation to chromium(VI) by reaction with manganese dioxide. Environ. Sci. Technol., 21, 1187-1193.

Eary, L.E.; Rai, D., 1988. Chromate removal from aqueous wastes by reduction with ferrous ion. Environ. Sci. Technol., 22 (8), 972-977.

Elzinga, E. J., Reeder, R. J., 2002. X-ray absorption spectroscopy study of Cu(II) and Zn(II) adsorption complexes at the calcite surface: Implications for site-specific metal incorporation preferences during calcite crystal growth. Geochim. Cosmochim. Acta, 66, 3943-3954.

Eriksson G., 1979. An algorithm for the computation of aqueous multicomponent, multiphase equilibria. Anal. Chim. Acta, 112: 375-383.

Fein, J. B. 2006. Thermodynamic modeling of metal adsorption onto bacterial cell walls: Current challenges. Adv. Agron. 90: 179-202.

Fein, J.B., Daughney, C.J., Yee, N., Davis, T.A., 1997. A chemical equilibriummodel formetal adsorption onto bacterial surfaces. Geochim. Cosmochim. Acta., 61, 3319–3328.

Fein, J.B., Boily, J.F., Yee, N., Gorman-Lewis, D., Turner, B.F., 2005. Potentiometric titrations of Bacillus subtilis cells to low pH and a comparison of modeling approaches. Geochim. Cosmochim. Acta., 69, 1123-1132.

Fendorf, S., Wielinga, B.W. and Hansel, C.M., 2000. Chromium transformations in natural environments: the role of biological and abiological processes in chromium(VI) reduction. International Geology Review, 42(8): 691-701.

Fidel, R.B., Laird, D.A., Thompson, M.L. Evaluation of modified Boehm titration methods for use with biochars. J. Environ. Qual. 2013, 42 (6), 1771–1778.

Flynn, S.L., Szymanowski, J.E.S., Fein, J.B., 2014. Modeling bacterial metal toxicity using a surface complexation approach. Chem. Geol., 374, 110-116.

Flynn, S.L., Gao, Q., Robbins, L.J., Warchola, T., Weston, J.N.J., Alam, M.S., Liu, Y., Konhauser, K.O., Alessi, D.S. 2017. Measurements of bacterial mat metal binding capacity in alkaline and carbonate-rich systems. Chem. Geol. 451: 17-24.

Fowle, D.A., Fein, J.B., 1999. Competitive adsorption of metal cations onto two gram positive bacteria: Testing the chemical equilibrium model. Geochim. Cosmochim. Acta 63:3059-3067.

Fredrickson, J.K., Zachara, J.M., Kennedy, D.W., Duff, M.C., Gorby, Y.A., Shu-mei, W.L. and Krupka, K.M., 2000. Reduction of U(VI) in goethite (α-FeOOH) suspensions by a dissimilatory metal-reducing bacterium. Geochim. Cosmochim. Acta, 64(18): 3085-3098.

Fox, P. M., Davis, J. A., Zachara, J. M., 2006. The effect of calcium on aqueous uranium(VI) speciaton and adsorpton to ferrihydrite and quartz. Geochim. Cosmochim. Acta., 70(6), 1379-1387.

Gao, N., Li, A., Quan, C., Du, L., Duan, Y., 2013. TG−FTIR and Py−GC/MS analysis on pyrolysis and combustion of pine sawdust. J. Anal. Appl. Pyrolysis, 100, 26−32.

Garrels, R.M., Christ, C.L., 1965. Solutions, Minerals, and Equilibria. Harper and Row, New York, 450 pp.

Georgakilas, V., Perman, J. A., Tucek, J., Zboril, R., 2015. Broad Family of Carbon Nanoallotropes: Classification, Chemistry, and Applications of Fullerenes, Carbon Dots, Nanotubes, Graphene, Nanodiamonds, and Combined Superstructures. Chem. Rev., 115, 4744−4822.

Goertzen, S.L., Thériault, K.D., Oickle, A.M., Tarasuk, A.C., Andreas, H.A., 2010. Standardization of the Boehm titration. Part I. CO2 expulsion and endpoint determination. Carbon., 48 (4), 1252–1261.

Goldberg, S. 1992. Use of surface complexation models in soil chemical systems. Adv. Agron. 47: 233-329.

Goldberg, S., 2014. Modeling selenite adsorption behavior on oxides, clay minerals, and soils using the triple layer model. Soil Sci.179(12): 568-576.

Gorman-Lewis D., Fein J.B., Jensen M.P., 2006. Enthalpies and entropies of proton and cadmium adsorption onto Bacillus subtilis bacterial cells from calorimetric measurements. Geochim. Cosmochim. Acta, 70:4862-4873.

Gorman-Lewis D., 2011. Enthalpies of proton adsorption onto Bacillus licheniformis at 25, 37, 50, and 75◦C. Geochim. Cosmochim. Acta, 75:1297-1307.

Gorman-Lewis, D., 2014. Enthalpies and Entropies of Cd and Zn Adsorption onto Bacillus licheniformis and Enthalpies and Entropies of Zn Adsorption onto Bacillus subtilis from Isothermal Titration Calorimetry and Surface Complexation Modeling. Geobio. J., 31: 383-359.

Gorski, C. A. et al., 2010. Determination of nanoparticulate magnetite stoichiometry by Mössbauer spectroscopy, acidic dissolution, and powder X-ray diffraction: A critical review. American Mineralogist., 95, 1017-1026.

Gray, C.W., Dunham, S.J., Dennis, P.G., Zhao, F.J., McGrath, S.P., 2006. Field evaluation of in situ remediation of a heavy metal contaminated soil using lime and red-mud. Environ Pollut 142:530–539.

Grant, C.A., Sheppard, S.C. 2008., Fertilizer impacts on cadmium availability in agricultural soils and crops. Hum. Ecol. Risk Assess. 14(2): 210-228.

Grenthe, I., Ots, H., Ginstrup, O., 1970. A calorimetric determination of the enthalpy of ionization of water and the enthalpy of protonation of THAM at 5, 20, 25, 35, and 50C. Acta Chemica Scandinavica., 24:1067-1080.

Guillaumont, R., Fanghänel, T., Fuger, J., Grenthe, I., Neck, V., Palmer, D. A., Rand, M. H., 2003. Update on the Chemical Thermodynamics of Uranium, Neptunium, Plutonium, Americium and Technetium. OECD Nuclear Energy Agency. Elsevier, Amsterdam: Vol. 5.

Guo, Y., Bustin, R. M., 1998. FTIR spectroscopy and reflectance of modern charcoals and fungal decayed woods: implications for studies of inertinite in coals. Int. J. Coal Geol., 37(1-2), 29-53.

Hadjittofi, L., Pashalidis, I., 2015. Uranium sorption from aqueous solutions by activated biochar fibres investigated by FTIR spectroscopy and batch experiments. J. Radioanal. Nucl. Chem., 304(2):897–904.

Harrold, Z.R., Gorman-Lewis, D., 2013. Thermodynamic analysis of Bacillus subtilis endospore protonation using isothermal titration calorimetry. Geochim. Cosmochim. Acta , 109: 296-305.

Han, X., Wong, Y.S., Wong, M.H., Tam, N.F.Y., 2007. Biosorption and bioreduction of Cr (VI) by a microalgal isolate, Chlorella miniata. J. Hazard. Mater. 146 (1), 65-72.

He, Y.T., Chen, C., Traina, S.J., 2004. Inhibited Cr(VI) reduction by aqueous Fe(II) under hyperalkaline conditions. Environ. Sci. Technol. 38:5535-5539.

He, Y.T. and Traina, S.J., 2005. Cr(VI) reduction and immobilization by magnetite under alkaline pH conditions: the role of passivation. Environ. Sci. Technol., 39(12): 4499-4504.

He, Z.L., Yang, X.E., Stoffella, P.J., 2005. Trace elements in agroecosystems and impacts on the environment. J. Trace Elem. Med. Biol., 19 (2−3), 125−140.

Herbelin, A. and Westall, J., 1996. FITEQL-a computer program for determination of chemical equilibrium constants from experimental data version 3.2 user's manual. Department of Chemistry, Oregon State University, Corvallis, OR, Report.: 96-01.

Holmgren, G.G.S., Meyer, M.W., Chaney, R.L., Daniels, R.B., 1993. Cadmium, lead, zinc, copper, and nickel in agricultural soils of the United States of America. J. Environ. Qual. 22(2): 335-348.

Hsu, N.H., Wang, S.L., Lin, Y.C., Sheng, G.D., Lee, J. F., 2009. Reduction of Cr(VI) by crop-residue-derived black carbon. Environ. Sci. Technol., 43(23), 8801-8806.

Hu, B., Hu, Q., Xu, D., Chen, C., 2017. The adsorption of U(VI) on carbonaceous nanofibers: A combined batch, EXAFS and modeling techniques, Sep. Purif. Technol., 175: 140-146.

Hu, Q., Zhu, Y., Hu, B., Lu, S., Sheng, G., 2018. Mechanistic insights into sequestration of U(VI) toward magnetic biochar: Batch, XPS and EXAFS techniques. J. Environ. Sci. 2018. In press.

Hunter, R. J. 1981. Zeta potential in colloid science: Principles and Applications, Academic Press,.

Igalavithana, A. D., Lee, S. -E., Lee, Y. H., Tsang, D.C.W., Rinklebe, J., Kwon, E. E., Ok, Y.S., 2017. Heavy metal immobilization and microbial community abundance by vegetable waste and pine cone biochar of agricultural soils. Chemosphere 174(1): 593-603.

Ingri N., Kakolowicz W., Sillén, L.G., Warnqvist, B., 1968. High-speed computers as a supplement to graphical methods-V. HALTAFALL, a general program for calculating the composition of equilibrium mixtures. Talanta, 14: 1261-1286. Errata: 15(3) (1968) xi-xii.

Igalavithana et al., 2017. Advances and future directions of biochar characterization methods and applications, Critical Reviews in Environmental Science and Technology, 47:23, 2275-2330.

Jaffe, R., Ding, Y., Niggemann, J., Vahatalo, A. V., Stubbins, A., Spencer, R. G. M., Campbell, J., Dittmar, T., 2013. Global charcoal mobilization from soils via dissolution and riverine transport to the oceans. Science, 340 (6130), 345-347.

Jensen, M.P., Morss, L.R., Beitz, J.V., Ensor, D.D., 2000. Aqueous complexation of trivalent lanthanide and actinide cations by N,N,N0,N0-Tetrakis (2-pyridylmethyl) ethylenediamine. J. Alloy. Compd., 303/304, 137-141.

Jiang, J., Rao, L., Bernardo, P.D., Zanonato, P. 2002. Complexation of uranium(VI) with acetate at variable temperatures. J. Chem. Soc., Dalton Trans, 1832-1838.

Jiang, W., Cai, Q., Xu, W., Yang, M., Cai, Y., Dionysiou, D. D., O'Shea, K. E., 2014. Cr(VI) adsorption and reduction by humic acid coated on magnetite. Environ. Sci. Technol., 48 (14), 8078-85.

Jiang, J., Xu, R., Jiang, T., Li, Z., 2012. Immobilization of Cu (II), Pb (II) and Cd (II) by the addition of rice straw derived biochar to a simulated polluted Ultisol. J. Hazard. Mater. 229–230:145–150.

Joseph, S., Camps-Arbestain, M., Lin, Y., Munroe, P., Chia, C., Hook, J., Van Zwieten, L., Kimber, S., Cowie, A. and Singh, B., 2010. An investigation into the reactions of biochar in soil. Soil Research, 48(7): 501-515.

Jung, Y., Choi, J., Lee, W., 2007. Spectroscopic investigation of magnetite surface for the reduction of hexavalent chromium. Chemosphere., 68, 1968-1975.

Kappler, A., Wuestner, M.L., Ruecker, A., Harter, J., Halama, M. and Behrens, S., 2014. Biochar as an electron shuttle between bacteria and Fe (III) minerals. Environmental Science & Technology Letters, 1(8): 339-344.

Karthikeyan, K. and Elliott, H.A., 1999. Surface complexation modeling of copper sorption by hydrous oxides of iron and aluminum. J. Colloid Interface Sci. 220(1): 88-95.

Katz, S. A.; Salem, H., 1993. The toxicology of chromium with respect to its chemical speciation: A review. J. Appl. Toxicol. 13 (3), 217−224.

Keiluweit, M., Nico, P. S., Johnson, M. G., Kleber, M., 2010. Dynamic molecular structure of plant biomass-derived black carbon (biochar). Environ. Sci. Technol., 44, 1247-1253.

King, E.J., 1965. Acid-Base Equilibria. Macmillan, New York.

Kjeargsgaard, A.A., 1972. Reconnaissance soil survey of the Tawatinaw map sheet (83-I). Report No. S-72-39. Alberta Institute of Pedology, University of Alberta.

Komárek, M., Koretsky, C.M., Stephen, K.J., Alessi, D.S., Chrastný, V. 2015. Competitive adsorption of Cd(II), Cr(VI), and Pb(II) onto nanomaghemite: A spectroscopic and modeling approach. Environ. Sci. Technol. 49(21): 12841-12859.

Koretsky, C., 2000. The significance of surface complexation reactions in hydrologic systems: a geochemist's perspective. J. Hydrology, 230(3): 127-171.

Kraepiel, A.M.L., Keller, K., Morel, F.M.M., 1999. A model for metal adsorption on montmorillonite. J. Colloid Interface Sci. 210: 43-54.

Kumar, S., Loganathan, V. A, Gupta, R. B., Barnett, M. O. 2011. An assessment of U(VI) removal from groundwater using biochar produced from hydrothermal carbonization. J. Environ. Manag. 92, 2504−2512.

Laird, D., Rogovska, N., 2015. Biochar effects on nutrient leaching. In: Biochar for Environmental Management: Science, Technology and Implementation, J. Lehmann and S. Joseph, Eds., Routledge, UK, pp. 521-542.

Lalonde, S., Konhauser, K. O., Amskold, L., McDermott, T., Inskeep, B.P., 2007a. Chemical reactivity of microbe and mineral surfaces in hydrous ferric oxide depositing hydrothermal springs. Geobio. J. 5: 219-234.

Lalonde, S., Amskold, L., Warren L.A., Konhauser, K.O. 2007b. Surface chemical reactivity and metal adsorptive properties of natural cyanobacterial mats from an alkaline hot spring, Yellowstone National Park. Chem. Geol. 243: 36-52.

Lalonde S. V., Smith D.S., Owttrim G.W. and Konhauser K.O., 2008a Acid–base properties of cyanobacterial surfaces I: influences of growth phase and nitrogen metabolism on cell surface reactivity. Geochim. Cosmochim. Act., 72, 1257–1268.

Lalonde S.V., Smith D.S., Owttrim G.W., Konhauser K.O., 2008b. Acid–base properties of cyanobacterial surfaces. II: silica as a chemical stressor influencing cell surface reactivity. Geochim. Cosmochim. Act., 72, 1269–1280.

Lalonde S.V., Dafoe L.T., Pemberton S.G., Gingras M. K. and Konhauser K.O., 2010. Investigating the geochemical impact of burrowing animals: Proton and cadmium adsorption onto the mucus lining of Terebellid polychaete worms. Chem. Geol., 271, 44-51.

Langmuir, D., 1978. Uranium solution-mineral equilibria at low temperatures with applications to sedimentary ore deposits. Geochim. Cosmochim. Acta., 42, 547−569.

Lehmann, J., Kuzyakov, Y., Pan, G., Ok, Y.S., 2015. Biochars and the plant-soil interface. Plant Soil 395: 1-5.

Liu, J.-F.; Zhao, Z.-S.; Jiang, G.-B., 2008. Coating Fe_3O_4 magnetic nanoparticles with humic acid for high efficient removal of heavy metals in water. Environ. Sci. Technol., 42 (18), 6949-6954.

Li, M., Liu, Q., Lou, Z., Wang, Y., 2014. Method to Characterize Acid-Base Behavior of Biochar: Site Modeling and Theoretical Simulation. ACS Sustainable Chem. Eng., 2 (11), 2501-2509.

Liu, L.N., Chen, H.S., Cai, P., Lianga, W., Huang, Q.Y., 2009. Immobilization and phytotoxicity of Cd in contaminated soil amended with chicken manure compost. J. Hazard. Mater. 163, 563–567.

Liu, W.J., Jian, H., Yu, H-Q., 2015. Development of Biochar-Based Functional Materials: Toward a Sustainable Platform Carbon Material. *Chem. Rev.*, 115 (22), pp 12251–12285.

Li, X., Coles, B. J., Ramsey, M. H., Thornton, I., 1995. Sequential extraction of soils for multielement analysis by ICP-AES. Chem. Geol. 124(1-2): 109-123.

Liu, Y., Yang, M., Wu, Y.Wang, H., Chen, Y., Wu, W., 2011. Reducing CH_4 and CO_2 emissions from waterlogged paddy soil with biochar. J. Soils Sediments., 11: 930-939.

Liu, Y., Alessi, D.S., Owttrim, G.W., Petrash, D.A., Mloszewska, A.M., Lalonde, S.V., Martinez, R.E., Zhou, Q., Konhauser, K.O., 2015. Cell surface reactivity of Synechococcus sp. PCC 7002: Implications for metal sorption from seawater. Geochim. Cosmochim. Acta, 169: 30-44.

López-Granados, F., Jurado-Expósito, M., Atenciano, S., García-Ferrer, A., Sánchez de la Orden, M., García-Torres, L., 2002. Spatial variability of agricultural soil parameters in southern Spain. Plant Soil 246(1): 97-105.

Lund, T. J., Koretsky, C. M., Landry, C. J., Schaller, M. S., Das, S., 2008. Surface complexation modeling of Cu(II) adsorption on mixtures of hydrous ferric oxide and kaolinite. Geochem. Trans. 9: 9.

Ma, Q. Y., Traina, S. J, Logan, T. J., Ryan, J. A., 1994. Effects of aqueous Al, Cd, Cu, Fe(II), Ni, and Zn on Pb immobilization by hydroxyapatite. Environ. Sci. Technol., 28, 1219-1228.

Manceau, A. and Charlet, L., 1994. The mechanism of selenate adsorption on goethite and hydrous ferric oxide. Journal of Colloid and Interface Science, 168(1): 87-93.

Mandal, S., Sarkar, B., Bolan, N., Ok, Y.S., Naidu, R., 2017. Enhancement of chromate reduction in soils by surface modified biochar. J. Environ. Manag., 186 (2), 277–284.

Manning, B.A. and Goldberg, S., 1997. Adsorption and stability of arsenic (III) at the clay mineral-water interface. Environ. Sci. Technol., 31(7): 2005-2011.

Marmier, N., Delisée, A. and Fromage, F., 1999. Surface complexation modeling of Yb (III) and Cs (I) sorption on silica. J. Colloid Interface Sci., 212(2): 228-233.

Martell, A., Hancock, R., 1996. Metal complexes in aqueous solution. Modern Inorganic Chemistry, Plenum Press, New York.

Masiello, C.A., Chen, Y., Gao, X., Liu, S., Cheng, H-. Y., Bennett, M.R., Rudgers, J.A., Wagner, D.S., Zygourakis, K., Silberg, J.J., 2013. Biochar and microbial signaling: production conditions determine effects on microbial communication. Environ. Sci. Technol. 47(20): 11496-11503.

Mellah, A., Chegrouche, S., Barkat, M., 2006. The removal of uranium(VI) from aqueous solutions onto activated carbon: Kinetic and thermodynamic investigations. J. Colloid Interface Sci., 296, 434−441.

Mkandawire, M., 2013. Biogeochemical behaviour and bioremediation of uranium in waters of abandoned mines. Environ. Sci. and Pollu. Resear., 20(11): 7740-7767.

Mohan, D. and Pittman, C.U., 2006. Activated carbons and low cost adsorbents for remediation of tri-and hexavalent chromium from water. J. Hazard. Materials, 137(2): 762-811.

Mohan, D., Rajput, S., Singh, V.K., Steele, P.H. and Pittman, C.U., 2011. Modeling and evaluation of chromium remediation from water using low cost bio-char, a green adsorbent. J. Hazard. Materal.,188(1): 319-333.

Naghdi, M., Taheran, M., Pulicharla, R., Rouissi, T., Brar, S. K., Verma, M., Surampalli, R. Y., 2017. Pine-wood derived nanobiochar for removal of carbamazepine from aqueous media: Adsorption behavior and influential parameters. Arabian J. Chem.

Nambu, K., Yonebayashi, K., 1999. Acidic properties of dissolved organic matter leached from organic layers in temperate forests. Soil Sci. and Plant Nutrition 45(1): 65-77.

Nancollas, G.H., 1966. Interactions in Electrolyte Solutions. Elsevier, Amsterdam.

Nash, K.L., Rao, L.F. and Choppin, G. \R., 1995. Calorimetric and Laser Induced Fluorescence Investigation of the Complexation Geometry of Selected Europium-gem-Diphosphonate Complexes in Acidic Solutions. In. Chem., 34, 2753–2758.

Novak, J.M., Busscher, W.J., Laird, D.L., Ahmedna, M., Watts, D.W., Niandou, M.A.S., 2009. Impact of biochar amendment on fertility of a Southeastern Coastal Plain soil. Soil Sci. 174(2): 105-112.

Owlad, M., Aroua, M.K., Daud,W.A.W., Baroutian, S., 2009. Removal of hexavalent chromium-contaminated water and wastewater: a review. Water, Air, Soil Pollut. 200 (1-4), 59-77.

Pagnanelli, F., Bornoroni, L., Moscardini, E., Toro, L., 2006. Non-electrostatic surface complexation models for protons and lead(II) sorption onto single minerals and their mixture. Chemosphere 63:1063-1073.

Palmer, C. D.; Wittbrodt, P. R., 1991. Processes Affecting the Remediation of Chromium Contaminated Sites. Environ. Health Perspect. 92, 25-40.

Pan, Z., Giammar, D. E., Mehta, V., Troyer, L. D., Catalano, J. G., Wang, Z., 2016. Phosphate-induced Immobilization of Uranium in Hanford Sediments. Environ. Sci. Technol., 50 (24), 13486-13494.

Pan, Z., Li, W., Fortner, J.D., Giammer, D.E., 2017. Measurement and Surface Complexation Modeling of U(VI) Adsorption to Engineered Iron Oxide Nanoparticles. Environ. Sci. Technol., 51 (16), pp 9219–9226.

Park, D., Yun, Y. S., Ahn, C. K., & Park, J. M., 2007. Reduction of Hexavalent chromium with the brown seaweed Ecklonia biomass. Environ. Sci. Technol., 38(18), 4860-4864.

Pastorova, I., Botto, R. E., Arisz, P., Boon, J., 1994. Cellulose char structure - a combined analytical PY-GC-MS, FTIR, and NMR-study. Carbohydr. Res., 262(1), 27-47.

Patterson, R. R., Fendorf, S., Fendorf, M., 1997. Reduction of hexavalent chromium by amorphous iron sulfide. Environ. Sci. Technol., 31, 2039-2044.

Pearson, R. G., 1968a. Hard and soft acids and bases, HSAB, part I: Fundamental principles. J. Chem. Educ., 45 (9), 581-587.

Pearson, R. G., 1968b. Hard and soft acids and bases, HSAB, part II: Underlying theories. J. Chem. Educ., 45 (10), 643-648.

Peterson, M.L., White, A.F., Brown, G.E., Parks, G.A., 1997. Surface passivation of magnetite by reaction with aqueous Cr(VI): XAFS and TEM results. Environ. Sci. Technol. 31, 1573-1576.

Pettit, L., Powell, K., 2005. IUPAC Stability Constants Database (SCDatabase). Academic Software Data Version 4.82., Otley, UK: Academic Software).

Querol, X., Alastuey, A., Moreno, N., Alvarez-Ayuso, E., Garcia-Sanchez, A., Cama, J., Ayora, C., Simon, M., 2006. Immobilization of heavy metals in polluted soils by the addition of zeolitic material synthesized from coal fly ash. Chemosphere 62, 171–180.

Rajapaksha, A.U., Alam, M.S., Chen, N., Alessi, D.S., Igalavithana, A.D., Tsang D.C.W., Ok, Y.S., 2018. Removal of hexavalent chromium in aqueous solutions using biochar: Chemical and spectroscopic investigations. Sci. Total. Environ., 625:1567-1573.

Rai, D., Sass, B. M., Moore, D. A., 2002. Chromium(III) hydrolysis constants and solubility of chromium(III) hydroxide. Inorg. Chem. 1987, 26 (3), 345-349.Rao, L., Jiang, J., Zanonato, P., Bernardo, P.D. Complexation of uranium(VI) with acetate at variable temperatures. Radiochim. Acta, 90, 581.

Rancourt, D.G., Ping, J.Y., 1991. Voigt-based methods for arbitrary-shape static hyperfine parameter distributions in Mössbauer spectroscopy. Nuclear Instruments and Methods in Physics Research., B58, 85-97.

Rao, L., Garnov, A.Y, Rai, D., Xia, Y, Moore, R.C., 2004. Protonation and complexation of isosaccharinic acid with U(VI) and Fe(III) in acidic solutions: potentiometric and calorimetric studies. Radiochim. Acta, 92, 575.

Ravel, A. and Newville, M., 2005. ATHENA, ARTEMIS, HEPHAESTUS: data analysis for X-ray absorption spectroscopy using IFEFFIT. J. Synchrotron Radiation, 12(4): 537-541.

Reeder, R.J., Schoonen, M.A.A. and Lanziro tti, A., 2006: Metal speciation and its role in bioaccessibility and bioavailability. In Medical Mineralogy and Geochemistry (N. Sahai & M.A.A. Schoonen, eds.). Rev. Mineral. Geochem. 64, 59-113.

Ren, X., Wang, S., Yang, S., Li, J., 2010. Influence of contact time, pH, soil humic/fulvic acids, ionic strength and temperature on sorption of U(VI) onto MX-80 bentonite. J. Radioanal. Nucl. Chem., 283 (1), 253−259.

Rees, F., Simonnot, M. O., Morel, J. L., 2014. Short-term effects of biochar on soil heavy metal mobility are controlled by intra-particle diffusion and soil pH increase. Euro. J. Soil Sci. 65: 149-161.

Ressler T., 1997. WinXAS: A new software package not only for the analysis of energy-dispersive XAS data. J. de Physique IV., 7(C2): 269-270.

Rihs, S. Gaillard, C., Reich, T., Kohler, S., 2014. Uranyl sorption onto brinssite: A surface complexation modeling and EXAFS study. Chem. Geo., 373, 59-70.

Robertson G.P., Sollins P., Ellis B.G., Lajtha K., 1999. Exchangeable ions, pH and cation exchange capacity. In: Robertson G.P., Coleman D.C., Bledsoe C.S. and Sollins P. (eds), Standard Soil Methods for Long-Term Ecological Research. LTER, New York, NY, USA.

Rogers, Nathan D., 2016. Chromium Oxidation by Disinfectants and Oxidants Used in Drinking Water Treatment. All Graduate Theses and Dissertations. Paper 5028. UthaState University

Römkens, P. F.A. M., Plette, A.C.C., Verstappen, G.G.C., 2002. Contribution of agriculture to the heavy metal loads of Dutch surface waters. In: Agricultural Effects on Ground and Surface Waters: Research on the Edge of Science and Society, J. H. A. M. Steenvoorden, F. Claessen, J. Willems, Eds. IAHS, Walligford, UK, publ. 273, pp. 337-342.

Sass, B.M.; Rai, D., 1987. Solubility of amorphous chromium(III)- iron(III) hydroxide solid solutions. Inorg. Chem., 26 (14), 2228-2232.

Scheidegger, A.M., Lamble, G.M. Sparks, D.L., 1996. Investigations of Ni sorption on pyrophyllite: An XAFS study. Environ. Sci. Technol., 30, 548−554.

Scheidegger, A.M., Lamble, G.M., Sparks, D.L., 1997. Spectroscopic evidence for the formation of mixed-cation hydroxide phases upon metal sorption on clays and aluminum oxides. J. Colloid Interface Sci. , 186, 118-128.

Schroeder, D.C., Lee, G.F., 1975. Potential transformations of chromium in natural waters. Water, Air, Soil Pollut. 1975, 4, 355-365.

Schroth, B. K., Sposito, G., 1997. Surface charge properties of clays. Clays Clay Miner. 45: 85-91.

Shahata, M.M., 2016. Adsorption of some heavy metal ions by used different immobilized substances on silica gel. Arabian J. of Chem., 9(6), 755-763.

Sherman, D.M., Peacock, C. L., Hubbard C.G., 2008. Surface complexation of U(VI) on goethite (a-FeOOH). Geochim. Cosmochim. Acta, 72:298–310.

Shevchenko, N.; Zaitsev, V.; Walcarius, A., 2008. Bifunctionalized mesoporous silicas for Cr(VI) reduction and concomitant Cr(III) immobilization. Environ. Sci. Technol. 42 (18), 6922-6928.

Smith, D.S., Kramer, J.R., 1999. Multi-site proton interactions with natural organic matter. Environ. Int. 25(2-3): 307-314.

Sparks, D.L., 2005. Toxic metals in the environment: the role of surfaces. Elements, 1(4): 193-197.

Spokas, K.A., 2010. Review of the stability of biochar in soils: predictability of O: C molar ratios. Carbon Manage., 1(2): 289-303.

Stipp S.L., Parks G.A., Nordstrom D.K., Leckie J.O., 1993. Solubility-product constant and thermodynamic properties for synthetic otavite, $CdCO_3$(s), and aqueous association constants for the Cd(II)-CO_2-H_2O system. Geochim. Cosmochim. Act., 57: 2699–2713.

Stubbs, J. E., Elbert, D. C., Veblen, D. R., Zhu, C., 2006. Electron microbeam investigation of uranium-contaminated soils from Oak Ridge, TN, USA. Environ. Sci. Technol., 40 (7), 2108−2113.

Su, H., Fang, Z., Tsang, P.E., Zheng, L., Cheng, W., Fang, J., Zhao., D., 2016. Remediation of hexavalent chromium contaminated soil by biochar-supported zero-valent iron nanoparticles, J. Hazard. Mater., 318, 533–540.

Sun, Y.B., Li, J.X., Wang, X.K., 2014. The retention of uranium and europium onto sepiolite investigated by macroscopic, spectroscopic and modeling techniques. Geochim. Cosmochim. Acta., 140, 621−643.

Sun, Y. B., Yang, S. B., Chen, Y., Ding, C. C., Cheng, W. C., Wang, X.K., 2015. Adsorption and desorption of U(VI) on functionalized graphene oxides: a combined experimental and theoretical study. Environ. Sci. Technol., 49, 4255−4262.

Sun, Y. B., Wu, Z. Y., Wang, X. X., Ding, C. C., Cheng, W. C., Yu, S. H., Wang, X. K., 2016. Macroscopic and microscopic investigation of U(VI) and Eu(III) adsorption on carbonaceous nanofibers. Environ. Sci. Technol., 50, 4459-4467.

Sylwester, E.R., Hudson, E.A., Allen, P.G., 2000. The structure of uranium (VI) sorption complexes on silica, alumina, and montmorillonite. Geochim. Cosmochim. Acta, 64, 2431−2438.

Tack, F. and Verloo, M.G., 1995. Chemical speciation and fractionation in soil and sediment heavy metal analysis: a review. International J. Environ. Anal. Chem., 59(2-4): 225-238.

Tan, X., Hu, J., Montavon, G. and Wang, X., 2011. Sorption speciation of nickel (II) onto Ca-montmorillonite: Batch, EXAFS techniques and modeling. Dalton Transactions, 40(41): 10953-10960.

Teixidó, M., Hurtado, C., Pignatello, J. J., Beltrán, J. L., Granados, M., Peccia, J., 2013. Predicting contaminant adsorption in black carbon (biochar)-amended soil for the veterinary antimicrobial sulfamethazine. Environ. Sci. Technol., 47 (12), 6197−6205.

Tessier, A., Campbell, P.G., Bisson, M., 1979. Sequential extraction procedure for the speciation of particulate trace metals. Anal. Chem. 51(7): 844-851.

Thomas, S.C., and Gale, N., 2015. Biochar and forest restoration: a review and meta-analysis of tree growth responses. New Forest. 6(6), 601-614.

Thompson, K.A., Shimabuku, K.K., Kearns, J.,P, Knappe, D.R.U., Summer, S., and Cook, S.M., 2016. Environmental Comparison of Biochar and Activated Carbon for Tertiary Wastewater Treatment. Environ. Sci. Technol., 50, 11253-11262.

Turkarslan et al., 2017. Mechanism for microbial population collapse in a fluctuating resource environment. Mol. System. Bio., 13, 919.

Uchimiya, M., Bannon, D.I. and Wartelle, L.H., 2012. Retention of heavy metals by carboxyl functional groups of biochars in small arms range soil. J. Agricul. Food Chem., 60(7): 1798-1809.

Van Leeuwen, H.P., Town, R.M., Buffle, J., Cleven, R.F., Davison, W., Puy, J., Van Riemsdijk, W.H. and Sigg, L., 2005. Dynamic speciation analysis and bioavailability of metals in aquatic systems. Environ. Sci. Technol., 39(22): 8545-8556.

Van Zwieten, L., Kimber, S., Morris, S., Chan, K. Y., Downie, A., Rust, J., Joseph, S., Cowie, A. 2010. Effects of biochar from slow pyrolysis of papermill waste on agronomic performance and soil fertility. Plant Soil, 327(1): 235-246.

Venkateswarlu, S., Lee, D., Yoon, M., 2016. Bioinspired 2D-Carbon Flakes and Fe_3O_4 Nanoparticles Composite for Arsenite Removal. ACS Appl. Mater. Interfaces, 8, 23876-23885.

Verheijen, F.G.A., Graber, E.R., Ameloot, N., Bastos, A. C., Sohi, S., Knicker, H., 2014. Biochars in soils: new insights and emerging research needs. Eur. J. Soil Sci. 65(1): 22-27.

Viollier, E., Inglett, P.W., Hunter, K., Roychoudhury, A.N., Van Cappellen, P., 2000.The ferrozine method revisted: Fe(II)/Fe(III) determination in natural waters. Appl Geochem., 15: 785-790.

Vithanage, M., Rajapaksha, A.U., Ahmad, M., Uchimiya, M., Dou, X., Alessi, D.S. and Ok, Y.S., 2015. Mechanisms of antimony adsorption onto soybean stover-derived biochar in aqueous solutions. J. Environ. Management, 151: 443-449.

von Gunten, K., Alam, M.S., Hubmann, M., Ok, Y.S., Konhauser, K.O., Alessi, D.S., 2017. Modified sequential extraction for biochar and petroleum coke: Metal release potential and its environmental implications. Bioresour. Technol. 236: 106-110.

Waite, T. D., Davis, J. A., Payne, T. E., Waychunas, G. A., Xu, N., 1994. Uranium(VI) adsorption to ferrihydrite: Application of a surface complexation model. Geochim. Cosmochim. Act., 58 (24), 5465−5478.

Wang, T., Zhang, L., Li, C., Yang, W., Song, T., Tang, C., Meng, Y., Dai, S., Wang, H., Chai, L., Luo, J., 2015. Synthesis of Core Shell Magnetic Fe_3O_4@poly(m-Phenylenediamine) Particles for Chromium Reduction and Adsorption. Environ. Sci. Technol., 49, 5654-5662.

Welch, A.H., Lico, M.S., 1998. Factors controlling As and U in shallow grounwater, southern Carson Desert, Nevada. Appl. Geochem., 13(4): 521-539.

Westall, J. C., 1982. FITEQL, a computer program for determination of chemical equilibrium constants from experimental data, Version 2.0. Department of Chemistry, Oregon State University, Corvallis, OR. Report 82-02.

Woolf, D., Amonette, J.E., Street-Perrott, F.A., Lehmann, J., Joseph, S., 2010. Sustainable biochar to mitigate global climate change. Nature Communication, 1: 56.

Xia K., Bleam W., and Helmke P. A., 1997a. Studies of the nature of binding sites of first row transition elements bound to aquatic and soil humic substances using X-ray absorption spectroscopy. Geochim. Cosmochim. Act., 61, 2223-2235.

Xiao, X. and Chen, B. 2017. A Direct Observation of the Fine Aromatic Clusters and Molecular Structures of Biochars. Environ. Sci. Technol., 51, 5473-5482.

Xu, S., Adhikari, D., Huang, R., Zhang, H., Tang, Y., Roden, E., Yang, Y., 2016. Biochar facilitated microbial reduction of hematite. Environ. Sci. Technol., 50, 2389-2395.

Yan, Y., Toghiani, H., Cai, Z., Zhang, J. 2014. Formation of nanocarbon spheres by thermal treatment of woody char from fast pyrolysis process. Wood Fiber Sci. 464(4): 437-450.

Yang, F., Zhao, L., Gao, B., Xu, X.Y., Cao, X.D., 2016. The interfacial behavior between biochar and soil minerals and its effect on biochar stability. Environ. Sci. Technol., 50, 2264e2271.

Yao, Y., Gao, B., Wu, F., Zhang, C., Yang, L., 2015. Engineered Biochar from Biofuel Residue: Characterization and Its Silver Removal Potential. ACS Appl. Mater. Interfaces., 7, 10634-10640.

Yasuda, M., Yamaskik, K., Ohtaki, H. 1960. Stability of complexes of several carboxylic acids formed with bivalent metals. Bull. Chem. Sot. Japan., 33, 1067-1070

Yu, L., Yuan, Y., Tang, J., Wang, Y., Zhou, S., 2015. Biochar as an electron shuttle for reductive dechlorination of pentachlorophenol by Geobacter sulfurreducens. Sci. Rep. 5, 16221.

Yuan, P., Fan, M., Yang, D., He, H., Liu, D., Yuan, A., Zhu, J., Chen, T., 2009. Montmorillonite supported magnetite nanoparticles for the removal of hexavalent chromium [Cr (VI)] from aqueous solutions. J. Hazard. Mater., 166, 821-882.

Yuan, Y., Bolan, N., Prévoteau, A., Vithanage, M., Biswas, J.K., Ok, Y.S., Wang, H., 2017. Applications of biochar in redox-mediated reactions. Bioresour. Technol., 246, 271–281.

Zachara, J. M., Smith, S. C., Resch, C. T., Cowan, C. E. 1992. Cadmium sorption to soil separates containing layer silicates and iron and aluminum oxides. Soil Sci. Soc. Am. J. 56: 1074-1084.

Zaitseva, N., Zaitsev, V., Walcarius, A. 2013. Chromium (VI) removal via reduction-sorption on bi-functional silica adsorbents. J. Hazard. Mater., 250, 454-461.

Zeng, H., Singh, A., Basak, S., Ulrich, K. U., Sahu, M., Biswas, P., Catalano, J. G., Giammar, D. E., 2009. Nanoscale size effects on uranium (VI) adsorption to hematite. Environ. Sci. Technol., 43, 1373-1378.

Zhang, Q-. Z., Dijkstra, F. A., Liu, X-. R., Wang, Y-. D., Huang, J., Lu, N. 2014. Effects of Biochar on Soil Microbial Biomass after Four Years of Consecutive Application in the North China Plain. PLoS One 9(7): e102062.

Zhang, Y., Luo, W., 2014. Adsorptive removal of heavy metal from acidic wastewater with biochar produced from anaerobically digested residues: Kinetics and surface complexation modeling. BioResources., 9(2): 2484-2499.

Zhang, Z., Cao, X., Liang, P., Liu, Y., 2013. Adsorption of uranium from aqueous solution using biochar produced by hydrothermal carbonization. J. Radioanal. Nucl. Chem., 295:1201–1208.

Zhao, J., Dong, Y., Xie, X., Li, X., Zhang, X., Shen, X., 2011. Effect of annual variation on available soil nutrients in pear orchards. Acta Ecol. Sin. 31(4): 212-216.

Zheng, Z., Tokunaga, T. T., Wan, J. 2003. Influence of calcium carbonate on U(VI) sorption to soils. Environ. Sci. Technol., 37, 5603-5608.

Zhitkovich, A., 2011. Chromium in drinking water: Sources, metabolism, and cancer risks. Chem. Res. Toxicol. 24 (10), 1617-1629.

Zhou, B., Wang, Z., Shen, D., Shen, F., Wu, C., Xiao, R., 2017. Low cost earthworm manure-derived carbon material for the adsorption of Cu^{2+} from aqueous solution: Impact of pyrolysis temperature. Ecologi. Eng., 98: 189-195.

APPENDIX A. SUPPLEMENTARY INFORMATION FOR CHAPTER 2

SUPPORTING METHODS AND MATERIALS

Chemicals and Reagents

18.2 MΩ water was used for the preparation of stock solutions and for all experiments. Hydrochloric acid (HCl), sodium hydroxide (NaOH), sodium nitrate ($NaNO_3$), nickel (II) nitrate hexahydrate ($Ni(NO_3)_2.6H_2O$), nickel acetate ($Ni(CH_3CO_2)_2.2H_2O$), zinc chloride ($ZnCl_2$), zinc acetate ($Zn(O_2CCH_3)_2$) and 4-(2-hydroxyethyl)-1-piperazineethanesulfonic acid (HEPES) were all of ACS grade and purchased from Fisher Scientific, Canada.

Biochar Characterization

Proximate analysis and X-ray diffraction (XRD)

The proximate analyses were carried out as described in Alam et al. (2016). The moisture contents of biochar samples were estimated using the difference between pre- and post-drying weight of samples after drying at 60°C for 24 h in a drying oven (ThermoScientific HERATHERM) (Ahmad, et al., 2012; Alam et al., 2016). Mobile matter or volatile matter were considered to be the non-carbonized portion of biochar. They were determined by measuring the weight loss after heating samples to 450°C for 30 min using a Thermolyne 62700 furnace (Ahmad, et al., 2012). Ash contents were estimated by weight loss after heating at 700°C for an additional 30 min. The fixed matter or residual matter of each biochar was calculated as the remnant portion of the biomass after deducting the total weight loss of moisture, ash and mobile matter steps. All measurements were conducted in duplicate.

Powder X-ray diffraction (XRD) was conducted on each biochar to identify major crystalline phases in the materials, as described in Alam et al. (2018a). The materials were crushed to a fine powder using a mortar and pestle, and analyzed using an X-ray diffractometer

(Rikagu Ultima IV) with a cobalt source, between a 2θ range of 5° to 90°. The resulting diffraction patterns were fit using the JADE 9.5 analysis package (KS Analytical Systems).

Elemental composition and surface area

Elemental compositions, including C, N, H, S, and O, were determined using a Carlo Erba EA1108 Elemental Analyzer combusted at 1000°C (Alam et al., 2016).

The specific surface area, pore volume and pore size distribution of each biochar were measured according to the Brunauer - Emmet - Teller (BET) and the Barret - Joyner - Halender (BJH) methods, on an Autosorb Quantachrome 1MP instrument. Samples were initially outgassed at 300°C for 3 h and then analyzed using 7 BET points, and 20 adsorption and desorption points. The specific surface areas were determined from N_2 adsorption isotherms, and pore size distributions were determined from N_2 desorption isotherms (Alam et al., 2016).

Morphological analysis

The surface morphologies of biochar samples were characterized using a Zeiss EVO MA 15 LaB_6 filament scanning electron microscope (SEM). The magnifications ranged from 20× to 20K×, with a resolution of approximately 100 nm to obtain high resolution images. An Everhart-Thornley detector was used to obtain secondary electron images, and a Si diode detector was used to collect backscattered images. Semi-quantitative elemental compositions were determined using a Peltier-cooled 10 mm^2 Bruker Quantax 200 Silicon drift detector X-ray spectroscopy (EDS) with a 123 eV resolution.

Fourier transform infrared spectroscopy (FT-IR) measurements were carried out to measure changes in the infrared vibrational bands of five biochar studied using Thermo Nicolet 8700 FT-IR. FT-IR was also carried out on each biochar after metal sorption. The samples were diluted with KBr at a 3% sample to 97% KBr ratio. Spectra were collected at a resolution of 4

cm^{-1} with 32 successive scans, and data were collected in a wavenumber range of 400–4000 cm^{-1} resolution of 4 cm^{-1} from 32 successive scans. The data was based line corrected and normalized as described at Alam et al. (2016).

Potentiometric titration

Titrations were performed in dynamic titration mode with a minimum dose of 0.5 µL and maximum of 0.15 mL for each addition while achieving an electrode stability of 0.2 mV/s between additions. In this method, the titrator adds smaller volumes of titrant when samples are more sensitive to pH changes. The average equilibration time between additions was ~20 s, and the pH was recorded after each step. The reverse titration started immediately after pH ~11 was achieved. These reverse 'down-pH' titrations from 11 to 3 were carried out to investigate the reversibility of proton binding to the biochar, and to ensure that the biochar surface chemistry was not physically altered during the titration process. Blank titrations (without biochar) for the 0.01 M $NaNO_3$ electrolyte solution were also carried out to account for the proton buffering capacity of the electrolyte solution itself.

The potentiometric titration data were used to determine the acidity constant (pK_a) values and concentrations of proton active functional groups of each biochar. To model the potentiometric titration data, a non-electrostatic surface complexation model was employed. Initially a linear programming approach, as implemented in MATLAB (Lalonde et al., 2008a and 2008b; Lalonde et al., 2010), was used to subtract the excess charge of the blank electrolyte titrations from the samples. A least-squares optimization routine, as implemented in FITEQL 4.0 (Herbelin and Westall, 1996), was employed to model a predetermined number of ligands, acidity constants (pK_a, or –log Ka), and ligand densities that best describe the excess charge data. Three-site models were found to adequately describe the titration data. In each titration step, the charge balance was calculated using the following equation:

$$[C_a - C_b] = [-Q] + [H^+] - [OH^-] \quad (1)$$

where $[C_a - C_b]$ is the concentration of acid added subtracted by the concentration of base added; [-Q] is the negative charge excess owing to deprotonation biochar ligands in solution, normalized to per gram of biomass; $[H^+]$ and $[OH^-]$ are concentrations of proton and hydroxyl ions, respectively; the brackets represent molar species concentrations (Lalonde et al., 2008a and 2008b; Lalonde et al., 2010).

Metal leaching from biochars

To investigate the metal leaching potentials of WS, WPC, and SSBC at 300°C, 500°C and 700°C, biochars were placed in polypropylene tubes containing 10 mL 0.01 M $NaNO_3$ electrolyte solution at 10 g L^{-1} solids. Solution pH was set to ~6.5, a pH where Ni and Zn sorption was maximum. The test tubes were sealed and put in shaker for 24 hours. The resulting supernatants were filtered through 0.45 µm nylon membranes (Millex HP) and analyzed using inductively coupled plasma - mass spectroscopy (ICP-MS/MS).

Ni (II) and Zn (II) adsorption and data modeling

To determine the equilibrium time for the metal adsorption experiments, 10 g L^{-1} biochar was mixed with 100 mL 0.01 M $NaNO_3$ electrolyte solution and then spiked with Ni and Zn to achieve 170 µM Ni and 170 µM Zn, respectively. The experiments were run at pH 6.5, held constant by adding 0.1 M HEPES buffer set to the target pH. Samples were collected at a range of time starting from 30 minutes to 6 days (i.e., 0.5 hrs, 2 hrs; 4hrs; 16 hrs; 24 hrs; 48 hrs; 72 hrs; 96 hrs and 144 hrs).

To determine stability constants for Ni and Zn to biochar functional groups, a least-squares optimization routine, as implemented in FITEQL 4.0 (Herbelin and Westall, 1996), was employed. Ni and Zn-ligand stability constants were calculated using the following equation:

$$K_{M^{++}} = \frac{[R-AM^{+}]a_{H^{+}}}{[R-AH^{0}]a_{M^{++}}} \quad (2)$$

where [R-A^{-}] represents the concentration of biochar surface functional group A that is complexed with divalent metal, M^{++}, which is either Ni (II) or Zn(II); and $a_{M^{++}}$ is the activity M^{++} of in solution after equilibrium is attained. To solve for the log K_{M}^{++} values for individual-metal complexes on a particular biochar, the acidity constants and sites concentrations modelled from potentiometric titration data for that biochar were used. The constants derived from individual-metal complexes were then taken to make predictions for systems containing biochar and both Ni and Zn, across a wide range of metal to sorbent ratios and pH. Six aqueous Ni hydrolysis reactions and 6 aqueous Zn hydrolysis reactions (Table A.S2.5) were included in the system of equations for modeling log K (Baes and Mesmer, 1976; Stipp et al., 1993).

The Ni and Zn stability constants for constant capacity model (CCM) were defined as:

$$K_{M^{++}} = \frac{[R-AM^{+}]m_{H^{+}} \cdot \gamma_{H^{+}\cdot}}{[R-AH^{0}]m_{M^{++}} \cdot \gamma_{M^{++}}} \exp(-F\psi/RT) \quad (3)$$

where exp(-$F\psi/RT$) is the electrostatic term, F the Faraday constant (C/mol), ψ the surface potential (V), R the molar gas constant (C/mol/K), T the absolute temperature (K), m is the molal concentration of the aqueous species, and γ is the corresponding activity coefficient calculated using the Davies equation (Davis, 1938; Davis and Kent, 1990).

Titration Calorimetry

Obtaining heats associated with metal-adsorption reactions onto the biochar with the *i*th addition of titrant (Q_i^{corr}) requires a background correction to subtract heats associated with the

reactions intrinsic to the titration process. Background heats (Q_i^{bkg}) were measured by titrating the same Ni-bearing or Zn-bearing solution into solution of 0.01 M $NaNO_3$ adjusted to match the pH of experiments. Background heats were then subtracted from the experimentally measured heat (Q_i^{exp}) associated with a given titrant addition. Corrected heats of metal adsorption (Q_i^{corr}) are related to the site-specific enthalpies of adsorption (ΔH_{HLy}) by Equation 4, where $\delta n_{HLy}{}^i$ is the change in the number of moles of the protonated sites and $\delta n_{MLy}{}^i$ is the change in the number of moles of surface-complexed metal ions caused by the *i*th addition of titrant.

$$\sum Q_i^{corr} = \sum \Delta H_{ML_y} \times \sum \delta n_{ML_y}^i - \sum \Delta H_{HL_y} \times \sum \delta n_{HL_y}^i \quad (4)$$

The δn^i values (a function of pH, K_y, site concentrations, metal concentration, and volume) and the site-specific enthalpies of protonation and metal adsorption determine the total heat produced with each addition of metal. We used pH and volume of metal solution added as independent variables to calculate δn^i values, and to subsequently derive site-specific enthalpies through optimization by minimizing the sum-of-squares difference between the measured experimental heats (Q_i^{corr}) and the model-derived heats (Q_i^{calc}). Uncertainties in model parameters are given at the 1σ confidence level, and are calculated from the inverse covariance matrix of a given fit.

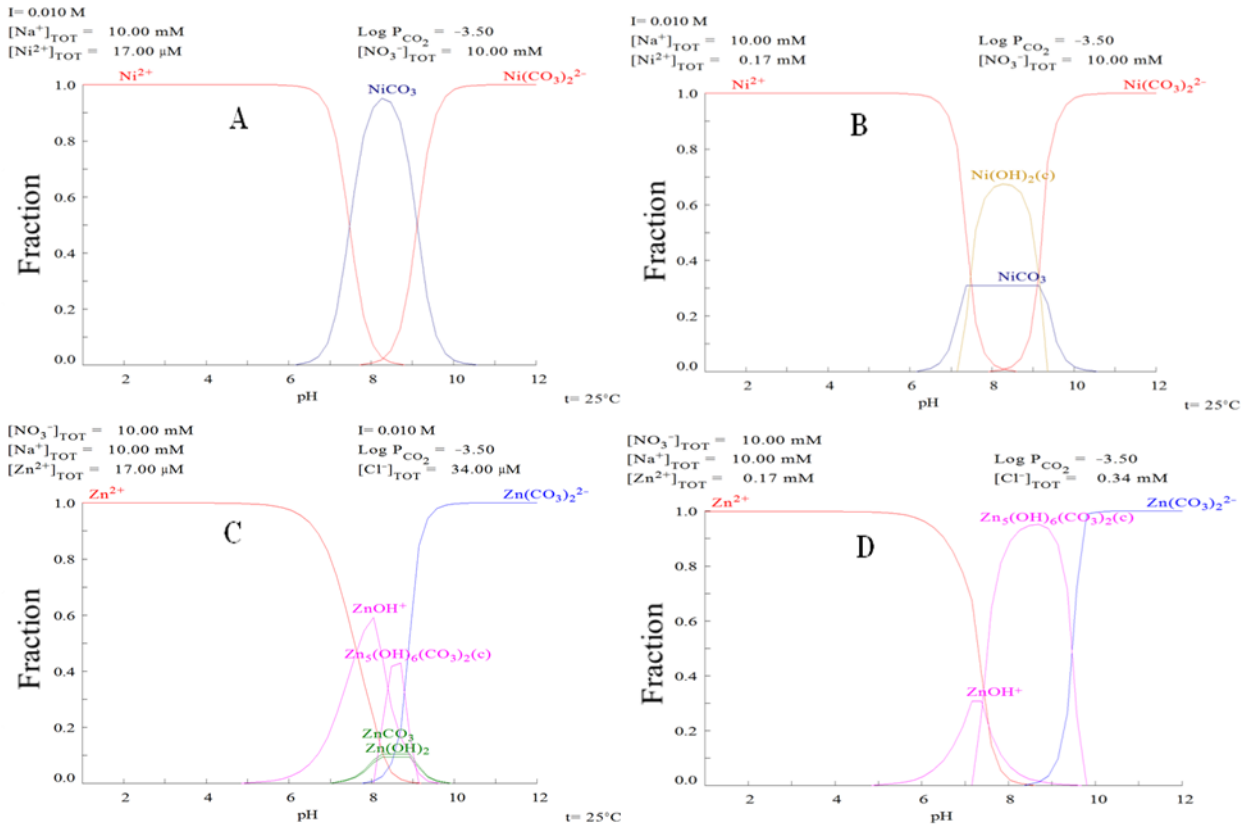

Figure A.S2.1. Ni and Zn aqueous speciation diagrams in background electrolyte solutions before adsorption as a function of pH: (A) 1.7×10^{-5} M Ni^{2+} in 0.01 M $NaNO_3$; (B) 1.7×10^{-4} M Ni^{2+} in 0.01 M $NaNO_3$; (C) 1.7×10^{-5} M Zn^{2+} in 0.01 M $NaNO_3$; and (D) 1.7×10^{-4} M Zn^{2+} in 0.01 M $NaNO_3$. Diagrams were made using Chemical Equilibrium Diagrams Hydra and Medusa (Ingri et al., 1968; Eriksson, 1979).

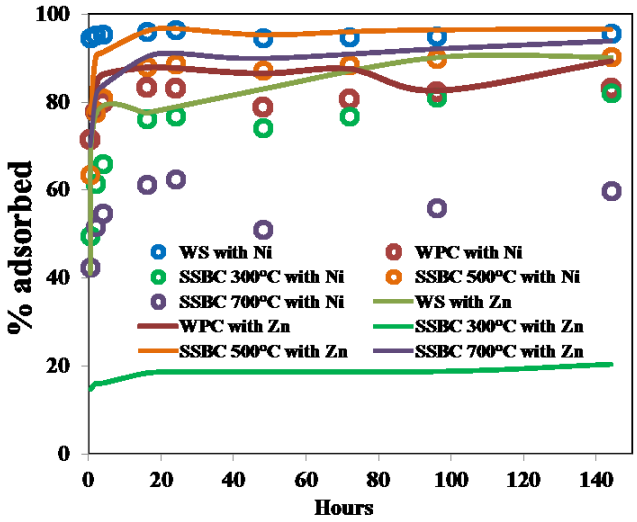

Figure A.S2.2. Adsorption kinetics of Ni(II) and Zn(II) onto each biochar.

Table A.S2.1. Percentage of moisture contents, mobile matter, ash content and fixed matter of WS, WPC, SSBC 300°C, SSBC 500°C and SSBC 700°C.

Sample	Yield (%)	Moisture content (%)	Mobile matter (%)	Ash content (%)	Residual or Fixed matter (%)
WS[1]	30 to 33	2.7	33	17	47.3
WPC[3]	30	1.5	88	3.7	6.8
SSBC 300°C	70.1	1.1	19.8	56.6	22.5
SSBC 500°C	53.8	0.7	7.5	71.9	20
SSBC 700°C	50.3	0.6	4.1	76.6	16.6

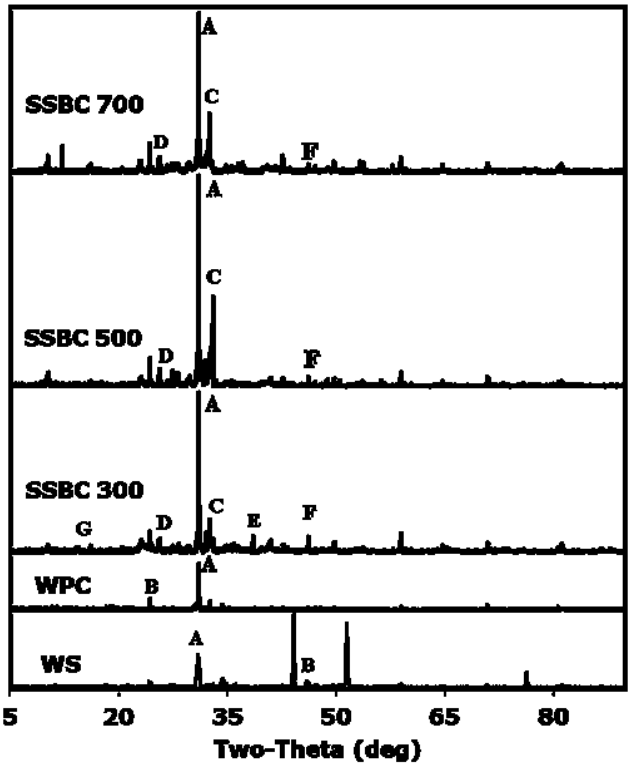

Figure A.S2.3. XRD patterns of WS; WPC; SSBC at 300°C; SSBC at 500°C and SSBC at 700°C. A. Quartz; B. Calcite; C. Albite; D. Muscovite; E. Pyrite; F. Microcline and G. Kaolinite.

Table A.S2.2. pH, elemental composition, molar ratio, BET surface area, and pore volume of WS, WPC, SSBC 300°C, SSBC 500°C and SSBC 700°C.

Properties			**Biochar**		
	WS[a]	WPC[b]	SSBC at 300°C	SSBC at 500°C	SSBC at 700°C
%C	69.7	84.6	30.7	21.4	22.1
%H	2.6	2.1	3.1	1.1	0.5
%O	8.7	9.4	11.1	9.1	7.1
%N	0.8	0.2	4.1	2.8	1.7
%S	0.07	-	0.7	0.4	0.4
Molar H/C	0.4	0.3	1.2	0.6	0.3
Molar O/C	0.09	0.08	0.27	0.32	0.24
Surface area m^2/g	26.6	224	4.5	26.2	54.8
Pore volume cc/Å/g	0.004	0.06	0.01	0.04	0.05

a. Alam et al. (2016)
b. Alam et al. (2018a)

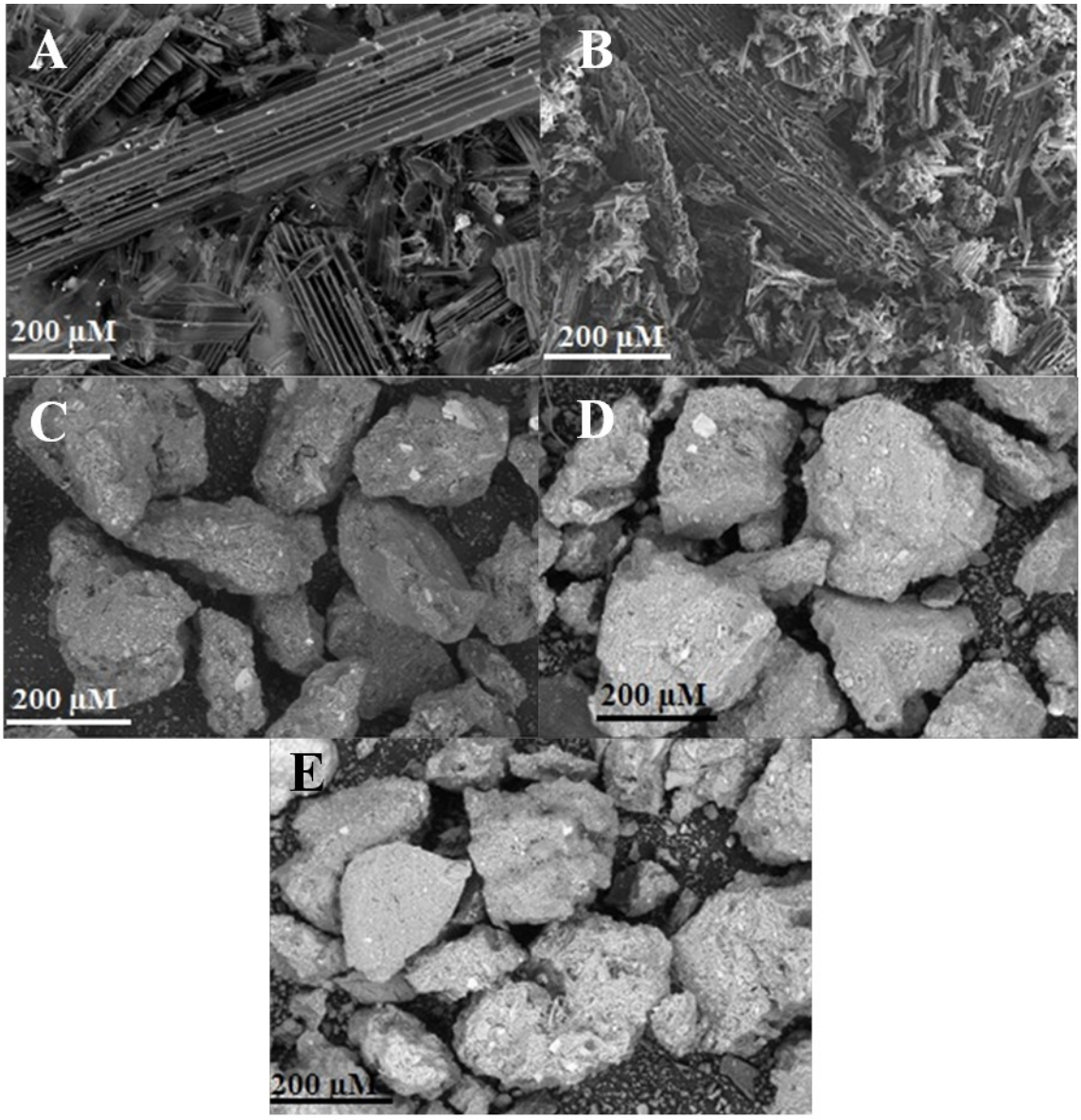

Figure A.S2.4. SEM images of: (A) WS; (B) WPC; (C) SSBC at 300°C; (D) SSBC at 500°C; and (E) SSBC at 700°C.

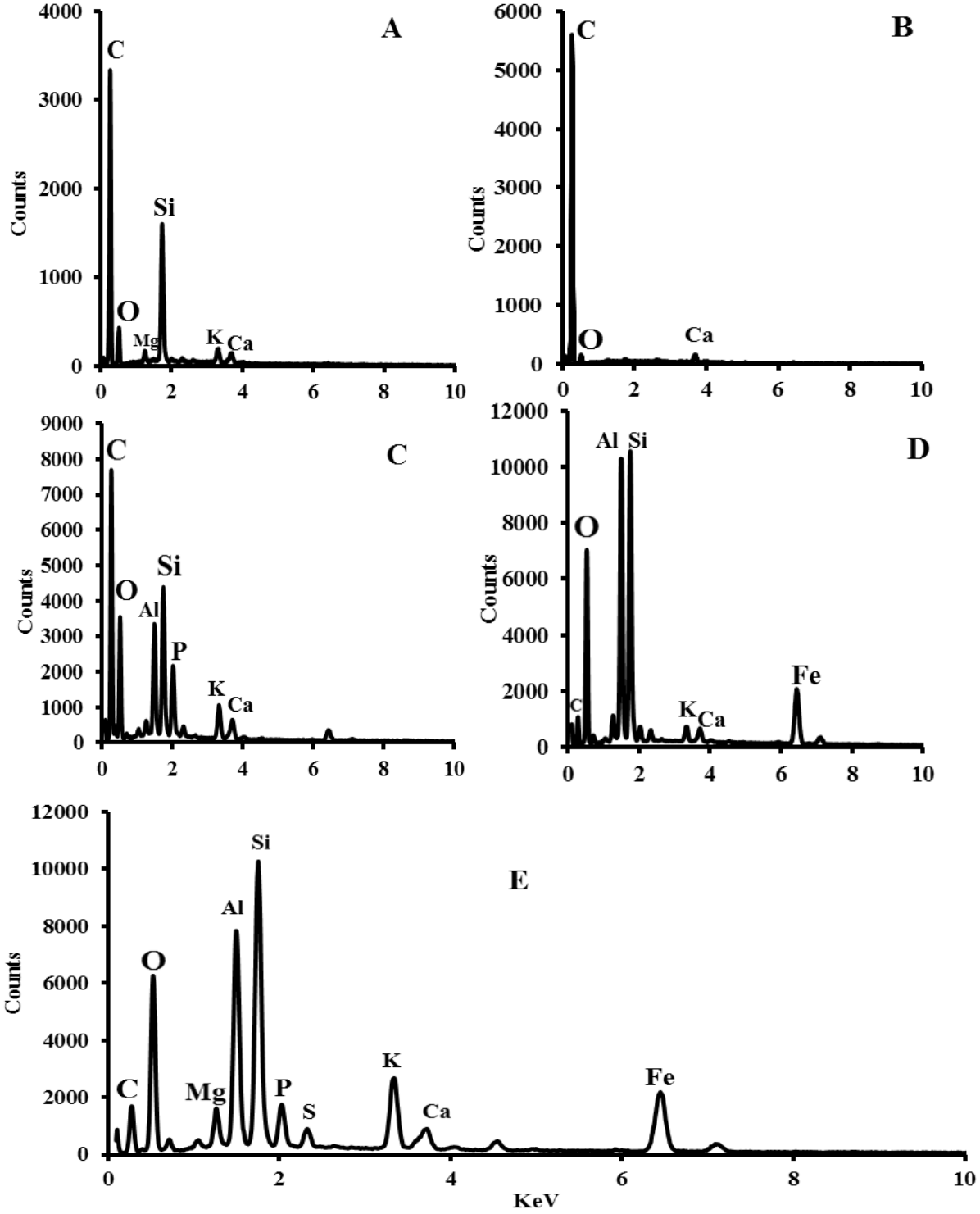

Figure A.S2.5. EDS spectra of: (A) WS; (B) WPC; (C) SSBC at 300°C; (D) SSBC at 500°C; and (E) SSBC at 700°.

Table A.S2.3. Elemental composition estimated from SEM-EDS analysis: (A) WS; (B) WPC; (C) SSBC at 300°C; (D) SSBC at 500°C; and (E) SSBC at 700°C.

A.

El	AN	Series	unn. C [wt.%]	norm. C [wt.%]	Atom. C [at.%]	Error (1 Sigma) [wt.%]
C	6	K-series	56.24	69.08	78.37	7.33
O	8	K-series	15.43	18.95	16.14	2.69
Si	14	K-series	6.42	7.88	3.82	0.31
K	19	K-series	1.08	1.32	0.46	0.07
Ca	20	K-series	1.00	1.23	0.42	0.07
Mg	12	K-series	0.72	0.88	0.49	0.08
P	15	K-series	0.17	0.21	0.09	0.04
S	16	K-series	0.17	0.21	0.09	0.04
Al	13	K-series	0.11	0.13	0.07	0.04
Cl	17	K-series	0.09	0.11	0.04	0.03
		Total:	81.41	100.00	100.00	

B.

El	AN	Series	unn. C [wt.%]	norm. C [wt.%]	Atom. C [at.%]	Error (1 Sigma) [wt.%]
C	6	K-series	88.24	88.24	91.84	10.36
O	8	K-series	9.53	9.53	7.45	1.95
Ca	20	K-series	1.57	1.57	0.49	0.08
Cl	17	K-series	0.25	0.25	0.09	0.04
Fe	26	K-series	0.22	0.22	0.05	0.04
Si	14	K-series	0.18	0.18	0.08	0.04
		Total:	100.00	100.00	100.00	

C.

El	AN	Series	unn. C [wt.%]	norm. C [wt.%]	Atom. C [at.%]	Error (1 Sigma) [wt.%]
C	6	K-series	49.65	50.16	61.68	6.17
O	8	K-series	33.24	33.58	31.00	4.32
Si	14	K-series	3.73	3.77	1.98	0.19
Al	13	K-series	3.25	3.28	1.79	0.19
Ca	20	K-series	2.81	2.84	1.04	0.11
P	15	K-series	1.53	1.55	0.74	0.09
Fe	26	K-series	2.15	2.17	0.57	0.09
K	19	K-series	1.03	1.04	0.39	0.06
S	16	K-series	0.52	0.53	0.24	0.05
Na	11	K-series	0.32	0.32	0.21	0.05
Mg	12	K-series	0.29	0.29	0.18	0.04
Cl	17	K-series	0.21	0.21	0.09	0.04
Ti	22	K-series	0.26	0.26	0.08	0.04
		Total:	98.98	100.00	100.00	

D.

El	AN	Series	unn. C [wt.%]	norm. C [wt.%]	Atom. C [at.%]	Error (1 Sigma) [wt.%]
O	8	K-series	40.39	44.22	51.76	4.98
C	6	K-series	13.85	15.16	23.64	2.35
Al	13	K-series	13.57	14.85	10.31	0.69
Si	14	K-series	11.30	12.37	8.25	0.52
Fe	26	K-series	7.20	7.88	2.64	0.22
Mg	12	K-series	1.42	1.55	1.20	0.11
P	15	K-series	0.82	0.90	0.54	0.06
K	19	K-series	0.93	1.02	0.49	0.06
Ca	20	K-series	0.94	1.03	0.48	0.06
Na	11	K-series	0.39	0.43	0.35	0.06
S	16	K-series	0.54	0.59	0.35	0.05
		Total:	91.34	100.00	100.00	

E.

El	AN	Series	unn. C [wt.%]	norm. C [wt.%]	Atom. C [at.%]	Error (1 Sigma) [wt.%]
O	8	K-series	40.62	41.03	46.93	4.94
C	6	K-series	20.23	20.44	31.14	2.96
Al	13	K-series	9.45	9.55	6.47	0.49
Si	14	K-series	9.39	9.49	6.18	0.44
Fe	26	K-series	6.87	6.94	2.27	0.21
K	19	K-series	4.25	4.29	2.01	0.16
Mg	12	K-series	2.06	2.08	1.57	0.15
P	15	K-series	2.00	2.02	1.19	0.11
Ca	20	K-series	1.58	1.59	0.73	0.07
Na	11	K-series	0.85	0.85	0.68	0.09
S	16	K-series	0.82	0.83	0.47	0.06
Ti	22	K-series	0.82	0.83	0.32	0.05
Cl	17	K-series	0.06	0.06	0.03	0.03
		Total:	98.99	100.00	100.00	

El = Element; AN = Atomic number; Unn. C = Unnormalized carbon; norm. C = Normalized carbon

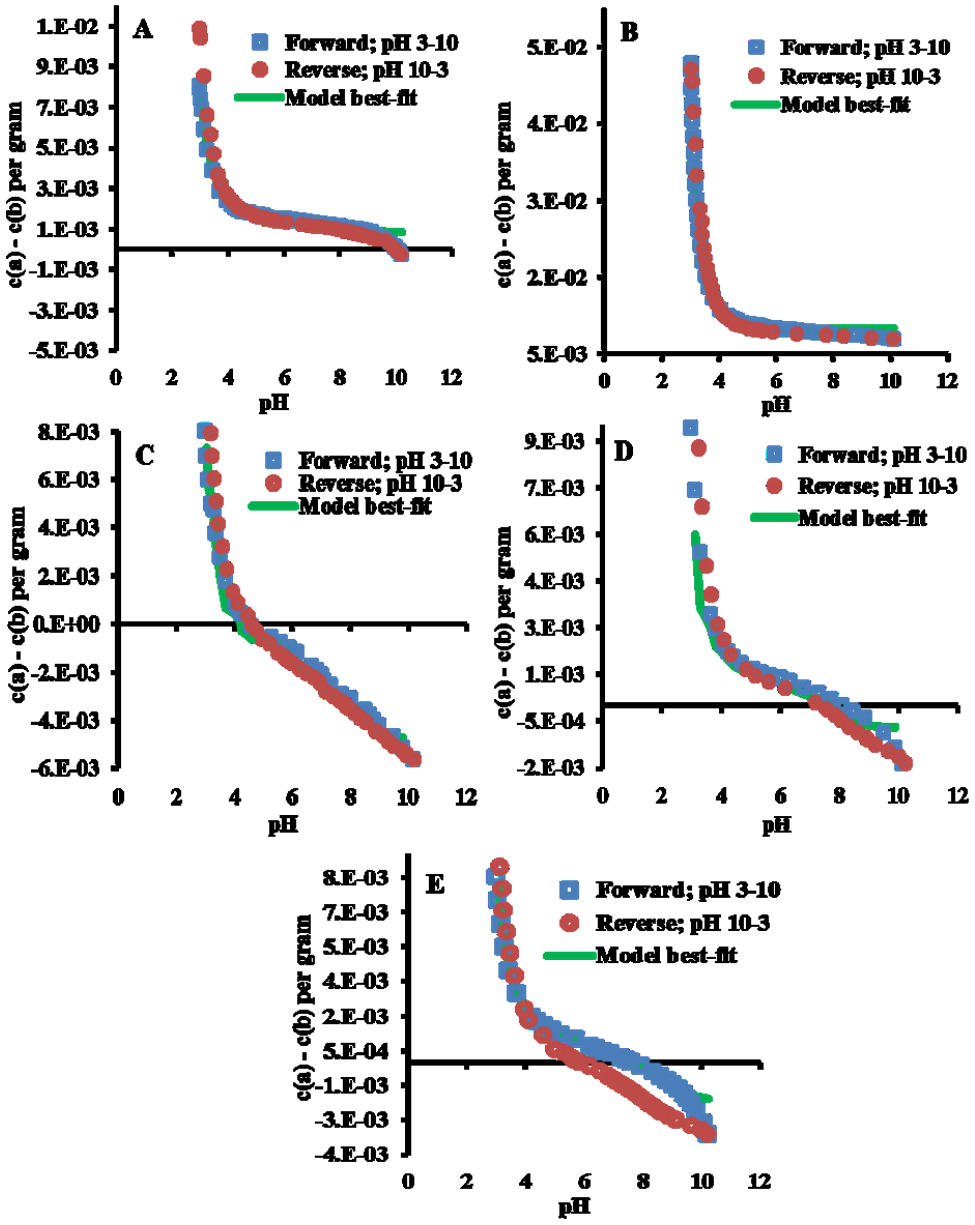

Figure A.S2.6. Potentiometric titration data for: (A) WS; (B) WPC; (C) SSBC at 300°C; (D) SSBC at 500°C; and (E) SSBC at 700°C.

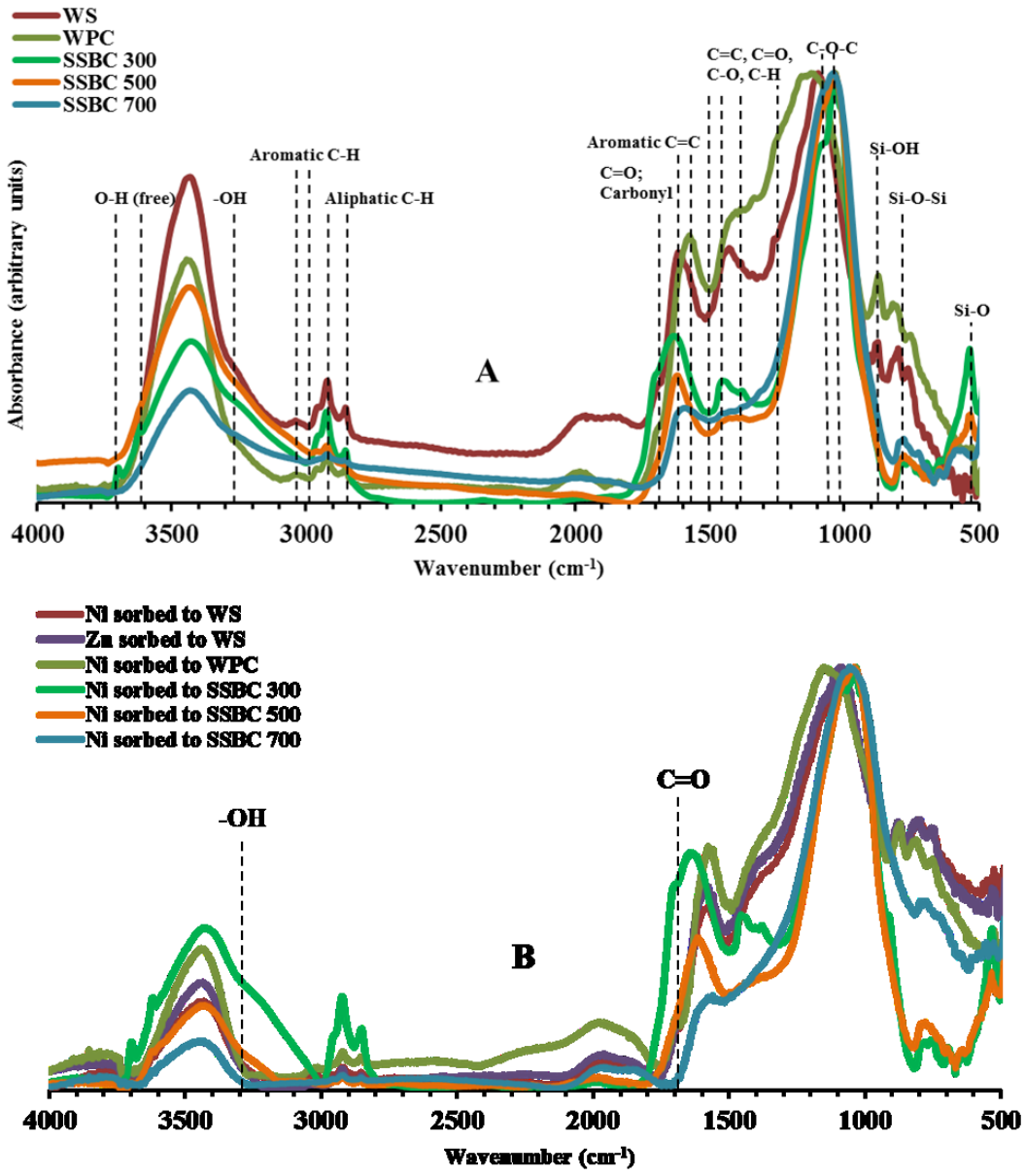

Figure A.S2.7: FTIR spectra of five biochars. (A) before metal sorption; and (B) after metal sorption.

Table A.S2.4. Leaching of Ni and Zn from WS, WPC, SSBC 300°C, SSBC 500°C and SSBC 700°C.

Biochar	Ni (ppm)	Zn (ppm)
WS	0.004213	0.01184
WPC	0.013399	0.275089
SSBC 300°C	0.007412	0.144867
SSBC 500°C	0.007365	0.031824
SSBC 700°C	0.005487	0.02112

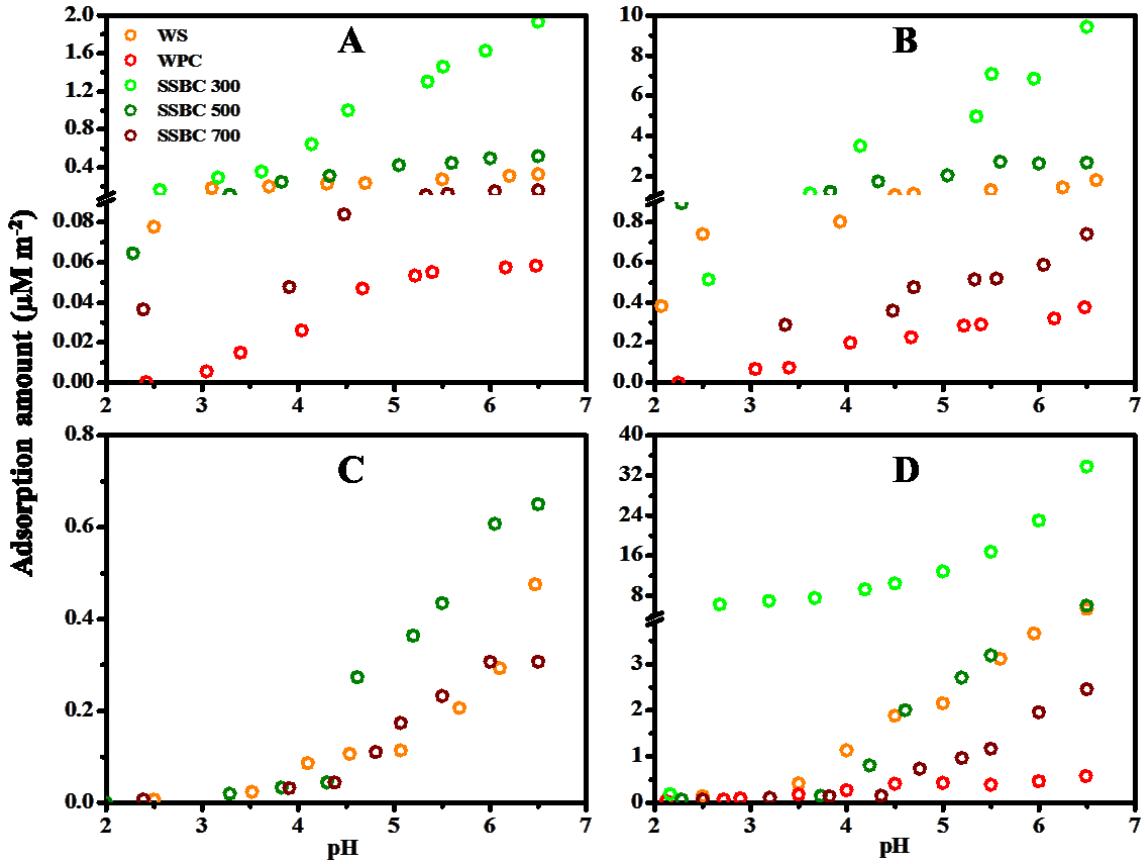

Figure A.S2.8. Surface area normalized adsorption densities of Ni and Zn onto WS, WPC, SSBC 300°C, SSBC 500°C and SSBC 700°C. (A) 17 μM Ni; (B) 170 μM Ni; (C) 17 μM Zn; and (D) 170 μM Zn.

Table A.S2.5. EXAFS fit results for the Ni adsorbed to wheat straw biochar system.

	Ni 17μM			Ni 85μM			Ni 170μM		
Path	CN	R(Å)	σ^2(Å^2)	CN	R(Å)	σ^2(Å^2)	CN	R(Å)	σ^2(Å^2)
Ni-O	6.0[1]	2.08	0.0017	6.0[1]	1.97	0.0016[1]	6.0[1]	2.04	0.0017[1]
Ni-O	-	-	-	4.0	2.65	0.0017[3]	3.5	2.71	0.0017[3]
Ni-C	2[2]	3.41	0.0016[3]	1.2	3.29	0.0016[2]	6.7	3.31	0.0016[2]
Ni-O	-	-	-	1.1	3.32	0.0017[2]	0.9	3.44	0.0017[3]
Ni-Si	2[2]	3.32	0.0026	6.6	3.30	0.0027[2]	4.9	3.33	0.0028

Table A.S2.6. EXAFS fit results for the Zn adsorbed to wheat straw biochar system.

	Zn 17μM			Zn 85μM			Zn 170μM		
Path	CN	R(Å)	σ^2(Å^2)	CN	R(Å)	σ^2(Å^2)	CN	R(Å)	σ^2(Å^2)
Zn-O	3.1	1.97	0.0049[1]	2.6	1.97	0.0055	3.8[1]	1.97[1]	0.0049[1]
Zn-C	0.5	2.0	0.0049[1]	2.0	2.08	0.0085	1.9	2.16	0.0100[2]
Zn-O	2.4	2.9	0.0058	2.1	2.90	0.0055[1]	2.5	2.9	0.0049[3]
Zn Si	2.4	3.0	0.0100[2]	1.6	2.99	0.0079	1.7	2.98[1]	0.0049[1]

1. Fixed to crystallography data
2. High limit of fitting constraint
3. Low limit of fitting constraint

Table A.S2.7. Aqueous Ni (II) and Zn (II) hydrolysis reactions and thermodynamic stability constants.

Reaction	log K
$Ni^{2+} + H_2O = NiOH^+ + H^+$	-9.86
$Ni^{2+} + 2H_2O = Ni(OH)_2(aq) + 2H^+$	-19
$Ni^{2+} + 3H_2O = Ni(OH)_3^- + 3H^+$	-30
$Ni^{2+} + 4H_2O = Ni(OH)_4^{2-} + 4H^+$	-44
$2Ni^{2+} + H_2O = Ni_2(OH)^{3+} + H^+$	-10.7
$4Ni^{2+} + 4H_2O = Ni_4(OH)_4^{4+} + 4H^+$	-27.74
$Zn^{2+} + H_2O = ZnOH^+ + H^+$	-8.96
$Zn^{2+} + 2H_2O = Zn(OH)_2(aq) + 2H^+$	-16.9
$Zn^{2+} + 3H_2O = Zn(OH)_3^- + 3H^+$	-28.4
$Zn^{2+} + 4H_2O = Zn(OH)_4^{2-} + 4H^+$	-41.2
$2Zn^{2+} + H_2O = Zn_2(OH)^{3+} + H^+$	-9.0
$2Zn^{2+} + 6H_2O = Zn_2(OH)_6^{2-}$	-57.8
$CO_2 + H_2O = H_2CO_3$	-1.46
$H_2CO_3 = H^+ + HCO_3^-$	-6.36
$HCO_3^- = CO_3^{2-} + H^+$	-10.33

Ni and Zn hydrolysis reactions and logK values were taken from Baes and Mesmer (1976); logK values of carbonic acids were taken from Stipp et al. (1993).

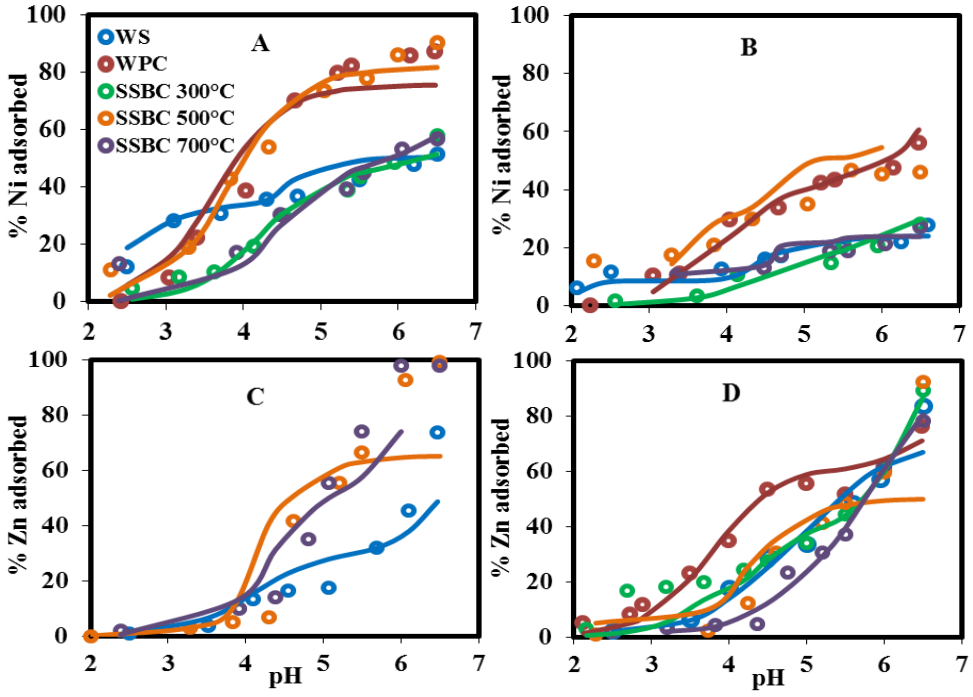

Figure A.S2.9. Adsorption of Ni and Zn onto WS, WPC, SSBC 300°C, SSBC 500°C and SSBC 700°C with 1-site best-fit models. (A) 17 µM Ni; (B) 170 µM Ni; (C) 17 µM Zn; and (D) 170 µM Zn. Open symbols represent experimental data and solid lines represent best-fit models.

Table A.S2.8. Stability constant obtained from 1-site best-fit models of Ni and Zn adsorption to WS, WPC, SSBC 300°C, SSBC 500°C and SSBC 700°C.

Biochar	Ni 17 µM log K	V(Y)	Ni 170 µM log K	V(Y)	Zn 17 µM log K	V(Y)	Zn 170 µM log K	V(Y)
WS	2.64	3.6	2.24	12	2.34	3.0	2.044	40
WPC	3.13	1.7	2.53	25	NA	NA	5.63	18
SSBC at 300°C	2.50	0.3	2.0	10	NA	NA	2.5	7
SSBC at 500°C	2.84	0.7	2.14	18	2.44	15	2.14	240
SSBC at 700°C	2.70	0.9	2.20	12	2.80	7	2.80	90

*NA = not available

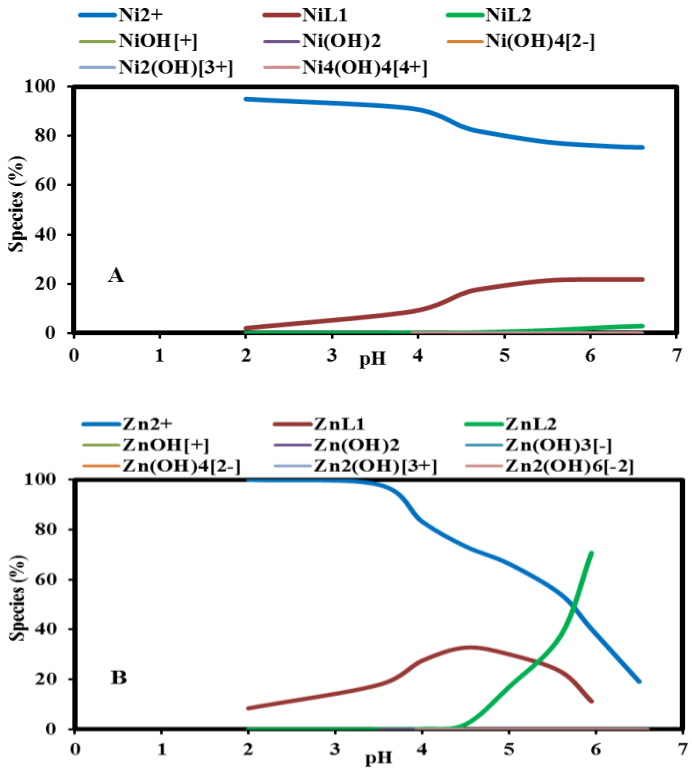

Figure A.S2.10. Ni and Zn speciation distribution after adsorption by WS as a function of pH, as predicted from non-electrostatic surface complexation models: (A) 170 µM Ni with a 2-site model fit; and (B) 170 µM Zn with a 2-site model fit.

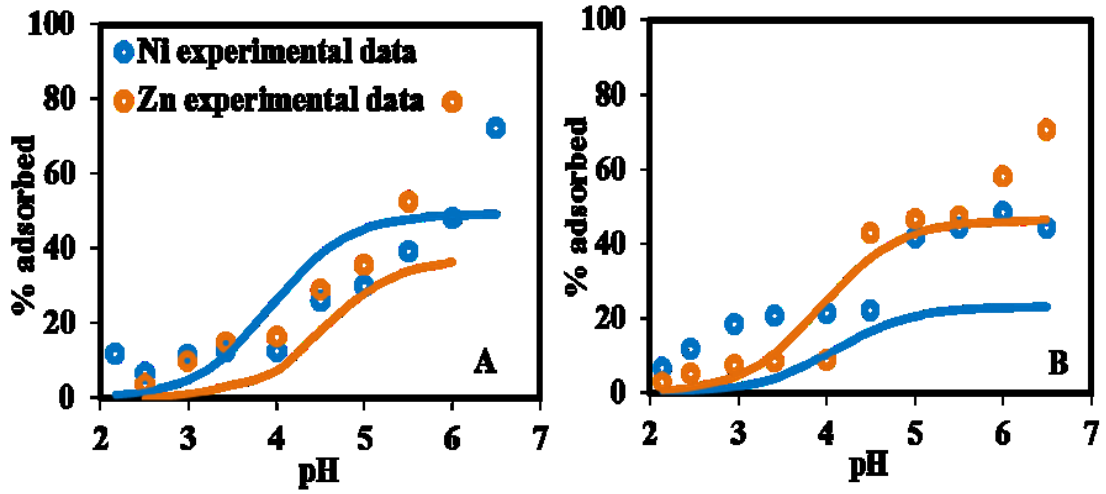

Figure A.S2.11. Competitive adsorption of Ni and Zn onto WS with 1-site best-fit models. (A) 8.5 µM Ni +8.5 µM Zn; and (B) 85 µM Ni + 85 µM Zn. Open symbols represent experimental data and solid lines represent best-fit models.

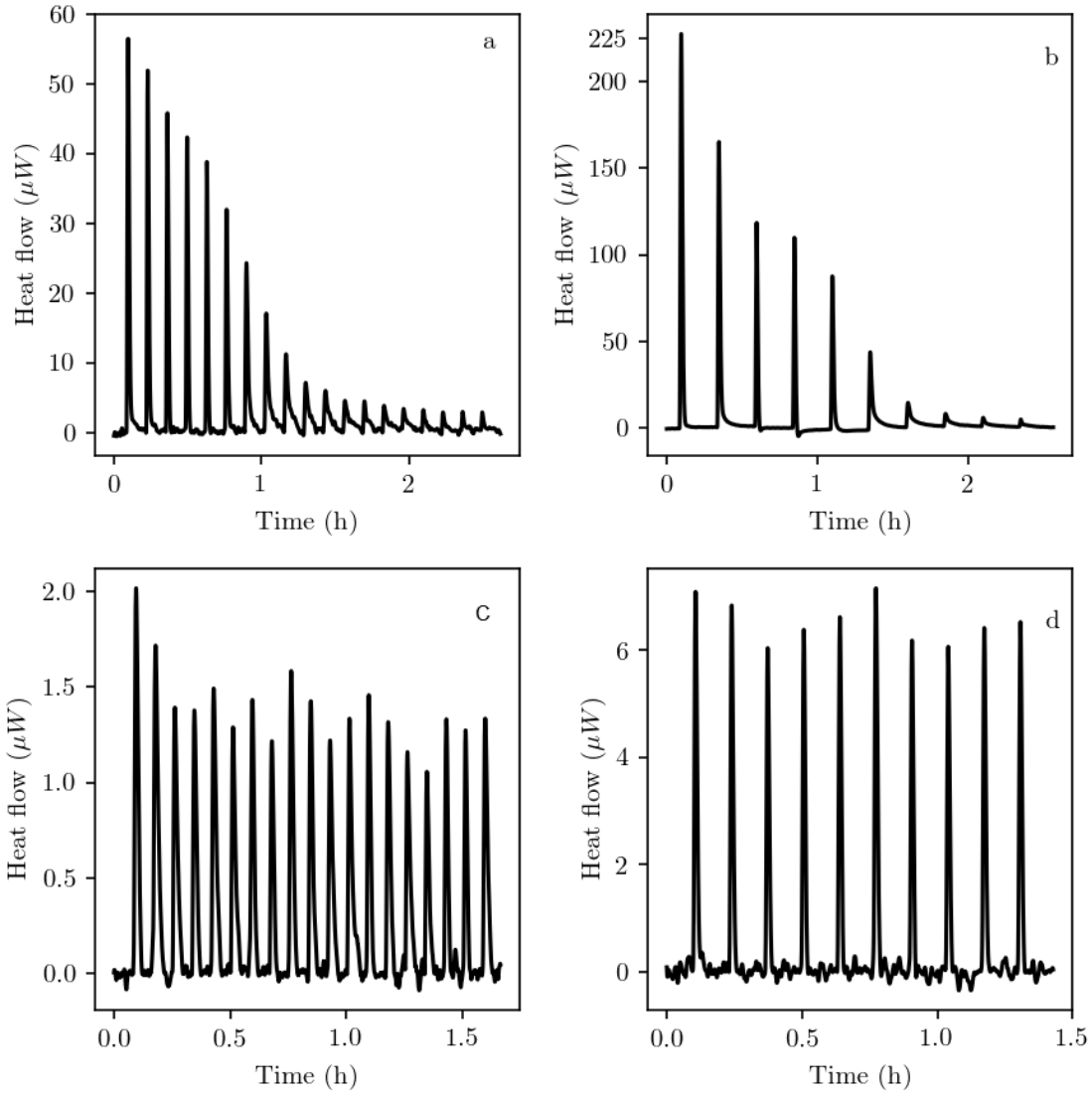

Figure A.S2.12. Heat flow curves for acid titrations with 0.1 M HNO_3: (a) WPC with 2 µL injections; (b) WS with 5 µL; (c) Background heats with 2 µL injections and (d) Background heats with 5 µL injections.

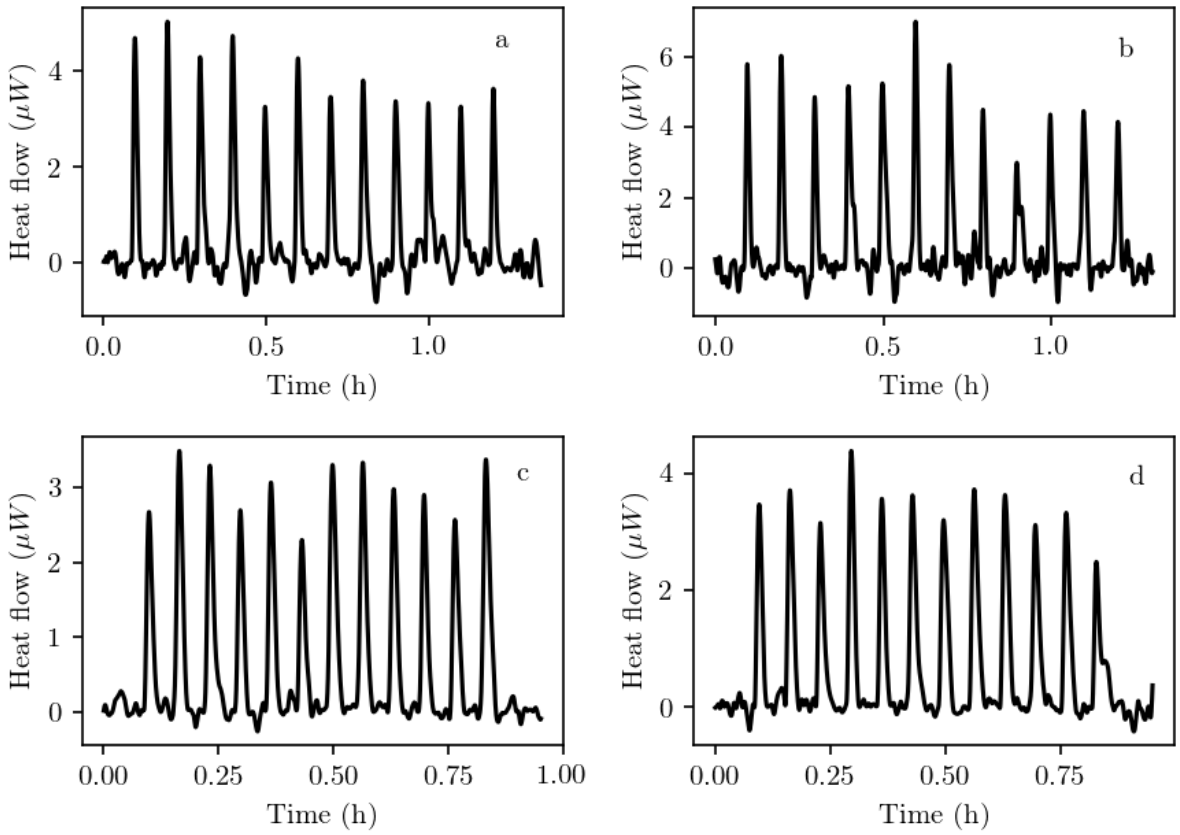

Figure A.S2.13. Heat flow curves of WS titrations with Ni(II) at pH 4.5 (a) and 6.3 (b) and with Zn(II) at pH 4.3 (c) and pH 5.0 (d).

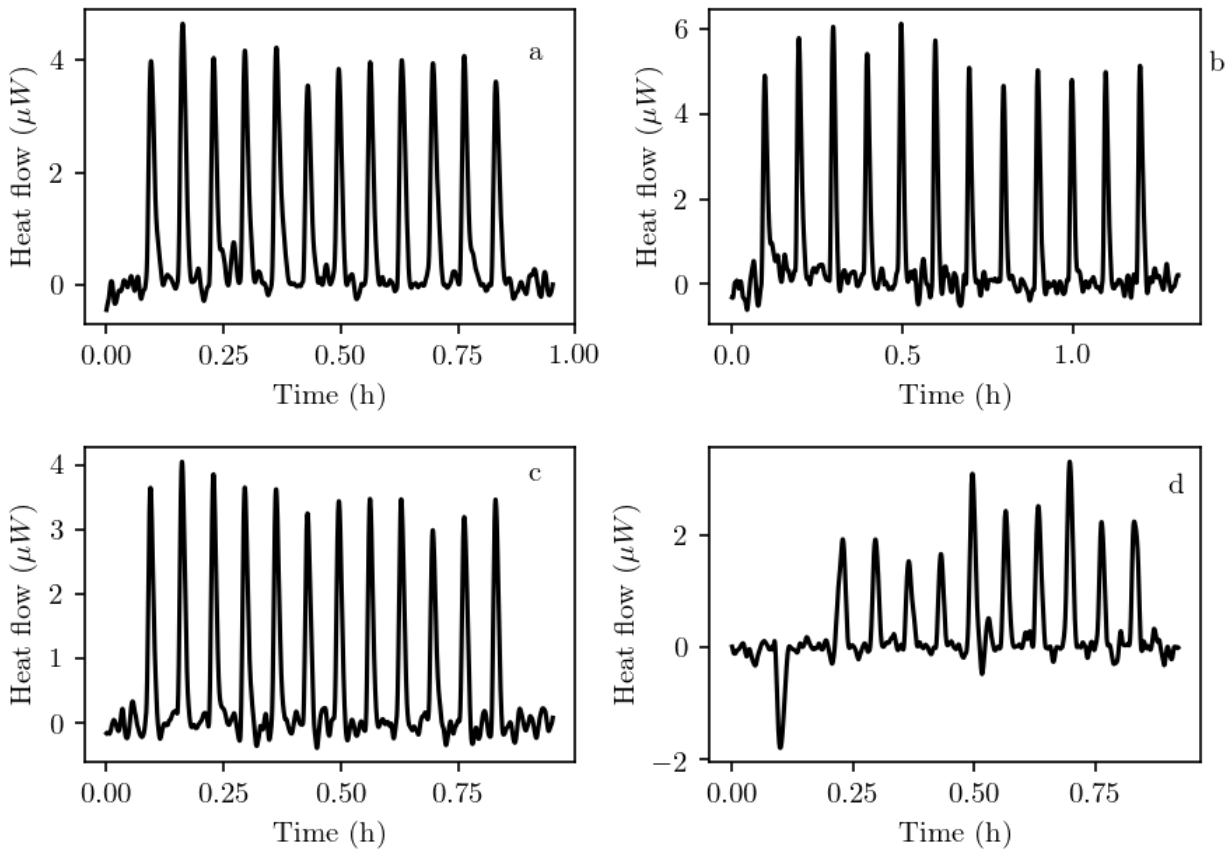

Figure A.S2.14. Heat flow curves of WPC titrations with Ni(II) at pH 4.3 (a) and 5.8 (b) and with Zn(II) at pH 4.3 (c) and pH 5.8 (d).

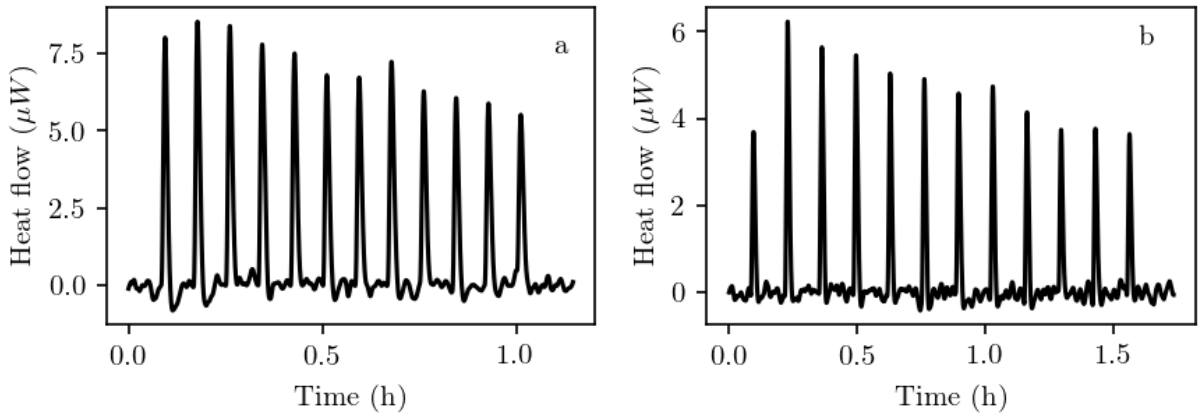

Figure A.S2.15. Heat flow curves of background heats for Zn(II) (a) and Ni(II) (b).

Table A.S2.9. Site-specific thermodynamic parameters for the adsorption of Ni derived from calorimetric titrations and the 2-site metal adsorption model.

Species	logK	Gibbs free energy, $\Delta G_r°$ (KJ/mol)	Enthalpy, $\Delta H_r°$ (KJ/mol)	$-T\Delta S_r°$ (KJ/mol)	Entropy, $\Delta S_r°$ (J/molK)
		WS			
L_1Ni^+	2.24(0.05)	-12.79(0.31)	0.81(0.14)	-13.59(0.34)	46(1)
L_2Ni^+	2.22(0.26)	-12.67(1.50)	-18.79(0.23)	6.12(1.52)	-21(5)
χ^2	6.812e-07				
		WPC			
L_1Ni^+	2.53(0.02)	-14.44(0.13)	3.01(0.08)	-17.45(0.15)	59(1)
L_2Ni^+	1.88(0.17)	-10.73(0.95)	-70.76(0.75)	60.03(1.21)	-201(4)
χ^2	3.922e-07				

Table A.S2.10. Site-specific thermodynamic parameters for the adsorption of Zn derived from calorimetric titrations and the 2-site metal adsorption model.

Species	logK	Gibbs free energy, $\Delta G_r°$ (KJ/mol)	Enthalpy, $\Delta H_r°$ (KJ/mol)	$-T\Delta S_r°$ (KJ/mol)	Entropy, $\Delta S_r°$ (J/molK)
		WS			
L_1Zn^+	2.44(0.12)	-13.93(0.69)	-0.39(0.40)	-13.53(0.80)	45(3)
L_2Zn^+	2.82(0.17)	-16.10(0.99)	46.32(8.62)	-62.42(8.68)	209(29)
χ^2	1.17e-06				
		WPC			
L_1Zn^+	2.83(0.02)	-16.15(0.13)	3.25(0.40)	-19.40(0.42)	65 (1)
L_2Zn^+	2.38(0.17)	-13.59(0.97)	10.79(2.00)	-24.38(2.22)	82(7)
χ^2	4.257e-07				

APPENDIX B. SUPPLEMENTARY INFORMATION FOR CHAPTER 3

SUPPORTING METHODS AND MATERIALS

Chemicals and Reagents

To prepare stock solutions and for all experiments, 18.2 MΩ water was used. The chemical used in this study are: hydrochloric acid (HCl), sodium hydroxide (NaOH), sodium nitrate ($NaNO_3$), calcium chloride hexahydrate ($CaCl_2$. $6H_2O$) and uranyl nitrate ($UO_2(NO_3)_2$). All were of ACS grade or higher, and purchased from Fisher Scientific, Canada.

Biochar Characterization

Morphological analysis and X-ray diffraction (XRD)

The surface morphologies of WS and WPC were characterized using a Zeiss EVO MA 15 LaB_6 filament scanning electron microscope (SEM) at magnifications between 20× to 20,000×, and the resolution was approximately 100 nm. Secondary electron images were collected using an Everhart-Thornley detector and backscattered images were collected by Si diode detector. A Peltier-cooled 10 mm^2 Bruker Quantax 200 Silicon drift detector X-ray spectroscopy (EDS) with a 123 eV resolution was used to collect semi-quantitative elemental compositions (Alam et al., 2016; Alam et al., 2018a).

To identify the major crystalline phases in WS and WPC, samples were analyzed by powder X-ray diffraction (XRD). An X-ray diffractometer (Rikagu Ultima IV) with a cobalt source collected data between a 2θ range of 5° to 90° was used to analyze the samples, and the JADE 9.5 analysis package (KS Analytical Systems) was used to fit the resulting diffraction patterns (Alam et al., 2016; Alam et al., 2018a).

Zeta potentials measurement

Zeta potential was obtained using a Malvern Instrument Zetasizer Nano ZS equipped with a 633 nm laser (Westborough, Massachusetts, USA) and measured in 173˚ backscatter mode at different pH, in which the Smoluchowski equation was used to determine the zeta potential value (Hunter, 1981).

Fourier transforms infrared spectroscopy (FT-IR)

FT-IR measurements for WS and WPC were carried out using a Thermo Nicolet 8700 FT-IR to measure the infrared vibrational bands in WS and WPC. FTIR was also carried with WS and WPC after U(VI) adsorption to identify the changes in infrared vibrational bands. Thirty-two successive scans were collected between wavenumber ranges of 400–4000 cm^{-1} with a resolution of 4 cm^{-1} and averaged to generate the final spectra. Data were baseline corrected and normalized.

Elemental composition and surface area

A Carlo Erba EA1108 Elemental Analyzer was used to analyze elemental compositions, including C, N, H, S, and O. To do so, the samples were combusted at 1000°C (Alam et al., 2016).

The specific surface area of WS and WPC were measured using Autosorb Quantachrome 1MP instrument, and according to the Brunauer - Emmet - Teller (BET) and the Barret - Joyner - Halender (BJH) methods. Samples were first outgassed at 300°C for 3 h, and after degassing samples were analyzed. The specific surface areas was then calculated from the resulting N_2 adsorption isotherms (Alam et al., 2016).

X-ray photoelectron spectroscopy (XPS)

XPS measurements for WS and WPC were carried out to determine the functional groups and their relative abundance on the biochar surface using a Kratos Axis 165 instrument. U(VI)-

loaded WS and WPC were also analyzed to identify the U(VI) oxidation states and to investigate how U(VI) interacted with biochar functional groups. A monochromatized Al Kα source (hν=1486.6 ev) was used at 12 mA and 14kV, and the base pressure in the sample analytical camber (SAC) was lower than 1 x 10^{-9} torr. The pass energy was 20 eV and the step was 0.1 eV with a dwell time of 200 ms.

Boehm Titrations

Acidic functional group concentrations of WS and WPC for three pK_a value ranges: 5 to 6.4, 6.4 to 10.3, and 10.3 to 13, were determined using modified Boehm titrations. To do so, biochar samples were mixed with 0.05 M HCl at a 1:50 solid to solution ratio, and were shaken at 200 rpm for 24 h. Biochar samples were then washed 2 times with 1 M $CaCl_2$ and four times with 18.2 MΩ water at a 1:50 solid to solution ratios to remove residual 0.05 M HCl, followed by 60 h of drying at 50°C. 0.5 g of pre-treated material were then added to 25 ml of 0.05 M solutions of $NaHCO_3$, Na_2CO_3 and NaOH, respectively, (the three bases used in the Boehm method) and shaken at 200 rpm for 24 h. Using a Büchner funnel apparatus, aliquots were filtered through 0.45 µm nitrocellulose membranes. The filtered aliquots were mixed to 1 M $BaCl_2$ solution at 1:1 ratio to remove DOC and carbonate ions. The extracts of $NaHCO_3$ and Na_2CO_3 were mixed to 0.05 M and 0.01 M NaOH, respectively to achieve final NaOH:$BaCl_2$:extract ratio of 1:1:1 followed by shaking at 200 rpm for 1 h. The supernatant was then centrifuged at 8,000 g for 30 min, and filtered through 0.02 µm nylon membranes (Sigma Aldrich, Milwaukee, WI). The resulting aliquots were acidified to pH < 2 using 12 M HCl, and titrated with 0.01M NaOH titrant using a Titroline 6000 titrator (SI Analytics, Mainz, Germany). The treatments mentioned above were also performed for background electrolytes of 0.01 M $NaNO_3$ as a blank, and the

resulting blank values were subtracted from experimental values. All the experiments were run in triplicate (Fidel et al., 2013; Alam et al., 2016).

Kinetics Experiments

The kinetic experiments were carried out using 20 μM U at pH 7 for 24 h for both WS and WPC. The sampling and analyzing procedure is the same as those described for U(VI) adsorption experiments in the main text.

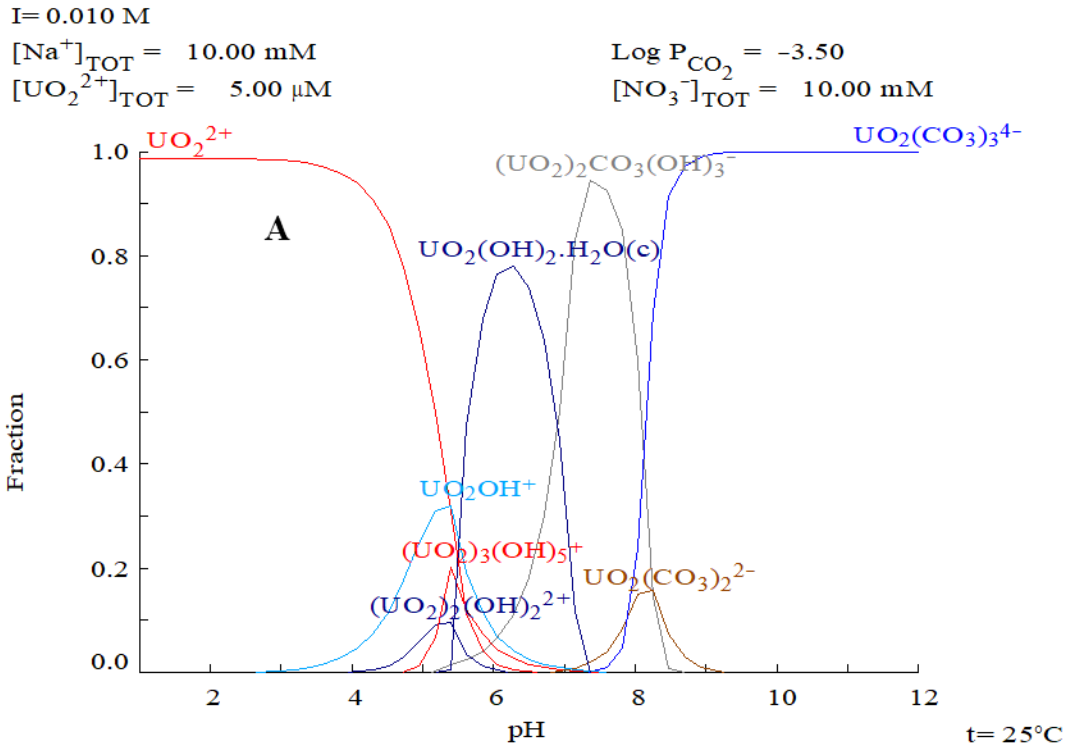
I= 0.010 M
[Na+]TOT = 10.00 mM
[UO2 2+]TOT = 5.00 µM
Log PCO2 = -3.50
[NO3-]TOT = 10.00 mM
A
UO2 2+
(UO2)2CO3(OH)3-
UO2(CO3)3 4-
UO2(OH)2.H2O(c)
UO2OH+
(UO2)3(OH)5+
UO2(CO3)2 2-
(UO2)2(OH)2 2+
Fraction
pH
t= 25°C

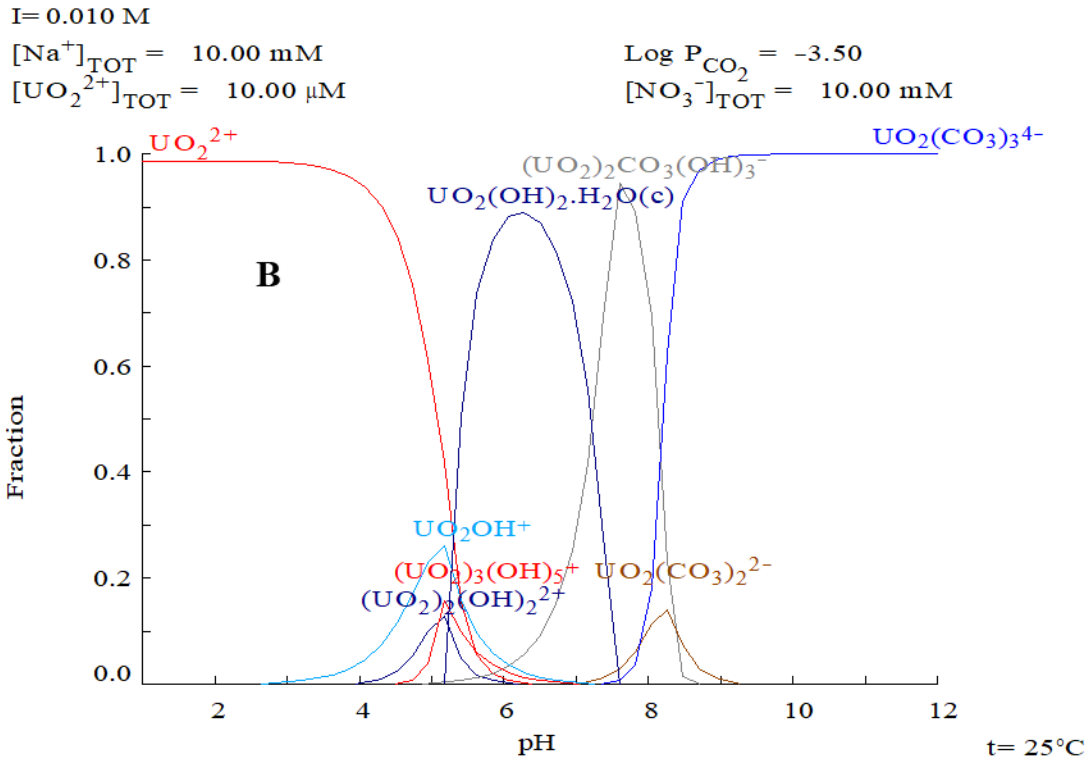
I= 0.010 M
[Na+]TOT = 10.00 mM
[UO2 2+]TOT = 10.00 µM
Log PCO2 = -3.50
[NO3-]TOT = 10.00 mM
B
UO2 2+
(UO2)2CO3(OH)3-
UO2(CO3)3 4-
UO2(OH)2.H2O(c)
UO2OH+
(UO2)3(OH)5+
UO2(CO3)2 2-
(UO2)2(OH)2 2+
Fraction
pH
t= 25°C

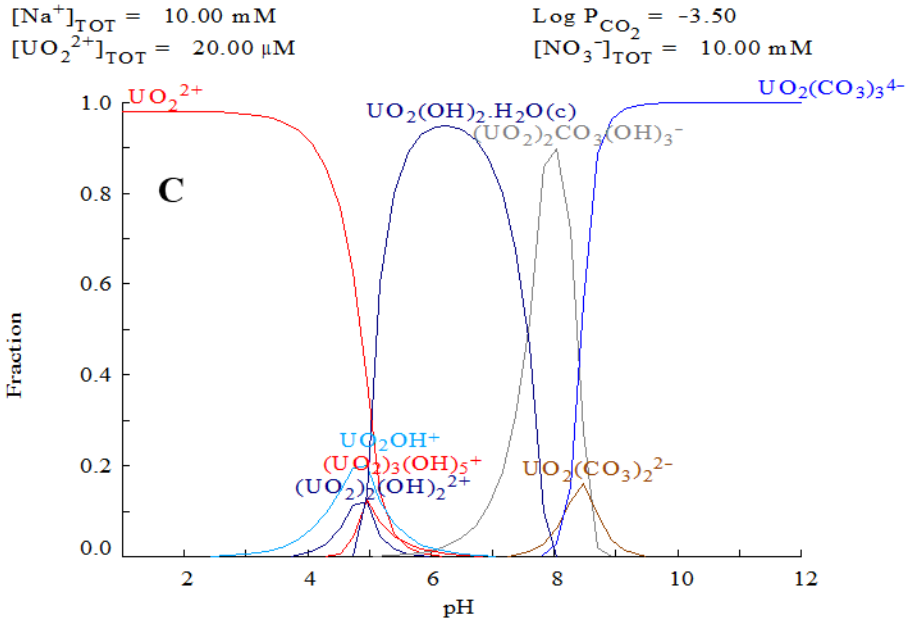

Figure B.S3.1. U(VI) aqueous speciation diagrams in background electrolyte solutions before adsorption as a function of pH: (A) 5µM U(VI) in 0.01 M $NaNO_3$; (B) 10µM U(VI) in 0.01 M $NaNO_3$; and (C) 20µM U(VI) in 0.01 M $NaNO_3$. Diagrams were made using Chemical Equilibrium Diagrams Hydra and Medusa (Ingri et al., 1968; Eriksson, 1979).

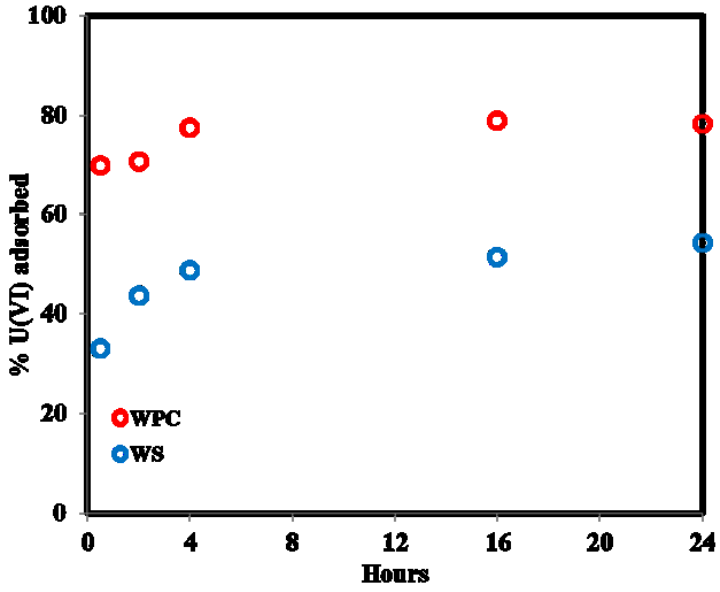

Figure B.S3.2. The kinetics of U(VI) adsorption onto WS and WPC.

Tables B.S3.1. Aqueous U(VI) complexation reactions and thermodynamic stability constants.

Reaction	**logK***
$H_2O \rightleftharpoons H^+ + OH^-$	-14.00
$UO_2^{2+} + H_2O \rightleftharpoons UO_2OH^+ + H^+$	-5.25
$UO_2^{2+} + 2H_2O \rightleftharpoons UO_2(OH)_2^+ + 2H^+$	-12.15
$UO_2^{2+} + 3H_2O \rightleftharpoons UO_2(OH)_3^+ + 3H^+$	-20.25
$UO_2^{2+} + 4H_2O \rightleftharpoons UO_2(OH)_4^+ + 4H^+$	-32.40
$2UO_2^{2+} + H_2O \rightleftharpoons (UO_2)_2(OH)^{3+} + H^+$	-2.70
$2UO_2^{2+} + 2H_2O \rightleftharpoons (UO_2)_2(OH)_2^{2+} + 2H^+$	-5.62
$3UO_2^{2+} + 4H_2O \rightleftharpoons (UO_2)_3(OH)_4^{2+} + 4H^+$	-11.90
$3UO_2^{2+} + 5H_2O \rightleftharpoons (UO_2)_3(OH)_5^+ + 5H^+$	-15.55
$3UO_2^{2+} + 7H_2O \rightleftharpoons (UO_2)_3(OH)_7^- + 7H^+$	-32.20
$4UO_2^{2+} + 7H_2O \rightleftharpoons (UO_2)_4(OH)_7^+ + 7H^+$	-21.90
$H^+ + CO_3^{2-} \rightleftharpoons HCO_3^-$	10.33
$2H^+ + CO_3^{2-} \rightleftharpoons H_2CO_3$	16.68
$Na^+ + H^+ + CO_3^{2-} \rightleftharpoons NaHCO_3^-$	10.08
$Na^+ + CO_3^{2-} \rightleftharpoons NaCO_3^-$	1.270
$UO_2^{2+} + CO_3^{2-} \rightleftharpoons UO_2CO_3$ (aq)	9.940
$UO_2^{2+} + 2CO_3^{2-} \rightleftharpoons UO_2(CO_3)_2^{2-}$	16.61
$UO_2^{2+} + 3CO_3^{2-} \rightleftharpoons UO_2(CO_3)_3^{4-}$	21.84
$3UO_2^{2+} + 6CO_3^{2-} \rightleftharpoons (UO_2)_3(CO_3)_6^{6-}$	54.00
$2UO_2^{2+} + 3H_2O + CO_3^{2-} \rightleftharpoons (UO_2)_2CO_3(OH)_3^- + 3H^+$	-0.86
$3UO_2^{2+} + 3H_2O + CO_3^{2-} \rightleftharpoons (UO_2)_3CO_3(OH)_3^+ + 3H^+$	0.65
$Ca^{+2} + UO_2^{2+} + CO_3^{2-} \rightleftharpoons CaUO_2(CO_3)_3^{2-}$	25.04
$2Ca^{+2} + UO_2^{2+} + 3CO_3^{2-} \leftrightarrow Ca_2UO_2(CO_3)_3^0$	30.6

* Guillaumont et al. (2003) and Pan et al (2016)

Table B.S3.2. pK_a values and site concentrations of WS and WPC.

Biochars	Total Sites	$logK_1$	$logK_2$	$logK_3$	Site1 concentration (mol/g)	Site2 concentration (mol/g)	Site3 concentration (mol/g)	Total reactive site (mmol/g)	V(Y)
WS[9]	3	4.24	5.82	7.87	7.5E-04	1.2E-04	1.0E-04	1.0	5.0
WPC[2,9]	3	4.23	6.18	7.94	9.8E-04	1.1E-04	1.4E-04	1.23	11

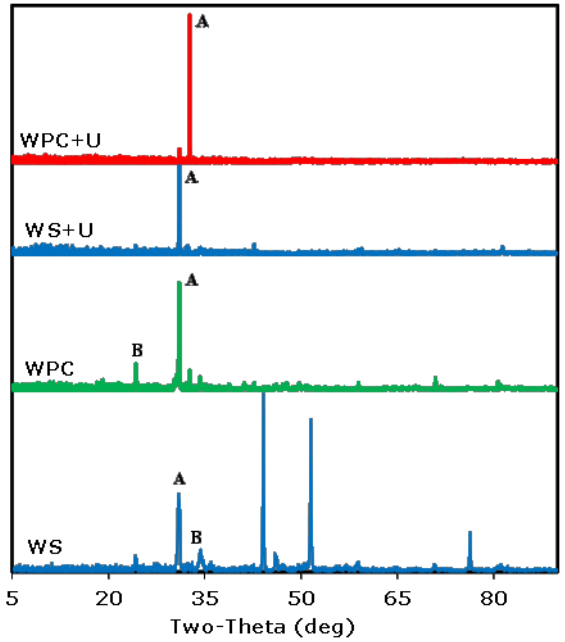

Figure B.S3.3. XRD pattern of: WS; WPC; WS+U; WPC+U. A. Quartz; B. Calcite.

Table B.S3.3. pH, elemental composition, molar ratio, BET surface area, and pore volume of WS and WPC.

Properties	**Biochar**	
	WS[1,9]	WPC[2,9]
%C	69.7	84.6
%H	2.6	2.1
%O	8.7	9.4
%N	0.8	0.2
%S	0.07	-
Molar H/C	0.4	0.3
Molar O/C	0.09	0.08
Surface area m^2/g	26.6	224

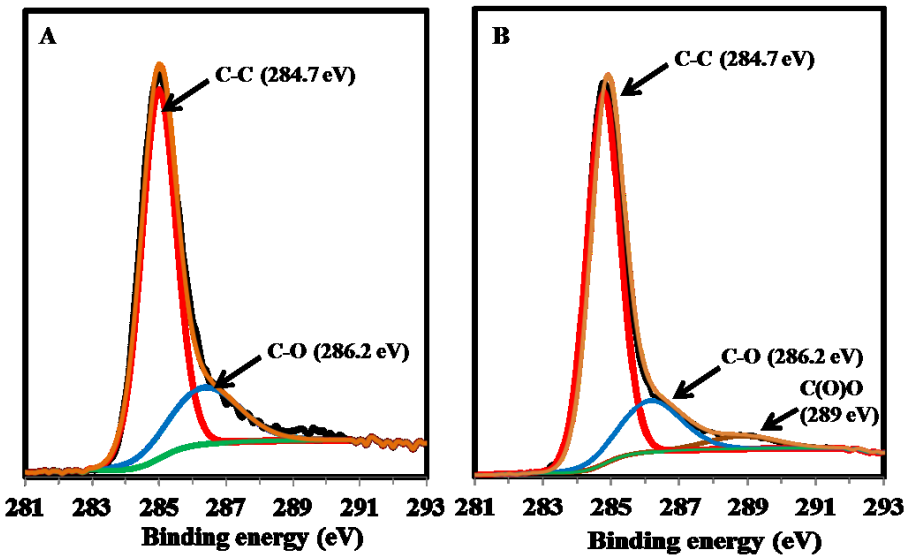

Figure B.S3.4. C 1S XPS of: WS and WPC.

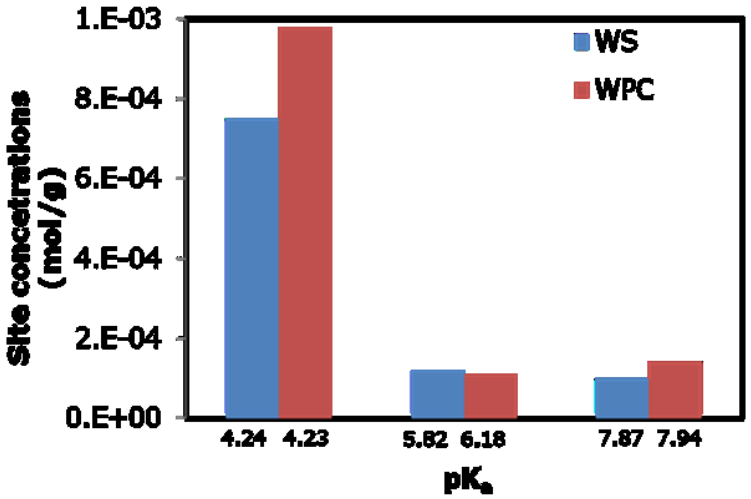

Figure B.S3.5. pK_a values and site concentrations of WS and WPC.

Table B.S3.4. Boehm titration data of WS and WPC.

Materials	**Functional group concentrations (mmol/g)**			
	$NaHCO_3$ pKa ~5 – 6.4	Na_2CO_3 pKa ~6.4 – 10.3	NaOH pKa ~10.3 – 13	Total reactive site (mmol/g)
Wheat straw (WS)	0.09	0.24	1.2	1.5
Wood pin chip (WPC)	2.6	2.1	0.01	4.7

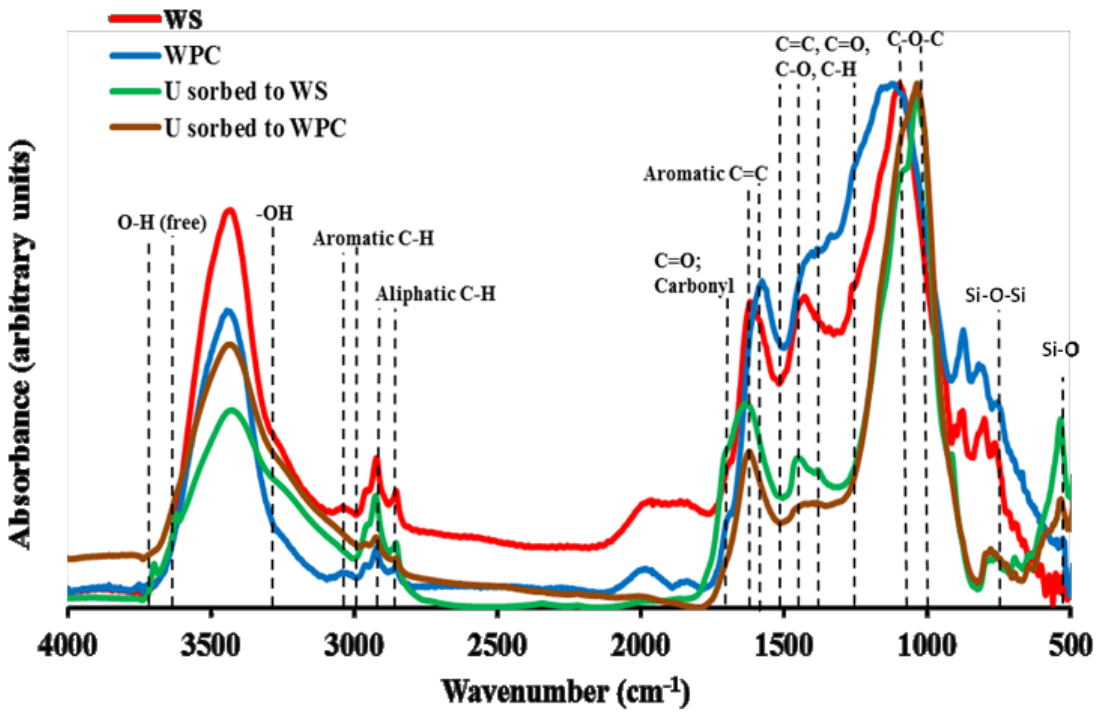

Figure B.S3.6. FT-IR spectra of WS and WPC before and after U(VI) sorption.

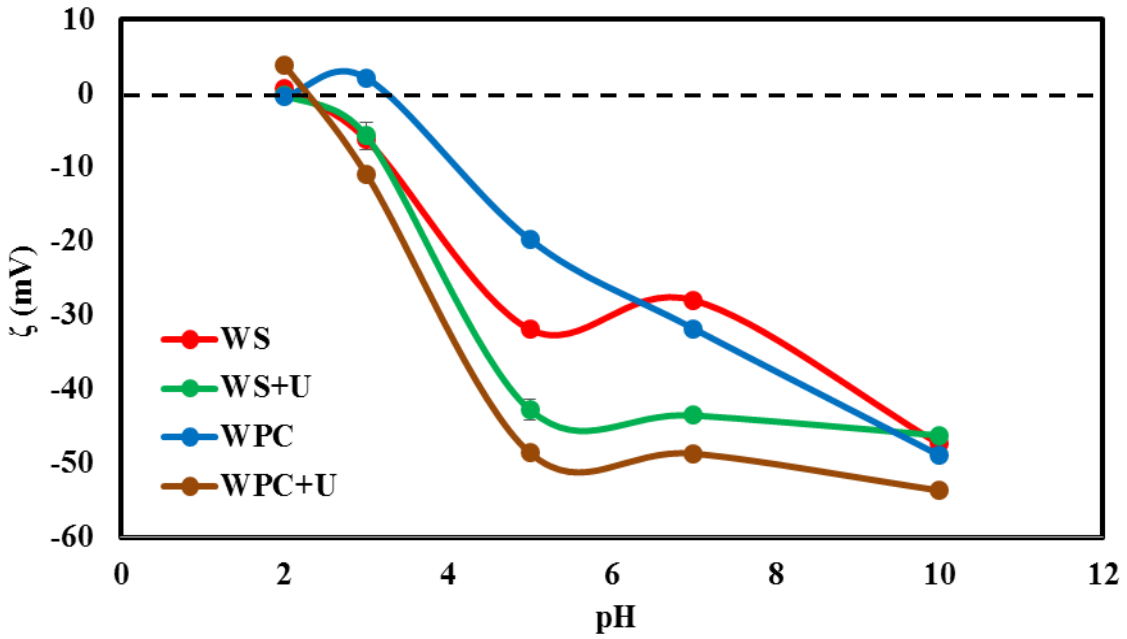

Figure B.S3.7. Zeta potentials of WS and WPC before and after U(VI) sorption.

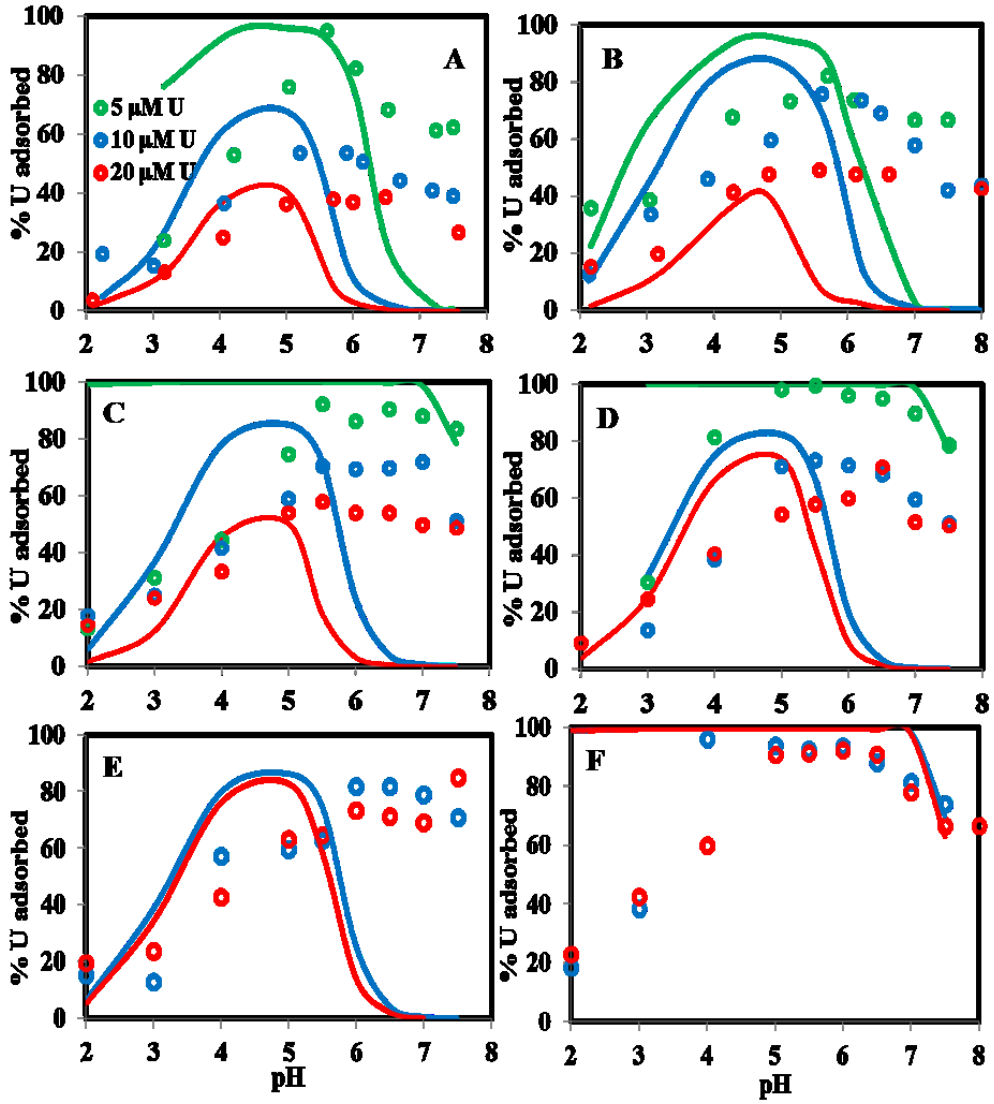

Figure B.S3.8. Adsorption of U(VI) onto WS and WPC with 1-site adsorption models: A. 0.2 gL^{-1} WS; B. 0.2 gL^{-1} WPC; C. 0.5 gL^{-1} WS; D. 0.5 gL^{-1} WPC; E. 1 gL^{-1} WS and F. 1 gL^{-1} WPC. Open circles represent experimental data and solid lines represent best-fit models.

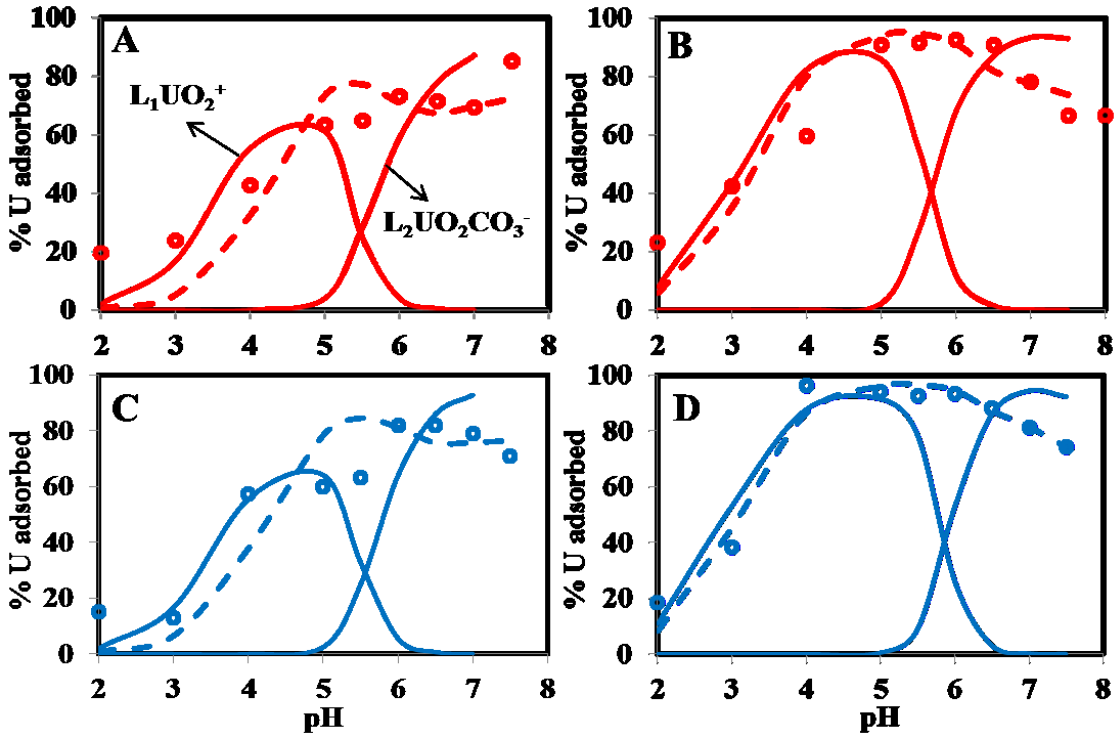

Figure B.S3.9. Contribution of site-1 and site-2 in adsorption of U(VI) onto WS and WPC with 2-site adsorption models: A. 1 gL^{-1} WS at 20 µM U(VI); B. 1 gL^{-1} WPC at 20 µM U(VI); C. 1 gL^{-1} WS at 10 µM U(VI); D. 1 gL^{-1} WPC at 10 µM U(VI). Open circles represent experimental data and solid lines represent the contribution from site 1 and site 2 and dashed line represents the best-fit model that invokes metal adsorption to the first two sites of the 3-site protonation model.

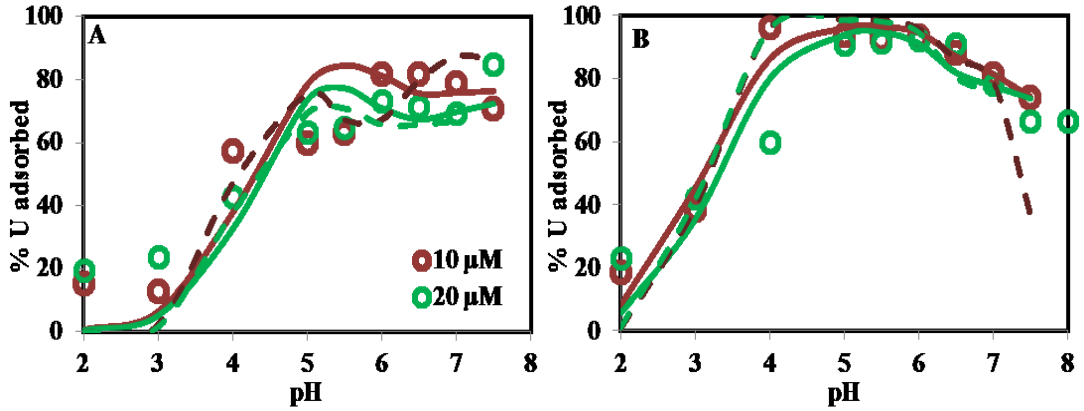

Figure B.S3.10. Adsorption of U(VI) onto the first two sites of the WS and WPC 3-site protonation models. (A) 1 gL^{-1} WS and (B) 1 gL^{-1} WPC. Open circle, solid line and dashed lines represent experimental data, monodandate U(VI) adsorption and bidendate U(VI) adsorption, respectively.

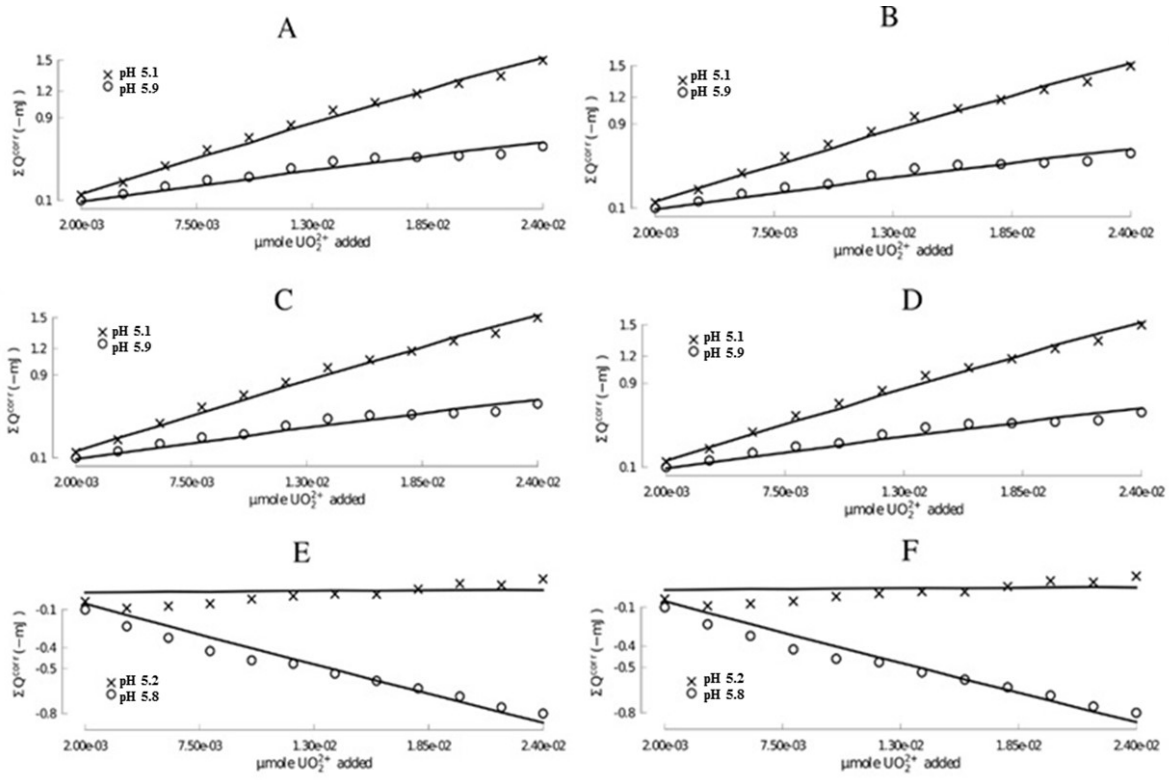

Figure B.S3.11. Corrected heat generated from U(VI) adsorption titrations of WS and WPC. A. 5 µM U(VI) adsorption onto 0.2 gL^{-1} WS; B. 10 µM U(VI) adsorption onto 0.2 gL^{-1} WS; C. 5 µM U(VI) adsorption onto 0.5 gL^{-1} WS; and D. 10 µM U(VI) adsorption onto 0.5 gL^{-1} WS; E. 5 µM U(VI) adsorption onto 0.2 gL^{-1} WPC; F. 10 µM U(VI) adsorption onto 0.5 gL^{-1} WPC. The dashed curve and solid curve represent the experimental data and the fit, respectively.

Table B.S3.5. Site-specific thermodynamic parameters for U(VI) adsorption onto WS and WPC derived from calorimetric titrations and metal adsorption onto the first two sites of the 3-site protonation model.

U(VI) concentration	Species	logK	$\Delta G_r°$ (KJ/mol)	$\Delta H_r°$ (KJ/mol)	$-T\Delta S_r°$ (KJ/mol)	$\Delta S_r°$ (J/molK)	χ^2
				WS (0.2 gL^{-1})			
5 μM U	$L_1UO_2^+$	5.25(0.24)	-29.97(1.37)	-104.56(0.64)	74.60(1.51)	-250(5)	8.514e-8
	$L_2UO_2CO_3^-$	6.66(0.31)	-38.02(1.77)	-40.58(0.86)	2.56(1.97)	-9(7)	
10 μM U	$L_1UO_2^+$	4.81(0.13)	-27.4(0.74)	-108.82(0.69)	81.36(1.01)	-273(3)	8.459e-8
	$L_2UO_2CO_3^-$	6.86(0.22)	-39.16(1.26)	53.09(0.67)	13.94(1.42)	47(5)	
				WS (0.5 gL^{-1})			
5 μM U	$L_1UO_2^+$	4.62(0.28)	-26.37(1.60)	-119.97(0.85)	93.60(1.81)	-314(6)	8.531e-8
	$L_2UO_2CO_3^-$	7.16(0.45)	-40.87(2.57)	-55.60(0.64)	14.73(2.65)	-49(9)	
10 μM U	$L_1UO_2^+$	4.64(0.12)	-26.49(0.68)	-105.89(0.65)	79.40(0.94)	-266(3)	8.439e-8
	$L_2UO_2CO_3^-$	6.28(0.13)	-35.8(0.74)	-47.39(0.76)	11.54(1.06)	-39(4)	
				WPC (0.2 gL^{-1})			
5 μM U	$L_1UO_2^+$	5.42(0.29)	-30.94(1.66)	-7.38(0.86)	-23.56(1.87)	79(6)	1.494e-7
	$L_2UO_2CO_3^-$	6.85(0.36)	-39.10(2.05)	92.01(2.33)	-131.11(3.10)	440(10)	
				WPC (0.5 gL^{-1})			
10 μM U	$L_1UO_2^+$	4.60(0.13)	-26.26(0.74)	-9.20(0.90)	-17.06(1.17)	57(4)	1.497e-7
	$L_2UO_2CO_3^-$	6.48(0.11)	-36.99(0.63)	55.03(1.33)	-92.02(1.47)	309(5)	

Table B.S3.6. Site-specific thermodynamic parameters for the reaction of H^+ derived from calorimetric titrations, and 3-site models from potentiometric titration data.

Species	logK	$\Delta G_r°$ (KJ/mol)	$\Delta H_r°$ (KJ/mol)	$T\Delta S_r°$ (KJ/mol)	$\Delta S_r°$ (J/molK)
			WS		
HL1	4.24(0.05)	-24.20(0.29)	-0.18(0.02)	24.02(0.29)	80.56(0.96)
HL2	5.82(0.17)	-33.22(0.97)	-3.88(0.20)	29.34(0.99)	98.41(3.32)
HL3	7.87(0.09)	-44.92(0.51)	-2.93(0.15)	41.99(0.53)	140.83(1.79)
			WPC		
HL1	4.23(0.02)	-24.15(0.11)	-0.09(0.01)	24.06(0.11)	80.69(0.38)
HL2	6.18(0.15)	-35.28(0.86)	-2.97(0.10)	32.31(0.86)	108.37(2.89)
HL3	7.94(0.07)	-45.32(0.40)	1.54(0.12)	46.86(0.42)	157.17(1.40)

APPENDIX C. SUPPLEMENTARY INFORMATION FOR CHAPTER 4

Sequential Extraction

Sequential extractions of metals from soils and biochar were conducted using finely grounded samples (1 g for soils, 0.5 g for biochar) in 50 mL polypropylene centrifuge tubes. After each extraction step, the resulting residues were used for the following extraction step. Exchangeable metals (fraction 1) were extracted at room temperature during 20 min with 8 mL of 0.5 M magnesium chloride ($MgCl_2$, ACS grade, Fisher Scientific) with continuous agitation. Metals bound to carbonates (fraction 2) were extracted at room temperature over a 5 h period, using 8 mL of 1 M sodium acetate ($C_2H_3NaO_2$, adjusted to pH 5 with acetic acid, ACS grade, Fisher Scientific) with continuous agitation. Metals loosely bound to Fe-Mn-oxides (fraction 3) were extracted at 95°C for 6 h, with 20 mL of 0.04 M hydroxylammonium hydrochloride ($NH_2OH \cdot HCl$, ACS grade, Fisher Scientific) with occasional agitation. Metals bound to organic matter and sulfides (fraction 4) were extracted by adding 3 mL of 0.02 M HNO_3 and 5 mL of 30% H_2O_2, and subsequently heating the sample slowly to 85°C. The sample was kept at this temperature for 2 h with occasional agitation. An additional 3 mL of H_2O_2 (adjusted to pH 2 with HNO_3) was added and the mixture was heated at 85°C for an additional 3 h. The mixture was then allowed to cool, and was finally amended with 5 mL of 3.2 M ammonium acetate ($C_2H_3O_2NH_4$, HPLC grade, Fisher Scientific) in 20% (v/v) HNO_3. Ultrapure water was added to a final volume of 20 mL and the mixture was agitated for 30 min.

To retrieve the extracts from fractions 1 to 4, the tubes with the suspensions were centrifuged at 17,000 relative centrifugal force (rcf) for 20 min. Supernatants were pipetted in clean centrifuge tubes: 5 mL for fractions 1 and 2, and 15 mL for fractions 3 and 4. The remaining liquid was

discarded. Before starting with the next step, the sample remains were flushed by adding 8-10 mL of ultrapure water and suspending the remains by shaking. The tubes were then centrifuged at 17,000 rcf for 20 min and the supernatant was discarded. Care should be taken when centrifugation is applied on biochar samples; because of the low density and hydrophobicity the biochar material does not settle effectively and losses may occur when liquids are pipetted or discarded vigorously. A more suitable method is described elsewhere (von Gunten et al., 2017). Blank control samples (no sample added) were set-up for each step of the sequential extraction to account for metal contamination from the extraction solutions. For the final fraction (fraction 5) the remains were digested with 5 mL HNO_3 (70%) and 15 mL HF (47-51%). The mixture was heated at 130°C to dryness and treated with the same amount of HNO_3 and HF a second time. The remains were dissolved in 50 mL with 2% HNO_3 and 0.5% HCl. All extraction and digestion solutions were analyzed by ICP-MS/MS (Agilent 8800). To test the sorption behavior of Se and Cd, both metals (100 µM each) were mixed with soil samples (10 g/L) and biochar (1 g/L). Sorption experiments were conducted for 24 hours at pH 2.5 and 7 for soils, and pH 3 and 7 for biochar. After sorption, the solids were separated from the solution by vacuum filtration, air dried and sequentially extracted as described above.

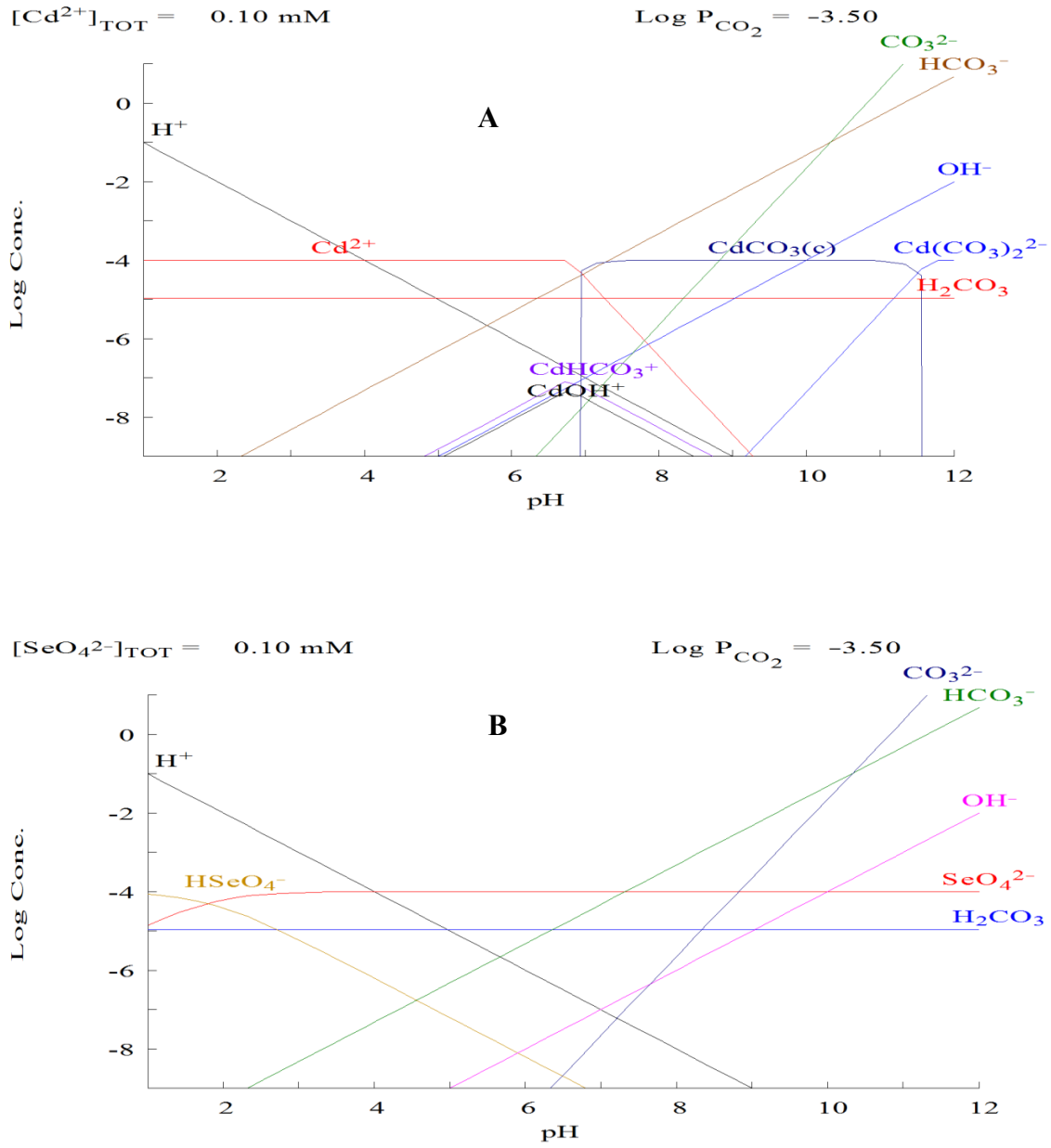

Figure C.S4.1. Aqueous speciation diagrams of (A) Cd(II) and (B) Se(VI) at experimental conditions.

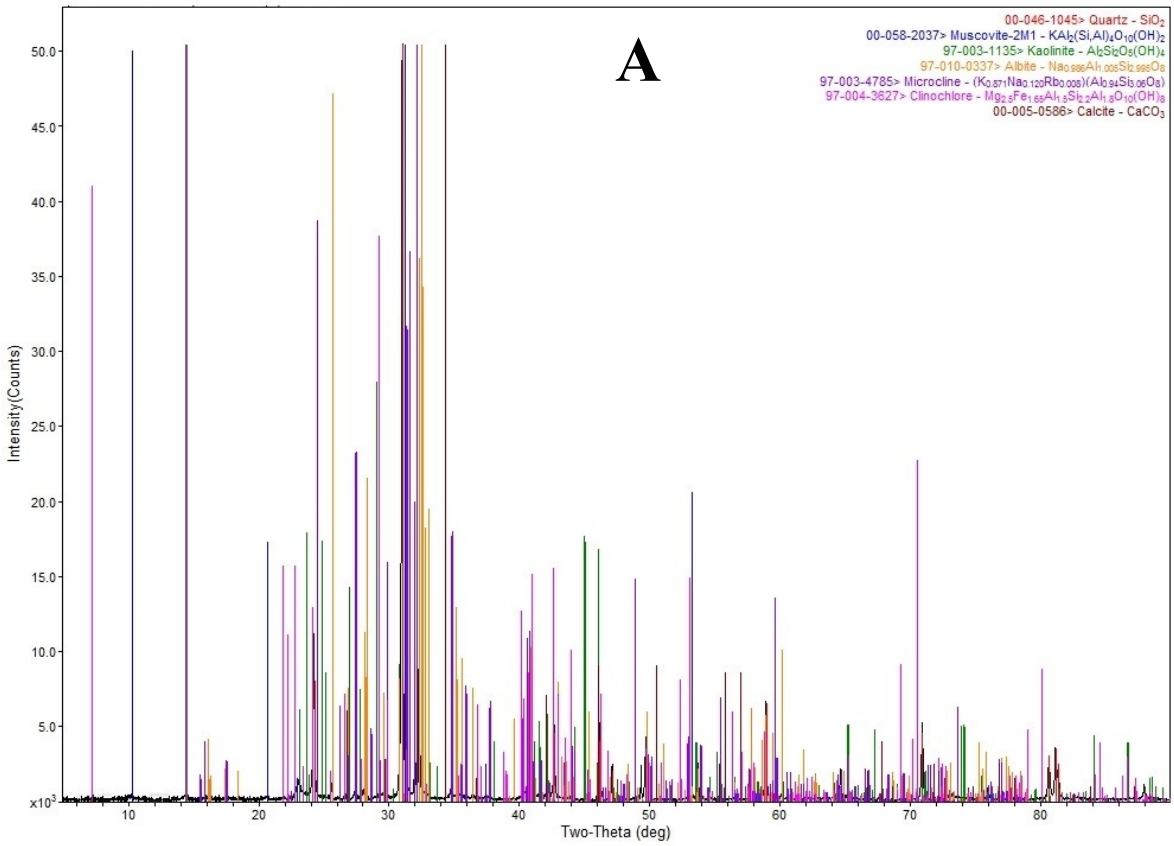
A
00-046-1045> Quartz - SiO_2
00-058-2037> Muscovite-2M1 - $KAl_2(Si,Al)_4O_{10}(OH)_2$
97-003-1135> Kaolinite - $Al_2Si_2O_5(OH)_4$
97-010-0337> Albite - $Na_{0.986}Al_{1.005}Si_{2.995}O_8$
97-003-4785> Microcline - $(K_{0.871}Na_{0.120}Rb_{0.008})(Al_{0.94}Si_{3.06}O_8)$
97-004-3627> Clinochlore - $Mg_{2.5}Fe_{1.65}Al_{1.5}Si_{2.2}Al_{1.8}O_{10}(OH)_8$
00-005-0586> Calcite - $CaCO_3$
Intensity(Counts)
x10³
50.0
45.0
40.0
35.0
30.0
25.0
20.0
15.0
10.0
5.0
10
20
30
40
50
60
70
80
Two-Theta (deg)

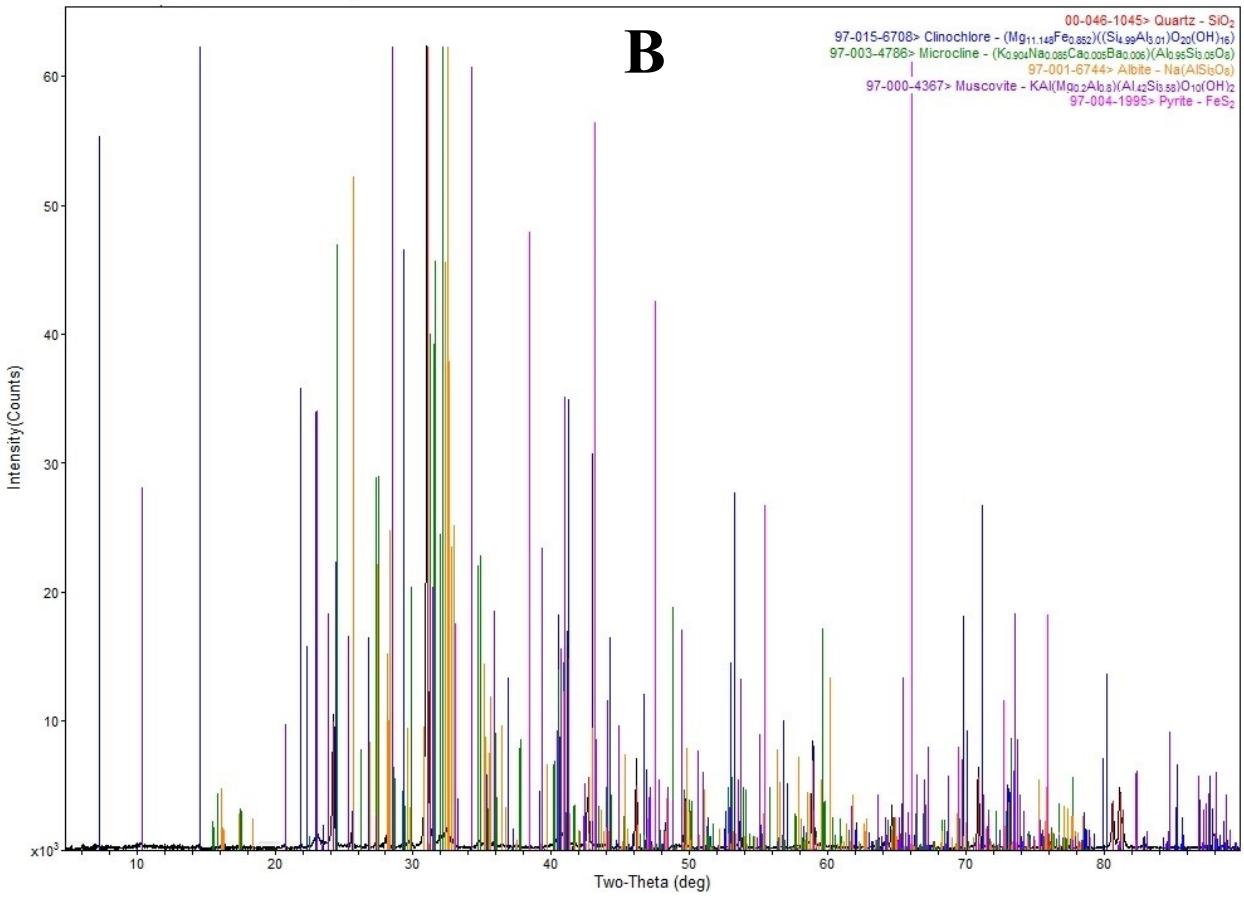
B
00-046-1045> Quartz - SiO2
97-015-6708> Clinochlore - (Mg11.148Fe0.852)((Si4.99Al3.01)O20(OH)16)
97-003-4786> Microcline - (K0.904Na0.085Ca0.005Ba0.006)(Al0.95Si3.05O8)
97-001-6744> Albite - Na(AlSi3O8)
97-000-4367> Muscovite - KAl(Mg0.2Al0.8)(Al1.42Si3.58)O10(OH)2
97-004-1995> Pyrite - FeS2
Intensity(Counts)
x10^3
Two-Theta (deg)

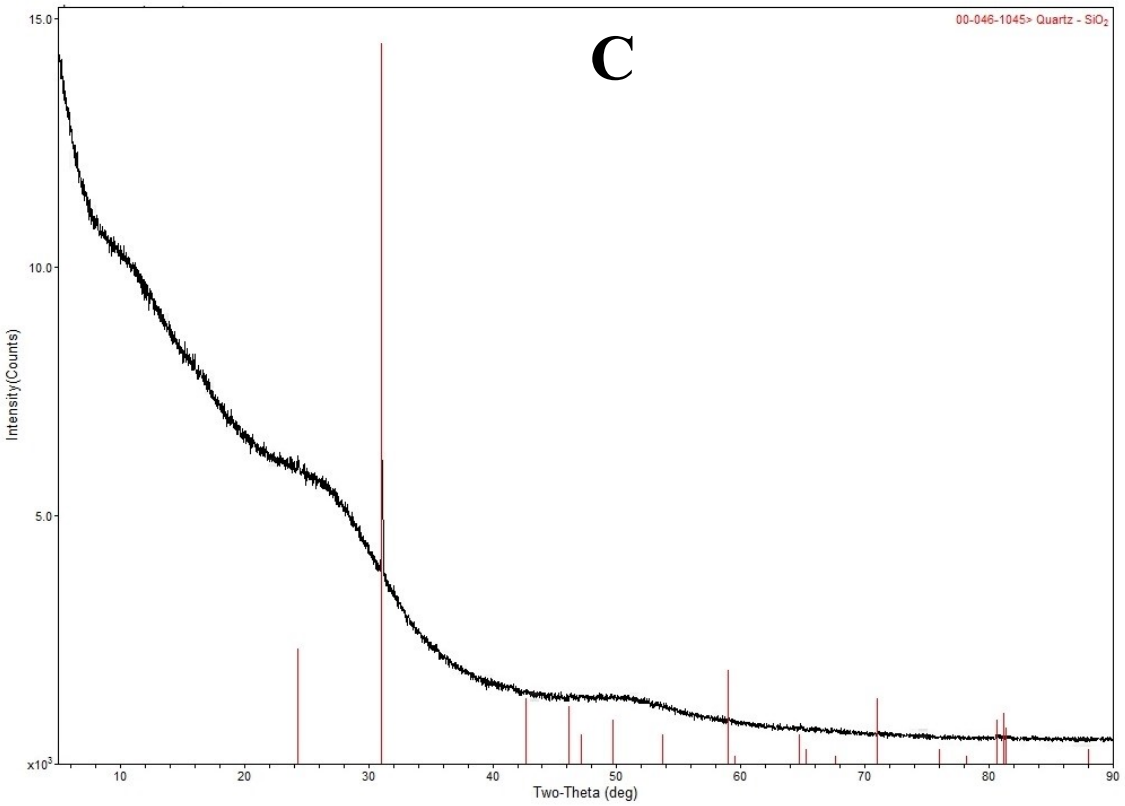

Figure C.S4.2. X-ray diffraction patterns and fits for (A) AFS, (B) CFS, and (C) WPC.

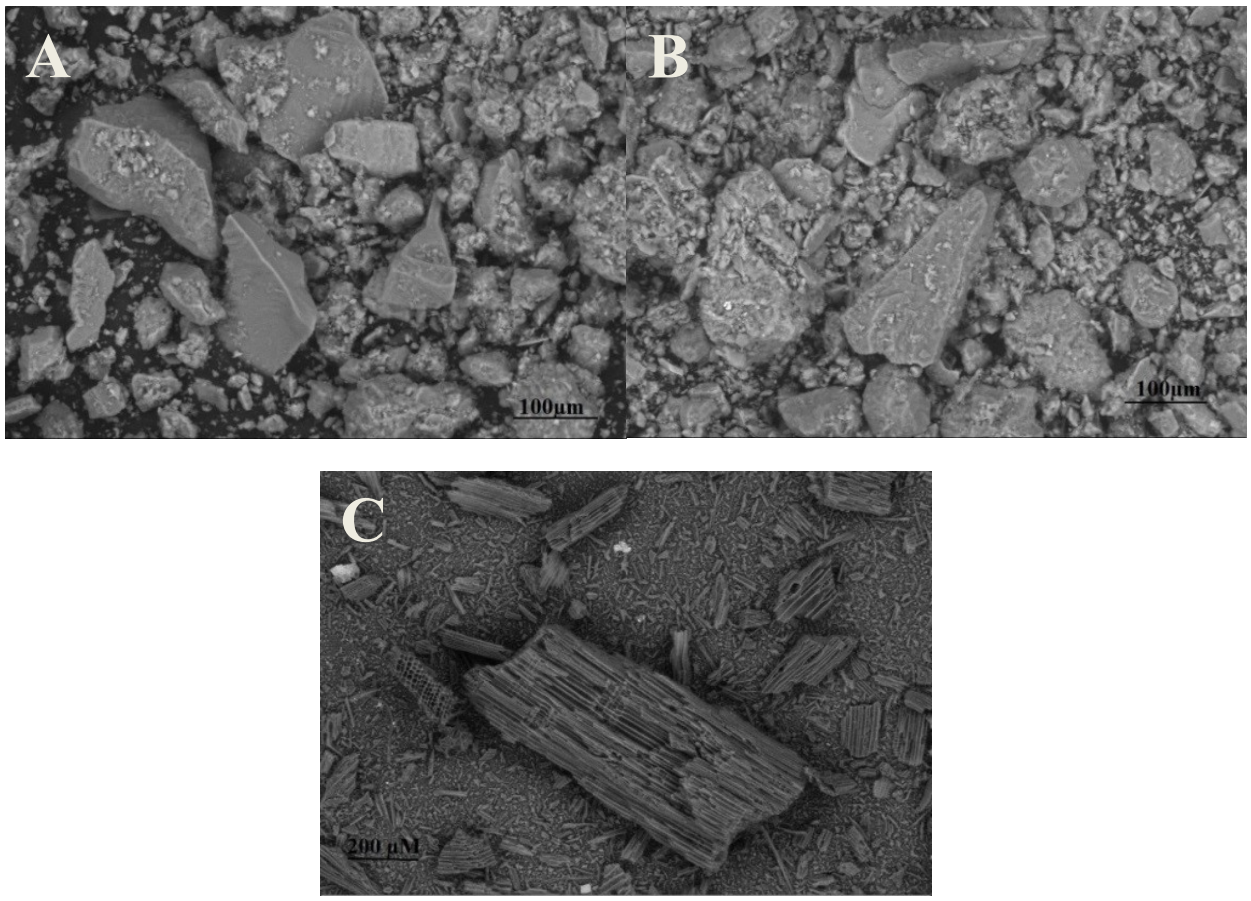

Figure C.S4.3. SEM images of (A) AFS, (B) CFS, and (C) WPC.

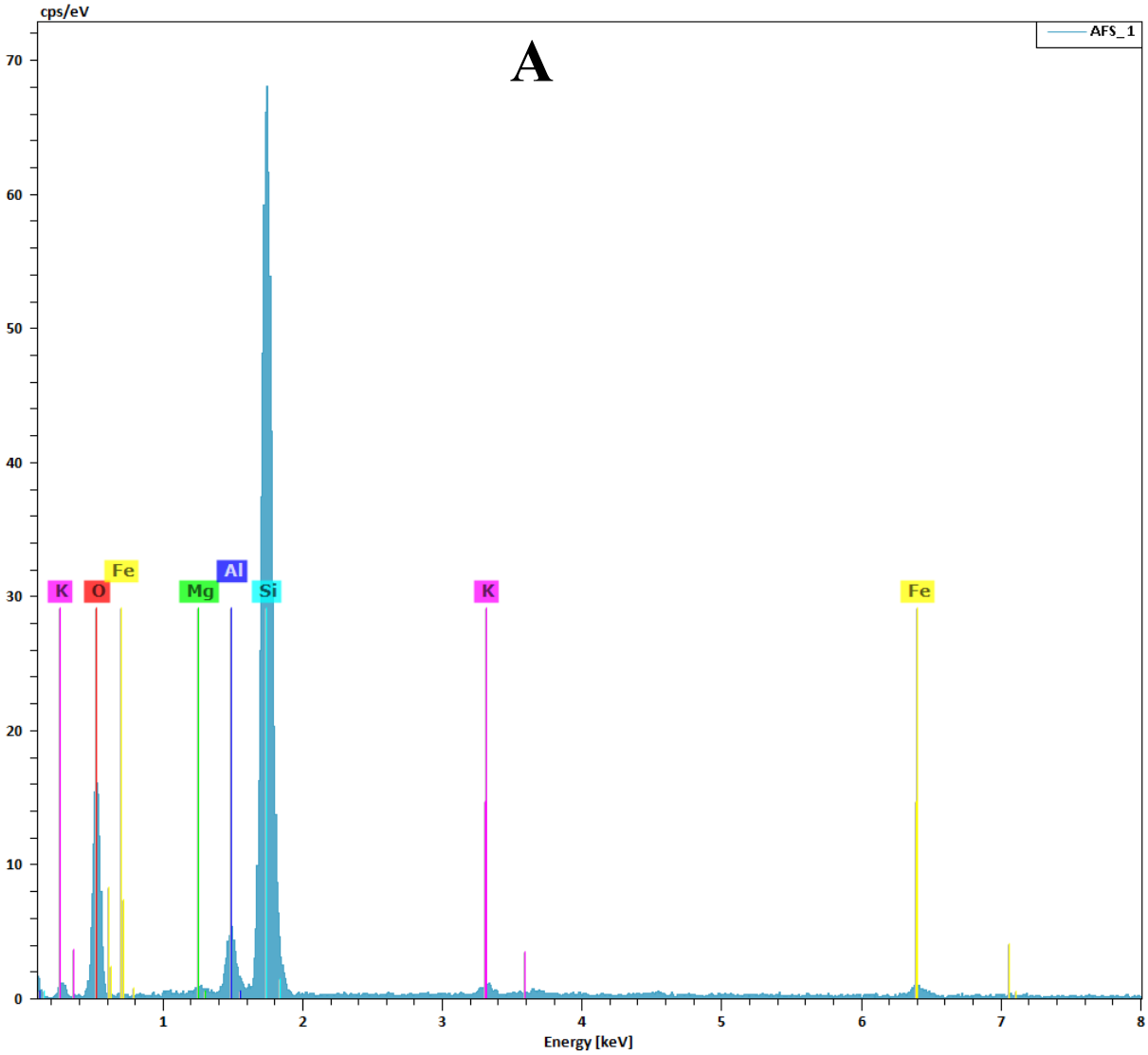
A
cps/eV
AFS_1
70
60
50
40
30
20
10
0
K
O
Fe
Mg
Al
Si
K
Fe
1
2
3
4
5
6
7
8
Energy [keV]

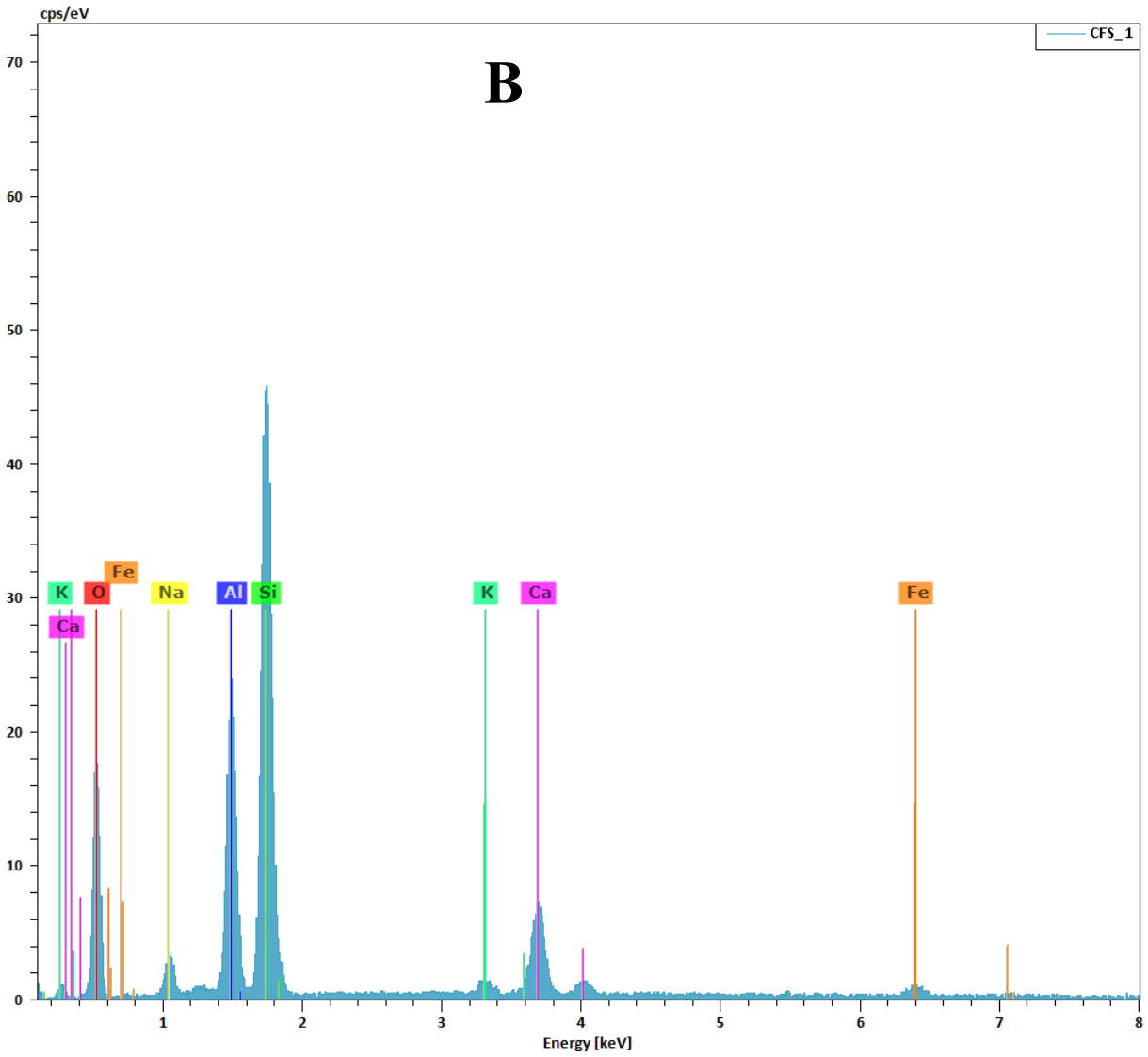
B
cps/eV
CFS_1
70
60
50
40
30
20
10
0
K
O
Fe
Ca
Na
Al
Si
K
Ca
Fe
1
2
3
4
5
6
7
8
Energy [keV]

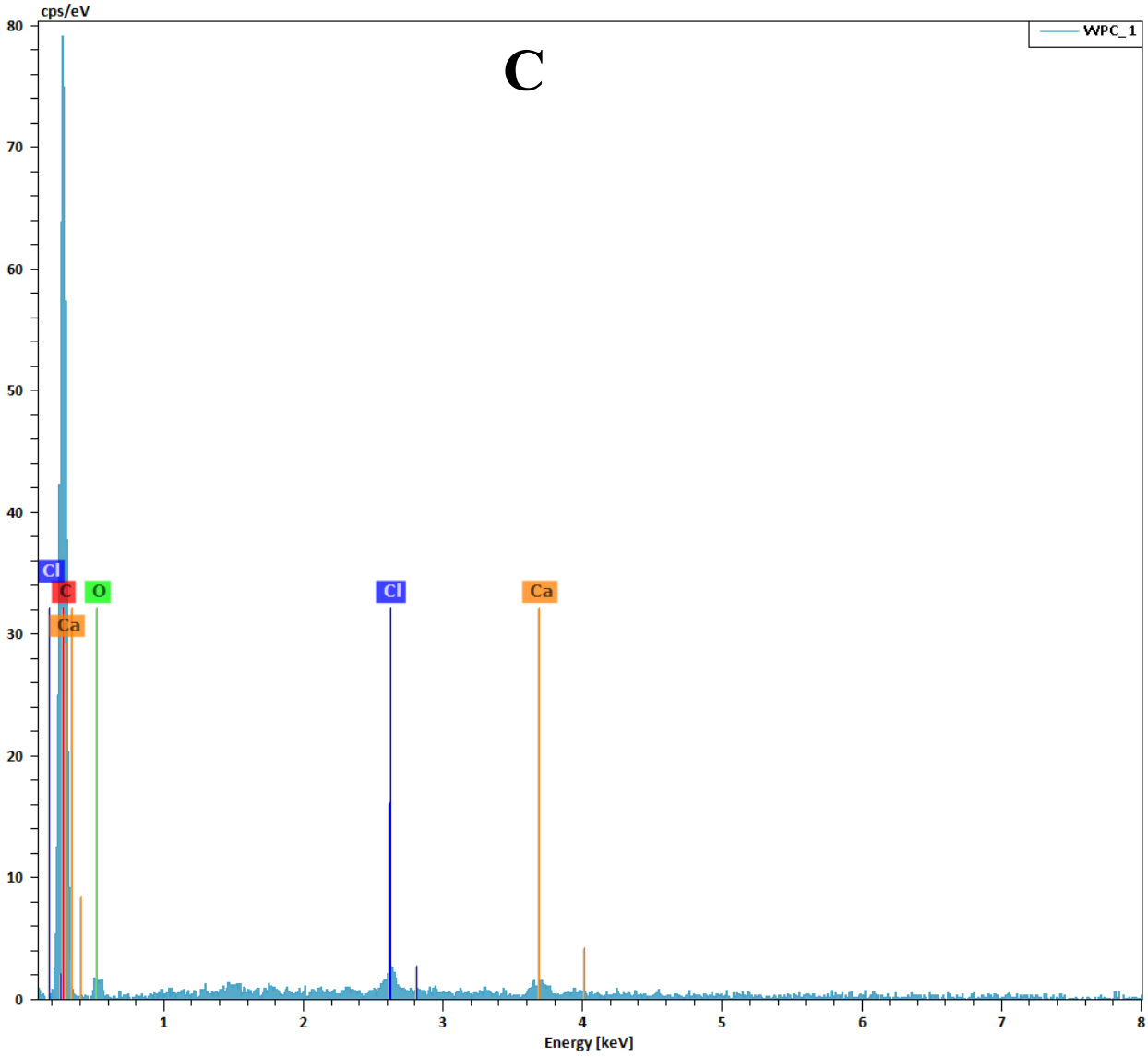

Figure C.S4.3. Average energy dispersive X-ray spectroscopy (EDS) spectra of SEM fields imaged in SI Figure 3, including (A) AFS, (B) CFS, and (C) WPC.

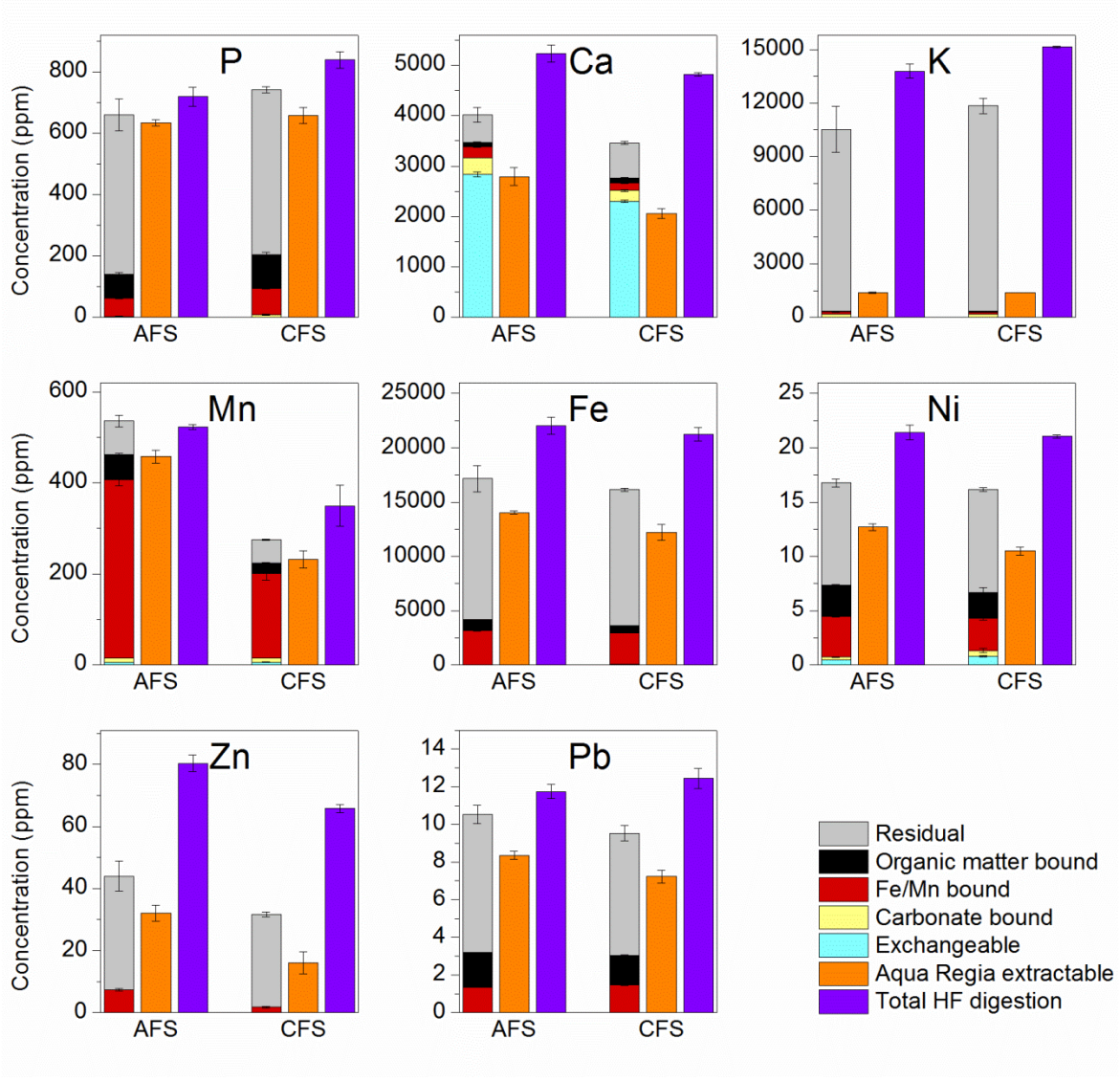

SI

Figure C.S4.5. Sequential extraction results for the soils AFS and CFS, shown together with aqua regia extractable metals and HF digestion results. Error bars represent standard deviation (n=3).

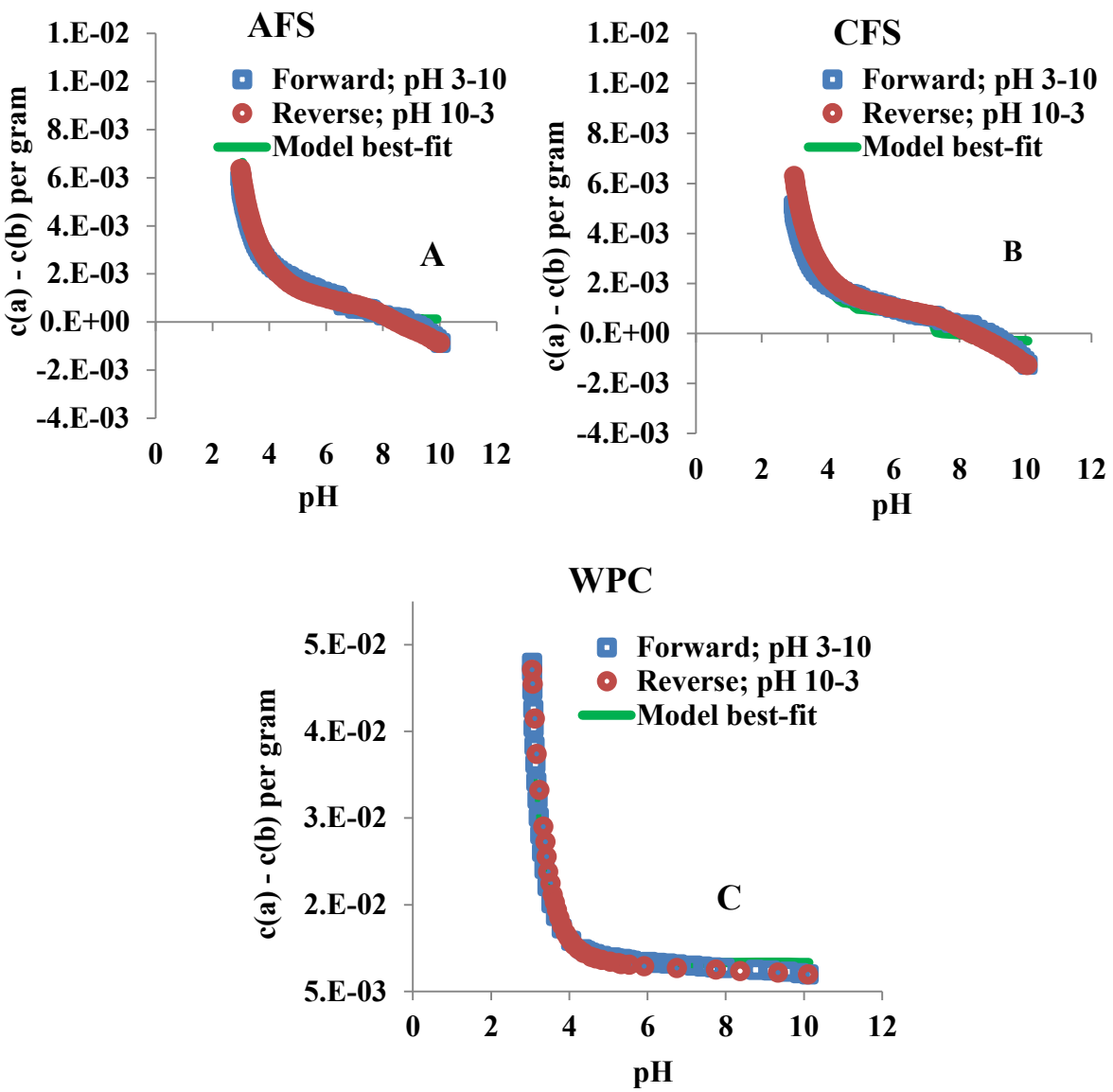

Figure C.S4.6. Potentiometric titration data and fits for (A) AFS, (B) CFS, and (C) WPC.

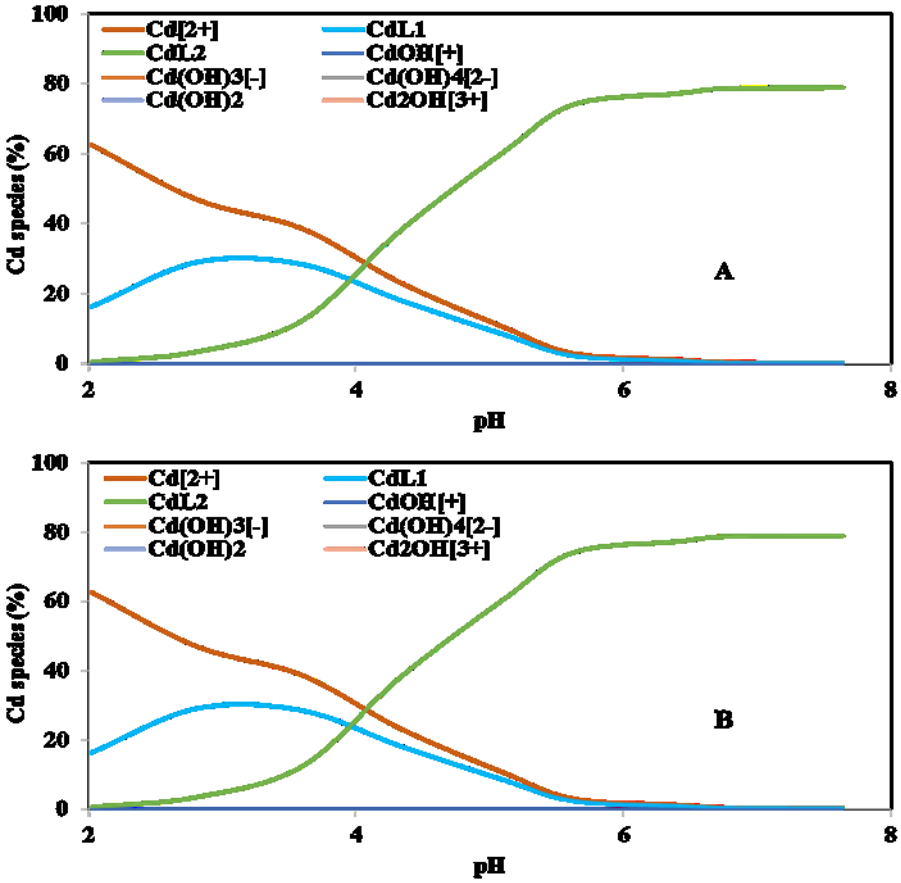

Figure C.S4.7. Model-predicted Cd speciation as a function of pH after adsorption (A) AFS, and (B) CFS.

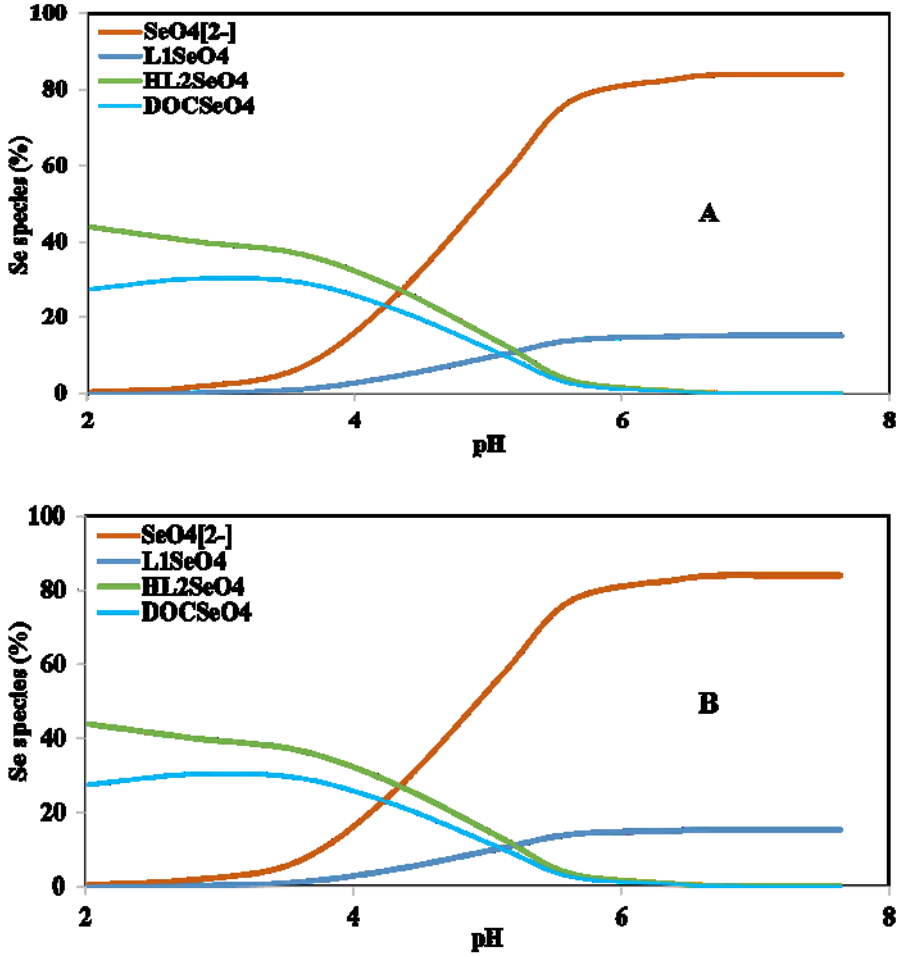

Figure C.S4.8. Model-predicted Se speciation as a function of pH after adsorption to (A) AFS, and (B) CFS.

Table C.S4.1. Aqueous Cd(II) and Se(VI) reactions and corresponding thermodynamic stability constants used in the surface complexation models.

Reaction	log K
$Cd^{2+} + H_2O = CdOH^+ + H^+$	-10.1
$Cd^{2+} + 2H_2O = Cd(OH)_2(aq) + 2H^+$	-20.3
$Cd^{2+} + 3H_2O = Cd(OH)^- + 3H^+$	-31.7
$Cd^{2+} + 4H_2O = Cd(OH)^{2-} + 4H^+$	-47.3
$2Cd^{2+} + H_2O = Cd_2(OH)^{3+} + H^+$	-9.4
$4Cd^{2+} + 4H_2O = Cd_4(OH)_4{}^{4+} + 4H^+$	-32.8
$SeO_3 + H_2O = H_2SeO_4$	-1.2
$H_2SeO_4 = HSeO_4^- + H^+$	-1.8
$CO_2 + H_2O = H_2CO_3$	-1.46
$H_2CO_3 = H^+ + HCO_3^-$	-6.36
$HCO_3^- = CO_3^{2-} + H^+$	-10.33

Cd hydrolysis reactions and log K values were taken from Baes and Mesmer (1976); Se log K values were taken from Golberg (2014); log K values of carbonic acids were taken from Stipp et al. (1993).

Table C.S4.2. Metals composition of the soil and biochar samples determined with HF digestion. The numbers represent average values (n=3) and standard deviations. Values in parentheses show the 95% confidence interval assuming a normal distribution.

Metal	AFS (ppm)	CFS (ppm)	WPC (ppm)
Na	6377.2 ± 285.1 (322.6)	7286.2 ± 52.0 (58.8)	635.0 ± 39.8 (45.1)
Mg	4439.7 ± 131.9 (149.2)	4144.8 ± 9.5 (10.8)	1338.8 ± 161.0 (182.1)
Al	47166.4 ± 964.8 (1091.7)	49462.8 ± 336.5 (380.7)	537.7 ± 70.0 (79.2)
P	718.8 ± 30.1 (34.1)	838.7 ± 28.1 (31.7)	871.1 ± 98.1 (111.0)
S	333.0 ± 10.3 (11.6)	353.1 ± 8.0 (9.0)	1551.4 ± 205.0 (231.9)
K	13776.2 ± 391.9 (443.5)	15152.6 ± 50.9 (57.6)	4265.0 ± 424.6 (480.5)
Ca	5232.5 ± 175.6 (198.8)	4820.8 ± 37.8 (42.8)	7603.3 ± 792.0 (896.2)
Ti	3383.1 ± 115.8 (131.0)	3767.5 ± 38.0 (43.0)	-
V	77.7 ± 2.1 (2.4)	76.2 ± 0.4 (0.4)	-
Cr	45.1 ± 1.6 (1.8)	47.1 ± 0.3 (0.4)	198.6 ± 42.0 (47.5)
Mn	522.3 ± 5.5 (6.2)	349.5 ± 44.9 (50.9)	464.6 ± 48.8 (55.2)
Fe	22034.9 ± 785.9 (889.3)	21236.2 ± 602.9 (682.3)	2404.5 ± 258.5 (292.5)
Co	9.2 ± 0.3 (0.4)	12.1 ± 6.2 (7.0)	2.3 ± 0.3 (0.4)
Ni	21.4 ± 0.7 (0.8)	21.1 ± 0.1 (0.2)	94.1 ± 18.4 (20.8)
Cu	17.8 ± 0.2 (0.2)	24.4 ± 8.6 (9.7)	690.6 ± 62.9 (71.2)
Zn	80.3 ± 2.6 (3.0)	65.8 ± 1.3 (1.4)	277.6 ± 25.7 (29.1)
As	7.0 ± 0.2 (0.3)	6.4 ± 0.3 (0.3)	0.2 ± 0.0 (0.0)
Se	<0.5	<0.5	<0.1
Sr	117.2 ± 4.0 (4.5)	122.9 ± 1.2 (1.3)	34.2 ± 3.4 (3.9)
Mo	0.8 ± 0.0 (0.0)	0.7 ± 0.0 (0.0)	5.9 ± 0.4 (0.5)
Cd	<0.5	<0.5	<0.2
Ba	585.0 ± 18.7 (21.1)	642.8 ± 3.0 (3.4)	192.8 ± 32.7 (37.1)
Pb	11.7 ± 0.4 (0.4)	12.4 ± 0.5 (0.6)	1.1 ± 0.1 (0.1)
Th	7.2 ± 0.4 (0.4)	7.7 ± 0.2 (0.2)	0.1 ± 0.0 (0.0)
U	1.9 ± 0.1 (0.1)	2.0 ± 0.0 (0.0)	<0.1

Table C.S4.3. Pedogenic oxides of AFS and CFS.

Constituent (%)	AFS	CFS
SiO_2	59.66	61.09
Na_2O	1.72	1.96
MgO	0.74	0.69
Al_2O_3	17.82	18.69
P_2O_5	0.33	0.38
K_2O	3.32	3.65
CaO	0.73	0.67
TiO_2	0.56	0.63
MnO	0.07	0.05
Fe_2O_3	6.30	6.07

Table C.S4.4 Aqua regia extractable metals of soil and biochar samples. The numbers represent average values (n=3) and standard deviations. Values in parentheses show the 95% confidence interval assuming a normal distribution.

Metal	AFS (ppm)	CFS (ppm)	WPC (ppm)
Al	9797.8 ± 568.8 (643.6)	8854.4 ± 43.8 (49.6)	123.9 ± 14.5 (16.5)
Si	1072.3 ± 234.5 (265.3)	1743.8 ± 321.3 (363.6)	140.7 ± 197.6 (223.6)
P	634.3 ± 10.1 (11.4)	658.0 ± 26.7 (30.2)	43.0 ± 9.4 (10.6)
S	253.8 ± 5.6 (6.3)	237.2 ± 15.2 (17.2)	45.6 ± 23.0 (26.0)
K	1529.5 ± 54.6 (61.8)	1535.1 ± 12.6 (14.3)	223.2 ± 138.6 (156.9)
Ca	2830.8 ± 8.6 (9.7)	2439.6 ± 193.1 (218.5)	441.1 ± 45.6 (51.6)
Cr	15.4 ± 1.3 (1.5)	13.7 ± 0.6 (0.7)	38.4 ± 6.7 (7.5)
Mn	524.5 ± 45.1 (51.0)	258.3 ± 21.5 (24.3)	33.9 ± 0.7 (0.8)
Fe	14987.5 ± 91.1 (103.1)	13063.8 ± 717.4 (811.8)	775.7 ± 90.8 (102.7)
Co	8.2 ± 0.6 (0.6)	7.4 ± 2.6 (2.9)	<0.9
Ni	15.7 ± 0.7 (0.8)	14.2 ± 0.3 (0.3)	17.2 ± 2.8 (3.2)
Cu	11.7 ± 0.4 (0.5)	12.1 ± 1.1 (1.2)	7.9 ± 1.0 (1.1)
Zn	32.0 ± 2.6 (2.9)	16.1 ± 3.6 (4.0)	<0.9
As	5.8 ± 0.5 (0.5)	5.1 ± 0.4 (0.4)	<0.9
Se	<0.7	<0.6	<0.9
Sr	31.3 ± 0.5 (0.6)	23.8 ± 0.8 (0.9)	2.3 ± 1.1 (1.2)
Cd	<0.5	<0.6	<1.1
Ba	177.6 ± 4.9 (5.5)	169.9 ± 5.3 (6.0)	6.5 ± 0.8 (1.0)
Pb	8.9 ± 0.1 (0.1)	8.0 ± 0.3 (0.4)	2.5 ± 1.4 (1.6)

Table C.S4.5. Cationic exchange capacity (CEC) of AFS, CFS and WPC.

	Ca	Fe	K	Mg	Mn	Na	Al	Sum of cations
Sample				cmol/kg				
AFS	13.64	0.0005	0.66	2.88	0.01	0.19	0.01	17.38
CFS	9.94	0.0008	0.94	1.77	0.06	0.12	0.05	12.88
WPC	10.28	0.0012	10.41	1.91	0.14	1.94	0.02	24.69

APPENDIX D. SUPPLEMENTARY INFORMATION FOR CHAPTER 5

Supporting Methods and Materials

Characterization

Morphological analysis

High-resolution transmission electron microscopy (HR-TEM) images and selected area electron diffraction (SAED) patterns were obtained by using a JEM-ARM200cF S/TEM microscope, operated at 200kV. Samples were prepared using ultrathin C film on holey carbon support films of 400 mesh on Cu (from Ted Pella, Inc., Prod No. 01824) and support films of lacey formar/carbon of 200 mesh on Cu (from from Ted Pella, Inc., Prod No. 01881-F).

Dynamic light scattering (DLS) and Zeta potentials measurement

DLS and Zeta potential was obtained using a Malvern Instrument Zetasizer Nano ZS equipped with a 633 nm laser (Westborough, Massachusetts, USA). Zeta potentials were measured in 173˚ backscatter mode at different pH, using the Smoluchowski equation (Hunter, 1981).

Mössbauer spectrometry analysis

Five Cr containing MNP-BC samples (Table D.S5.1), were stored in the dark at -20 °C prior to analysis. For Mössbauer sample preparation, the samples were thawed until viscous and approximately 70 mg of the wet sample was transferred into plexiglas holders (1 cm^2) and frozen. Frozen samples were fixed and sealed with airtight and cold-resistance Kapton tape and kept at -20 °C until measurement. Samples were transferred to the instrument (WissEL, Gmbh) and loaded inside a closed-cycle exchange gas cryostat (Janis cryogenics). After completion of the analysis, the material was immediately transferred back to the freezer. All five spectra were recorded at 140 K, which is the standard temperature for measuring magnetite containing samples as it falls above the Verwey transition (~121 K), and should be low enough to ensure

superparamagnetic magnetite is fully magnetically ordered (Gorski et al., 2010). Measurements for all eight samples were collected using a constant acceleration drive system in transmission mode with a ^{57}Co/Rh source and calibrated against a 7μm thick α-^{57}Fe foil measured at room temperature. All spectra were analyzed using Recoil (University of Ottawa) by applying a Voigt Based Fitting (VBF) routine (Rancourt et al., 1991). The half width at half maximum (HWHM) was fixed to a value of 0.13 mm/s for all samples.

Table D.S5.1. Sample list

Sample Number	Sample Description
1	10 mM Fe + 0.5 gL^{-1} BC + 350 μM Cr(VI) at time = 0
2	10 mM Fe + 0.5 gL^{-1} BC + 350 μM Cr(VI) at time = 2 days
3	10 mM Fe + 0.5 gL^{-1} BC + 350 μM Cr(VI) at time = 4 days
4	2 mM Fe + 1 gL^{-1} BC + 170 μM Cr(VI) at time = 0
5	2 mM Fe + 1 gL^{-1} BC + 170 μM Cr(VI) at time = 1 day

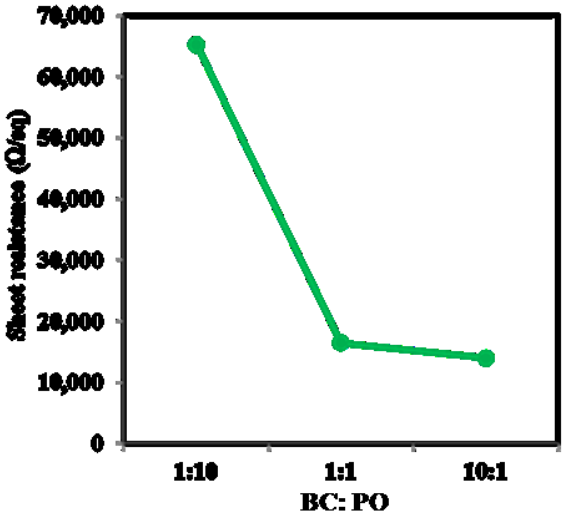

Figure D.S5.1. Sheet resistance of BC at different concentration.

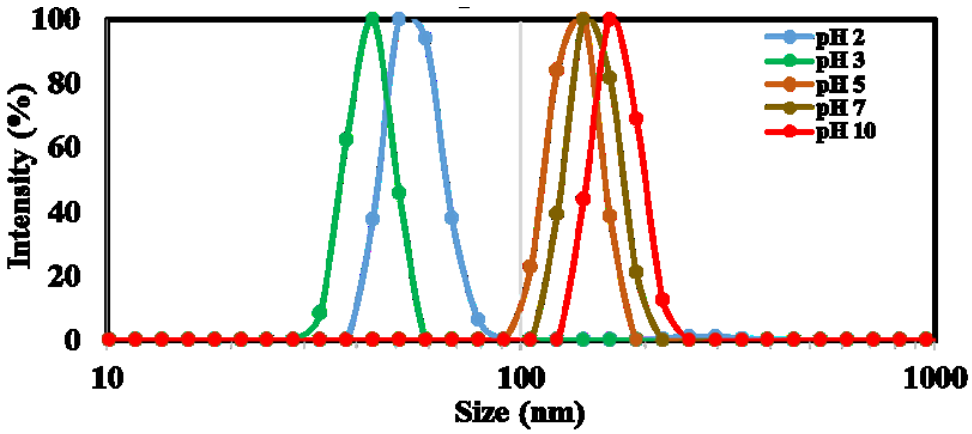

Figure D.S5.2. Size distribution of MNPs at different pH conditions.

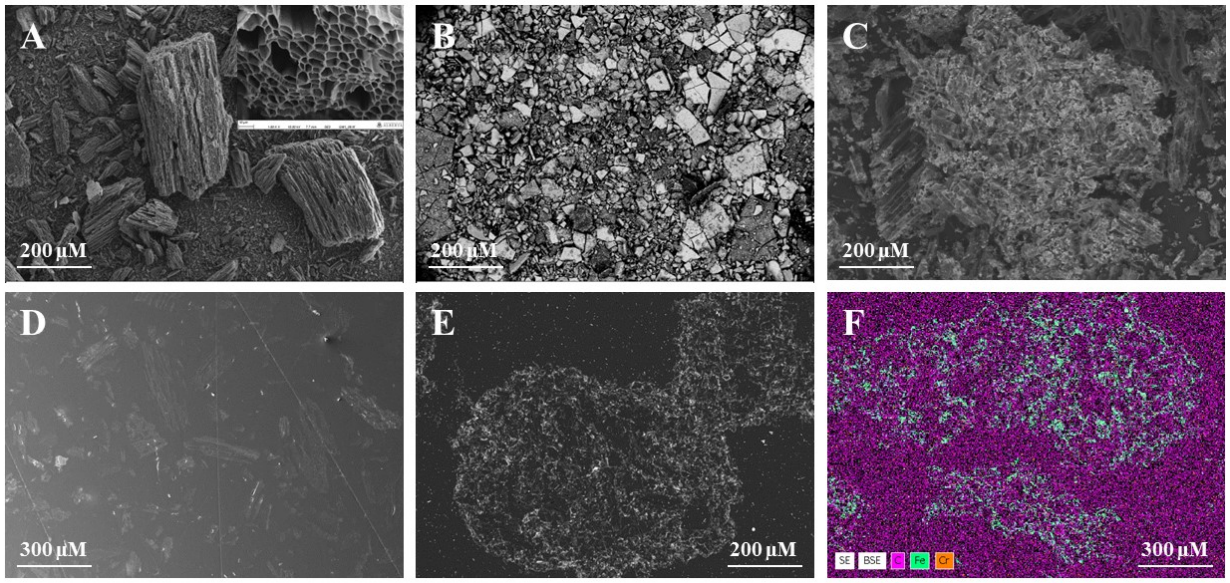

Figure D.S5.3. SEM images of (A) BC; (B) MNPs; (C) MNP-BC (high Fe concentration); (D) back scattered electron (BSE) map of BC in thin section; (E) BSE map of MNP-BC in thin section; and (F) EDS of MNP-BC.

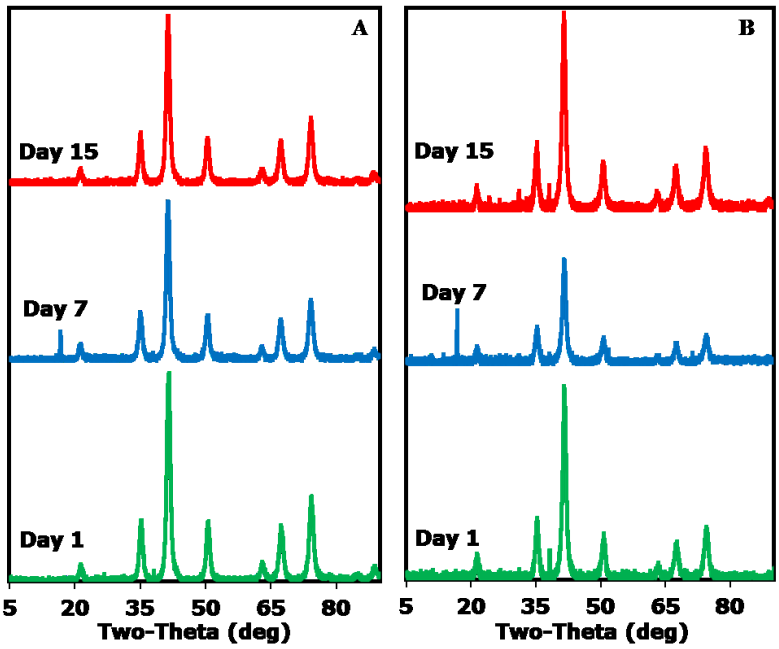

Figure D.S5.4. XRD patterns of (A) MNPs and (B) MNP-BC.

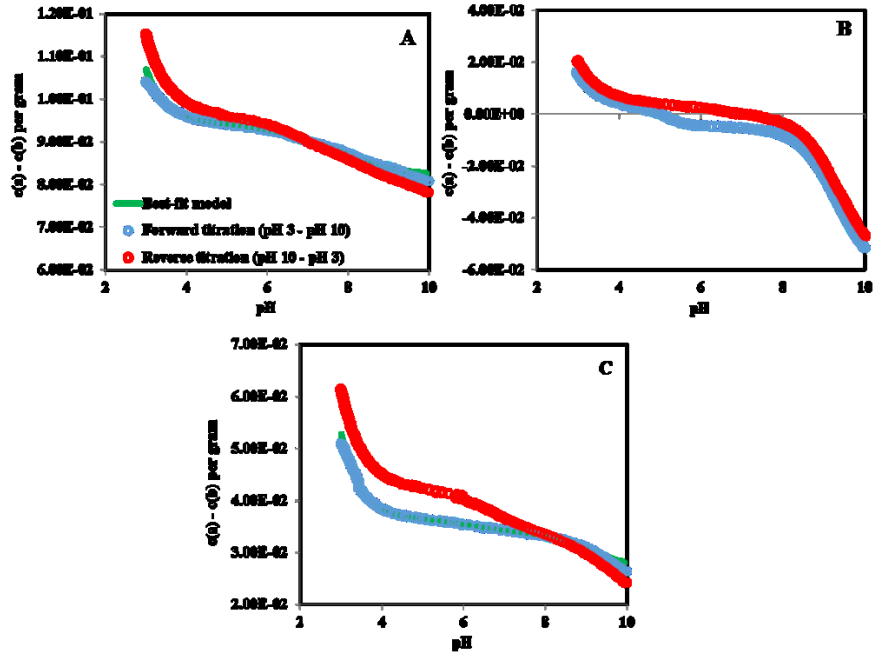

Figure D.S5.5. Potentiometric titration of (A) BC; (B) MNPs and (C) MNP-BC.

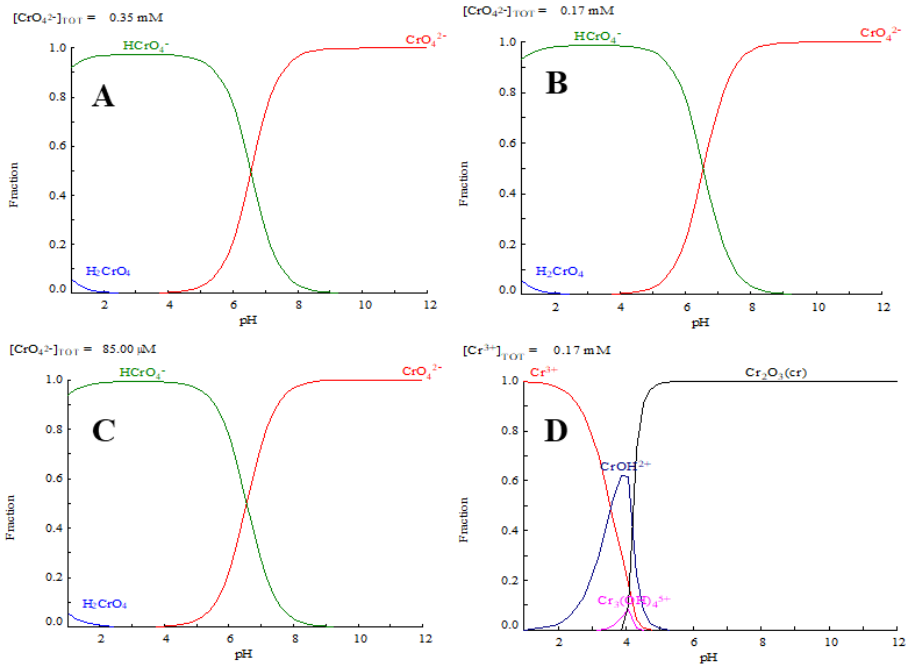

Figure D.S5.6. Speciation diagram of Cr(VI) and Cr(III). (A) 350 µM Cr(VI); (B) 170 µM Cr(VI); (C) 85 µM Cr(VI) and (D) Cr(III).

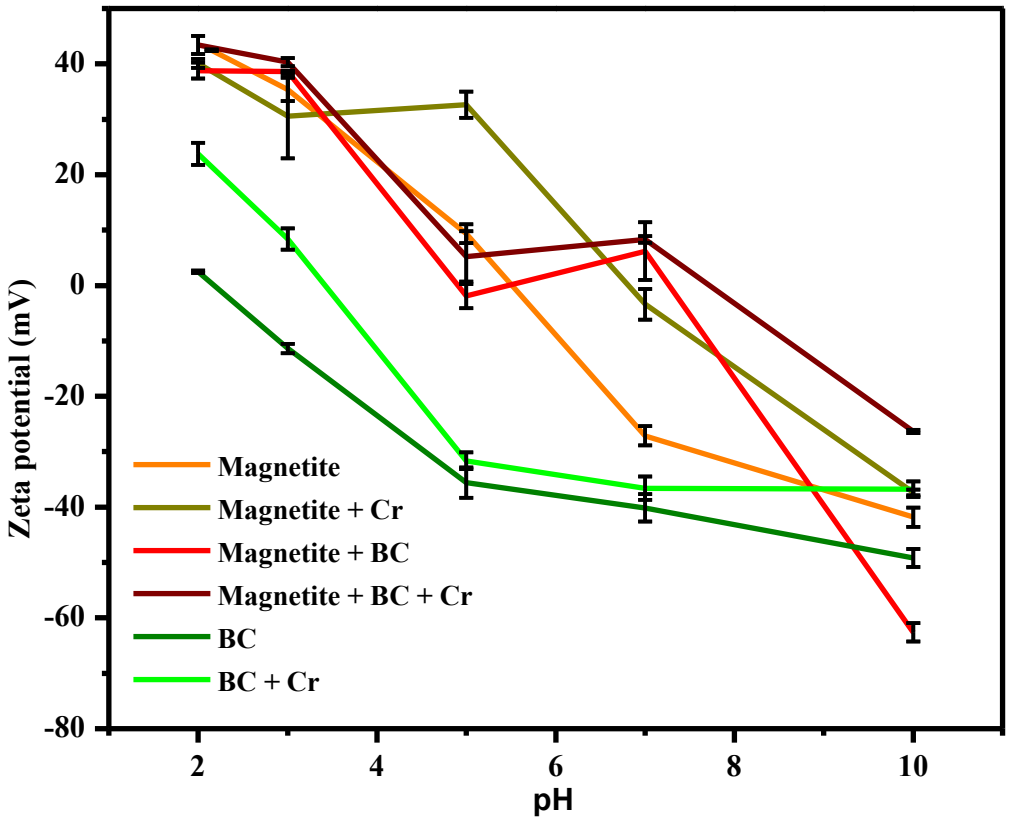

Figure D.S5.7. Zeta potentials of MNPs, MNP-BC and BC with and without Cr-sorption.

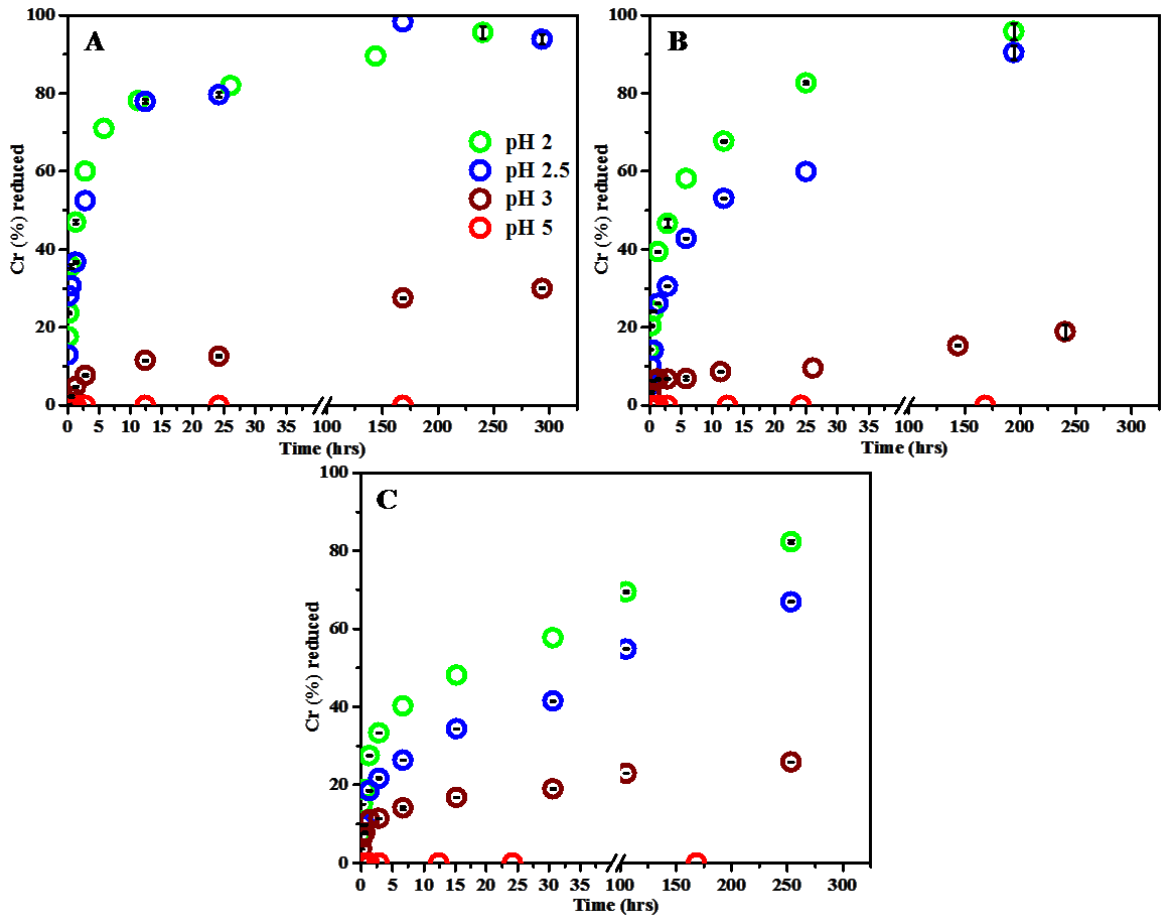

Figure D.S5.8. Cr(VI) reduction by 1 gL^{-1}BC at different pH conditions. (A) 350 µM Cr(VI); (B) 170 µM Cr(VI) and (C) 85 µM Cr(VI).

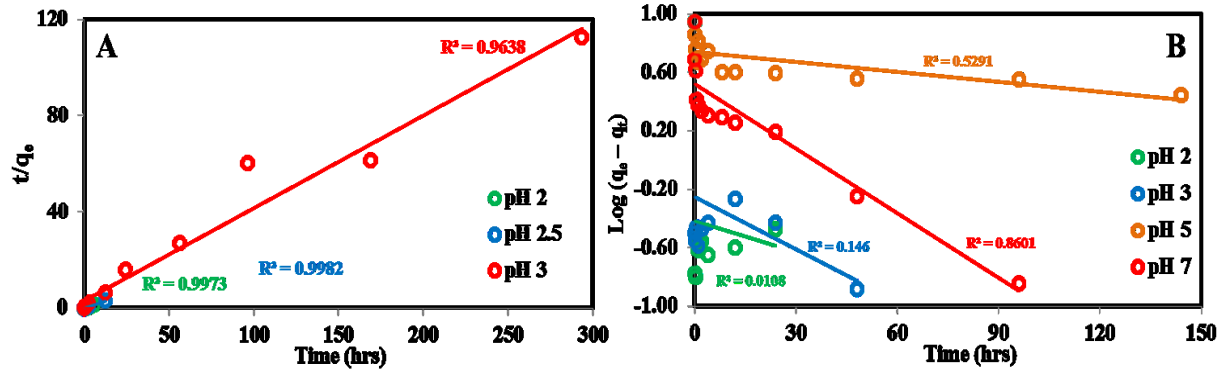

Figure D.S5.9. Adsorption kinetics for Cr(VI) adsorption on BC and MNP-BC. (A) Cr(VI) adsorption on BC fitted with pseudo-second-order and (B) Cr(VI) adsorption on MNP-BC fitted with pseudo-first-order models.

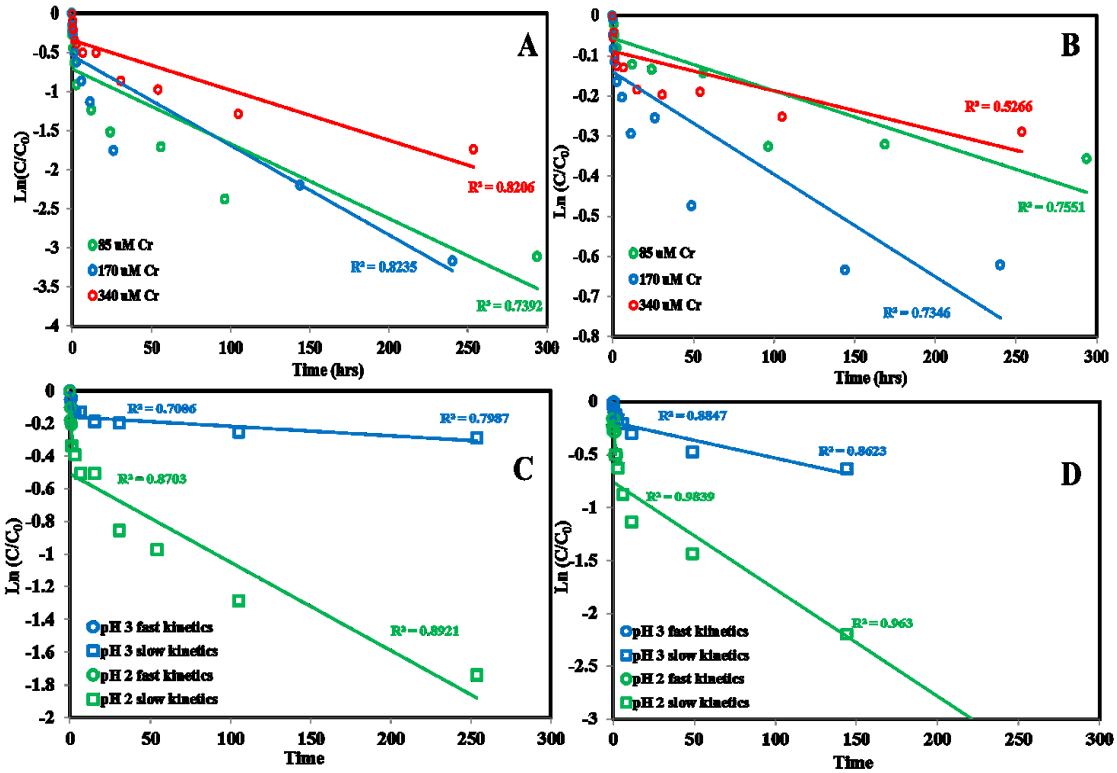

Figure D.S5.10. Reduction kinetics for Cr(VI) reduction by BC at different Cr concentrations and pH conditions. (A,B) Cr(VI) reduction on BC fitted with pseudo-first-order model at pH 2 and 3, respectively, and (C,D) Cr(VI) reduction on BC fitted with pseudo-first-order model using fast and slow kinetics at pH 2 and 3, respectively.

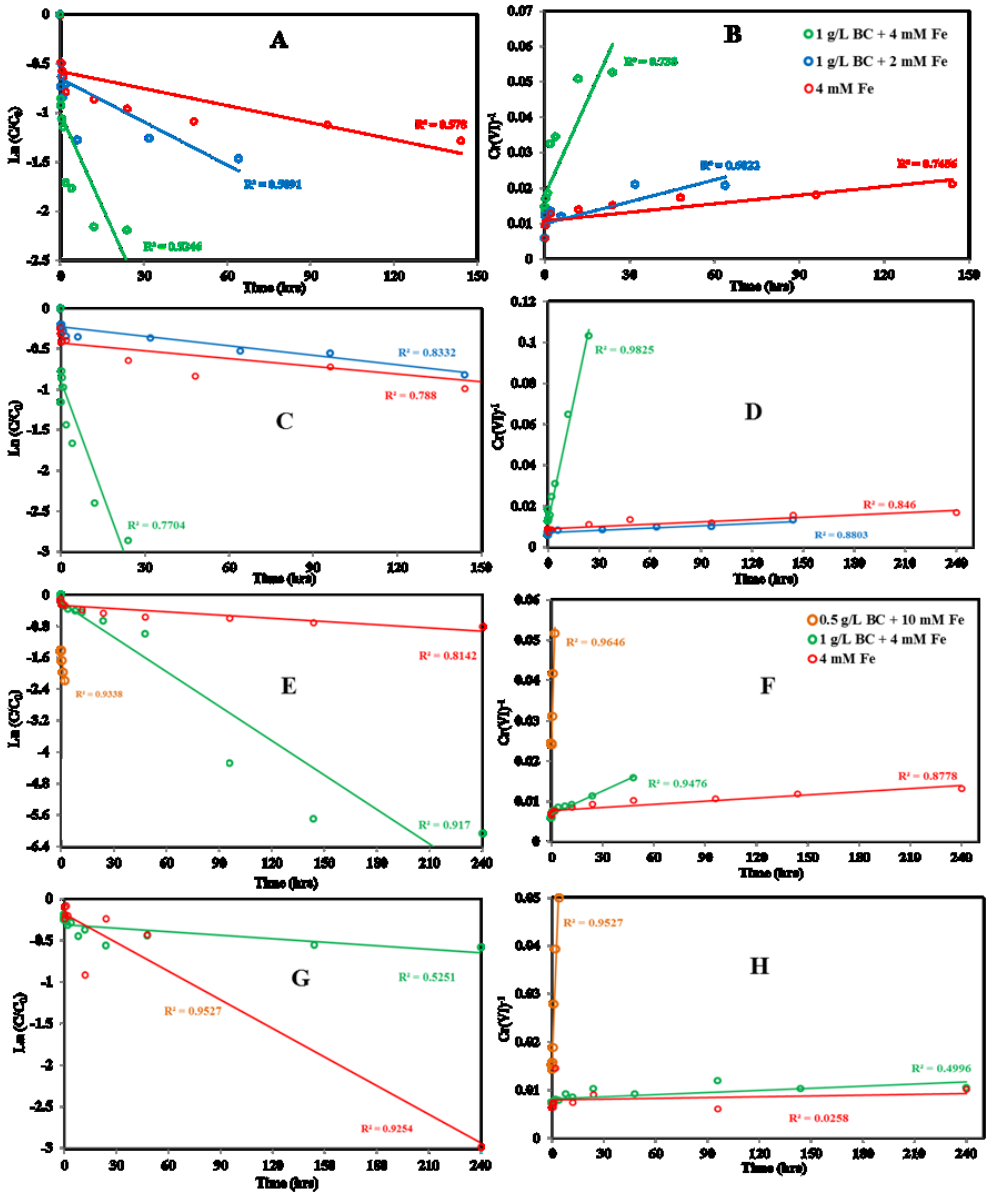

Figure D.S5.11. Reduction kinetics for Cr(VI) reduction by MNP-BC and MNPs at different concentrations and pH conditions. (A,B) pseudo-first-order and second order model at pH 2; (C,D) pseudo-first-order and second order model at pH 3; (D,E) pseudo-first-order and second order model at pH 5 and (E,F) pseudo-first-order and second order model at pH 7, respectively.

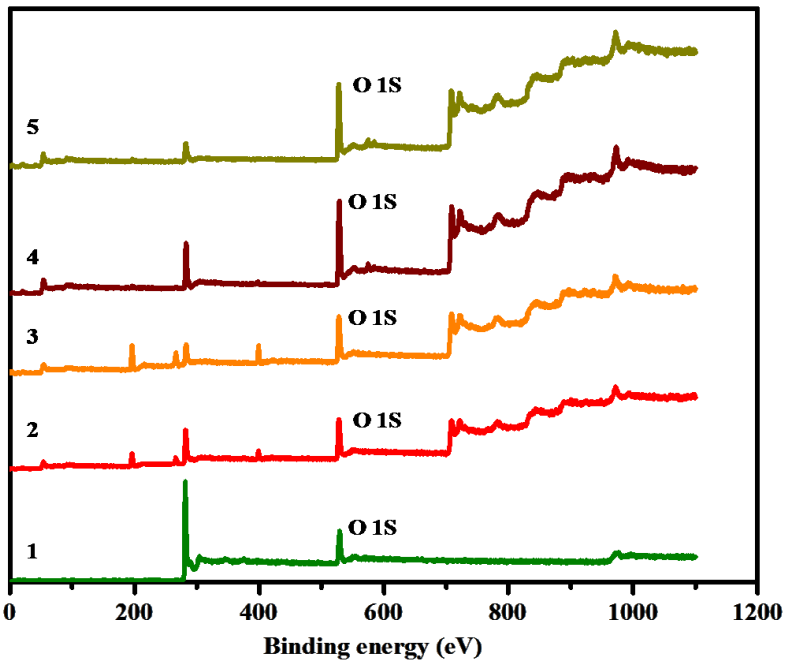

Figure D.S5.12. XPS survey O 1s spectra. (1) WS; (2) MNP-BC; (3) MNPs; (4) Cr-sorbed MNP-BC and (5) Cr-sorbed MNPs

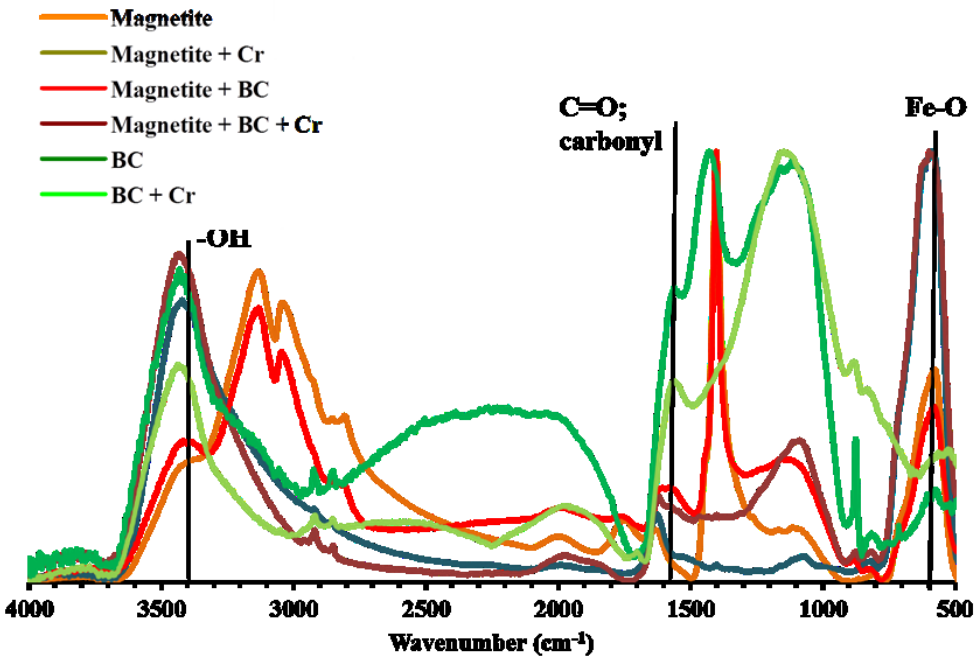

Figure D.S5.13. FT-IR spectra of MNPs, MNP-BC and BC with, and without, Cr-sorption.

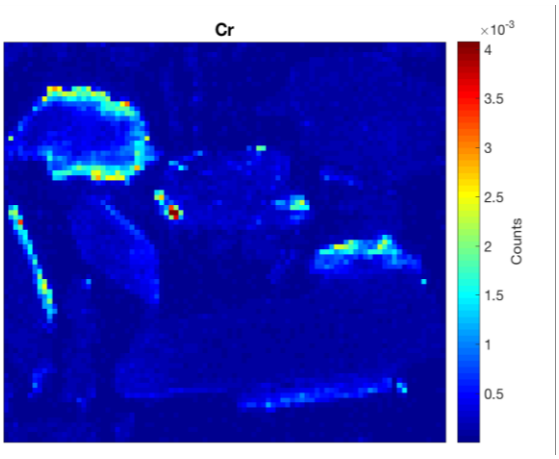

Figure D.S5.14. XRF map of Cr distribution onto BC.

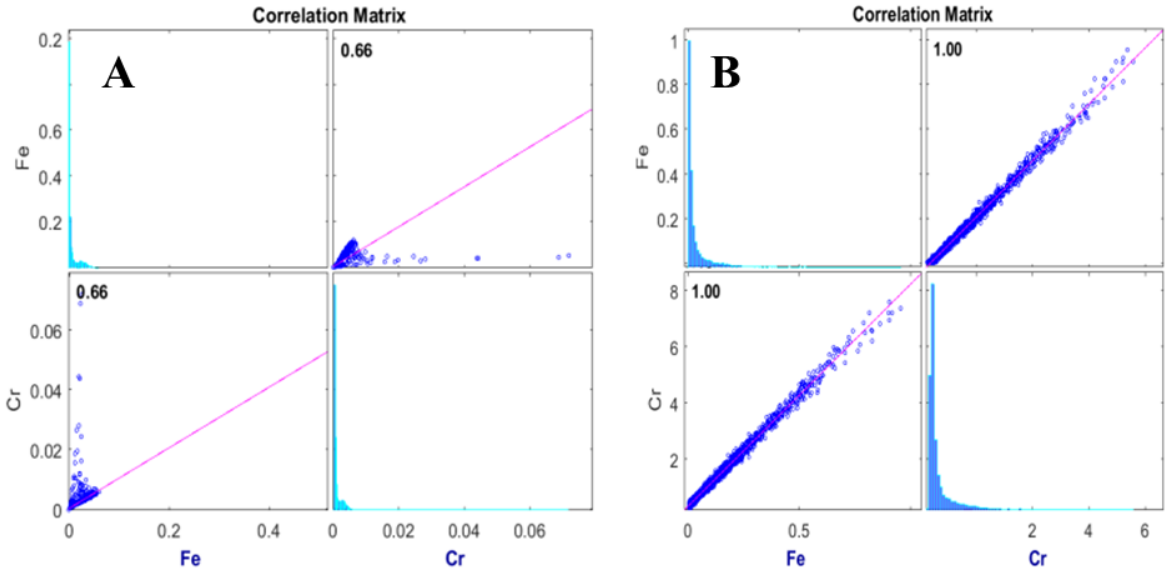

Figure D.S5.15. Correlation matrix of Fe in MNP-BC with adsorbed Cr at different pH conditions. (A) pH 5 and (B) pH 7.

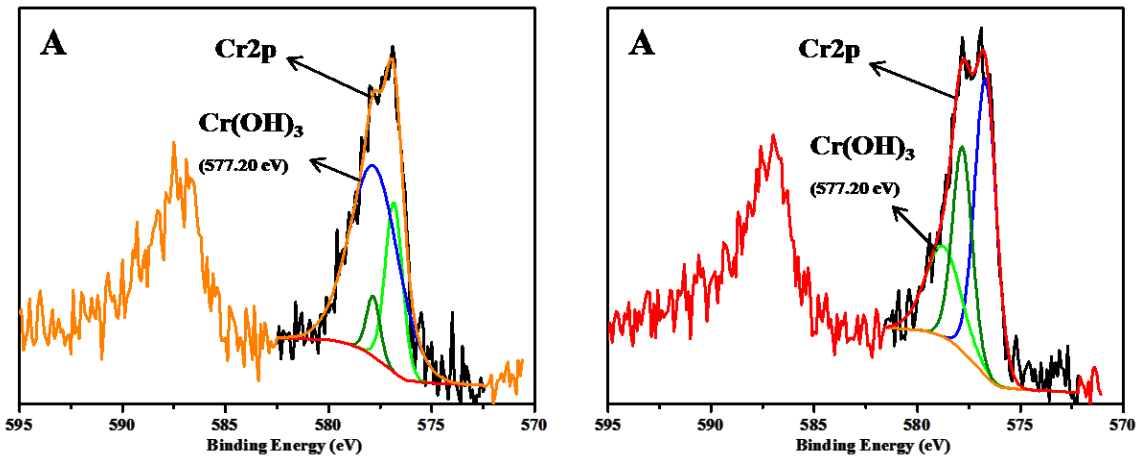

Figure D.S5.16: Cr 2p XPS spectra of Cr(VI) loaded (A) MNPs and (B) MNP-BC.

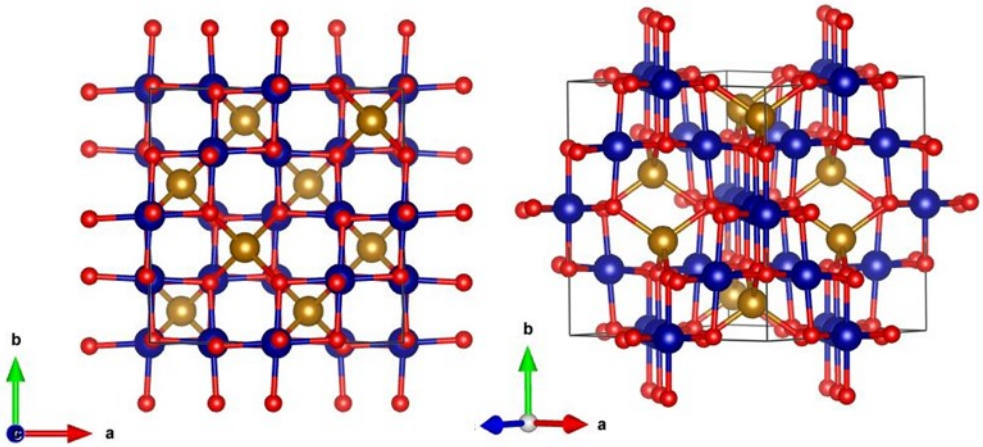

Figure D.S5.17. The projection of XANES modeled Cr_2FeO_4 structure along the crystallography "c" axis and a 3D view of structure formed on the surface of MNPs and MNP-BC.

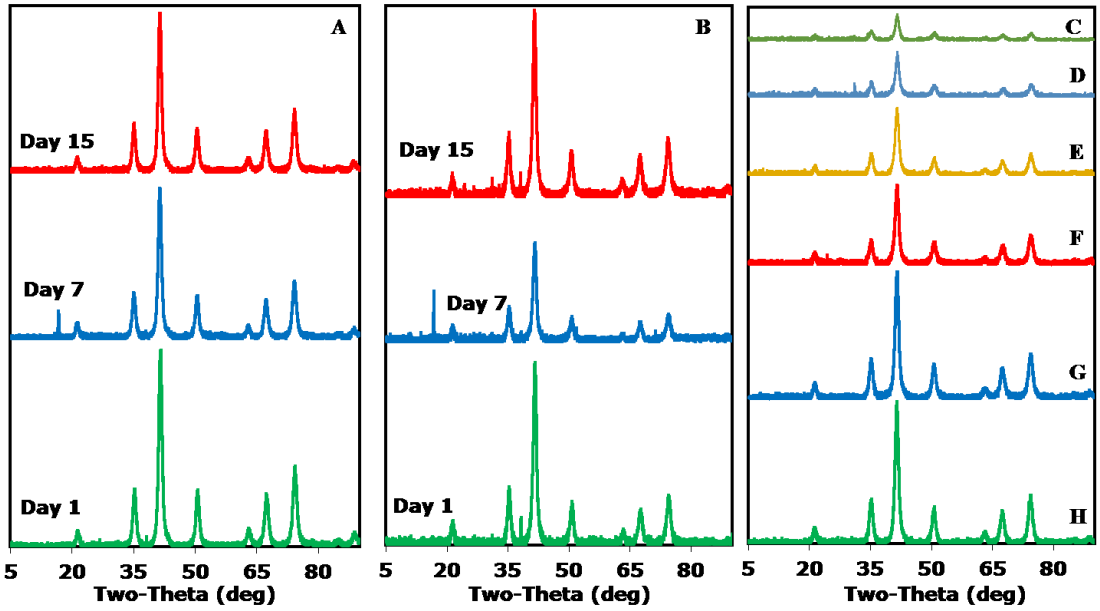

Figure D.S5.18. XRD patterns of MNPs and MNP-BC over time with or without Cr sorption. (A) Pure MNPs; (B) MNP-BC; (C) 2 mM Fe + 1 gL^{-1} BC + 170 µM Cr(VI) at t = 2 days; (D) 2 mM Fe + 1 gL^{-1} BC + 170 µM Cr(VI) at t = 0; (E) 10 mM Fe + 0.5 gL^{-1} BC + 350 µM Cr(VI) at t = 4 days; (F) 10 mM Fe + 0.5 gL^{-1} BC + 350 µM Cr(VI) at t = 0; (G) 10 mM Fe + 350 µM Cr(VI) at t = 4 days and (H) 10 mM Fe + 350 µM Cr(VI) at t = 0 days. The time with Cr samples represents reaction time.

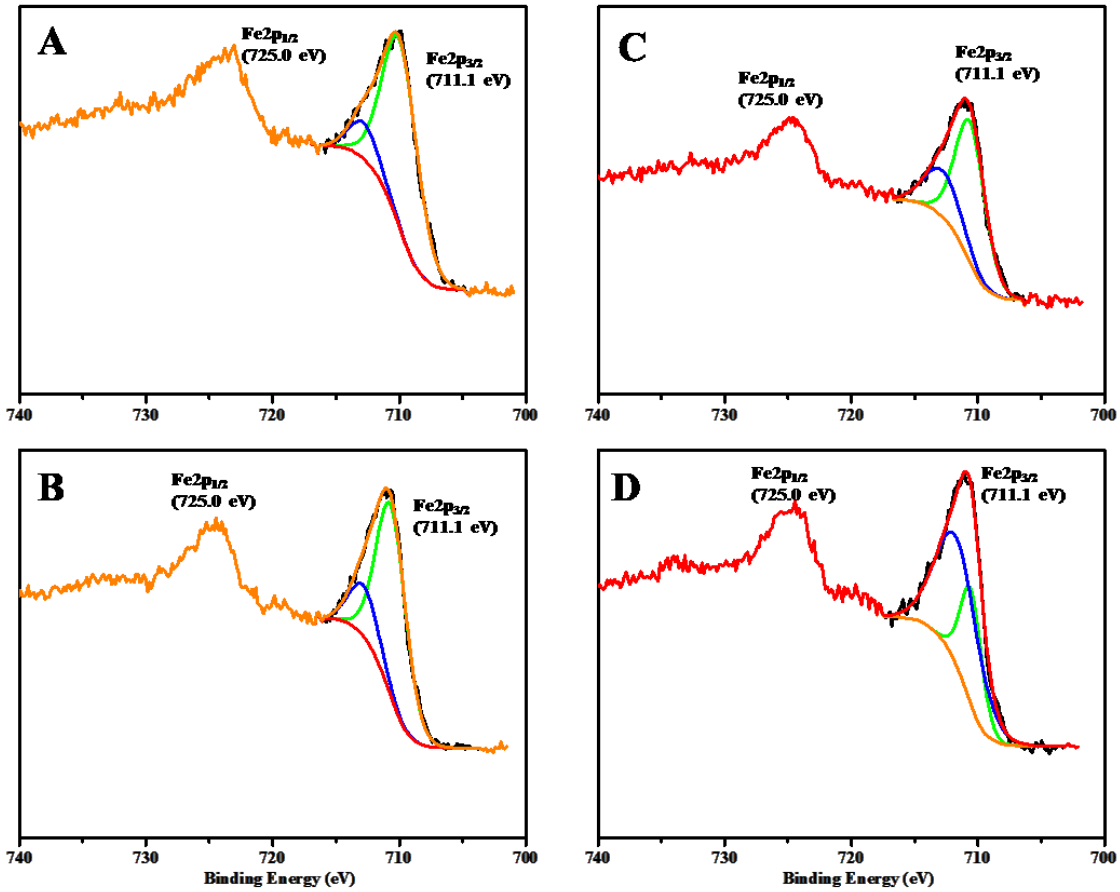

Figure D.S5.19. Fe 2p XPS spectra of MNPs and MNP-BC with or without Cr sorption. (A) Pure MNPs; (B) Cr-loaded MNPs; (C) Pure MNP-BC and (D) Cr-loaded MNP-BC.

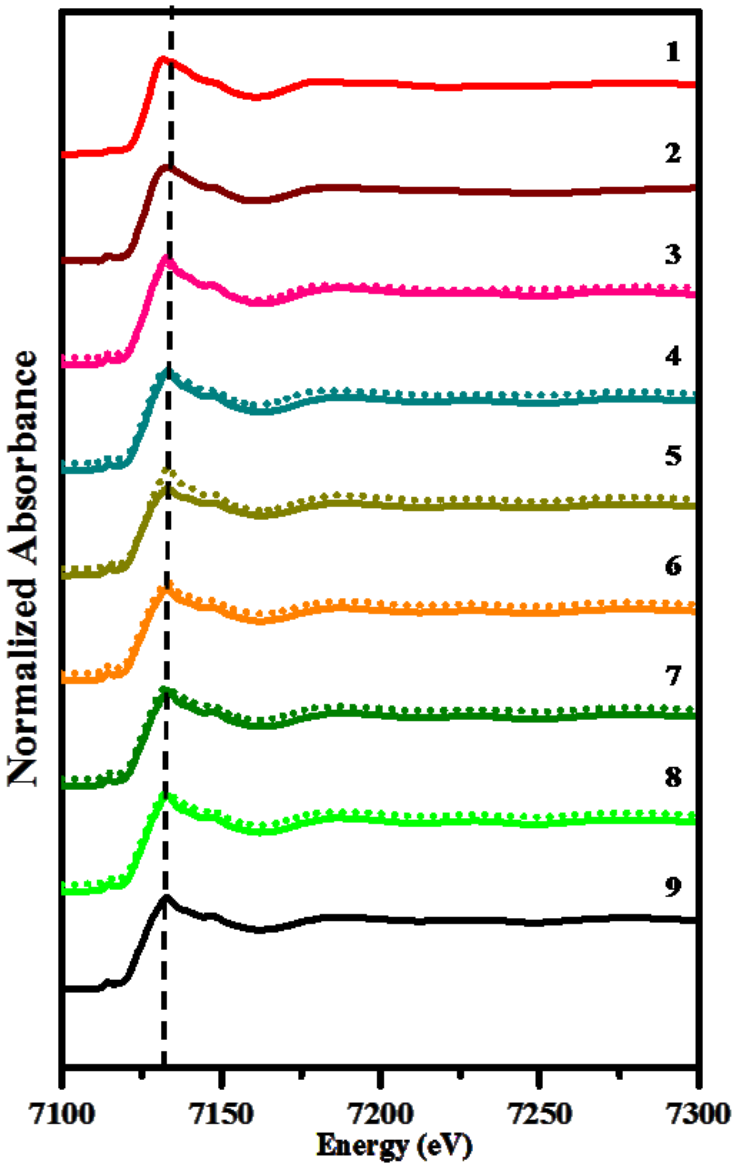

Figure D.S5.20. Fe K-edge XANES spectra of Fe references and Cr-loaded MNP-BC and MNPs. **(1)** Goethite standard; **(2)** Ferrihydrite standard; **(3)** 4 mM Fe + 1 gL^{-1} BC + 350 µM Cr(VI) at t = 4 days; **(4)** 4 mM Fe + 1 gL^{-1} BC + 350 µM Cr(VI) at t = 0; **(5)** 10 mM Fe + 350 µM at t = 4 days; **(6)** 10 mM Fe + 350 µM at t = 0; **(7)** 10 mM Fe + 1 gL^{-1} BC + 350 µM Cr(VI) at t = 4 days; **(8)** 10 mM Fe + 1 gL^{-1} BC + 350 µM Cr(VI) at t = 0 and **(9)** Magnetite standard. Experiments were conducted at pH 7. The time with Cr samples represents reaction time.

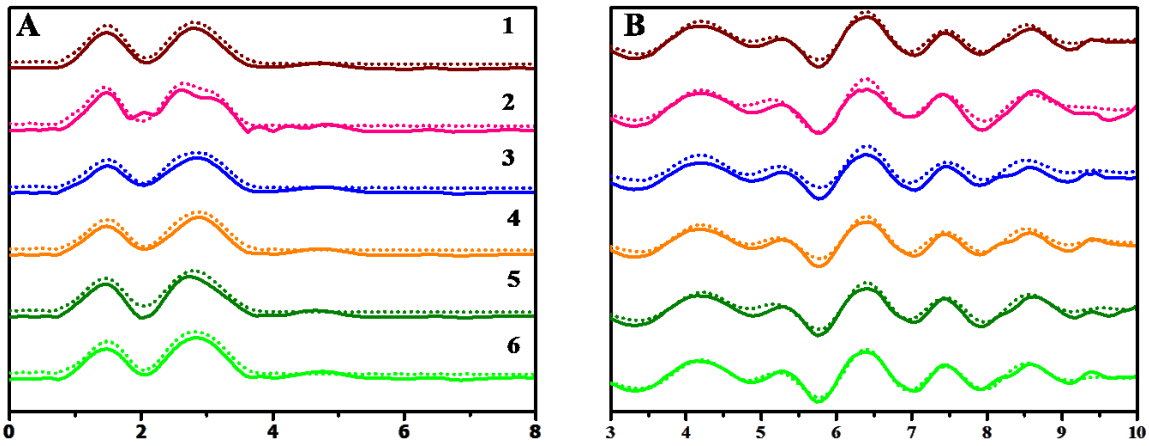

Figure D.S5.21. Fe K-edge EXAFS signals weighted by (A) the radial distribution function of Cr-loaded samples and (B) k^3 spectra. **(1)** 4 mM Fe + 1 gL-^{1} BC + 350 µM Cr(VI) at t = 4 days; **(2)** 4 mM Fe + 1 gL-^{1} BC + 350 µM Cr(VI) at t = 0; **(3)** 10 mM Fe + 350 µM at t = 4 days; **(4)** 10 mM Fe + 350 µM at t = 0; **(5)** 10 mM Fe + 1 gL^{-1} BC + 350 µM Cr(VI) at t = 4 days and **(6)** 10 mM Fe + 1 gL^{-1} BC + 350 µM Cr(VI) at t = 0. Experiments were conducted at pH 7. The time with Cr samples represents reaction time.

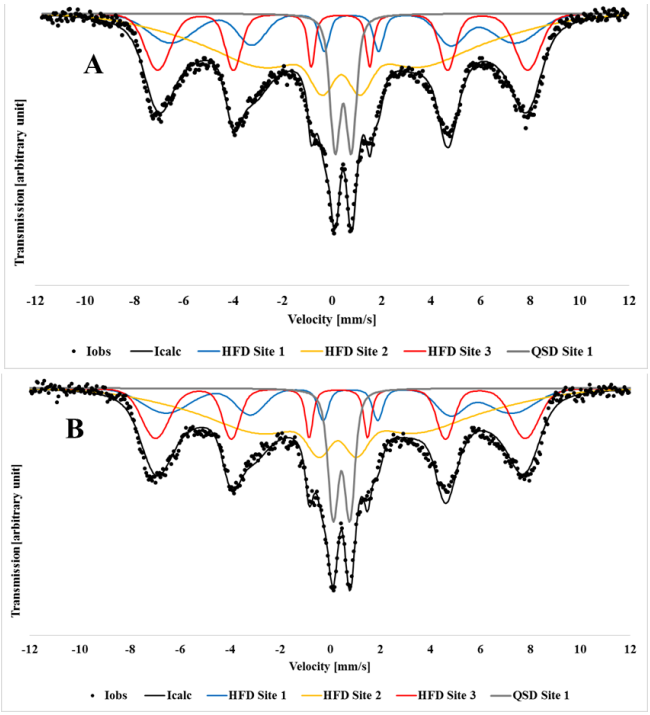

Figure D.S5.22. Mössbauer spectroscopy of Cr-loaded MNP-BC (2 mM Fe + 1 gL^{-1} BC + 170 µM Cr(VI)) at different reaction time with Cr(VI). (A) t = 0 and (B) t = 1 day.

Table D.S5.2. Elemental composition, molar ratio, BET surface area, TOC and DOC of BC.

Properties	**BC**
%C	76.6
%H	1.6
%O	10.2
%N	0.6
Molar H/C	0.3
Molar O/C	0.1
Surface area m^2/g	319
TOC (w/w%)	73
DOC (mg/L)	28

Table D.S5.3. pKas and site concentrations of BC, MNPs and MNP-BC.

Adsorbents	Total Sites	$logK_1$	$logK_2$	$logK_3$	Site 1 concentration (mol/g)	Site 2 concentration (mol/g)	Site 3 concentration (mol/g)
BC	3	2.4	6.3	8.3	8.8E-04	4.2E-04	6.3E-04
MNPs	2	5	6.2		3.2E-03		
MNP-BC	3	2.8	6.3	9.08	1.4E-03	2.5E-04	6.0E-04

Table D.S5.4. Kinetics rate constants of Cr(VI) adsorption on BC and MNP-BC.

Materials	C_0	pH	Pseudo-first-order model		Pseudo-second-order model	
			K_1 (hr^{-1})	R^2	K_2 (g/mg.hr)	R^2
BC	85 µM	2	0.28	0.96	0.25	0.99
		2.5	0.11	0.90	0.23	0.99
		3	0.001	0.70	0.38	0.96
MNP-BC		2	0.006	0.01	0.12	1
(4 mM Fe +	170 µM	3	0.02	0.1	0.11	0.99
1 gL^{-1} BC)		5	0.01	0.86	0.13	0.93
		7	0.002	0.5	0.20	0.96

Table D.S5.5. The fitted parameters of intraparticle diffusion model for Cr(VI) adsorption on BC and MNP-BC.

Materials	C_0	pH	K_1 (mg $g^{-1}hr^{-0.5}$)	R^2	K_2 (mg $g^{-1}hr^{-0.5}$)	R^2	K_3 (mg $g^{-1}hr^{-0.5}$)	R^2
BC	85 µM	2	3	0.85	0.21	0.8	NA	NA
MNP-BC (4 mM Fe + 1 gL^{-1} BC)	170 µM	7	9.6	0.9	0.4	0.95	0.3	0.96

Table D.S5.6. Kinetics rate constants of Cr(VI) reduction by BC.

Materials	C_0	pH	Pseudo-first-order model		Pseudo-first-order model (fast)		Pseudo-first-order model (slow)		Pseudo-first-order model (fast)		Pseudo-first-order model (slow)	
			K_{1obs} (hr^{-1})	R^2	K_{1obs} (hr^{-1})	R^2	K_{2obs} (hr^{-1})	R^2	K_{1int} (hr^{-1})	R^2	K_{2int} (hr^{-1})	R^2
BC	85 µM	2	0.0096	0.73				NA				
		3	0.0013	0.75								
	170 µM	2	0.012	0.82	0.27	0.98	0.01	0.96	0.5	1	0.5	1
		3	0.0026	0.73	0.085	0.88	0.003	0.86				
	350 µM	2	0.0064	0.82	0.21	0.87	0.005	0.89	0.6	1	0.9	1
		3	0.001	0.52	0.05	0.70	0.006	0.80				

Table D.S5.7. Kinetics rate constants of Cr(VI) reduction by MNP-BC and MNPs.

Materials	C_0	pH	Second-order model	
			K_{obs} (μMhr^{-1})	R^2
10 Fe + 0.5 gL^{-1} BC	170 µM	5	0.014	0.96
		7	0.0094	0.95
4 mM Fe + 1 gL^{-1} BC	170 µM	2	0.0018	0.74
		3	0.0039	0.98
		5	0.0002	0.95
	170 µM	7	1E-05	0.50
2 mM Fe + 1 gL^{-1} BC		2	0.0002	0.68
		3	4E-05	0.88
		5	6E-06	0.20
		7	2E-06	0.11
4 mM Fe	170 µM	2	8E-05	0.75
		3	4E-05	0.86
		5	3E-05	0.87
		7	5E-06	0.02

Table D.S5.8. The linear combination fitting (LCF) results for Cr K-edge XANES spectra of Cr-laden samples.

Samples	Reference materials' proportion samples (%)		
	K_2CrO_7	$Cr(OH)_3$	Cr(III)acetate
1 g L^{-1} BC + 170 µM Cr(VI) at pH 2	Nil	85	15
1 g L^{-1} BC + 170 µM Cr(VI) at pH 3	10	88	2
10 mM Fe + 350 µM Cr(VI) at pH 5	Nil	100	Nil
10 mM Fe + 350 µM Cr(VI) at pH 7	Nil	100	Nil
10 Fe + 0.5 gL^{-1} BC + 350 µM Cr(VI) at pH 5	Nil	100	Nil
10 Fe + 0.5 gL^{-1} BC + 350 µM Cr(VI) at pH 7	Nil	100	Nil
4 Fe + 1 gL^{-1} BC + 350 µM Cr(VI) at pH 5	12	82	6
2 Fe + 1 gL^{-1} BC + 350 µM Cr(VI) at pH 7	Nil	92	8

Table D.S5.9. Fe K edge EXAFS fitting results at different reaction time with Cr(VI).

Samples	Paths	CN	R(Å)	σ^2 (Å^2)
10 mM Fe + 0.5 gL^{-1} BC + 350 µM Cr(VI) at t = 0	Fe-O	4.5	1.94	0.009
	Fe-Fe	3.0	2.99	0.008
	Fe-Fe	5.4	3.46	0.009
	Fe-O	3.3	3.53	0.01
10 mM Fe + 0.5 gL^{-1} BC + 350 µM Cr(VI) at t = 2 days	Fe-O	4.5	1.92	0.009
	Fe-Fe	3.0	2.99	0.008
	Fe-Fe	4.9	3.45	0.009
	Fe-O	2.5	3.52	0.001
10 mM Fe + 350 µM Cr(VI) at t = 0	Fe-O	4.1	1.94	0.009
	Fe-Fe	2.2	2.99	0.008
	Fe-Fe	5.1	3.46	0.009
	Fe-O	3.8	3.53	0.001
10 mM Fe + 350 µM Cr(VI) at t = 2 days	Fe-O	3.9	1.95	0.0097
	Fe-Fe	2.4	2.97	0.008
	Fe-Fe	5.0	3.45	0.0085
	Fe-O	3.0	3.53	0.01
4 mM Fe + 1 gL^{-1} BC + 350 µM Cr(VI) at t = 0	Fe-O	5.1	1.91	0.009
	Fe-Fe	3.7	2.97	0.008
	Fe-Fe	5.3	3.46	0.009
	Fe-O	1.2	3.52	0.01
4 mM Fe + 1 gL^{-1} BC + 350 µM Cr(VI) at t = 2 days	Fe-O	5.1	1.95	0.009
	Fe-Fe	2.8	2.99	0.008
	Fe-Fe	5.7	3.46	0.008
	Fe-O	4.7	3.58	0.01

Table D.S5.10. The linear combination fitting (LCF) results for Fe K-edge XANES spectra of Cr-laden samples at different reaction time with Cr(VI).

Samples	Reference materials' proportion samples (%)		
	Magnetite	Ferrihydrite	Goethite
4 mM Fe + 1 gL^{-1} BC + 350 µM Cr(VI) at t = 4 days	40	Nil	60
4 mM Fe + 1 gL^{-1} BC + 350 µM Cr(VI) at t = 0	100	Nil	Nil
10 mM Fe + 350 µM Cr(VI) at t = 4 days	100	Nil	Nil
10 mM Fe + 350 µM Cr(VI) at t = 0	100	Nil	Nil
10 mM Fe + 1 gL^{-1} BC + 350 µM Cr(VI) at t = 4 days	70	10	20
10 mM Fe + 1 gL^{-1} BC + 350 µM Cr(VI) at t = 0	100	Nil	Nil